Institute of Thermal Engineering

TU Graz
Graz University of Technology

Development of Numerical Models in order to predict Convective Air Flow and Combined Heat Transfer Effects for Functional Façade Applications

Performed for the purpose of attainment the academic degree of a

Doctor of Engineering Sciences

by

Dipl.-Ing. Daniel Brandl

Submitted at the Graz University of Technology

Faculty of Mechanical Engineering and Economic Sciences

Graz, May, 2017

This dissertation has been approved by:

- Univ.-Prof. Dr. Christoph Hochenauer (Graz University of Technology)

- Univ.-Prof. DDr. Peter Kautsch (Graz University of Technology)

Eidesstattliche Erklärung

Ich erkläre an Eides statt, dass ich die vorliegende Arbeit selbstständig verfasst, andere als die angegebenen Quellen/Hilfsmittel nicht benutzt, und die den benutzten Quellen wörtlich und inhaltlich entnommenen Stellen als solche kenntlich gemacht habe. Das in TUGRAZonline hochgeladene Textdokument ist mit der vorliegenden Dissertation identisch.

Affidavit

I declare that I have authored this thesis independently, that I have not used other than the declared sources/resources, and that I have explicitly indicated all material which has been quoted either literally or by content from the sources used. The text document uploaded to TUGRAZonline is identical to the present doctoral dissertation.

_____	_____
Datum / Date	Unterschrift / Signature

Danksagung

Abstract

The need to avoid using fossil fuels in order to reduce CO_2 emissions has led to increasing demand for renewable energy sources for the energy supply of buildings. For example, it is already common to install photovoltaic panels on buildings' roofs in order to generate electricity, or to install solar thermal collectors to generate hot water. Establishing a dominant supply of solar energy can only be achieved by also using buildings' facades for solar energy conversion. However, the integration of solar energy conversion technologies into facades can lead to the massive disturbance of both the thermal behaviour and flow characteristic of the façade constructions. It is essential to have a detailed understanding of the thermal effects and the fluid dynamics of these technologies, both for scientific advancement, and for the realization of this new generation of façade systems.

For this reason, this work focuses on the modelling and numerical simulation of thermal behaviour and convective airflow characteristics. With the help of Computational Fluid Dynamics (CFD), the thermal behaviour and the fluid dynamics in façade systems are considered in great detail, and are compared with measured data from laboratory experiments and field tests. In the course of this work, different modelling approaches were selected and developed further with the help of case studies.

In the initial investigation, stationary and two-dimensional CFD models were created in order to determine the still-unidentified combined heat transfer effects and air flow characteristics inside historical box-type windows (BTW). Based on simulation results in addition to data from in-situ measurements, concepts for thermal improvement were established and evaluated. The results of this evaluation can be used to improve the refurbishment market, where the number of BTWs requiring refurbishment is estimated to be more than one hundred million pieces in Europe alone.

The two-dimensional CFD model was subsequently developed into a three-dimensional model in the course of the analysis of thermal behaviour and flow characteristics inside a complex multifunctional façade system. During the design and assembly of a prototype multifunctional façade, different CFD models were developed to determine the impact of PV modules, solar thermal collectors, shading devices, and periphery ventilation openings on the thermal behaviour of the façade. The simulation results were then compared with the data collected from a test façade containing a variety of measurement sensors.

The next step in the development from stationary to transient three-dimensional CFD models was to investigate the thermal behaviour and flow characteristics of a solar passive façade system (using a solar honeycomb made of cellulose) with integrated PV cells. One of the main objectives was to determine the proper arrangement of the PV cell, which provides a high electrical output without counteracting the effect of the solar honeycomb.

The CFD models developed in this dissertation were compared and assessed in terms of their applicability, simulation duration, and model size.

Kurzfassung

Die Notwendigkeit den Einsatz fossiler Energieträger zu vermeiden und den CO_2 Ausstoß zu reduzieren lässt den Druck zur Nutzung erneuerbarer Energiequellen für die Energieversorgung von Gebäuden stetig steigen. So ist es bereits üblich solarthermische und photovoltaische Anlagen auf Dächern zu installieren um Warmwasser und elektrischen Strom zu generieren. Eine überwiegend solare Energieversorgung von Gebäuden kann aber erst in Betracht gezogen werden, wenn es gelingt auch die Gebäudefassaden für Energiekonversion nutzbar zu machen. Die Integration thermischer Kollektoren oder photovoltaischer Module verändert jedoch das thermische und strömungstechnische Verhalten der Fassadenkonstruktion massiv. Ein detailliertes Verständnis der ablaufenden thermischen, strahlungs- sowie strömungstechnischen Effekte ist essentiell für die wissenschaftliche Weiterentwicklung und in der Folge für die Realisierung dieser neuen Generation an Fassadensystemen.

Aus diesem Grund setzt sich diese Arbeit mit der Modellierung der physikalischen Effekte auseinander, die einen wesentlichen Einfluss auf Fassadensysteme haben. Mit Hilfe der Simulationsmethode der Computational Fluid Dynamics (CFD) lassen sich das thermische Verhalten und die Strömungsvorgänge in Fassadesystemen mit einem hohen Detaillierungsgrad abbilden und mit Messwerten aus Labor- und Feldversuchen vergleichen. Im Zuge der Arbeit wurden unterschiedliche Modellierungsansätze gewählt und anhand von Fallbeispielen weiterentwickelt.

Als Ausgangspunkt der Untersuchungen wurden stationäre zweidimensionale CFD Modelle erstellt, um das bislang noch nicht untersuchte kombinierte Verhalten von Wärmeübergangseffekten und Luftströmungen in historischen Kastenfenstern zu untersuchen. Basierend auf den Simulationsergebnissen und den Messwerten aus einem Versuchsaufbau wurden wärmetechnische Sanierungskonzepte erarbeitet, die einen Beitrag zur Hebung des europaweit auf mehrere hundert Millionen Stück geschätzten Sanierungsmarktes leisten.

Die Weiterentwicklung von der zweidimensionalen in eine dreidimensionale Modellierung wurde auf der Grundlage einer multifunktionalen Fassade durchgeführt. Für einen hierzu entwickelten Prototypen wurden CFD Modelle für unterschiedlichste Fassadenkonfigurationen erstellt und mit den Messwerten einer entsprechenden Testfassade abgeglichen. Dabei wurde der Einfluss von photovoltaischen Paneelen, solarthermischen Kollektoren, Verschattungssystemen sowie peripheren Ventilationsöffnungen auf das thermische und strömungstechnische Verhalten in und im näheren Umfeld der Fassaden untersucht.

Der weiterführende Schritt zur transienten dreidimensionalen Modellierung wurde für eine solar passive Fassade (Solarwabe aus Zellulose) mit integrierten photovoltaischen Zellen durchgeführt. Im Rahmen dieser Untersuchungen wurde in Kombination mit einer Reihe von Versuchen unter Laborbedingungen ein CFD Modell entwickelt mit dem sich das thermische Verhalten sehr gut nachbilden ließ. In weiterer Folge wurde mit Hilfe des CFD Modells eine Optimierung der Anordnung sowie der Anzahl an photovoltaischen Zellen an der Glasabdeckung, unter Berücksichtigung der Aufrechterhaltung eines gewissen Anteils des Aufheizungseffekts an der Solarwabe, durchgeführt.

Im Zuge der in dieser Dissertation zusammengefassten wissenschaftlichen Untersuchungen, wurden die für den jeweiligen Untersuchungsgegenstand entwickelten CFD Modelle bzw. Modellierungsmethoden auch untereinander verglichen. Vergleichsparameter waren zum einen der Aufwand für die Erstellung und Entwicklung der CFD Modelle bzw. Netzgitter, die Simulationsdauer bis zum Erhalt sinnvoller Ergebnissen. Zum anderen wurde auch die Notwendigkeit wichtiger Details in der Modellierung des thermischen Verhaltens für Fassaden aufgedeckt, die je nach Fassadentyp oder vorherrschender klimatischer Einflüsse auf die Fassade stark variieren können.

Table of Contents

Table of Contents

1 Introduction

1.1 Motivation

In the field of building constructions, the development of contemporary building envelopes is about to take a big step forward. In the past, the construction and design processes focused solely on aspects of building physics. Thermal and acoustic protection, as well as the investigation of building moisture, played the most important roles in the design and research of building facades. Nowadays, there is an ambitious movement to extend the functionalities of building facades. The need to reduce carbon dioxide (CO_2) emissions and to avoid using fossil fuels has led to innovative research efforts in the field of building integrated solar energy devices. Due to the limited space on roofs for solar collectors, the building's façade has been of increasing interest to researchers.

The integration of (solar) energy conversion applications in the façade has enhanced the complexity of façade construction systems. The extent to which solar thermal collectors, pipes, and photovoltaic modules influence the physical behaviour of the façade systems is unknown. Furthermore, research is beginning to consider decentralised energy technology to supply offices and residential spaces with heating, cooling, and even ventilation. To an increasing extent, the devices for these functionalities are integrated into the façade system itself.

It is obvious that these façade systems entail an increased level of complexity. The conventional methods and tools used are not sufficient for the design of these façade applications. More sophisticated models have to be developed in order to enable a detailed understanding of the thermal processes, and the flow behaviour both inside and outside the façade construction system. A deep and detailed understanding of the thermal behaviour, radiation processes, and fluid dynamics that occur in all of the façade components implemented must be seen as an indispensable foundation to further developments in this field of research.

1.2 Method

Computational Fluid Dynamics (CFD) is a method that meets all of the postulated requirements and is capable of providing a high-performance base for the development of the sophisticated models required. A central requirement of the method was the ability to create both two-dimensional and three-dimensional transient models. CFD was originally developed and used for the modelling of automotive aerodynamics, combined chemical processes, and flow processes in the industry and mobility sector. The idea of working with a development method not originally devised for the field of buildings physics was an additional motivating factor in the choice of CFD for this investigation. This investigation sought to address research questions from the field of buildings physics by means of methods originally created for the mechanical and thermal engineering research sectors.

This interdisciplinary approach was used to support and facilitate the continuous enhancement of the computing power necessary to develop new and sophisticated models of innovative building facades, which are at the intersection of building physics and energy technology, traditionally considered the research field of mechanical engineering.

1.3 Content

After the presentation of the fundamental numerical basics as well as a short introduction to the field of flow and heat transfer effects in façade systems, this dissertation will describe a variety of CFD models. The content of this dissertation will cover different interrelated approaches, which are illustrated in Figure 1-1. First, different CFD models were used in Chapters 3 through 5. The simulation models evolved from simple "two-dimensional" and "steady state" performance (as addressed by two studies presented in Chapters 3.2 and 3.3) into complex "three-dimensional" models of "transient" behaviour. Stationary three-dimensional models were used in two further studies, which are presented in Chapters 4.2 and Chapter 4.3. Finally, Chapter 5.2 deals with transient three-dimensional CFD models, as a further development of the model used in Chapter 4.3. Additionally, the numerical models used were

enhanced: in particular, with regard to the radiative heat transfer models and the consideration of the solar radiation that occurred in the simulations.

This dissertation also considers different façade types, beginning with "historical box type windows" (presented in Chapter 3.2), on to "multifunctional façade" elements with implemented solar gathering systems (Chapters 3.3 and 4.2) and "integral façade" elements, with both solar radiation converting elements and a solar passive function (Chapters 4.3 and 5.2). Furthermore, in the individual investigations, different measurement methods were applied in order to collect data for a sufficient comparison with the simulations´ outcome. The measurement data were partly used as boundary conditions in the CFD models. The measurements and experiments were realized in the course of three different research projects.

Chapter 3.2.3 presents in situ measurements, where a historical building was available for measurements, and measurement sensors were installed directly inside the cavities of the existing windows. The in-situ measurements were performed in the course of the research project "denkmalaktiv I" [1].

Chapter 3.3.3 describes a section of a very complex test façade, which was designed in the course of the research project, "Multifunctional Plug & Play Façade" [2]. The measurement setup has more than two hundred measuring points where data were collected over an entire year. The measuring points and measurement sensors described in detail in this chapter were also used for the numerical analyses of Chapters 3.3 and 4.2.

A number of measurements with a solar honeycomb (SHC) façade element and different PV cell configurations were performed in a laboratory environment using a solar simulator (presented in Chapter 4.3.3). The laboratory experiments were performed in the course of the alpS-project "B02 eNVELOP Teil C" [3]. The data generated at stationary conditions was used to obtain the thermal behaviour inside the ventilation cavity and for the evaluation of PV configurations. Additionally, a transient heating phase of the SHC façade element without attached PV cells was monitored, and the data collected was used as a basis for comparison with the results from transient CFD simulations.

Finally, Chapter 6 presents the findings of each study, and describes both the benefits and disadvantages of the different CFD-model approaches used. Chapter 6.4 contains a brief discussion of the outlook for such technologies, and offers some proposals for the improvement of future CFD simulations in the field of the thermal behaviour.
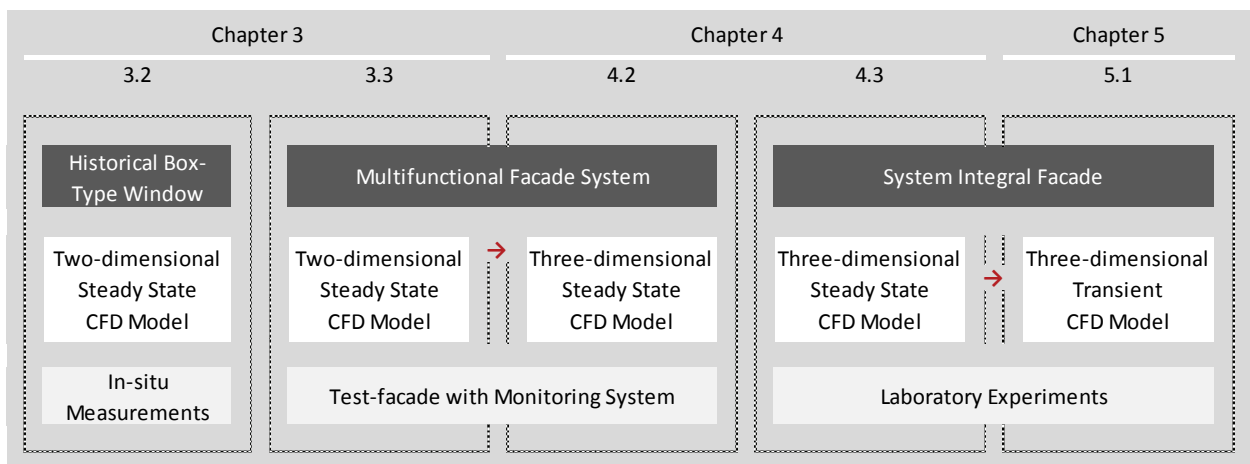
Figure 1-1: Illustration of the Dissertation´s different Approaches

2 Fundamental Basics

For the innovative coupling of the detailed air flow and heat transfer effects in the field of the thermal building physics, a various number of fundamental basics are required. In the field of ventilated building envelopes, "natural" and "forced" convective air flow can occur either individually or in combination. The heat transfer through solid and fluid domains is as important as the heating effects caused by solar radiation. Furthermore, the effects of integrated functional components and systems have to be considered in the overall thermal behaviour (e.g. an electricity converting PV cell array or a water filled absorber of a solar thermal collector). In addition to the physical basics, it was also important to find a proper simulation method or environment that would allow the combined calculation of the modelling equations. The following fundamental basics served as the theoretical background for all of the research performed in the course of the dissertation.

2.1 Numerical (CFD) Method

For all of the investigations carried out in this study, the numerical method of Computational Fluid Dynamics (CFD) was used. This is a special simulation method where a multitude of physical, chemical, and other processes can be described with the help of different mathematical equations. Numerical modelling has the advantage of costing less money and less time in comparison compared to the development of test rigs, where the same behaviour can be experimentally modelled.

Generally, the CFD model needs a domain geometry (one-, two- or three-dimensional) which is divided into a large number of very small cells called "finite volumes". Based on these cells, all of the mathematical considerations can be calculated in an iterative process for the prepared simulation domain containing the large number of finite volumes. Thereby, the volumes can be differently shaped (pyramids, tetrahedral, hexahedral, etc.) by considering skewness or orthogonal quality, for example. The so-called CFD mesh, which is formed by all volumes, can be generated with special meshing tool software.

In the simulations of this study, the air flow behaviour was determined at the same time as the thermal and radiative heat transfer effects. The mathematical models involved in this process are presented below. Generally, two different meshing tools were used for the mesh development of this study (Gambit [4], ICEM [5]), along with two different CFD tools were used (Fluent and CFX [5]). For the performance of the physical phenomena, the software package Fluent was found to be more suitable, so ultimately all simulations were performed with ANSYS Fluent 14.0 or 15.0 [5], [6], [7].

2.2 Fluid Mechanics and Heat Transfer Effects

In order to determine the fluid characteristics and flow behaviour inside the façade´s closed and ventilated cavities, the following governing equations (Equation 2-1 - Equation 2-23), mainly derived from the Navier-Stokes equations, are essential. The Navier-Stokes equations characterize the flow of liquids and gases, and consist of mass, momentum, and energy conservation. These equations lead to a non-linear partial differential equation system of the second order, which serves as a basis for the numerical flow models.

2.2.1 Mass Conservation (Continuity Equation)

The principle of mass conservation is required for all of the simulations performed. In the CFD software package, mass conservation is considered as represented in Equation 2-1 and Equation 2-2. Almost all equations in this chapter have been extracted from the ANSYS Theory Guide [7] and the lector notes entitled "Strömungslehre und Wärmeübertragung I" [8], [9]. In this form, the mass conservation is valid for compressible and incompressible flow.

$$\frac{\partial \rho}{\partial t} + (\vec{\nabla} \cdot \rho \vec{v}) = 0 \qquad \text{Equation 2-1}$$

$$\frac{\partial \rho}{\partial t} + \frac{\partial}{\partial x}(\rho v_x) + \frac{\partial}{\partial y}(\rho v_y) \frac{\partial}{\partial z}(\rho v_z) = 0 \qquad \text{Equation 2-2}$$

2.2.2 Momentum Conservation (Momentum Equation)

The momentum conservation of the moving fluid also has to be considered in the CFD simulations, according to Equation 2-3 from the ANSYS Theory Guide [7] or Equation 2-4 to Equation 2-6 [9].

$$\frac{\partial}{\partial t}(\rho \vec{v}) + \nabla \cdot (\rho \vec{v}\vec{v}) = -\nabla p + \nabla \cdot (\bar{\bar{\tau}}) + \rho \vec{g} + \vec{F}$$

Equation 2-3

x-component:

$$\rho \left(\frac{\partial v_x}{\partial t} + v_x \frac{\partial v_x}{\partial x} + v_y \frac{\partial v_x}{\partial y} + v_z \frac{\partial v_x}{\partial z} \right) = -\frac{\partial p}{\partial x} + \left(\frac{\partial \tau_{xx}}{\partial x} + \frac{\partial \tau_{yx}}{\partial y} + \frac{\partial \tau_{zx}}{\partial z} \right) + \rho g_x$$

Equation 2-4

y-component:

$$\rho \left(\frac{\partial v_y}{\partial t} + v_x \frac{\partial v_y}{\partial x} + v_y \frac{\partial v_y}{\partial y} + v_z \frac{\partial v_y}{\partial z} \right) = -\frac{\partial p}{\partial y} + \left(\frac{\partial \tau_{xy}}{\partial x} + \frac{\partial \tau_{yy}}{\partial y} + \frac{\partial \tau_{zy}}{\partial z} \right) + \rho g_y$$

Equation 2-5

z-component:

$$\rho \left(\frac{\partial v_z}{\partial t} + v_x \frac{\partial v_z}{\partial x} + v_y \frac{\partial v_z}{\partial y} + v_z \frac{\partial v_z}{\partial z} \right) = -\frac{\partial p}{\partial z} + \left(\frac{\partial \tau_{xz}}{\partial x} + \frac{\partial \tau_{yz}}{\partial y} + \frac{\partial \tau_{zz}}{\partial z} \right) + \rho g_z$$

Equation 2-6

2.2.3 Energy Conservation (Energy Equation)

For the combination of fluid flow and heat transfer effects, the following equations, Equation 2-7 [7] and Equation 2-8 [8], are used to conserve the energy inside the simulation domain. The important terms of this equation are described in more detail in Equation 2-9.

$$\frac{\partial}{\partial t}(\rho E) + \nabla \cdot \left(\vec{v}(\rho E + p) \right) = \nabla \cdot \left(\lambda_{eff} \nabla T - \sum_j h_j \vec{J}_j + \left(\bar{\bar{\tau}}_{eff} \cdot \vec{v} \right) \right) + S_h$$

Equation 2-7

$$\frac{\partial}{\partial t}\left(\rho \left(e + \frac{\vec{v}^2}{2} \right) \right) + \left(\vec{\nabla} \cdot \rho \vec{v} \left(e + \frac{\vec{v}^2}{2} \right) \right)$$

$$= \rho \left(\vec{v} \cdot \vec{f}^B \right) - \left(\vec{\nabla} \cdot p \vec{v} \right) + \frac{\partial}{\partial x}\left(v_x \tau_{xx} + v_y \tau_{xy} + v_z \tau_{xz} \right)$$

$$+ \frac{\partial}{\partial y}\left(v_x \tau_{yx} + v_y \tau_{yy} + v_z \tau_{yz} \right) + \frac{\partial}{\partial z}\left(v_x \tau_{zx} + v_y \tau_{zy} + v_z \tau_{zz} \right)$$

$$- \left(\vec{\nabla} \cdot \vec{q} \right) + \dot{q}_Q$$

Equation 2-8

$$E = h - \frac{p}{\rho} + \frac{\vec{v}^2}{2} = e + \frac{\vec{v}^2}{2}, \quad h = \sum_j Y_j h_j, \quad h = \sum_j Y_j h_j + \frac{p}{\rho}, \quad h_j = \int_{T_{ref}}^{T} c_{p,j} dT$$

Equation 2-9

In the numerical simulations, heat transfer has to be considered in solid (conductive heat transfer) as well as in fluid zones (convective heat transfer). For convective heat transfer, it is possible to differentiate between forced and natural convection.

2.2.4   Conductive Heat Transfer

In the simulations of the combined flow characteristic and thermal behaviour, heat transfer through the solids of the CFD domain also plays an important role. These effects are considered in the CFD model in the form of the energy equation in solid regions (Equation 2-10) [8].

$$\rho \frac{\partial e}{\partial t} = -(\vec{\nabla} \cdot \vec{q}) + \dot{q}_Q, \quad \frac{\partial T}{\partial t} = a\Delta T + \frac{\dot{q}_Q}{\rho c_p}$$

Equation 2-10

2.2.5   Natural Convective Heat Transfer

One of the most important effects in the CFD simulations of closed and ventilated facades is the naturally occurring convective air flow. The fluid gets a buoyancy impulse due to the lower density in regions where the fluid is heated, either by heating components or solar irradiation. This effect occurs when the influence of forced convection (where the resulting flow is based on a pressure difference caused by a fan, for example) is very low or negligible. The Rayleigh (Ra) or the Grashof (Gr) number (in Equation 2-11) is the essential indicator for the estimation of the natural convective influence.

$$\frac{Gr}{Re^2} = \frac{g\beta\Delta TL}{v^2}, \quad Ra = \frac{g\beta\Delta TL^3\rho}{\mu a}, \quad \beta = -\frac{1}{\rho}\left(\frac{\partial p}{\partial T}\right)_p, \quad a = \frac{\lambda}{\rho c_p}$$

Equation 2-11

Furthermore, the ANSYS Theory Guide [7] recommends that, for low Mach (Ma) numbers (Equation 2-12), the effect of the compression of the fluid can be neglected. This means that the fluid can be considered an incompressible ideal gas in order to model natural convective air flow in the CFD simulations.

$$Ma = \frac{v}{c}, \quad c = \sqrt{\kappa R_S T}$$

Equation 2-12

2.2.6   Radiative Heat Transfer

In the field of the thermal and flow characteristic inside closed and ventilated façade elements the effect of the radiative heat transfer plays a very important role. Equation 2-13 is representing the consideration of radiative transfer (absorption, emission, scattering) through a medium (fluid or solid).

$$\frac{dI(\vec{r},\vec{s})}{ds} + (a_R + \sigma_S)I(\vec{r},\vec{s}) = a_R n^2 \frac{\sigma T^4}{\pi} + \frac{\sigma_S}{4\pi}\int_0^{4\pi} I(\vec{r},\vec{s}')\Phi(\vec{s}\cdot\vec{s}')d\Omega'$$

Equation 2-13

2.2.7   Turbulence Model

In the simulations for the prediction of the thermal behaviour of façade elements, different versions of the k-ε turbulence model were used, all of which were derived from the Reynolds Averaged Navier-Stokes equations (RANS). Basically, this semi-empirical model uses two transport equations, one for the kinetic energy (k, Equation 2-14) and one for the dissipation rate (ε, Equation 2-15).

$$\frac{\partial}{\partial t}(\rho k) + \frac{\partial}{\partial x_j}(\rho k v_j) = \frac{\partial}{\partial x_j}\left[\left(\mu + \frac{\mu_t}{\sigma_k}\right)\frac{\partial k}{\partial x_j}\right] + G_k + G_b - \rho\varepsilon - Y_M + S_k$$

Equation 2-14

$$\frac{\partial}{\partial t}(\rho\varepsilon) + \frac{\partial}{\partial x_j}(\rho\varepsilon v_j) = \frac{\partial y}{\partial x_j}\left[\left(\mu + \frac{\mu_t}{\sigma_\varepsilon}\right)\frac{\partial\varepsilon}{\partial x_j}\right] + C_{1\varepsilon}\frac{\varepsilon}{k}(G_k + G_b C_{3\varepsilon}) - C_{2\varepsilon}\rho\frac{\varepsilon^2}{k} + S_\varepsilon$$

Equation 2-15

There are three different variations of the k-ε-turbulence model in the numerical software used, which are vary in terms of turbulent viscosity, the turbulent Prandtl numbers as well as the generation term in the ε-equation.

The Standard k-ε model (SKE) uses the following assumption for the turbulent viscosity (Equation 2-16). In the SKE model, the constant $C_{1\varepsilon}$ has a value of 1.44, $C_{2\varepsilon}$ a value of 1.92, C_μ is 0.09, σ_k is 1.0 and σ_ε has a value of 1.3. These constants have been experimentally determined in the past.

$$\mu_t = \rho C_\mu \frac{k^2}{\varepsilon}$$

<div align="right">Equation 2-16</div>

In the Re-Normalisation Group k-ε turbulence model (RNG), the first term on the right sight of the k-ε transport equations has been modified (Equation 2-17 and Equation 2-18). Furthermore the RNG model has an additional term in the ε-transport equation in order to improve its accuracy for rapidly strained flows. The effect of swirling flows on turbulence has also been included in the RNG model. These and other minor differences between SKE and RNG can be found in [7]. The values for the constants in the RNG model are 0.0845 for C_μ, 1.42 for $C_{1\varepsilon}$, 1.68 for $C_{2\varepsilon}$ and 0.07 for the swirl factor α_S.

$$\frac{\partial}{\partial x_j}\left[\left(\mu + \frac{\mu_t}{\sigma_k}\right)\frac{\partial k}{\partial x_j}\right] = \frac{\partial}{\partial x_j}\left[\alpha_k \mu_{eff} \frac{\partial k}{\partial x_j}\right]$$

<div align="right">Equation 2-17</div>

$$\frac{\partial}{\partial x_j}\left[\left(\mu + \frac{\mu_t}{\sigma_\varepsilon}\right)\frac{\partial k}{\partial x_j}\right] = \frac{\partial}{\partial x_j}\left[\alpha_\varepsilon \mu_{eff} \frac{\partial \varepsilon}{\partial x_j}\right]$$

<div align="right">Equation 2-18</div>

Another variation is the realizable k-ε model (RKE), which has a different formulation of the ε-transport equation (Equation 2-19) as well as an alternative formulation of the turbulent viscosity [7]. An additional model constant, C_2 with a value of 1.9 is used in the RKE model. While the remaining constants have the same values as in the SKE model, the constant σ_ε has been changed to a value of 1.2.

$$\frac{\partial}{\partial t}(\rho \varepsilon) + \frac{\partial}{\partial x_j}(\rho \varepsilon v_j) = \frac{\partial y}{\partial x_j}\left[\left(\mu + \frac{\mu_t}{\sigma_\varepsilon}\right)\frac{\partial \varepsilon}{\partial x_j}\right] + \rho C_1 S_\varepsilon - \rho C_2 \frac{\varepsilon^2}{k + \sqrt{v\varepsilon}} + C_{1\varepsilon}\frac{\varepsilon}{k}C_{3\varepsilon}G_b + S_\varepsilon$$

<div align="right">Equation 2-19</div>

The effect of buoyancy (Equation 2-20) and the convective heat and mass transfer (Equation 2-21) are considered in the k-ε models according to the following two equations, which were again extracted from [7].

$$G_b = -g_i \frac{\mu_t}{\rho Pr_t}\frac{\partial \rho}{\partial x_i}$$

<div align="right">Equation 2-20</div>

$$\frac{\partial}{\partial t}(\rho E) + \frac{\partial}{\partial x_i}[v_i(\rho E + p)] = \frac{\partial}{\partial x_j}\left(\lambda_{eff}\frac{\partial T}{\partial x_j} + v_i(\tau_{ij})_{eff}\right) + S_h$$

<div align="right">Equation 2-21</div>

2.2.8 Wall Functions

A critical issue when using CFD models is the description of the correct thermal and flow related effects in transition zones between solid to fluid zones. For turbulent fluid flows in particular, the velocities as well as the temperature fields are strongly affected by the presence of a wall. Generally, for the correct description of the transition between solid and fluid zones, there are two approaches, which are described in detail in the ANSYS Theory Guide [7]. These regions can thus be fully resolved using a "Near Wall Model", or in the form of a "Wall Function", containing all the required transition effects. These are considered by means of empirical equations in the first fluid cell row adjacent to the wall in the CFD model. The simulations performed for this dissertation used either the "Standard Wall Function" or the "Enhanced Wall Treatment".

Using the "Standard Wall Function" has the advantage that fewer cells are required for the CFD mesh, which improves the simulation performance and makes it possible to calculate larger fluid domains. The

"Enhanced Wall Treatment" is a combination of an improved wall function and a two-layer model. Therefore, the first row of cells adjacent to the wall in the CFD mesh has to be divided into several rows, which increases the mesh size dramatically. Nevertheless, both approaches provided acceptable results in the simulations performed in the course of this study.

When using the wall functions mentioned above, the criteria for the so-called y^+ value (Equation 2-22) have to be fulfilled.

$$y^+ \equiv \frac{\rho}{\mu} \cdot u_\tau \cdot y_c, \quad u_\tau = \sqrt{\frac{\tau_W}{\rho}}$$

Equation 2-22

The "Enhanced Wall Treatment" can be used when $y^+ \approx 1$, for the "Standard Wall Functions" the y^+ value is limited to between 30 and 300, appoximately.

2.2.9 Discrete Ordinate (DO) Radiation Model

Generally, the "Surface-to-Surface" (S2S) radiation model is sufficient when considering the radiative heat transfer of ventilated façade elements. The main advantage of this numerical model is the fast calculation time per iteration during the entire simulation. Because this study is intended to present a more sophisticated understanding of solar heating effects and radiative heat transfer issues, the "Discrete Ordinate" (DA) radiation model was used for all CFD simulations. The DO model covers both the surface-to-surface radiation and the radiation transfer through the fluid domains. Additionally, it provides the option of using either a grey radiation or a non-grey radiation approach, in which it is possible to define different quantities of grey bands. A further advantage of the DO model is its consideration of opaque and semi-transparent solids, whereas the S2S model only considers opaque surfaces. With the DO model, the radiation is solved by cell, using a special radiation transport equation (Equation 2-23).

$$\nabla \cdot \left(I_\gamma(\vec{r}, \vec{s})\vec{s} \right) + \left(a_\gamma + \sigma_S \right) I_\gamma(\vec{r}, \vec{s}) = a_\gamma n^2 I_{b\gamma} \frac{\sigma T^4}{\pi} + \frac{\sigma_S}{4\pi} \int_0^{4\pi} I_\gamma(\vec{r}, \vec{s}')\Phi(\vec{s}, \vec{s}')d\Omega'$$

Equation 2-23

With the help of angular discretization, the accuracy of the radiation transports can be improved and the numerical diffusion can be reduced.

2.3 Introduction to Flow and Heat Transfer Effects in Façade Systems[1]

2.3.1 Closed Cavities

Generally, air circulation occurs in a closed cavity due to the temperature difference between the exterior and the interior, which has a negative influence on thermal protection. Baïri [10] investigated the convective heat transfer phenomena that take place inside a façade′s cavity, varying the cavity shape and aspect ratio (AR, Equation 2-24). For this purpose, two-dimensional transient CFD calculations were performed and compared with results from other numerical and experimental investigations.

$$AR = \frac{H_{ac}}{L_{ac}}$$

Equation 2-24

Recent literature describes several studies on natural convection and the (numerical) analysis of convection in a closed cavity, in the cavities of façade elements, or in double pane windows of varying length (AR > 20) [11], [12], [13]. Xaman et al. [13] present an investigation into heat transfer by natural convection in closed tall cavities with façade elements of varying aspect ratios. This study shows the temperature and velocity profiles as a result of two-dimensional CFD models, and a comparison of the resulting Nusselt numbers (Nu, Equation 2-25) with five correlations with other literature.

$$Nu = \frac{\alpha \cdot L}{\lambda}$$

Equation 2-25

The paper by Manz [11] shows a comparison of the heat transfer and air flow characteristics of double skin façade elements with different aspect ratios and for different Rayleigh numbers (Ra, Equation 2-26). The laboratory experiments in the study of Wright et al. [14] covered Rayleigh numbers from 4850 to 54800, where natural convection inside a tall vertical cavity was investigated.

$$Ra = Gr \cdot Pr = \frac{g \cdot \beta}{\nu \cdot a} \cdot (T_S - T_\infty) \cdot L^3$$

Equation 2-26

Aydin [15] identified the optimum air layer thickness in double pane windows using a numerical approach. The heat transfer in a multi-layer wall with an included air layer was analysed by Armando et al. [16].

2.3.2 Ventilated Cavities

To prevent the facades' cavities from overheating, the cavities are often ventilated by means of small openings to the exterior, usually positioned at the top and bottom of the façade elements. The effects of such ventilation and the thermal behaviour thereof have also been compelling topics for recent studies. Pappas and Zhai [17] carried out a numerical investigation of the thermal performance of ventilated double facades. The varying parameters of this work included the cavity depth, height, and the integration of different shading devices, using three-dimensional simulation models. Manz [18] determined the total solar energy transmittance of ventilated glass in the sun protection systems of double facades while taking into account different sun protection systems. Guardo et al. [19] conducted an analysis of the thermal performance of a glass double façade with varying in-cavity depths. The study of Sanjuan et al. [20] compared the thermal performance of an open-joint façade and a conventional sealed cavity façade.

If the exterior layer contains transparent materials, the sun will heat the air inside the façade cavities. In order to prevent overheating in summer, a façade′s cavity is ventilated with external air. In addition to decreasing air temperatures inside the cavity, this measure can have a major impact on the airflow inside the cavity. Literature provides a large number of studies on this issue. Balocco [21] developed a simple model to determine the energy performance of a ventilated façade.

---

1. Parts of this Chapter have been published earlier in [17], [18], [19], [20] and [21].

Ciampi et al. [22] used a simple analytical method for the calculation of the energy performance to determine the reduction of the thermal loads for buildings' facades in summer. The paper by Faggembauu et al. [23] presented a one-dimensional numerical model to describe the thermal behaviour of ventilated facades in Mediterranean climates. The model was validated with data from experimental measurements from real-site test facilities. Baldinelli [24] carried out an analysis of a ventilated double façade with an external moveable shading device. One of the main goals of that study was to optimise the winter and summer energy performance of the façade. In that study, a CFD model with a spectral optical model was used, and the results were compared with data from experiments. The paper of Chow et al. [25] determined the thermal performance of a ventilated double pane window for cooling in summer and heating in winter in subtropical and temperate climate zones. In the study of Guardo et al. [26], the influence of a variety of construction and operation parameters for an active transparent façade on the thermal performance were evaluated.

Gan conducted a very interesting study [27], in which the results of airflow and heat transfer inside a vertical cavity for different heat fluxes and cavity geometries were presented. This study also recorded the impact of different computational domain sizes on the simulation results. Suarez et al. [28] carried out research on heat transfer and mass flow phenomena in ventilated facades. The aim of their study was to obtain accurate results in terms of correlations for the average Nusselt number and for the mass flow induced in the cavity. The effect of natural ventilation in an opaque ventilated façade was investigated by Lopez et al. [29], who considered the effect of the local wind speed on ventilation efficiency. In the study of Bhamjee et al. [30], a mathematical and CFD model for an air supply window was developed. This was ventilated by both natural and forced airflow, and validated by means of Laser Doppler Velocimetry (LDV). Sanvicente et al. [31] presented a study on natural convective flows and heat transfer in differently heated open channel configurations, where they used Particle Image Velocimetry (PIV) in their experiments to visualize airflow in the cavity. Carlos and Corvacho [32] evaluated the thermal performance indices of a ventilated double window and calculated the corresponding U_W-values.

2.3.3 Double Facades with Shading Devices

Particularly in hot climates, double facades are equipped with shading systems that have an impact on the thermal behaviour and airflow characteristics inside their cavities. In Pasut and De Carli [33], a venetian blind was installed between the two window panes, and an investigation of the thermal behaviour was performed using different model strategies. They also investigated the impact of the simulation's airflow domain and the temperature in the cavity. For this comparison, they used the results of two- and three-dimensional CFD simulations. Safer [34] presented a detailed view of the convective airflow of two cases featuring a double façade with an integrated venetian blind.

Further studies have explored the influence of different shading devices on the flow characteristics inside double glazed facades. Almost all of these studies include numerical simulations using two-dimensional (e.g. [35], [36], [37]) or three-dimensional (e.g. [34], [17]) CFD models.

2.3.4 Solar Radiation Gaining Facades

Currently, much effort is being made to activate buildings' surfaces to gain solar radiation so as to provide additional energy and increase energy efficiency. The integration of energy-converting systems (such as photovoltaic modules or solar thermal collectors), daylighting, or HVAC systems directly into the façade (multifunctional or integral facades) presents a major goal. With the installation of such components, previously simple façade structures become increasingly complex in terms of both their construction and flow characteristics. Integrated systems can cause additional thermal bridges and air cavities, which strongly impact the thermal behaviour of the façade. Furthermore, the integration of thin PV cells on the exterior layer of facades increases their heat loads and can lead to higher temperatures in the facades' cavities. Ventilation plays a very important role in reducing the temperatures in the cavity and in improving PV efficiency. Therefore, many studies have addressed the determination of heat transfer and ventilation effects of a variety of ventilated facades with attached PV cells.

Han et al. [38] conducted a 2D numerical analysis of the convective airflow and heat transfer in PV-cells implemented in a double-pane window with low emission coatings. In a further study by Han et al. [39], the thermal performance of a ventilated double-sided PV façade was compared with a conventional clear glass façade. Additional studies also contain an analysis of the thermal effects of building integrated PV-cells or PV-panels. Zogou et al. [40] created a special testing device and investigated the ventilation effects of a building-integrated photovoltaic module, using three different ventilation strategies. The flow was visualized with the help of a smoke gun and a laser, and was recorded with a HD camera. Additional airflow velocity was measured with a hot wire anemometer. A simple model based on a one-dimensional loop analysis of naturally ventilated PV claddings was created by Brinkworth et al. [41]. The study carried out by Charron and Athienitis [42] optimised the performance of double facades with integrated PV panels and motorized blinds. Two configurations of integrated PV were investigated, as well as their thermal and electrical efficiency, by using a one-dimensional finite difference model. Yun et al. [43] analysed the overall energy performance of a ventilated PV façade for different PV configurations. The façade has the function of pre-heating in winter and reducing the temperatures in the cavity in summer. The influence of the PV coverage on the thermal and electrical performance of a Trombe wall was analysed by Jiang et al. [44]. With the help of CFD simulations, Gan [45] determined the adequate air gap size for ventilated, building-integrated photovoltaic. The study of Koyunbaba and Ylmaz [46] compared the thermal performance and the flow characteristic of a Trombe wall with single glass, double glass, and PV panels. They used two-dimensional CFD models for the comparison where the computational domain consisted of the Trombe wall and the interior room. Lau et al. [47] investigated the thermal behaviour and ventilation effects of a building-integrated PV at different inclination angles during uniform heat flux. The results from the two-dimensional CFD simulations were compared with laboratory experiments. Cipriano et al. [48] numerically analysed the most appropriate heat transfer correlations for ventilated double skin PV facades. Sun et al. [49] showed the results of measurements of the performance of a PV Trombe wall in winter.

2.3.5   *Transient Thermal Behaviour for Facades*

In the field of numerical simulations of façade heat transfer mechanisms, there are different approaches to determining the heat loads for a building in order to calculate its heating and cooling demands. The efficiency of heating and cooling in a building can be improved dramatically by using more accurate numerical models of the transient physical behaviour between the external environment and the interior spaces.

Balocco [21], for example, used a simple model in his study of the energy performance of ventilated facades during a hot summer's day and a cold winter's day. In the research of Faggembauu et al. [23], a one-dimensional numerical model was developed to reduce calculation time. Since the model is able to consider solar-active layers, like integrated phase change materials, selective surfaces or improved glasses and their thermal performance under changing climate conditions can be analysed over one whole year with an adequate calculation duration. Another study on determining heating and cooling loads was performed by Chow et al. [25] where the thermal performance of ventilated windows in temperate and subtropical climate zones was investigated. In the study of Lopez et al. [29], a zonal approach involving a building simulation tool was applied to analyse the thermal behaviour of a ventilated opaque façade. Jiang et al. [44] investigated the influence of PV coverage on the thermal and electrical performance of a PV-Trombe wall, using the FORTRAN environment to develop their simulation program.

Recent research also includes an analysis of the transient thermal behaviour of facades using two-dimensional CFD models. Koyunbaba and Ylmaz [46] provided a comparison of the thermal performance of different glazing types for a Trombe wall and a two-dimensional CFD model of the façade and the corresponding interior room over a period of two days in February. Guardo et al. [26] performed a parameter analysis of an active transparent façade under Mediterranean climate conditions, again using a two-dimensional CFD model. The study by Liu et al. [50] presented the heat storage characteristic of a Trombe wall with the help of experiments and transient CFD simulations. In the study of Pappas and Zhai [17], the results of three-dimensional CFD simulations of a double skin façade were integrated into a building energy simulation program.

2.3.6 Measurements

Measurements in an experimental set-up are very useful for the verification of a simulation's outcome, and for the development of an adequate numerical model of the solar honeycomb (SHC) façade. For this purpose, data from recently performed measurements was used [51]. Generally, there are several measurement techniques to collect data for such comparisons. One of these methods is the creation of an outdoor test facility, where the impact of solar radiation on the facades can be directly observed. In a recent study by Zöllner et al. [52], such an outdoor test facility was constructed to determine the heat transfer and ventilation effects in the vertical channels of so-called double facades. Han et al. [39] conducted another study that included a sophisticated outdoor experiment. They developed two identical boxes, which were placed side by side outdoors. One box had a conventional clear glass façade, while the other was equipped with a ventilated double-sided PV façade. In such outdoor test facilities, exposure to solar radiation varies over time. In order to prevent such transient thermal behaviour, a laboratory experiment requires constant incident radiation. Eicker's study et al. [53], for example, shows a laboratory set-up in which a test façade is placed between a cooling box and a solar simulator, whereas Kuznik et al. [54] created a whole test facility with coated test cells and a solar simulator. In these experiments, it was possible to provide constant incident radiation and external temperatures on the test facades, as well as the test cells. Strachan et al. [55] describe experiments on an outdoor test stand in order to quantify the performance of passive solar building components. Liu et al. [50] conducted an analysis of the ventilation and heat storage characteristics of a Trombe wall, for which they built an outdoor test box containing a large number of sensors for monitoring temperature, radiation, and air velocities. Mortensen et al. conducted an analysis of the microclimate inside a box by Particle Image Velocimetry (PIV) [56]. In their experimental setup, a chiller was attached to one side of the box and 2D-sectional flow patterns were observed for different geometry parameters of the cavity. Bhamjee et al. [30] used the Laser Doppler Velocimetry (LDV) measurement method to validate their numerical calculations for a supply air window considering forced and natural convective flow.

3 Stationary, Two-dimensional Numerical Models[2]

3.1 Applications and CFD Approaches

The first section (3.2) of stationary, two-dimensional numerical models contains the results of two recently published studies [57], [58], in addition to a national [1] and an international research project [59] on the natural convection and heat transfer effects of historical box type windows. No literature was found on the topic of convective air flows inside the BTW´s cavity, nor could any literature be found on the infiltration effects through the BTW´s air-permeable joints. One of these studies presents a comparison between a numerical simulation and monitored data from in-situ measurements [57], whereas the other contains an analysis of the impact of some promising thermal improvements on the thermal performance of BTWs [58]. Furthermore, Section 3.2 contains a comprehensive heat flux analysis and a virtual test box for U-value estimation. In the simulation models, the radiative heat transfer of the long wave radiation is considered, while the impact of solar heating effects was neglected since the analysis of the thermal behaviour only considered cold climate conditions.

The integration of multifunctional components into the construction of façade changes the physical behaviour inside the construction, as well as in the immediate surroundings of the façade. In particular, the installation of components that produce electricity or heat from solar irradiation can cause changes to the temperatures and airflows that occur in the (ventilated) air cavities behind them. Increases in temperature in the air cavities usually not only affect the performance of electrical and thermal energy production, but can also have an impact on the interior rooms behind the façade. Over the course of the research project "MPPF" [60], two-dimensional CFD models were created to describe these physical phenomena by investigating the thermal and fluidic behaviour of the prototype of a multifunctional façade for two extreme climatic conditions (Chapter 3.3). Both cold winter and hot summer were considered with regard to the heating effects of solar irradiation. The contents of Chapter 3.3 originate from a chapter of the recently published "MPPF book" [61] and from a publication in the Journal *Energy and Buildings* [62]. While only one room was examined in the BTW simulations, an entire three-story building was investigated in the CFD simulations here. The simulation domain therefore became very complex, containing a large number of different solid and fluid zones. An original contribution of this study was the creation of an innovative façade model with an integrated solar thermal collector.

---

2. Segments of this Chapter have already been published in [17], [18], [57], [58], [60] and [19].

3.2 Analysis of Natural Convection and Heat Transfer Effects in Traditional Box Type Windows[3]

3.2.1 Introduction

Wooden Box Type Windows (BTW) are an integral part of many historical cities. While this type of window has been a crucial element of the design of buildings' facades for centuries, the use of BTW is currently decreasing due to the modernization. European Cities in temperate climate zones still contain a large number of buildings that were built between the 19th and the mid-20th centuries. Furthermore, several of these are classified as historical monuments. For example, in Germany and Austria, more than 100 million BTWs can be found on the facades of historical buildings [63], [64]. Instead of replacing a historical BTW with a modern window, these can easily be renovated to reduce the embodied energy and avoid the waste of polluting materials. Furthermore, there are some promising ways to improve the BTW´s thermal performance and therefore reduce the building's energy consumption.

Two-dimensional Computational Fluid Dynamics (CFD) simulations were used to reproduce the complex physical processes that occur inside the BTW cavity and the nearby environment. The results of the simulations of two different BTW concepts were compared with in-situ measurements so as to determine their quality. Additionally, six different concepts for the improvement of BTWs' thermal performance were evaluated with help of the developed CFD model.

3.2.2 BTW Characteristic and Improvement Concept

Figure 3-1 shows the composition of a typical BTW and their main components. Principally, a BTW consists of two casements with single glazing (interior (1), exterior (2)), a wooden base (3), and a wooden shutter box (4), in which the shading system is integrated.
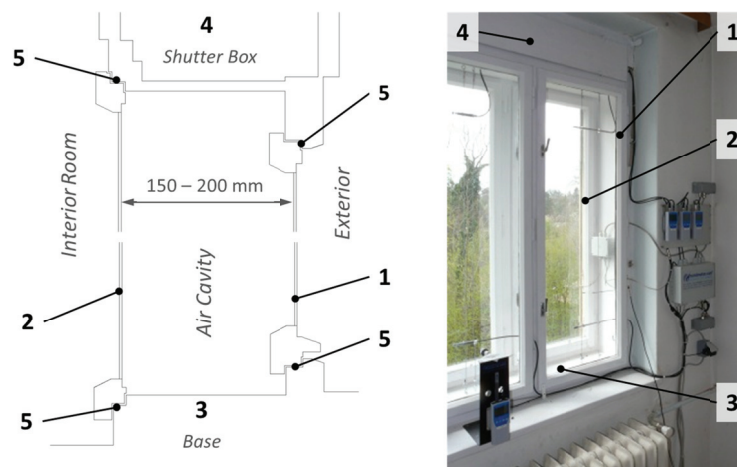

Figure 3-1: Schematic of a BTW indicating the Main Components: Schematic from the SB13 Conference Presentation [58]; Right, Picture of a BTW equipped with a Number of Measurement Sensors: Picture from the "Denkmal Aktiv I" Research Project

The distance between the exterior and the interior casement usually is between 150 and 200 mm. Between the casements and the wooden box frame structure are small, air-permeable joints (5), where external air can enter and leave the BTW´s cavity, thereby providing a natural change of air for the interior room. The joint´s width is about 1 to 2 mm for the interior casement and approximately 3 to 4 mm for the exterior casement.

The weather conditions of temperate climates often lead to the deformation of wooden BTW parts, affecting the casement frames in particular. Due to deformation, the width of air-permeable joints can increase, and negatively influence the indoor climate. To prevent this source of discomfort for the indoor climate, six concepts for improvement have been chosen for investigation based on the refurbished BTW. Schematics of the refurbished BTW (A) and the improvement concepts are shown in Figure 3-2.

---

3. Parts of this section have been published earlier in [17], [18], [57] and [58].
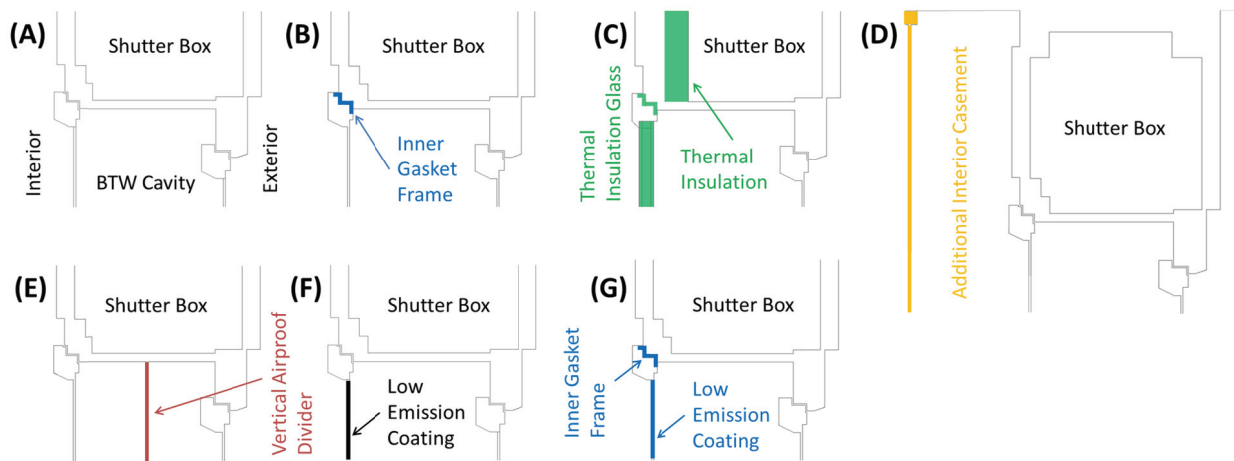
Figure 3-2: Schematic of the Refurbished BTW and an Additional Six Promising Concepts for Thermal Improvement

In the first concept, the air permeable joints of the interior casement are closed with an inner gasket frame (B), so that air from the outside cannot enter the interior room. In the next concept, the interior glass is exchanged with a thermal insulation glass (C). A further improvement is the integration of thermal insulation in the BTW´s shutter box. This concept also affects the inner gasket frame, used in improvement concept (B). An additional interior casement is attached in concept (D), which forms a cavity between the BTW and interior room. In both concepts (B) and (D), the flow of air from outside to inside is prevented. Another concept to improve the thermal performance of BTWs is the use of an airproof vertical divider for the BTW´s cavity, to split it into two air chambers (E). The air can thus infiltrate the BTW´s cavity from the external environment as well as from the interior room. In concept (F), the refurbished BTW (A) has a low emission coating on the interior glass in order to reduce the effect of the radiant heat exchange between the glasses. Concept (G) also has a low emission coating on the interior glass, in combination with the inner gasket frame from concept (B).

The geometry of a BTW - joints neglected - is similar to that of a cavity with an aspect ratio AR of about 8 (Equation 2-24, Chapter 2.3.1). Almost all existing literature on this topic focuses on the problem of overheating on hot summer days in a warmer climate. In a colder climate, the heating effort necessary to achieve a comfortable indoor temperature is significantly higher than the cooling effort. No literature about the BTW´s thermal performance for winter conditions was found, neither for the Austrian regions nor other locations. As a result, this study focused carrying out BTW CFD simulations for a typical cold winter day in Graz, Austria.

3.2.3 Measurement

Different measuring approaches exist to determine the thermal quality of windows. In a test setting in a laboratory, thermal behaviour for windows is determined under controlled boundary conditions [30], widely using the hot box method [65], while in full-scale outdoor test facilities the thermal behaviour is influenced by external climate conditions [52]. Integrating sensors directly in the windows of existing buildings is known as "in-situ" measurement, and was used for the BTW described in this paper. The historical building at Schönbrunngasse 30, 8043 Mariatrost, in Graz, Austria was one of this project's reference buildings, a former mental hospital, currently used as a kindergarten [1] (see Figure 3-3). Since the building's attic floors were not being used during this research project, it was possible to introduce measurement facilities and monitoring devices. Two rooms with similar geometries and identical BTWs were perfectly suited for an investigation of the thermal behaviour of the windows and their near surroundings. The windows´ main dimensions are ($W_{BTW}/H_{BTW}/L_{BTW}$) 1.63 x 1.76 x 0.28 m. The windows are made of three parts, with a shutter box at the lintel. The six wooden-framed casements can be opened inwards. The adjacent masonry of the building is about 0.55 m thick. The joints between the frame and the casements have varying widths of approximately 0.5 and 5 mm. The inner cavity's dimensions are ($W_{ac}/H_{ac}/L_{ac}$) 1.36 x 1.49 x 0.21 m.

Both BTWs (type (A) and (G), Figure 3-2) were refurbished by renovating the wooden parts, adjusting the fittings, and carrying out the appropriate painting. BTW (G) was improved by implementing a low-

emission coating on the outer surface of the inner panel and a gasket frame for the inner casement. Both windows were equipped with the same type and position of sensors for temperature, humidity, air flow, and global radiation metering.
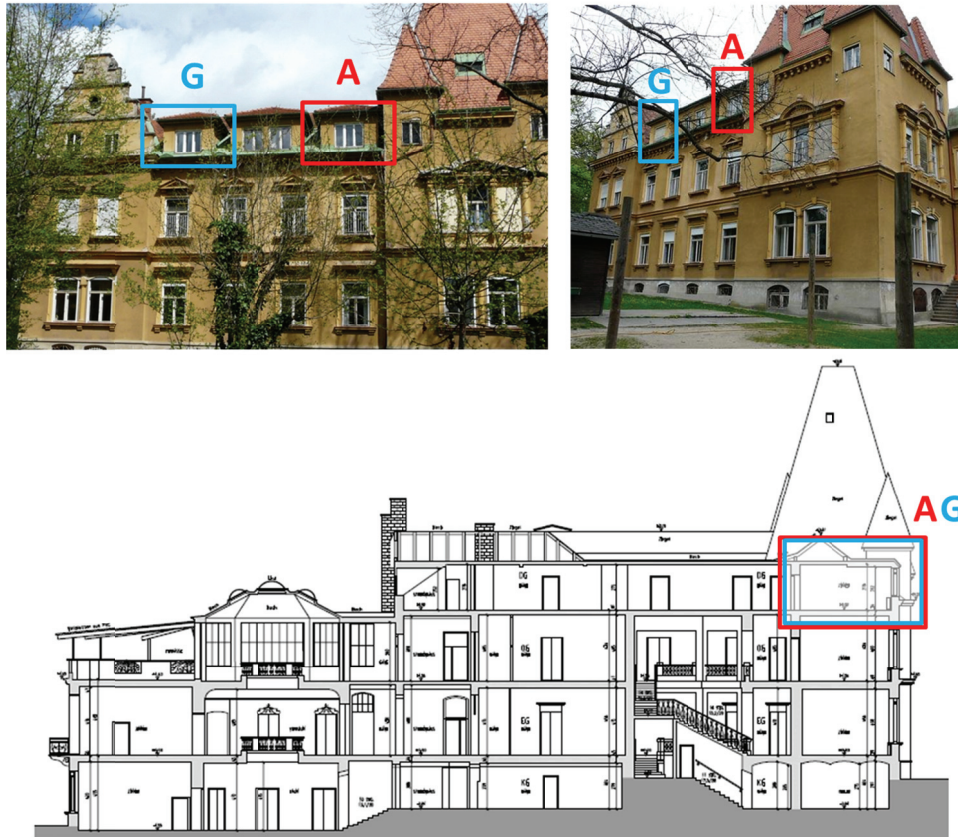

Figure 3-3: Reference Object of the Research Project "denkmalaktiv I": Schönbrunngasse 30, 8034 Mariatrost in Graz, Austria, a Former Mental Institution built in 1885, now a Public Kindergarten

The following four temperature sensors are important for the validation of the simulations (Figure 3-4): T-bot was positioned 0.2 m above the base, T-top was mounted 0.2 m below the shutter box´s bottom edge, and two sensors were fixed on the interior (T-int) and external (T-ext) panes, 0.34 m above the base.

Both global radiation and external temperature were monitored by sensors positioned outside the window; a pyranometer and a temperature sensor ca. 0.3 m above each window's sill made it possible to monitor the interior conditions.
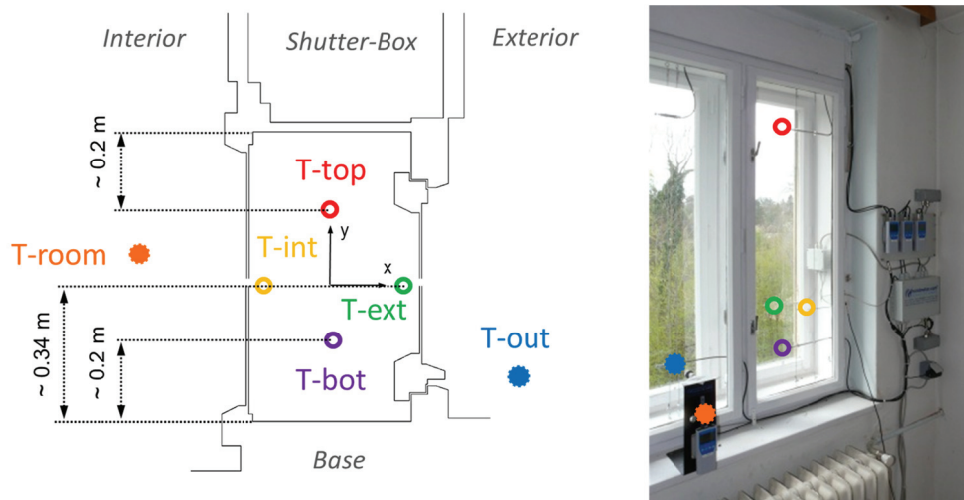

Figure 3-4: Schematic and Picture of the BTW, where Measurement Sensor Positions are indicated

Figure 3-5: Extraction of the Monitored Temperatures in February 2012 for (A) Refurbished and (G) Improved BTWs

Data was collected over an entire year. Figure 3-5 shows an extraction of temperature measurements in February 2012 of the refurbished (A) and of the improved (G) BTW. The external temperature (T-out) lies between -1.0 and -15.0 °C and had an influence on temperatures in the inner cavity as well as the interior. During this period the inner layer of BTW (G) was exposed to more heat from the radiator below, which could not be properly adjusted. Therefore, the internal temperatures are higher than at BTW (A). The interior temperature (T-room) varies between 20.7 and 29.8 °C for BTW (A) whereas the temperature is between 29.8 and 39.0 °C for BTW (G). At the sensor position T-ext very similar temperatures can be observed: the temperature was approximately 1 K higher for BTW (G). At the bottom sensor position inside the BTW´s cavity the temperature profiles of both BTW types exhibit similar behaviour: the temperature for BTW (G) is slightly higher (1.5 K on average). While the temperature at the sensor positions T-int and T-top are almost the same for BTW (A), the temperature at the interior glass pane is approximately 3 K higher than at the top of the BTW´s cavity for BTW (G). Generally the temperatures at these sensor positions are significant higher for BTW (G) than for BTW (A) due to the higher interior temperatures.

Several peaks of higher temperature at all sensor positions can be observed in Figure 3-5, which were caused by the influence of solar radiation. The highest temperatures were reached on February 8th, for the sensor at the top of the BTW´s cavity. The temperature reaches up to a maximum value of 28.8 °C for the BTW (A) and 43.0 °C for BTW (G) at 12:30 pm in the monitored data. Between these peaks of higher temperature the temperatures were nearly constant. These periods are appropriate for a comparison of the monitored data with steady state CFD simulations (presented in Chapter 0).

3.2.4 CFD Model of the BTW

In-situ measurements can only provide sample values for validation. For a more detailed view of the thermal behaviour inside BTWs, a numerical simulation is required. Computational Fluid Dynamics make it possible to reproduce the physical behaviour of the BTW interior space and close environment. The simulations in this study were performed with ANSYS Fluent software [5], geometries and meshes were built with Gambit [4].

The "Pave" method was deemed the best approach to generating the mesh. This made it possible to implement the broad range of cell sizes necessary for the mesh. The meshing process begins with the very small cells inside the air permeable joints. During this process, the cell size increases with the

distance to the joints (see Figure 3-6 and Figure 3-7). Starting at the air-permeable joints, the mesh then extends to the other partitions of the BTW-simulation geometry.
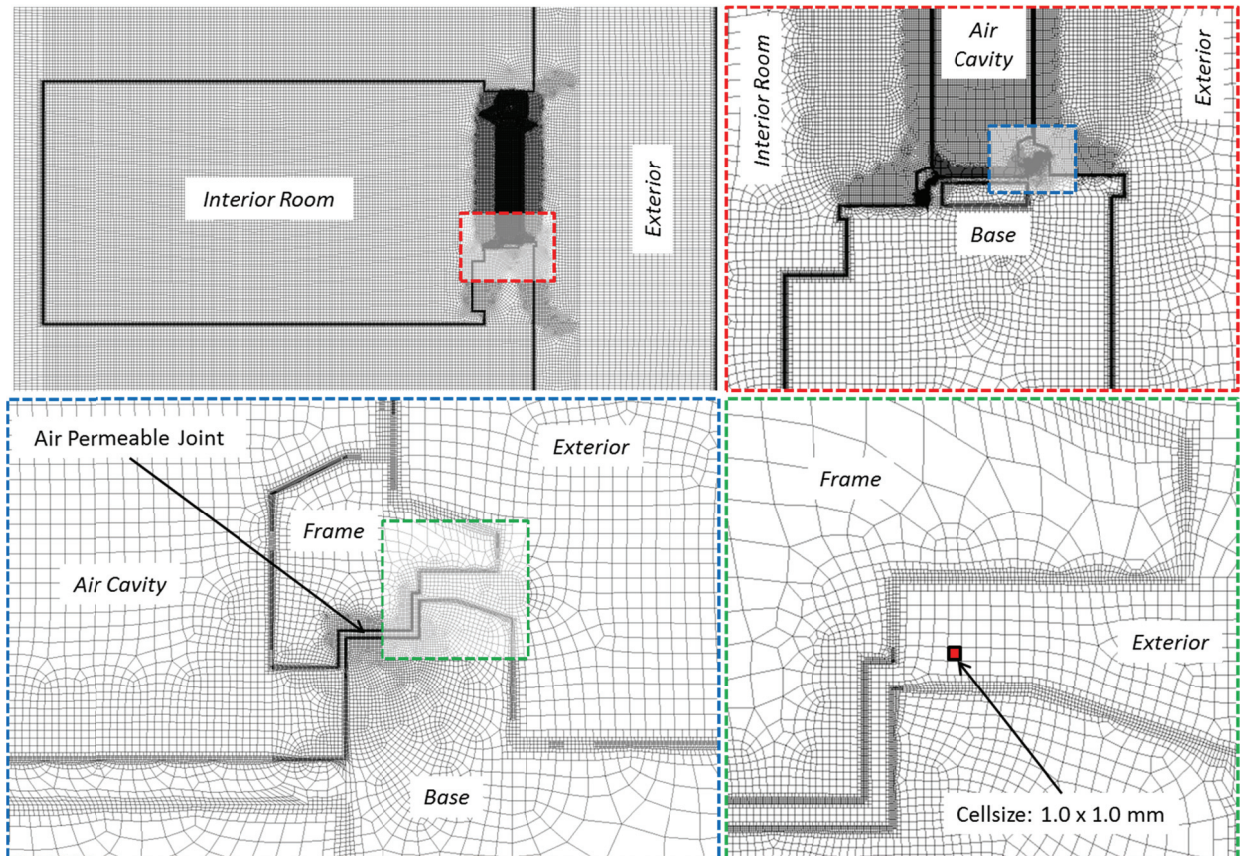

Figure 3-6: Zoom Insight the CFD Mesh of the BTW CFD Model at the Exterior Bottom´s Base
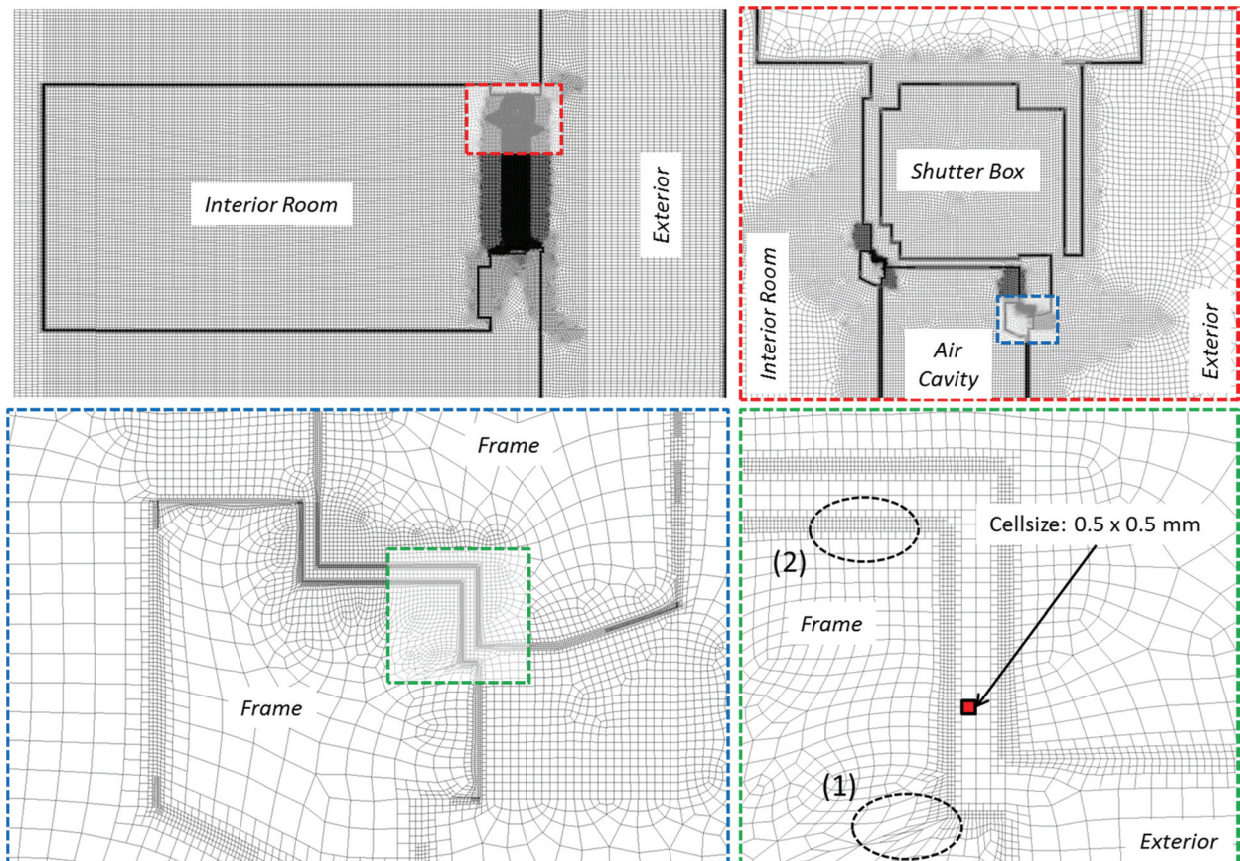

Figure 3-7: Zoom Insight of the CFD Mesh of the BTW CFD Model at the Exterior Top´s Region below the Shutter Box

Stationary, Two-dimensional CFD Models

With regard to enhanced wall treatment, the mesh was adapted to reduce the y^+ value to below 1.0 for all relevant cells (see Chapter 2.2.8). For the following analysis, the mesh used contained approximately 250,000 cells before, and 500,000 cells after the y^+ refinement. Cell size varied between 0.05 x 0.05 mm and 64 x 32 mm. The image on the left in Figure 3-6 gives a sectional view of the mesh structure by showing the region of the bottom-located exterior joint. This joint is located between the exterior casement and the wooden base plate. A zoomed-in section shows the detailed cell structure of the air-permeable joint.

In addition to the broad range of cell sizes, both the orthogonal quality and the skewness exhibit large deviations due to the pave meshing method. The orthogonal quality varies between 0.15 and 1.0 (1.0 is the best value, representing a rectangle) and amounts to 0.97 on average. The minimum skewness is 0, although the worst cells for the CFD simulation have a maximum skewness of 0.9. From the cell number-averaged skewness of 0.021, it is possible to conclude that only a few cells have a very high skewness, so the present mesh is well qualified for further CFD investigations. Furthermore, the cells with the worst orthogonal quality and high skewness only occur in solid domains (position (1) in Figure 3-7), the fluid contains squares with a minimal skewness, to a large extent (position (2) in Figure 3-7). A more detailed description of the quality measures (skewness and orthogonal quality) can be found in the ANSYS Theory Guide [7].

The following models were used to evaluate the air flow of the BTW simulations. The RKE model was the most appropriate for modelling natural convective flow and the subsequent comparison with measurement data. Further specifications for the viscous model were "Enhanced Wall Treatment" and the "Thermal Effects". The "Full Buoyancy Effect" as well as "Gravity Force" were essential to providing the natural convection in the simulations.

Because a turbulence model was proposed for the simulations, this chapter contains a Rayleigh number calculation (Ra_x, Equation 3-1 and Equation 3-2), which was performed for different temperature differences between the BTW´s interior and exterior spaces, in order to prove the characteristic of the natural convective airflow.

$$Ra_x = \frac{g \cdot \beta}{\nu \cdot a} \cdot (T_s - T_\infty) \cdot x^3 = Gr_x \cdot Pr$$

Equation 3-1

$$a = \frac{\lambda}{\rho \cdot c_p}; \qquad \beta = \frac{1}{T_0} \dots for\ ideal\ gases$$

Equation 3-2

The interior temperature was a constant (25 °C), while the exterior temperature varied from -20 to +40 °C. All calculated Rayleigh numbers are listed in Table 3-1. A Rayleigh number above a value of 1E+9 clearly indicates a turbulent flow whereas a value below 1E+8 indicates a laminar flow characteristic.

Table 3-1: Rayleigh Number Calculation for the Refurbished (A) and the BTW with the Inner Gasket frame (B).

Exterior Temperature °C	-20	-10	0	10	20	30	40
Interior Ra Number BTW (A)	2.96E+10	2.85E+10	2.73E+10	2.63E+10	2.54E+10	2.46E+10	2.37E+10
Exterior Ra Number BTW (A)	2.08E+9	1.47E+9	9.65E+8	5.53E+8	1.76E+8	1.27E+8	4.04E+8
	Turbulent	Turbulent	Turbulent/ Transition	Turbulent/ Transition	Turbulent/ Transition	Turbulent/ Transition	Turbulent/ Transition
Interior Ra Number BTW (B)	3.04E+10	2.89E+10	2.76E+10	2.64E+10	2.54E+10	2.45E+10	1.36E+10
Exterior Ra Number BTW (B)	2.14E+9	1.39E+9	8.75E+8	5.08E+8	1.32E+8	1.69E+8	4.03E+8
	Turbulent	Turbulent	Turbulent/ Transition	Turbulent/ Transition	Turbulent/ Transition	Turbulent/ Transition	Turbulent/ Transition

The Rayleigh number was also calculated for the interior and the exterior BTW panes. Generally, the Rayleigh number was higher at the interior than at the exterior, and showed turbulent flow characteristics at all exterior temperatures. For exterior temperatures of -10 and -20 °C, the flow

characteristic was still turbulent at the exterior. For the remaining temperatures, the flow behaviour was in the transition area from turbulent to laminar. As a very low exterior temperature (below -10 °C) was used in all further simulations, the selected RKE turbulence model was appropriate to determine the air flow characteristic and heat transfer effects.

In contrast to the turbulent air flow characteristic inside the BTW´s cavity, the air-filled joints between the attachment frame and the panes were defined as laminar zones. This assumption was made because the calculated Reynolds numbers (Equation 3-3) did not exceed a value of 500.

$$Re_x = \frac{\rho \cdot v \cdot x}{\eta} = \frac{v \cdot x}{\nu}$$

Equation 3-3

For the computation of radiation exchange between surfaces, the DO radiation model was applied. The absorptivity for long-wave radiation was assumed to have a value of 1 for involved materials, except the surfaces with low-emission coating. The radiation equation was solved every 25 time steps, "Theta Division", "Phi Division", "Theta Pixels" and "Phi Pixels" were set to a number of 6 to provide reasonable computing time and adequate accuracy.

The choice of a proper solution method was another important consideration. In this study, the "SIMPLE" method was used for pressure-velocity coupling with a "Body Force Weighted" pressure discretization. The discretization for the gradients was the "Least Squares Cell Based" method as well as the "Second Order Upwind Scheme", which was used for convective, energy, and radiation terms. All numerical solution methods as well as the discretization parameters and the Under-Relaxation Factors (URF) used for the solution controls are summarized in Table 3-2.

Table 3-2: Numerical Solution Methods, Discretization Parameter and Under-Relaxation Factors

Solution Methods	Pressure-velocity coupling	Gradients	Pressure	Momentum	Turbulent Kinetic Energy	Turbulent Dissipation Rate	Energy	Discrete Ordinates
	SIMPLE-scheme	Least Squares Cell Based	Body Force Weighted	Second Order Upwind	Second Order Upwind	Second Order Upwind	Second Order Upwind	Second Order Upwind
Solution Controls (URF)	Pressure	Density/Turbulent Viscosity	Body Forces	Momentum	Turbulent Kinetic Energy	Turbulent Dissipation Rate	Energy	Discrete Ordinates
	0.8	1	1	0.2	0.8	0.8	0.99	1

For solid materials involved in the simulation, thermal conductivity was of importance. The material properties of all materials relevant to the simulation are summarized in Table 3-3. The value was 0.13 W/mK for the wooden parts and 1.0 W/mK for the panes. The low of the masonry wall of approximately 0.38 W/mK was measured in a laboratory.

Table 3-3: Material Properties for the Two-dimensional BTW CFD Simulations

	Density ϱ	Specific Heat Capacity c_p	Thermal Conductivity λ
	kg/m^3	$J/(kg \cdot K)$	$W/(m \cdot K)$
Glass	2500	720	1.0
Masonry	1620	882	0.38
Wooden Parts	600	2720	0.13
Thermal Insulation	500	1000	0.05

3.2.5 CFD Boundary Conditions

According to the structure and geometry of the BTW and the interior of the measurement layout, a two-dimensional simulation model was developed for a deeper analysis of thermal behaviour and flow characteristic (Figure 3-8).

The BTW geometry was assumed from the building´s inventory. A simplified assumption of a width of 2 mm for all air permeable joints was made. A recent study of ventilated double glazed facades from Pasut et al. [33] showed the importance of considering the window's environment to achieve higher quality simulation results. Therefore, the BTW simulation model also includes an interior zone and a section of the external environment. The interior zone is 2.67 m high and 4.8 m deep (see Figure 3-8). In

the CFD model, the interior is delimited by the corridor wall, the floor boundary, the ceiling and the building envelope, while the external environment is enclosed by a velocity in- and outlet as well as a virtual air boundary. The outer boundaries are all specified with constant temperatures. Assuming that the room below is kept at the same temperature as the test room, there is no heat exchange across the floor boundary. Another element is a heater below the window sill. The implementation of the velocity in- and outlet makes it possible to consider the impact of wind.
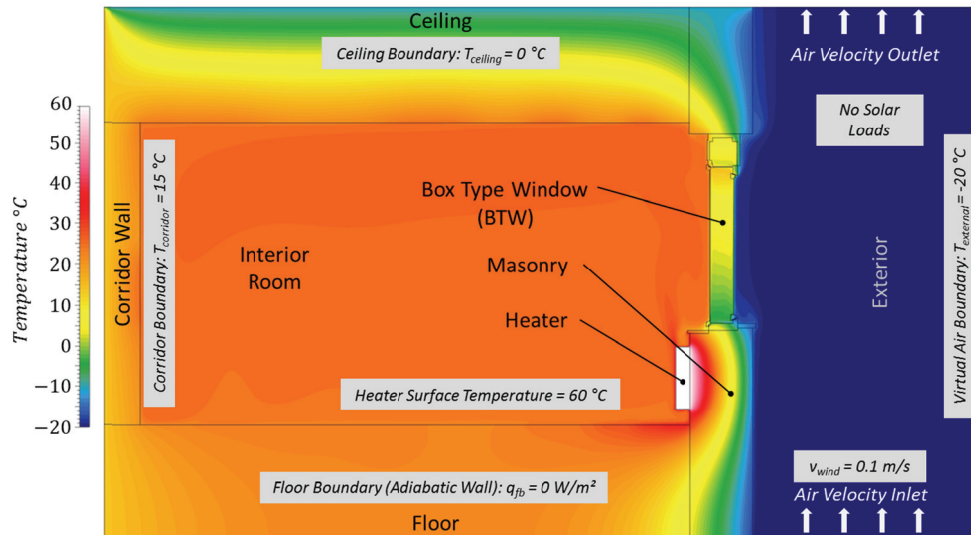
Figure 3-8: CFD Model Geometry and Boundary Conditions.

The BTW was investigated for a cold winter night with an ambient temperature of -20 °C, and without solar radiation. As per the results from wind speed measurements and a building aerodynamic simulation [1], a wind speed of 0.1 m/s along the buildings envelope's height was assumed. The investigated interior room with the BTW is located on the second floor, with the assumption that the room below is at the same temperature (no heat transfer through the floor boundary). In order to consider heat losses through the ceiling, a simplified solid block with a ceiling temperature of 0 °C was implemented. The corridor wall has a boundary temperature of 15 °C. According to measurements, the heater inside the interior room has a surface temperature of 60 °C.

3.2.6 CFD Mesh Assessment

Before a comprehensive analysis with the help of the CFD models, the influence of the mesh structure and the cell size on the simulation results was investigated. Therefore, the same CFD model geometry was divided into 50,000 (coarse), 250,000 (medium), and 500,000 (fine) cells before the y+ refinement, and was computed at the same boundary conditions. The interior temperature was assumed to be 25 °C while the external temperature was set to -20 °C for this mesh assessment. The rest of the boundaries (except for the heater temperature) were kept at the same values as were used in the evaluation of the improvement concepts. The resulting temperature and air velocity profiles are compared in the following Figures (Figure 3-9 and Figure 3-10).
The six diagrams in Figure 3-9 show the temperature (on the left) and air velocity profiles (on the right) for a section through the bottom, centre, and top of the BTW´s cavity for the coarse, middle and fine meshes of the BTW model. The temperature profiles of the coarse mesh deviate from the results of the medium and fine meshes (between 2 and 4 K). While only the results of the middle and fine meshes are similar in terms of their temperature profiles, the resulting velocity profiles of all three meshes match very well. From the resulting temperature profiles, it is possible to conclude that the coarse mesh is inappropriate for further CFD simulations. The diagrams in Figure 3-10 show the temperature (on the left) and the air velocity profiles (on the right) for sections through the BTW cavity's height (parallel and close to the interior as well as exterior glass). The temperature profile of the coarse mesh deviates from the results of the medium and fine mesh. Small deviations occur in the velocity profiles parallel to the glass panes between all three mesh sizes. The deviations between the velocity profiles of the medium and fine meshes are much smaller compared to that of the coarse mesh and can be neglected.
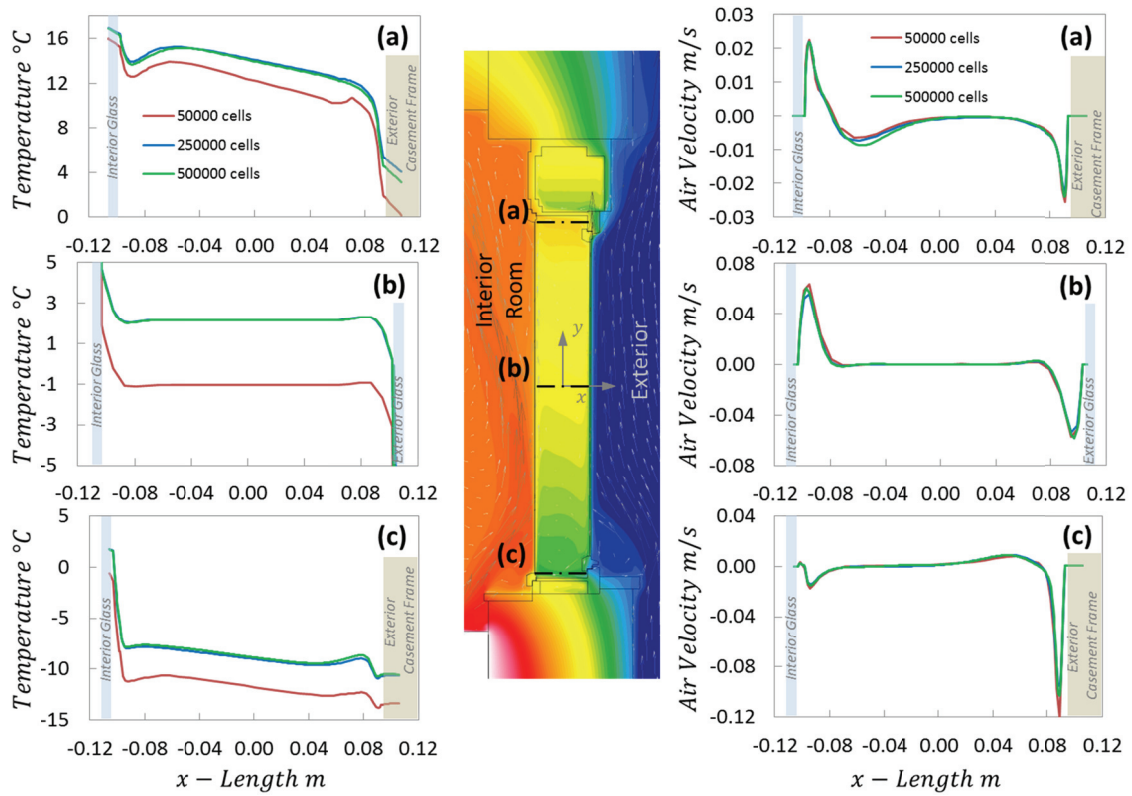
Figure 3-9: Temperature and Velocity Profiles from the Mesh Assessment's Simulation Results for a Section through the BTW´S x- Length

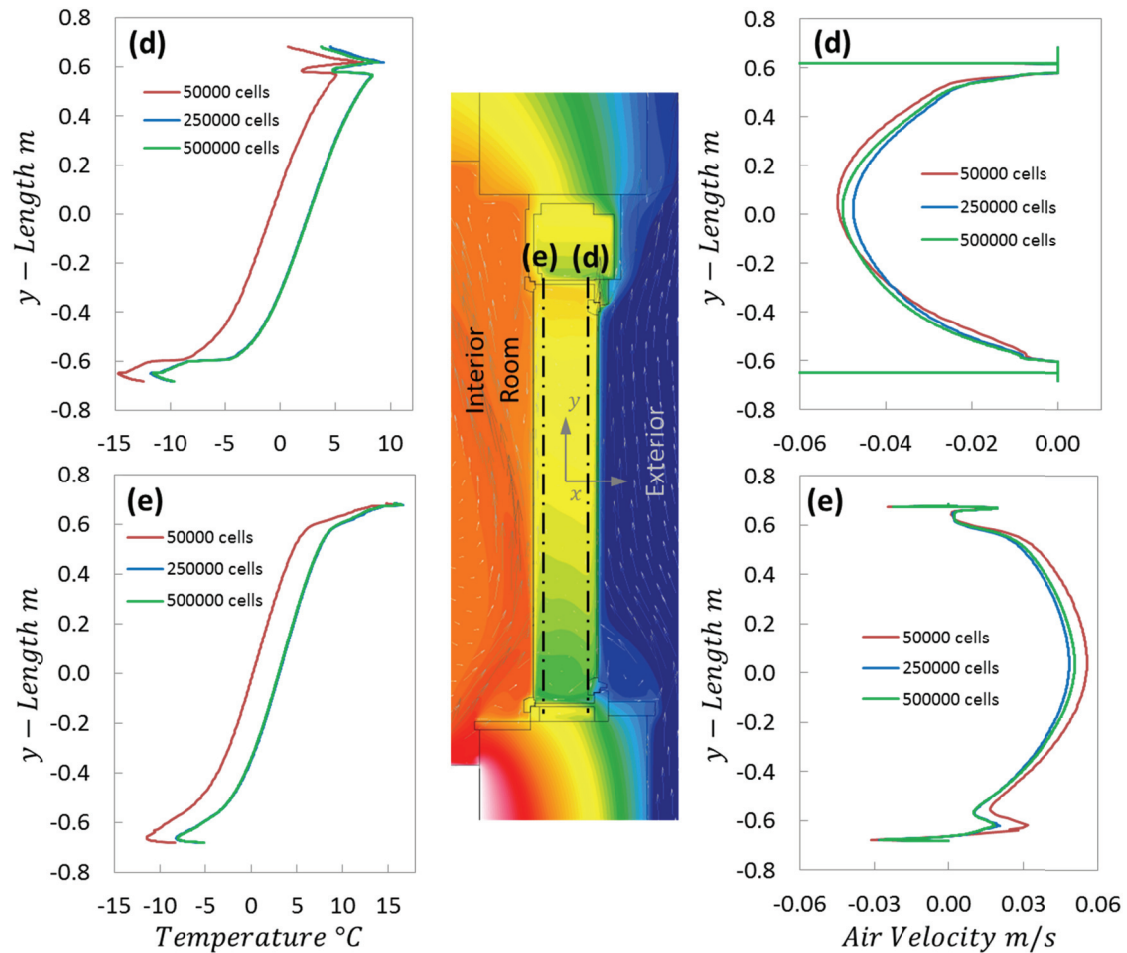**Figure 3-10: Temperature and Velocity Profiles from the Mesh Assessment's Simulation Results for a Section through the BTW´S y-Length**

From the results, it was possible to conclude that the coarse mesh is unsuitable for further simulations because the temperature and velocity profiles deviated too much from the results with the medium and the fine meshes. The temperature profiles determined for the medium and fine meshes did match very well. Since the velocity profiles of the two were also in good agreement, the medium mesh (with 250,000 cells) was deemed to be the most suitable for further investigations.

3.2.7   Comparison of Measurement and Simulation

Before analysing the thermal behaviour and investigating the air-flow characteristics, the simulation output had to be validated through a comparison of the measured and simulated temperatures inside the BTW´s air cavity. The first task was to find a suitable point of time when measured temperatures were approximately constant. Constant temperatures are required because the simulations were all performed for steady state condition. From 12 pm on February 2nd to 4 am on February 5th, the in-situ temperature measurements indicated perfect conditions for the validation of the steady state simulation of a cold winter day. The simulation model was therefore fed with the external temperature from 10 pm on February 4th, which was -10.3 °C. Temperatures measured were 24.7 °C for improved (G) and 35.1 °C for the refurbished BTW´s (A) interior room. Data from the temperature sensor at the position of T-room (see Figure 3-4) made it possible to compare the measurement and CFD simulation air temperatures directly above the heater. The heater surface temperature was modified until the measured and simulated air temperature at the position T-room matched. In the simulation results, the heater´s surface temperature was 51.0 °C for the refurbished BTW (A) and 69.0 °C for the improved BTW (G). The temperature of the ceiling boundary was set to 0.0 °C with a corridor temperature of 15.0 °C. Emissivity of 0.6 for the low emission coating at the interior pane was assumed for the simulation of the improved BTW.

Figure 3-11 presents a comparison of the measured temperatures of the interior window space and the sectional temperature profiles at the corresponding x-ordinate for refurbished (A) and improved (G) BTWs. To compensate for different heater surface temperatures, a dimensionless formulation of temperature (T/T_h) was used in these diagrams.
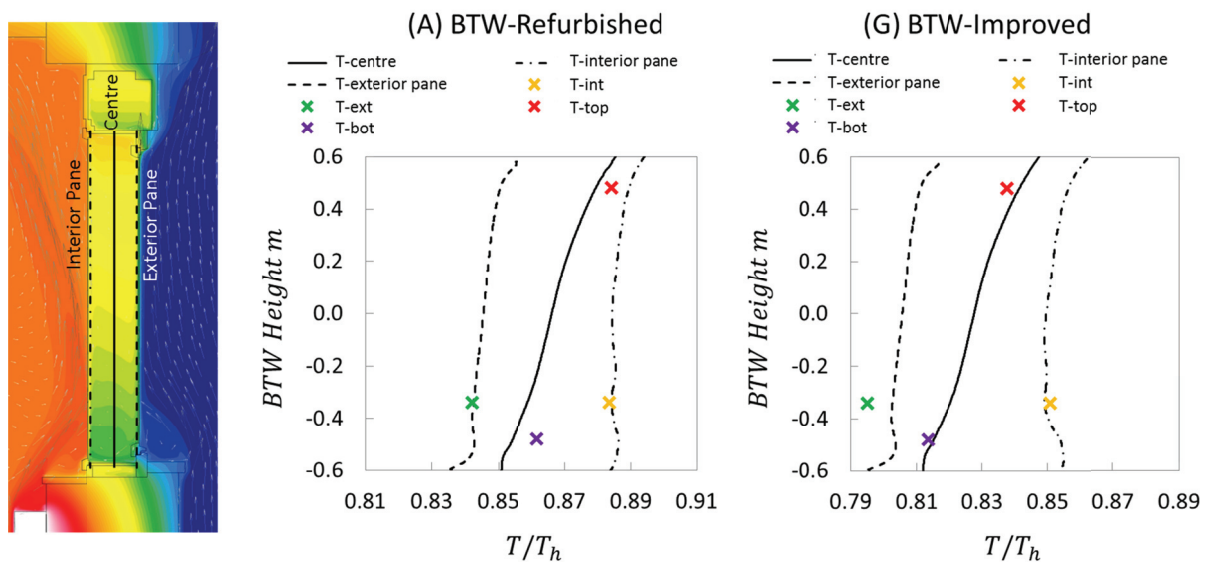

Figure 3-11: Comparison of the Measured and Simulated Temperatures of the Refurbished (A) and Improved (G) BTWs

The deviations between the measured and simulation results for each measurement point were as follows. With a temperature difference of -3.36E-04 for ΔT_{dim} (Equation 3-4) or -0.11 K for ΔT_{m-s} (Equation 3-5), good agreement was achieved between the measured and simulated temperature for the position at the external pane for the refurbished (A) BTW. T_{meas} was referred to as measured, ΔT_{sim} as the computed temperature in the following equations.

$$\Delta T_{dim} = \frac{T_{meas}}{T_h} - \frac{T_{sim}}{T_h}$$

Equation 3-4

Equation 3-5

$$\Delta T_{m-s} = T_{meas} - T_{sim}$$

The temperature at the interior pane was also almost matching, with a difference of ΔT_{dim} = -4.67E-04 (ΔT = 0.15 K). Evaluating the temperatures at the control points on the top and the bottom, it is possible to see lower temperatures in simulation results. The difference was higher at the bottom (ΔT_{dim} = 7.29E-03; ΔT = 2.36 K) than at the top (ΔT_{dim} = 4.89E-03; ΔT = 1.59 K). These distinctions can be explained by the assumption of the uniform width of the joints and the two-dimensional geometry used in the simulations.

Higher temperatures of approximately ΔT_{dim} = 7.50E-03 (ΔT = 2.57 K) were indicated in the simulation in comparison to the measurement for the improved (G) BTW at the external pane's validation position. The simulated temperature at the interior pane was about ΔT_{dim} = 1.70E-03 (ΔT = 0.5 K) below the measured value. As discovered during the evaluation of the refurbished BTW, the measured temperatures at the top (ΔT_{dim} = 3.83E-03; ΔT = -1.31 K) and the bottom (ΔT_{dim} = 1.82E-03; ΔT = 0.62 K) of the improved BTW were higher than those computed. These deviations could also be explained by the assumption of the joint's width and the use of a two-dimensional simulation model.

3.2.8   Comparison between Different Numerical Models

After the comparison of the measurement and simulation results, the influence of different numerical CFD model equations for the turbulence and the radiation on the temperature and air velocity inside the BTW's cavity was investigated (Figure 3-12). Therefore, the boundary conditions were taken from the comparison between the measurement and simulation results.
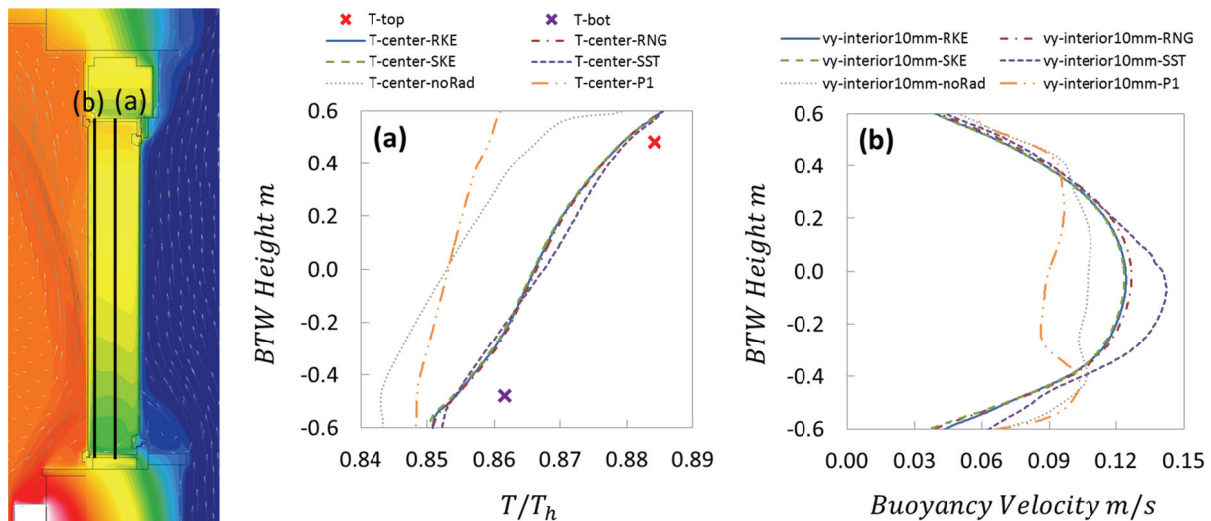

Figure 3-12: Comparison between Different Numerical Radiation and Turbulence Models for the Refurbished BTW (A)

Four of the most qualified existing formulations for the characterization turbulence of convective flow were compared: the RKE, SKE, RNG and SST models [6]. Observation temperatures and air velocity for the same sections inside the interior window space as in the validation of measurement data and the description of the general flow characteristic indicated that the RKE, SKE and RNG matched well. The SST model's results showed a higher temperature gradient and a thinner convective flow along the window panes, especially at the centre region referred to as the window's height. The influence of radiation inside the BTW was investigated by means of the DO and the P1 models in comparison with the case where radiation was excluded from the simulation. The ANSYS Fluent theory guide [6] proposes using the P1 model only for fluids with a high optical density. The P1 model showed the lowest temperature gradient, and generally lower temperatures along the interior window's height. When the radiation model was deactivated during the simulation, the temperature was also lower than that measured while using the DO model.

3.2.9 Air Flow and Temperature Characteristic inside the BTW Cavity

After all of the above mentioned comparisons, the two-dimensional CFD model of the BTW was computed according to the boundary conditions and model parameters presented in Chapters 3.2.4 and 3.2.5. In this chapter, the temperature distribution and air flow characteristics are described with the help of the resulting temperature contours and air flow vector plots from the refurbished (A) BTW, illustrated in the two following figures (Figure 3-13 and Figure 3-14).
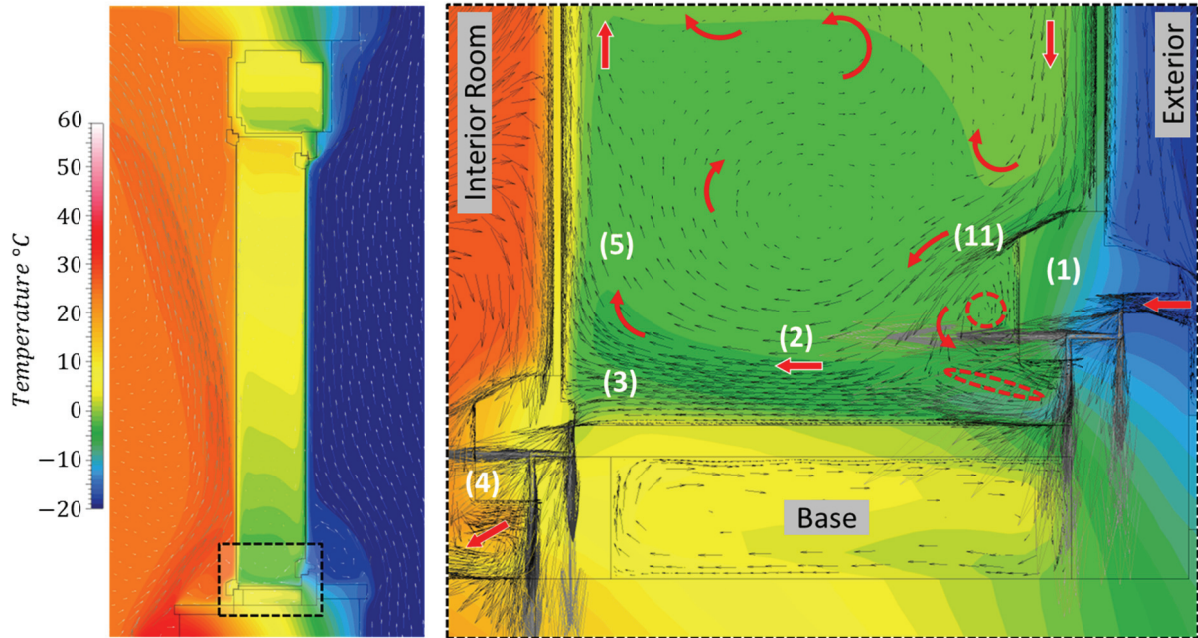
Figure 3-13: Temperature Contours and Air Flow Vectors at the Bottom Region Inside the Cavity of the Refurbished BTW (A)
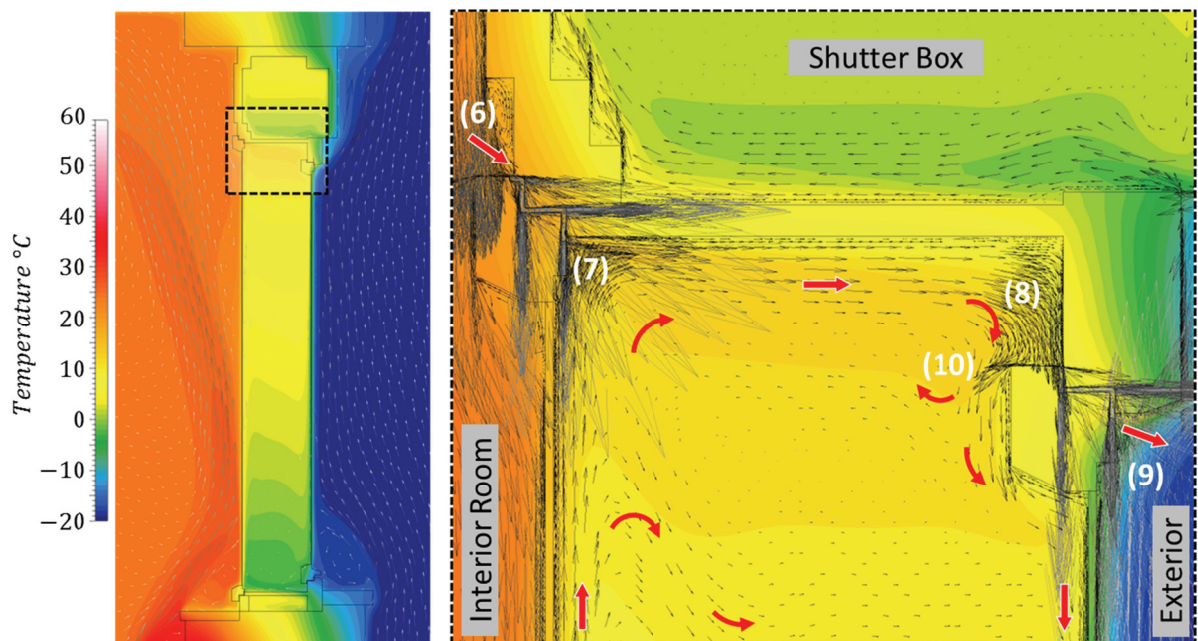
Figure 3-14: Temperature Contours and Air Flow Vectors at the Top Region Inside the Cavity of the Refurbished BTW (A)

The temperature contours and air flow vector plots of the refurbished BTW (A), showed the infiltration of air from the exterior into the BTW's air cavity (1) through the bottom exterior joint with a velocity of 0.18 m/s and a temperature of 14.6 °C. A convective air flow proceeded through the bottom of the air cavity to the interior casement (2). Close to the interior casement, the flow was split into two streams (3). One of these streams infiltrated the interior room (4) with an air velocity of 0.16 m/s and a temperature of 2.0 °C, while the other was redirected upwards towards the bottom frame of the interior pane (5). Above the interior pane, the air was heated, which resulted in buoyancy-driven

convective airflow. Infiltrating air from the interior room (6) was mixed with the upwards-flowing air at the top of the interior window casement inside the air cavity (7). The velocity of air in the interior top joint amounted to 0.16 m/s with a temperature of 19.5 °C. At the BTW air cavity's top, the airflow was redirected at the exterior casement and streamed downwards (8). Air was partly lost into the exterior environment (9) through the upper exterior joint at a velocity of 0.20 m/s and a temperature of 8.6 °C. A small fraction of air formed a recirculation at the height of the top, exterior window frame (10). On the edge of the lower external window frame, air was split up and several turbulences appear (11).

3.2.10 Thermal Evaluation of the BTW Renovation Concepts

This chapter describes the results of the CFD simulations of the improvement concepts (mentioned in Chapter 3.2.2). Figure 3-15 shows the resulting temperature contours from the two-dimensional CFD simulations. Because the improvement concepts (F) and (G) showed similar temperature contours as those of (A) and (B), their illustration is not necessary in this figure. The present evaluation concerns a comparison of the temperature and air velocity profiles at significant positions inside the BTW´s air cavity, a detailed heat flux analysis, as well as a comparison of the calculated U-values.
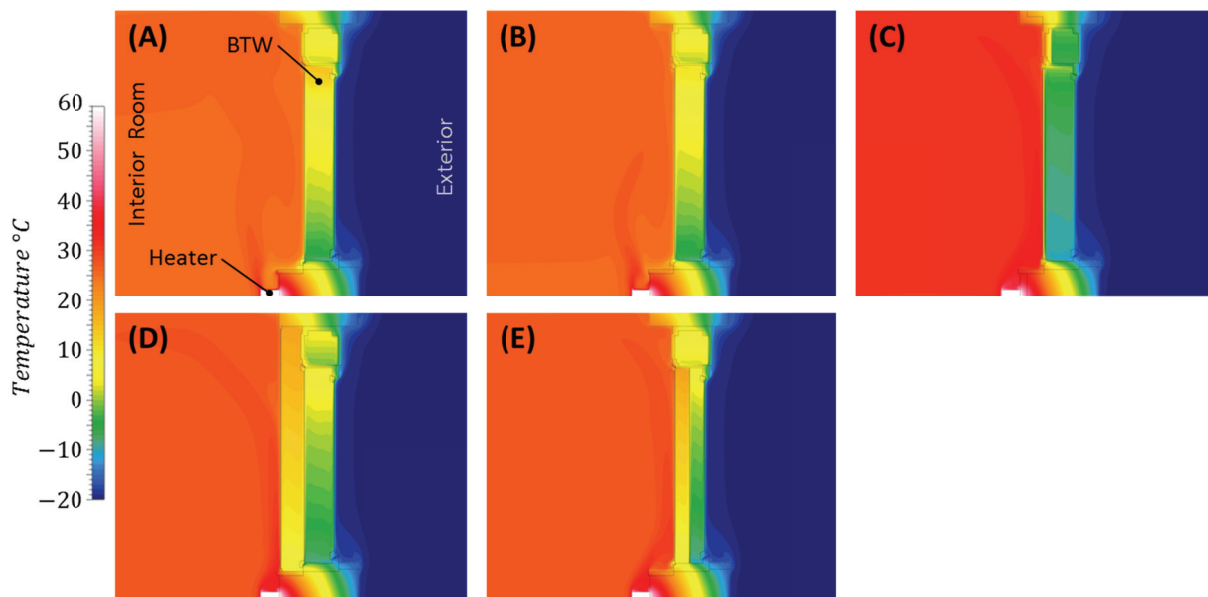

Figure 3-15: Comparison of the Temperature Contours between the Different Improvement Concepts

Temperature and Velocity Profiles

With the help of temperature and air velocity profiles at the three most important sections through the BTW´s cavity, it is possible to compare the thermal behaviour and flow characteristic (at cold climate conditions) of the different renovation concepts.

The first figure, Figure 3-16, presents a comparison of the temperature and air velocity profiles for a section through the centre of the BTW´s cavity, as is indicated in the left contour plot.
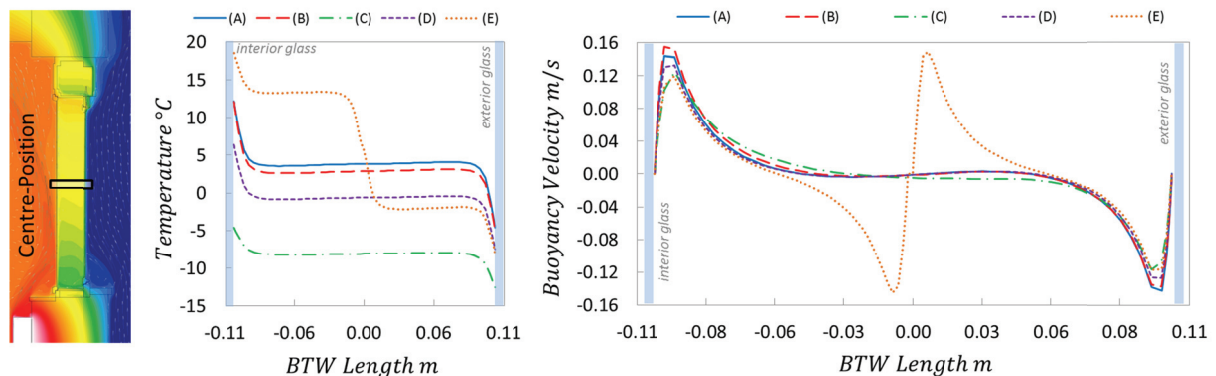

Figure 3-16: Comparison of Temperature and Air Velocity Profiles between the Interior and Exterior Casements at the Centre of the BTW´s Height

The temperature profile shows a similar trend for all renovation concepts except for concept (E), with the airproof divider. The temperature transition layer thickness at the interior and the exterior glass is approximately 30 mm. Due to the large distance between the interior and exterior casement frame, a region of almost constant temperature can be observed for all concepts. In this region of the BTW cavity, the temperature was 3.8 °C for the refurbished BTW (A), 2.8 °C for the BTW with the inner gasket frame (B), -8.1 °C for the thermally insulated BTW (C), and -0.6 °C for concept (D), with the additional interior casement frame. Two separate cavities occurred in concept (E), which led to two regions at constant temperatures: 13.4 °C in the inner cavity and -2.0 °C in the outer cavity.

The highest air velocity occurs 5-7 mm away from the glass panes, where the air velocity amounts to 0.143 m/s at the interior and 0.142 m/s at the exterior side in the case of the refurbished BTW (A). The concept with the inner gasket frame (B) shows a slightly higher air velocity (0.155 m/s) on the interior side, and a marginally lower velocity (0.137 m/s) on the exterior side in comparison to BTW (A). In the concept of the thermally insulated BTW (C), the maximum air velocity amounts to 0.124 m/s on the interior side and 0.117 m/s on the exterior side of the BTW´s cavity. With an air velocity of 0.132 m/s on the interior side and 0.127 m/s on the exterior side, concept (D), with the additional casement frame, is classified between concepts (A) und (C). In concept (E), with the divider, the air velocity is lower at the glass panes (0.12 m/s at the inner and 0.117 at the exterior glass) than at the airproof divider (0.145 m/s on the interior and 0.149 m/s on the exterior side).

In the next figure, Figure 3-17, a comparison of the temperature and air velocity profiles parallel and 10 mm away from the interior glass is presented for the renovation concepts shown in Figure 3-15.
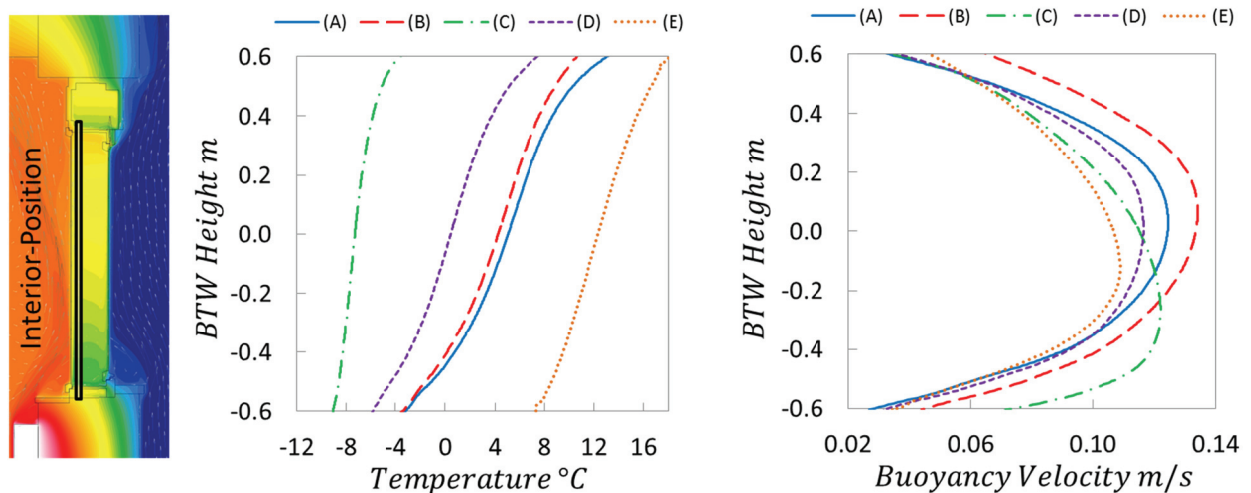

Figure 3-17: Comparison of Temperature and Air Velocity Profiles Parallel to and 10 mm away from the Interior Glass

The lowest temperatures occurred for concept (C), with the thermal insulation where the air is heated from -8.9 to -3.8 °C upwards along the interior glass. Renovation concept (D), with the additional interior casement frame, follows, in which the air is heated from -5.7 to 7.3 °C. In the refurbished BTW (A) and the BTW with the inner gasket frame (B), the air temperature is approximately -3.2 °C at the bottom region close to the interior glass and is heated up to 13.1 °C for BTW (A) and 10.6 °C for BTW (B). By means of an airproof divider (E), the air is heated from 7.4 to 18.0 °C along the BTW's interior glass.

In renovation concept (E), the maximum air velocity appears to be approximately 100 mm below the centre of the BTW´s height, with a magnitude of 0.109 m/s. For concept (C), the maximum air velocity also occurs below the centre (280 mm below) with a value of 0.122 m/s. The maximum velocity is close to the centre of the BTW for concepts (A) and (D), and amounts to 0.125 m/s for (A) and 0.117 m/s for (D). The maximum velocity occurs approximately 80 mm above the centre for concept (B), with a magnitude of 0.134 m/s. The last comparison of temperature and air velocity profiles inside the BTW´s cavity is illustrated in Figure 3-18. This figure shows the profiles parallel to and 10 mm away from the exterior glass for the renovation concepts shown in Figure 3-15.
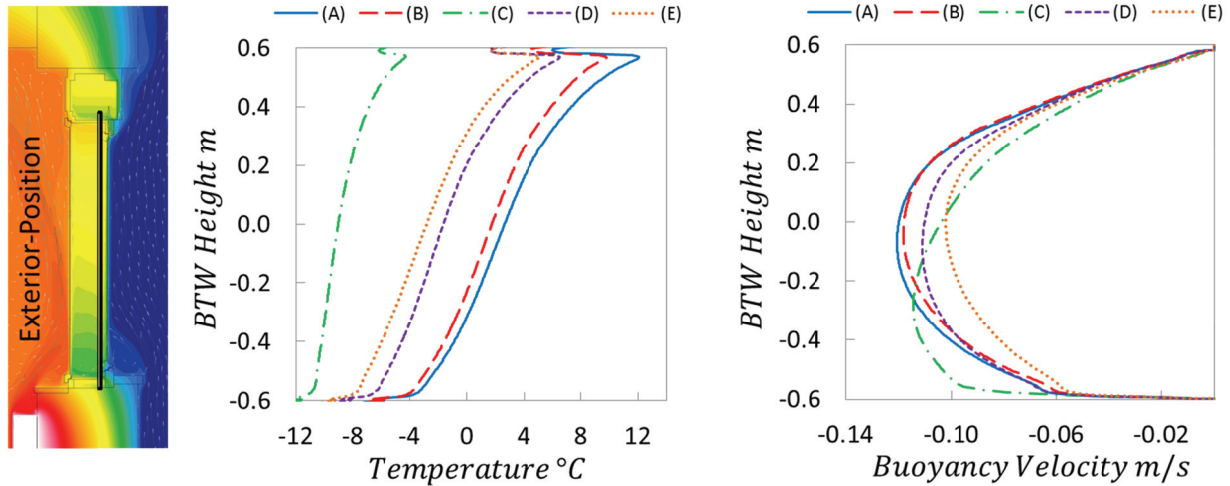
Figure 3-18: Comparison of Temperature and Air Velocity Profiles Parallel to and 10 mm away from the Exterior Glass

Again, the air temperature can be seen to increase from the bottom towards the top of the BTW´s cavity. In comparison to the temperature profiles with the same improvement concept 10 mm parallel to the interior glass in Figure 3-17, the temperature is generally slightly lower ($\Delta T \approx$ 1-3 K) for each single profile 10 mm parallel to the exterior glass. One exception occurs for the improvement concept (E), with the airproof divider, where the temperature profile close to the exterior glass is significantly lower than the profile close to the interior glass $\Delta T \approx$ 15 K). Close to the exterior glass, the maximum air velocity occurs approximately 300 mm below the centre of the BTW for concept (C), with a value of 0.115 m/s. The maximum velocity of 0.102 m/s for concept (E) can be observed close to the middle of the BTW´s height. Approximately 100 mm below the centre of the BTW, the maximum air velocity occurs for concept (D), with a magnitude of 0.111 m/s. The maximum velocity, with a value of 0.118 m/s, occurs approximately 50 mm below the BTW´s centre for concept (B), whereas the maximum velocity of 0.121 m/s for the refurbished BTW (A) occurs approximately 70 mm below the centre.

Heat flux Analysis

This section presents a detailed heat flux analysis for all BTW concepts. Again, the boundary conditions of a cold winter day were used for all simulations of the heat flux analysis (boundary conditions as described in Chapter 3.2.5). In the following seven figures, (Figures 3-19 through 3-25), the relevant surface heat fluxes are indicated by red arrows, while the magnitudes of the fluxes are inscribed beside the corresponding arrows in W/m².

In Figure 3-19, the heat fluxes for the refurbished BTW (A) are indicated with magnitude and direction. The highest heat losses occurred through the window glasses, with more than 100 W/m². Less than half of the heat loss through the glass can be observed through the shutter box. Even less heat is transferred to the exterior through the masonry below the BTW, with a value below 30 W/m², or above the BTW, with a value below 20 W/m². Inside the BTW´s cavity, including the cavity of the shutter box, heat is transferred from the bottom to the top due to the resulting temperature stratification (illustrated in Figure 3-13, Figure 3-14 and Figure 3-15). The heat loss through the BTW´s exterior frame is higher at the top than at the bottom of the BTW, whereas the opposite behaviour occurs for the BTW´s interior frame. While the heater is held at a constant surface temperature of 60 °C, the surface-averaged heat transfer from the heater to the interior room amounts to almost 350 W/m², while slightly less than 100 W/m² is transferred to the masonry.
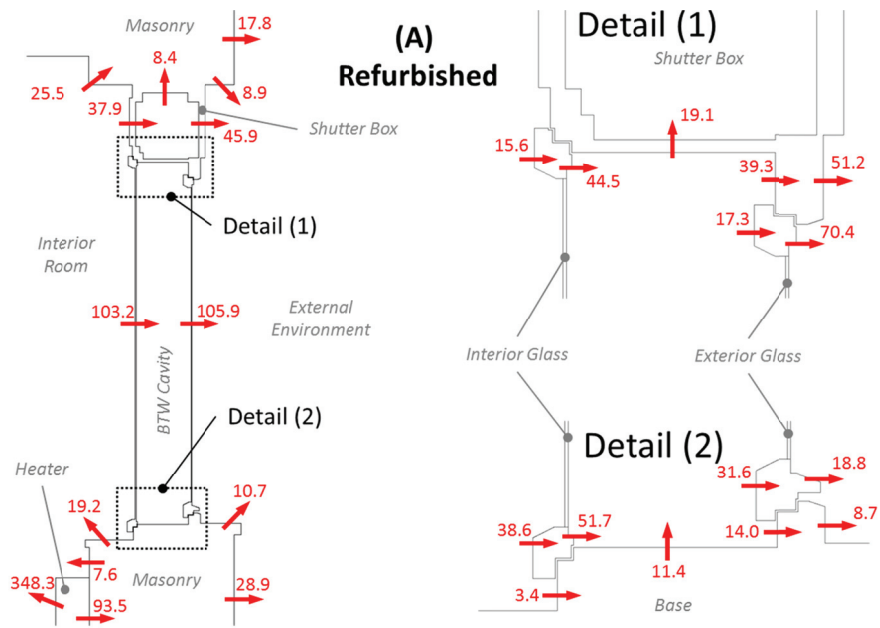
Figure 3-19: Section of the Simulation Geometry of the Refurbished BTW (A), where the relevant Surface Heat Fluxes are indicated (Red Arrows). The Heat Fluxes' Unit is W/m².

In Figure 3-20, the resulting heat fluxes for renovation concept (B), with the inner gasket frame to prevent the infiltration of air from the BTW cavity to the interior room, are illustrated. The heat flux analysis results in almost the same behaviour as exhibited by the refurbished BTW (A). A slightly lower heat loss (2%) to the environment through the exterior glass can be achieved with the integration of an inner gasket frame. For concept (B), 65% more heat is transferred from the base to the bottom of the BTW's cavity, but 18% less is transferred from the BTW to the masonry above the BTW. Further deviations in the amount of heat transferred occur at the region close to the air joints with the airproof gasket. On the whole, these deviations have hardly any influence on the overall thermal performance (U-value, as summarized in Table 3-4). The heating power required to maintain a constant heater surface temperature is reduced by 1%.
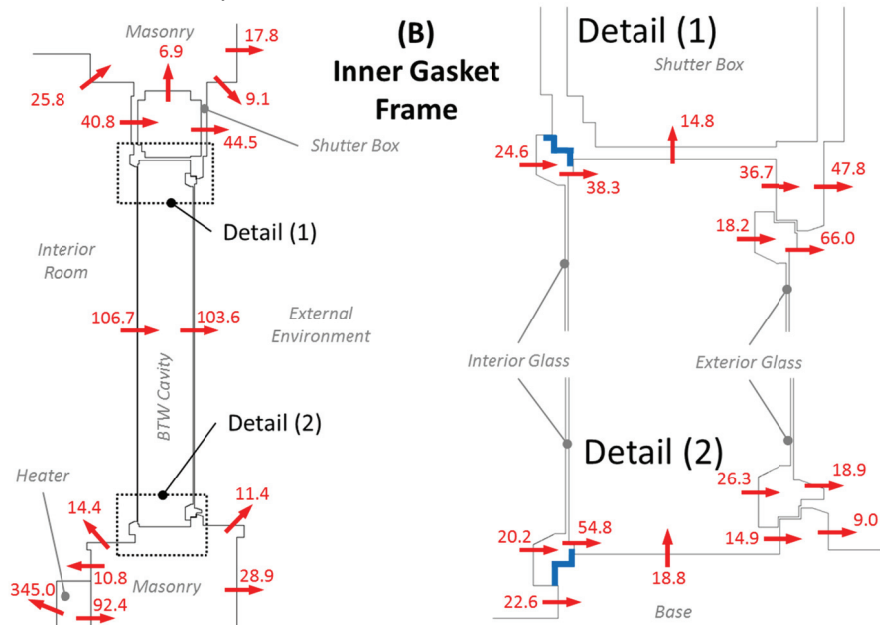

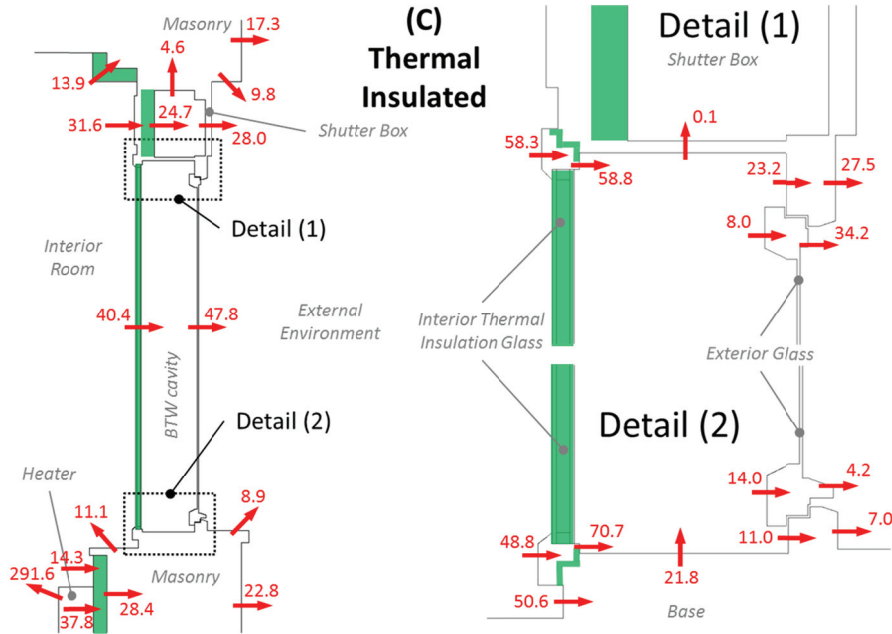**Figure 3-20: Section of the Simulation Geometry of the BTW with the (B) Inner Gasket Frame. Relevant Surface Heat Fluxes are indicated by Red Arrows. The Heat Fluxes' Unit is W/m².**

Figure 3-21 presents the heat flux analysis for the thermally insulated BTW (C). Heat loss through the exterior glass is dramatically reduced (-55% compared to BTW (A)), in particular due to the thermal

insulation glass installed at the interior casement. The increase in heat transfer for the timbered parts of the interior has only a marginal influence on the overall thermal performance of this renovation concept. The heat transferred from the BTW´s base to the cavity increased by approximately 91%. This effect can be prevented by installing additional thermal insulation at the BTW´s base. Compared to BTW (A), 55% less heat is transferred from the shutter box to the masonry above the BTW with renovation concept (C). This renovation concept (C) can therefore reduce the heating power required by 16%.

Figure 3-21: Section of the Simulation Geometry of the BTW with the (C) Thermal Insulation Glass. The relevant Surface Heat Fluxes are indicated by Red Arrows. The Heat Fluxes' Unit is W/m².

With the help of the following figure, Figure 3-22, the heat flux behaviour of renovation concept (D), with the additional interior casement, is analysed. Approximately 20% less heat is transferred through the exterior glass compared to the refurbished BTW (A). While 28% more heat is transferred from the BTW´s base to the cavity, the heat transferred from the shutter box to the masonry is reduced by 37%. The heating power required can therefore be reduced by 8% thanks to the additional interior casement.
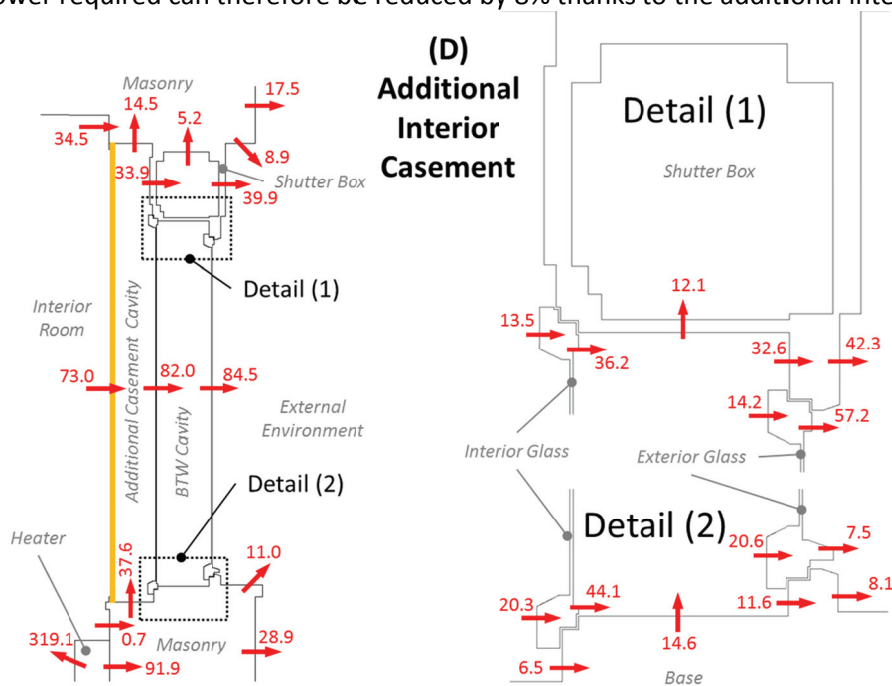

Figure 3-22: Section of the Simulation Geometry of the BTW with the (D) Additional Interior Casement. The relevant Surface Heat Fluxes are indicated by Red Arrows. The Heat Fluxes' Unit is W/m².

In Figure 3-23, the heat fluxes of the BTW with the airproof divider (E) are illustrated. Approximately 24% less heat is transferred through the exterior glass to the environment compared to BTW (A). Due to the divider inside the BTW´s cavity, two different heat fluxes occur at the base. The surface average of these two values is roughly 10% of the heat transfer rate of BTW (A). Only 4% less heat is transferred from shutter box to the masonry in this renovation concept. Similar to concept (D), approximately 8% less power from the heater is required.
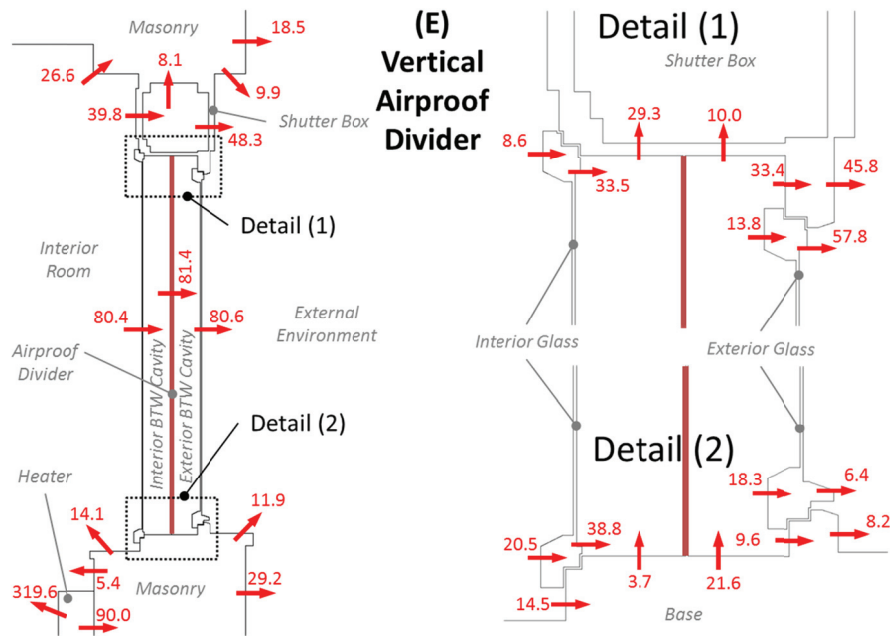
Figure 3-23: Section of the Simulation Geometry of the BTW with the (E) Vertical Airproof Divider. The relevant Fluxes are indicated by Red Arrows. The Heat Fluxes' Unit is W/m².

A low emission coating on the inner side of the interior glass for the BTW (A) leads to a reduction in heat transfer of approximately 24%. The heat flux analysis of this concept, (F), is illustrated in the next figure, Figure 3-24. Furthermore, in this concept, 65% more heat is transferred to the BTW´s cavity from the base, while 18% less heat is transferred from the shutter box to the masonry. As in the previous two concepts, a reduction of heating power of approximately 8% is achieved.
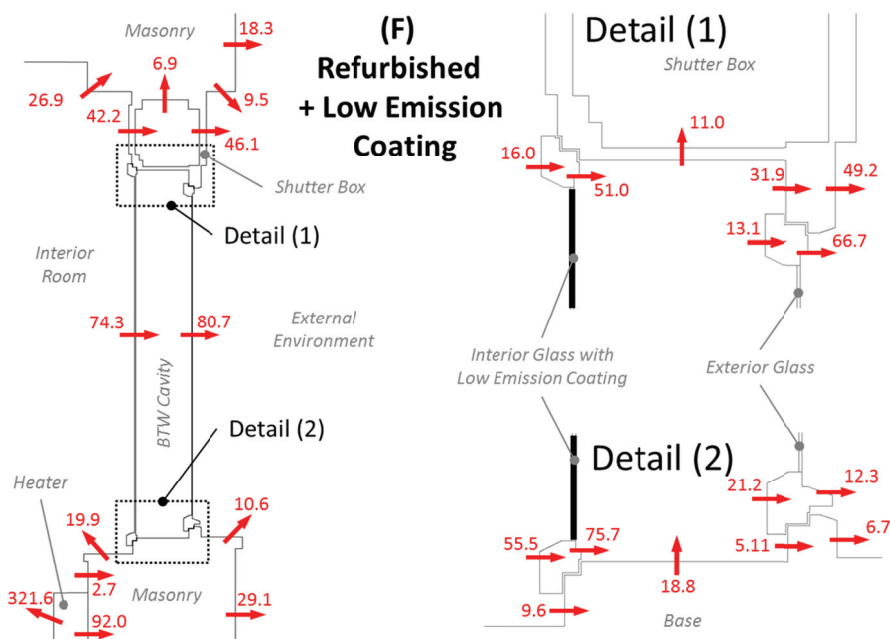

Figure 3-24: Section of the Simulation Geometry of the Refurbished BTW with a Low Emission Coating on the Interior Glass (F). The Relevant Surface Heat Fluxes are indicated by Red Arrows. The Heat Fluxes' Unit is W/m².

The combination of an inner gasket frame and a low emission coating (concept (G), presented in Figure 3-25) results in 28% less heat transfer through the exterior glass. Furthermore, 152% more heat is transferred from the base to the cavity, and 33% less heat is transferred from the shutter box to the masonry. Finally, the heating power can be reduced by roughly 9% by using the thermal improvement measures of concept (G).
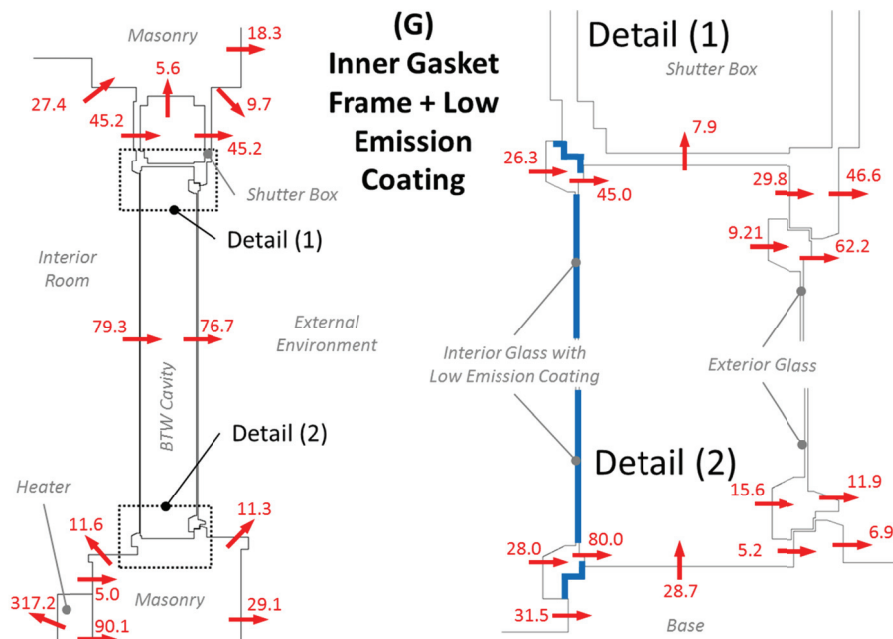

Figure 3-25: Section of the Simulation Geometry of the BTW with the Inner Gasket Frame and Additional Low Emission Coating on the Interior Glass (G). The Relevant Surface Heat Fluxes are indicated by Red Arrows. The Heat Fluxes' Unit is W/m².

At the end of the heat flux analysis, the most important differences gleaned during the heat transfer analysis are summarized in the following section. The heat fluxes through the masonry were very similar for all concepts. Only concept (C), with the integrated thermal insulation, showed a slightly lower heat flux from the masonry to the exterior. The heat fluxes through the shutter box were lower for the concepts (C) and (D). The heat flux of the heater varied because of the assumption of a constant heater surface temperature. The lower the heat flux from the heater to the interior room, the better the concepts functioned in terms of their thermal protection. The highest heat flux differences occurred for the BTW´s casements, and especially for the window glasses. For concepts (A) and (B), the heat fluxes through the glass were higher than 100 W/m², whereas they were between 40 and 50 W/m² for concept (C). For the other concepts, the heat flux value varied between 73 and 85 W/m².

Calculated U-Values

Sections of the origin CFD model (Figure 3-8) were prepared for the determination of the U-value. For the numerical determination of the U-value, the BTW and a small part of the exterior and interior were kept in the new simulation geometry. Generally, the U-value calculation for the BTW in this section uses two different CFD models. While the first variation contains both the BTW and the masonry wall, (shown in (1), Figure 3-26), the second variation only considers the BTW alone (shown in (2), Figure 3-26). These simulation models, which can also be referred as a virtual hot box, have four boundaries, with the following specifications: A temperature of 25 °C was assumed for the left boundary (interior), while the temperature was -20 °C at the right boundary (exterior). The influence of the heater was excluded in these simulations and the top and bottom boundaries were defined as an adiabatic wall.
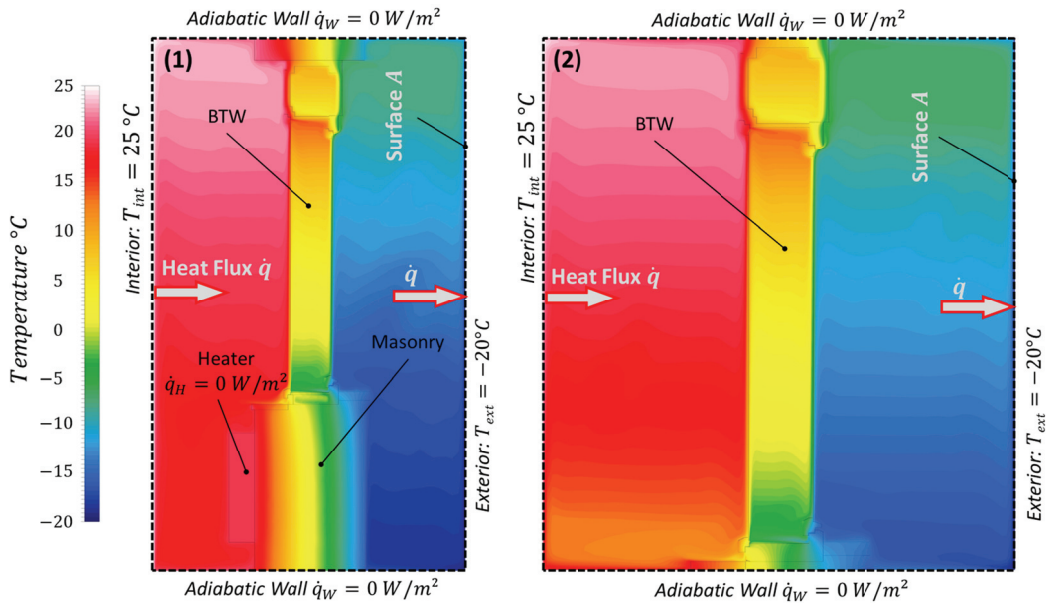
Stationary, Two-dimensional CFD Models

Figure 3-26: Sections of the Original Simulation Geometry (Figure 3-8) used for the U-Value Determination of (1) the BTW and (2) a Part of the BTW Masonry

In addition to the temperature difference (ΔT in K), the U-value calculation requires the heat transfer rate ($\dot{q}$ in W/m²) from the left to the right boundary of the CFD model (Equation 3-6 - Equation 3-9). The U values calculated from the simulation results are illustrated in Table 3-4.

$$\dot{Q} = U \cdot A \cdot \Delta T = U \cdot A \cdot (T_{int} - T_{ext})$$

Equation 3-6

$$\dot{q} = U \cdot \Delta T = U \cdot (T_{int} - T_{ext})$$

Equation 3-7

$$U = \frac{\dot{q}}{\Delta T}$$

Equation 3-8

$$U = \frac{1}{\frac{1}{\alpha_e} + \frac{s}{\lambda} + \frac{1}{\alpha_i}}$$

Equation 3-9

Table 3-4: U-value Comparison

Improvement Concept		(A) Refurbished	(B) Inner Gasket Frame	(C) Thermal Insulated	(D) Additional Interior Casement	(E) Vertical Airproof Divider	(F) (A) + Low Emission Coating	(G) (B) + Low Emission Coating
BTW	U-values $W/(m^2 \cdot K)$	1.74	1.69	0.76	1.32	1.32	1.38	1.32
	heat flux W/m^2	78.1	76.2	34.2	59.2	59.4	62.0	59.4
BTW & Masonry	U-Values $W/(m^2 \cdot K)$	1.37	1.35	0.65	1.09	1.08	1.12	1.08
	Heat Flux W/m^2	61.6	60.5	29.2	48.8	48.6	50.5	48.6

The U-values made it possible to rank thermal performance on a cold winter day. Regarding to the refurbished BTW (A), a 56% lower U-value was obtained for the fully thermal insulated BTW (C). With the integration of an additional interior casement (D) or a vertical airproof divider (E), the U-value was reduced by 24%, whereas a gasket frame (B) for the interior casement caused a reduction in the U-value of only approximately 3%. However, the integration of a low-emission coating for the interior glass ((F), (G)) reduced the U-value by about 21%.

3.3 Flow Characteristics and Thermal Behaviour of Multifunctional Façade Constructions [4]

3.3.1 Introduction

Over the course of the recently completed "MPPF" [2] research project, a prototype for a new type of multifunctional façade was designed. This prototype was attached to the south façade of the "Hans Höllwart Forschungszentrum für integrales Bauwesen AG" office building in Stallhofen, Austria. Figure 3-27 shows the variety of different functional components implemented. The entire prototype is made up of six parapet carriers and eight façade components, each equipped with different functionalities.

Figure 3-27: Left, MPPF-prototype 2: the South-oriented Façade of an Office Building in Stallhofen, Austria

Solar thermal collectors (ST façade element) (1) were implemented in the two parapet carriers at the top of the prototype as well as in one façade element on the second floor. These are part of a solar thermal system for the generation of domestic hot water. A façade-integrated fan coil unit (2) on the left side and a transparent façade element with roller blinds (3) are also part of the building´s envelope on the second floor. The façade element (TR), on the right side of the second floor (4), bears a conventional Raffstore shading device and which can be exchanged for a photovoltaic daylight module. Both the parapet carriers between the first and second floor and two façade elements on the first floor, contain different types of polycrystalline photovoltaic modules (PV façade element) for the production of electrical power (5). One façade element on the first floor is equipped with a special photovoltaic roller blind (6). The façade element on the right side of the first floor (8) is equipped with transparent glass panes covered with semi-transparent thin film photovoltaic modules.

---

4. Parts of this Chapter have already been published in [60] and [19].

3.3.2 Ventilation cavities and data monitoring

The façade elements containing the polycrystalline photovoltaic modules are equipped with air cavities between the exterior and interior shell with a distance of 140 mm (Figure 3-28, left) while the cavity width (x-length) in the elements with the solar thermal collector is about 80 mm (Figure 3-28, centre). All elements of this test façade have periphery openings to prevent the overheating of the façade elements. Insect grills are installed to protect the ventilation cavity insects and vermin. As a result of the construction concept the openings of the air cavities are near the outer shell.

A large number of measurement sensors were integrated into the test façade during manufacturing and assembly. The measurement and the monitoring systems were installed in the interior rooms behind the façade after assembly. The position and description of the sensors required for this study are illustrated in Figure 3-28. For all temperature measurements, Pt 100 elements were used. In the façade element with the polycrystalline photovoltaic, two hot wire anemometers were integrated inside the cavity, 1.306 m above and below the centre of the element, in order to measure temperature and velocity (PV0.81 and PV3.06). The data collected from these sensors is essential for the boundary setup and the validation of the CFD simulation models. For the hot wire anemometer installed, the velocity measuring range of the sensors is 0.08 to 2.0 m/s with an accuracy of ± (0.04 m/s +1% of the measured value) and a resolution of 0.001 m/s. These sensors have a temperature measuring range from -20 to +70 °C with a resolution of 0.1 K and an accuracy of ± 0.7 K. The Pt 100 sensors used (with 4 conductors) are classified with Class B accuracy according to DIN EN 60 751, and the measuring range of -35 to +180 °C.
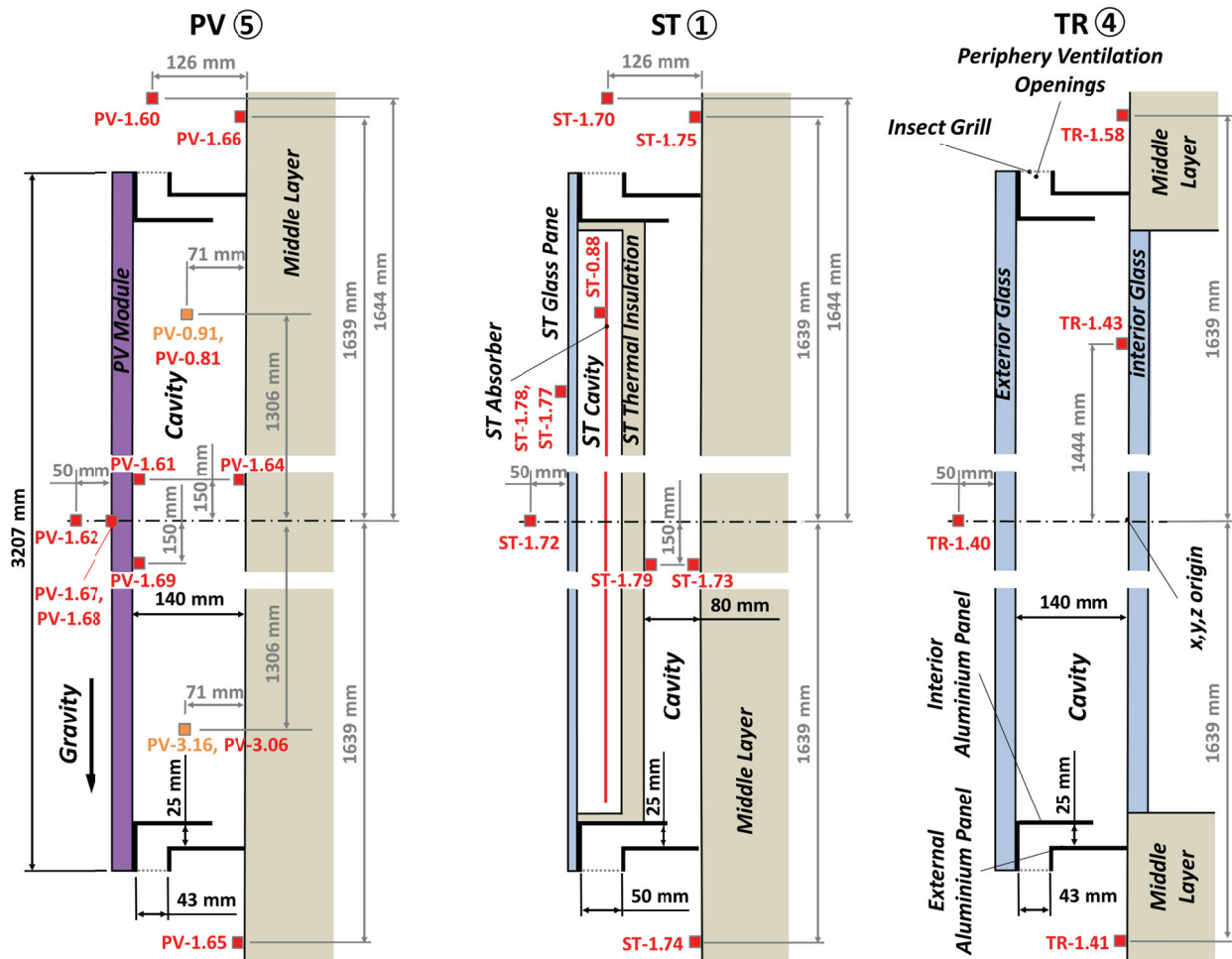

Figure 3-28: Schematic of the Façade Elements with the Integrated Photovoltaic Modules (PV), the Integrated Solar Thermal Collector (ST), and a Glass Pane (TR), also including the Positions of the Measurement Sensors used for the CFD Boundary Setting and Validation (Chapters 3.3.7 and 4.2.4)

3.3.3   Measurements and Data Monitoring

After the assembly of the test façade and the installation of the measuring system, data was collected for the entire year of 2013. This chapter presents some samples from of these in-situ measurements, as well as a discussion and cross-comparison of results from the essential façade elements in this study.

Data was monitored over the year 2013 in the course of the MPPF project [2]. From this extensive collection, daily profiles of the days with both the highest exterior temperatures and the highest solar irradiation were extracted for further investigations. Finally, two daily climate profiles were representative enough to perform CFD simulations of the functional façade elements for a typical hot summer day in the region Graz, Austria (Figure 3-29).

Vertical solar radiation was measured with pyranometers at two positions. One was positioned above the façade element with the special photovoltaic roller blind (sensor G-3.27, façade element number 6, shown in Figure 3-27 while the other was mounted in the attic above the solar thermal collector (G-0.08). Additionally, horizontal solar radiation was captured by another pyranometer mounted in the attic above the ST façade element (sensor G-0.82). The external temperature (G-0.03) was measured by means of a weather station located on the roof of the office building. The weather station's temperature measurements have an accuracy ± 0.3 K with a resolution of 0.1 K. To measure solar radiation star pyranometers were used which capture radiation in the spectral range of 0.3 to 3 μm. These sensors have a metering range from 0 to 1500 W/m², a resolution of 0.1 W/m² and an accuracy of 6% of the measured value.

Figure 3-29 illustrates the data measured over the course of July 29th, 2013 and August 21st, 2013. Data from August 21st represents a typical summer day for the region of Graz, Austria, with a maximum external temperature of 25 °C (used to validate the three-dimensional CFD models presented in chapter 4.2.4). On July 29th, the maximum outdoor temperature for that year was recorded, at 38.9 °C. This temperature was used for comparison with the dimensional CFD simulations.
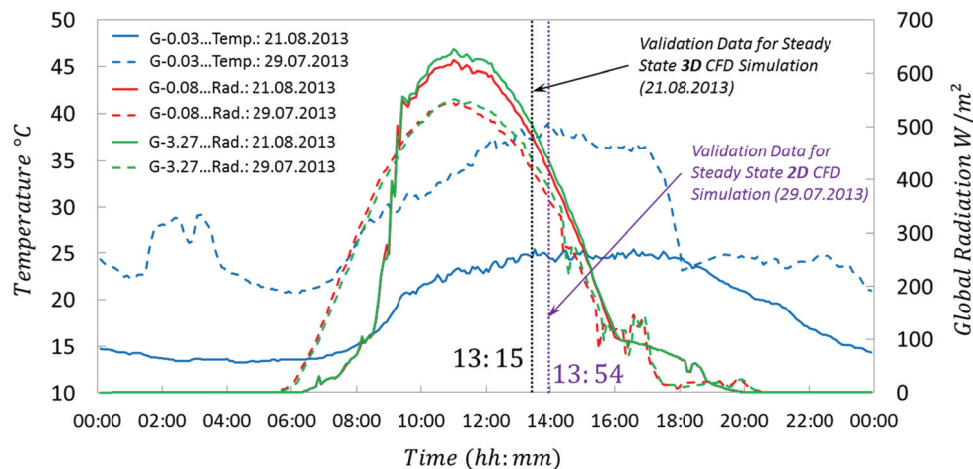

Figure 3-29: Measured External Temperatures and Vertical Global Radiation on 21.08.2013 and 29.07.2013

Figure 3-30 shows the comparison of the interior wall (glass) temperature as well as the air temperature 50 mm in front of the corresponding façade element´s centre. The positions of the corresponding measurement sensors are indicated in Figure 3-28. To investigate the TR façade element (Figure 3-27, position 4) the shading system was considered to be fully retracted.

The maximum temperature measured on the interior wall surface of the TR element was slightly higher than that of the PV façade element, and much higher than that of the ST element on August 21st, although the measured external air temperatures were close together on this day. On July 29th, the maximum external air temperature was higher, whereas the highest peak in the measured global radiation was lower compared to the values of August 21st. On July 29th, the measured air temperatures in front of the façade elements were again close (in a similar range to August 21st), except for a few higher peaks of air temperature in front of the PV façade element. The interior wall temperature for the ST façade element was not significantly higher than the air temperature in front of the façade. The interior wall temperature of the PV façade element was higher than that of differed from the measurements taken on July 29th.
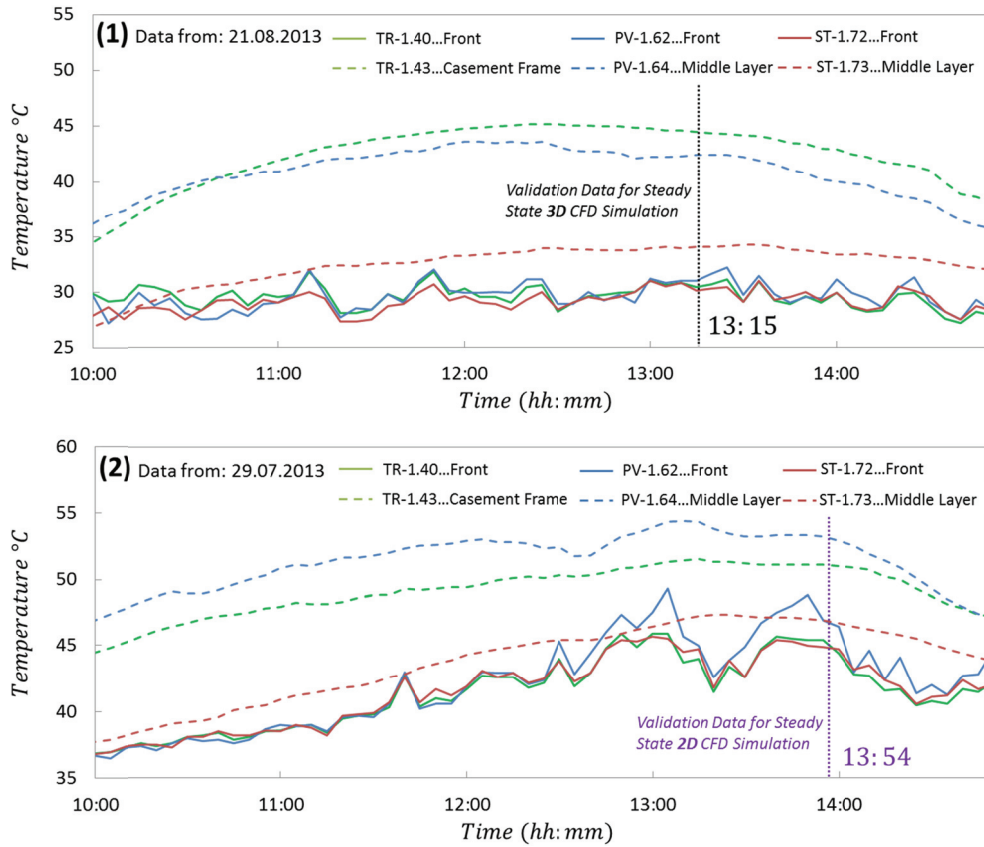
Figure 3-30: Comparison of the Middle Layer (Casement Frame) Surface Temperature and the Air Temperature 50 mm in front of the MPPF Façade Elements, TR, PV, and ST, from (1) 21.08.2013 and (2) 29.07.2013
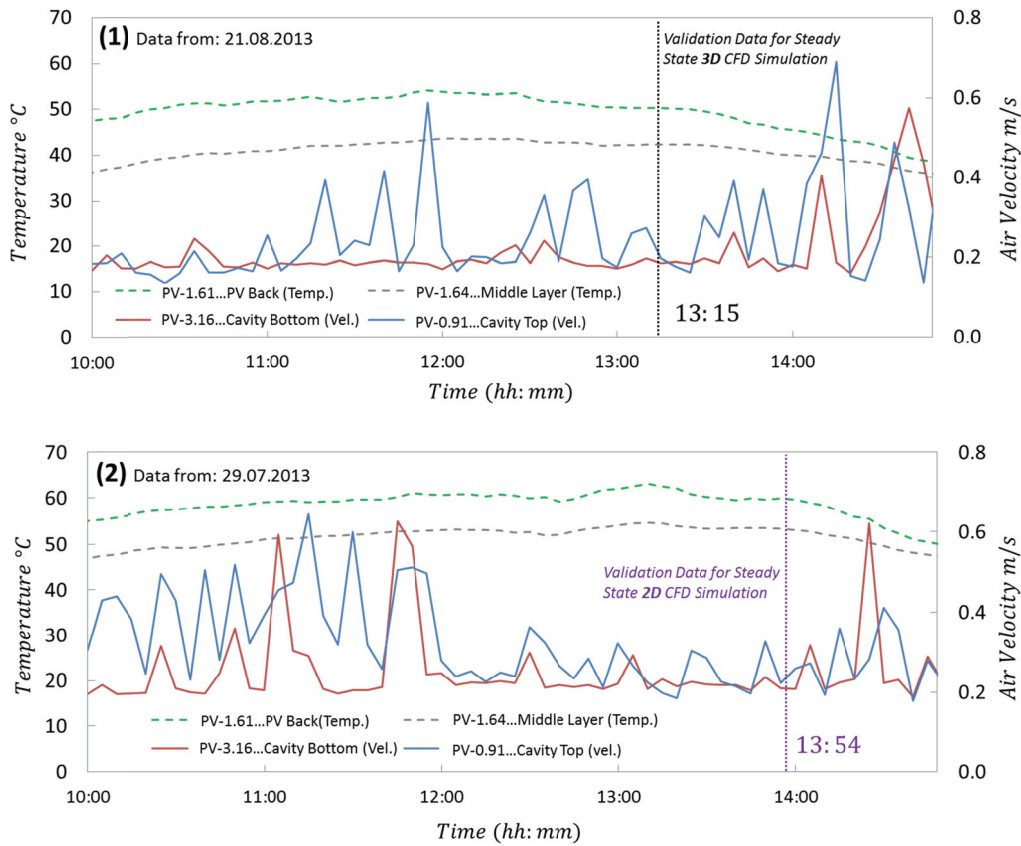

Figure 3-31: Comparison of the Monitored Air Velocities and Temperatures Inside the Ventilation Cavity of the MPPF-Façade Element, with an Integrated Photovoltaic Module from (1) 21.08.2013 and (2) 29.07.2013, Showing the Temperatures at the PV Rear Surface and the Interior Wall Surface

Further data taken from the PV façade elements can be seen in the diagrams in Figure 3-31. These diagrams show the monitored air velocity and temperature inside the cavity of the PV façade element (PV-0.81/PV-0.91 and PV-3.06/PV-3.16) as well as the PV rear surface temperature and the interior wall surface temperature. The temperature sensors PV 1.61 and PV 1.64 indicate the surface temperatures at the PV rear side and the interior wall.

On both July 29th and August 21st, the velocity shows a minimum value below 0.2 m/s during the time period illustrated in Figure 3-31. Several peaks of higher air velocity were observed, which may have been affected by external wind. On July 29th, a maximum air velocity of 0.63 m/s was obtained at the bottom measurement sensor (PV-3.16), whereas the maximum velocity was slightly higher, at sensor position PV-0.91 at the top of the ventilation cavity, with a value of 0.64 m/s. The maximum velocities were 0.69 m/s for the bottom (PV-0.91) and 0.58 m/s for the top (PV-3.16) measurement sensors on August 21st.

Generally, fewer fluctuations were observed from 12:00 to 14:00, the time period which was used for the comparison between the measurement and CFD simulation results (Chapters 3.3.7 and 4.2.4).

3.3.4 CFD model design

Due to the thermal lift, the main flow direction is assumed to be vertical; therefore, the approach involves representing the four vertical façade sections A-A, B-B, C-C and D-D in a two-dimensional simulation model (Figure 3-32).

(1) Solar Thermal Collector
(2) Opaque Element with Itegrated Façade Fan Coil Unit
(3) Window Element with Roller Blind
(4) Photovoltaic Daylight Module
(5) Photovoltaik Module (Polycrystalline Glas-Glas Module)
(6) Window Element with Photovoltaik Roller Blind
(7) Crystalline Silicon on Glass
(8) Amorphous Semi-transparent Silicon Thin-film Modules
(9) Opaque Element with LED-Display
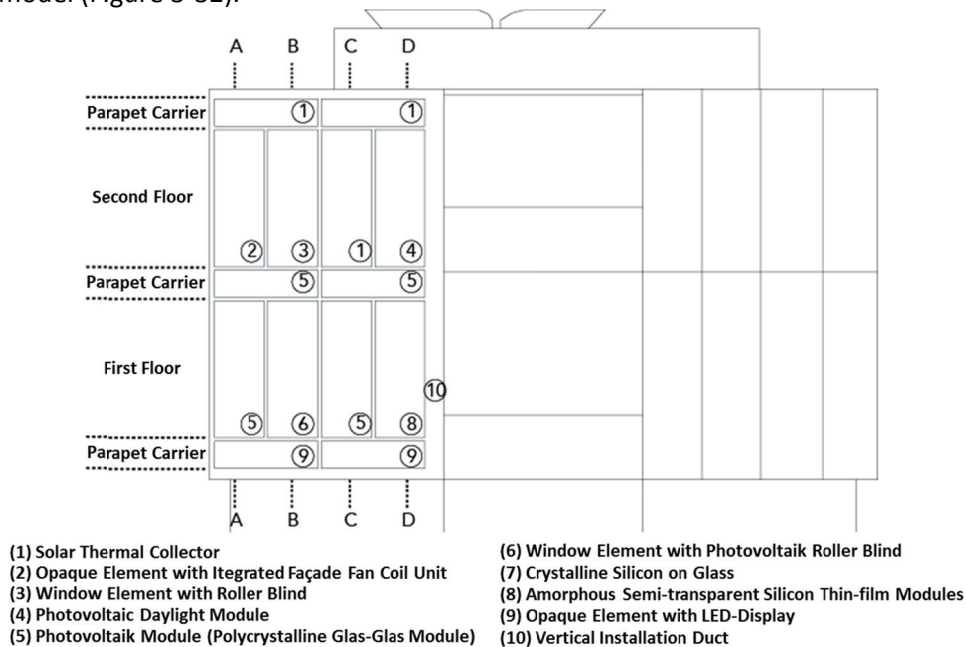(10) Vertical Installation Duct

Figure 3-32: Schematic of the MPPF Prototype 2, including a brief Description of the Integrated Multifunctional Components, indicating the Sections Relevant to the Two-Dimensional CFD Simulations through the Façade

In order to represent the climatic conditions and flows in the façade, the simulation domain also includes a part of the outside environment and a section of the adjacent interior. This chapter took section C-C as for a sample evaluation of thermal behaviour and the visualization of flow characteristics. The simulation domain (see Figure 3-33) extended over all three floors of the office building. The focus of the considerations was the area around the solar thermal collectors integrated into the façade on the first floor, and the photovoltaic modules integrated into the façade on the second floor. The ground floor was taken into account in the simulation model in all sections in a simplified form in order to consider its influence on upward flowing air at the façade. In order to obtain accurate simulation results for the thermal and fluidic behaviour in and around the façade construction, on the basis of the prototype 2, the simulation domain was extended with parts of the interior rooms and a section of the exterior space. The entire two-dimensional simulation domain measures 15 x 11 m (height x width). The external border of the domain is about 4.5 m from the façade, the depth of the interior amounts to approximately 6.0 m. The upper border is approximately 2.5 m over the highest building edge. The domain consists of 380 components altogether (both fluid and solid), while the mesh consists of more

than one million cells (Chapter 3.3.6). Due to the mesh adaptation, especially at the regions close to the walls, the y^+ value did not exceed a value of 1.5. In the cavities of the façade elements, the y^+ value was below 1.0.

The CFD meshes were produced with the help of the software Gambit [4]. Figure 3-33 shows the mesh of section C-C with the solar thermal façade collector and the façade-integrated PV module. Figure 3-34 shows the detail of the window with an installed roller blind located in section B-B (shown in the schematic in Figure 3-32).
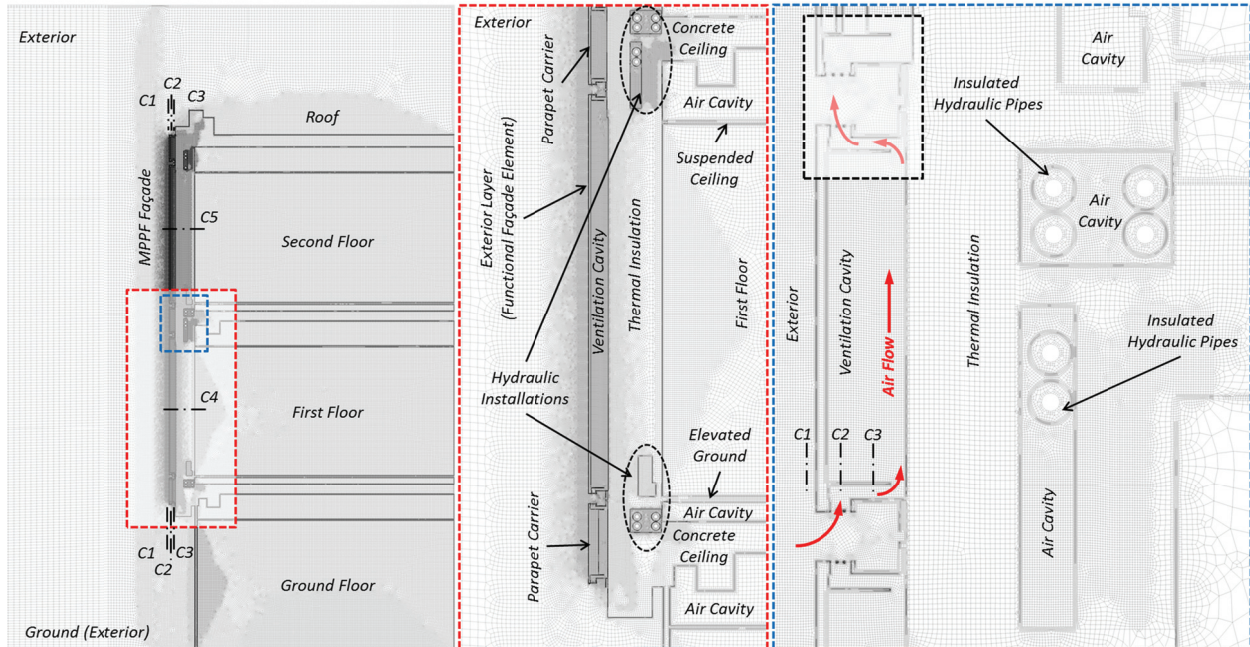
Figure 3-33: CFD Mesh from Simulation Model of the Section C-C (Figure 3-32).
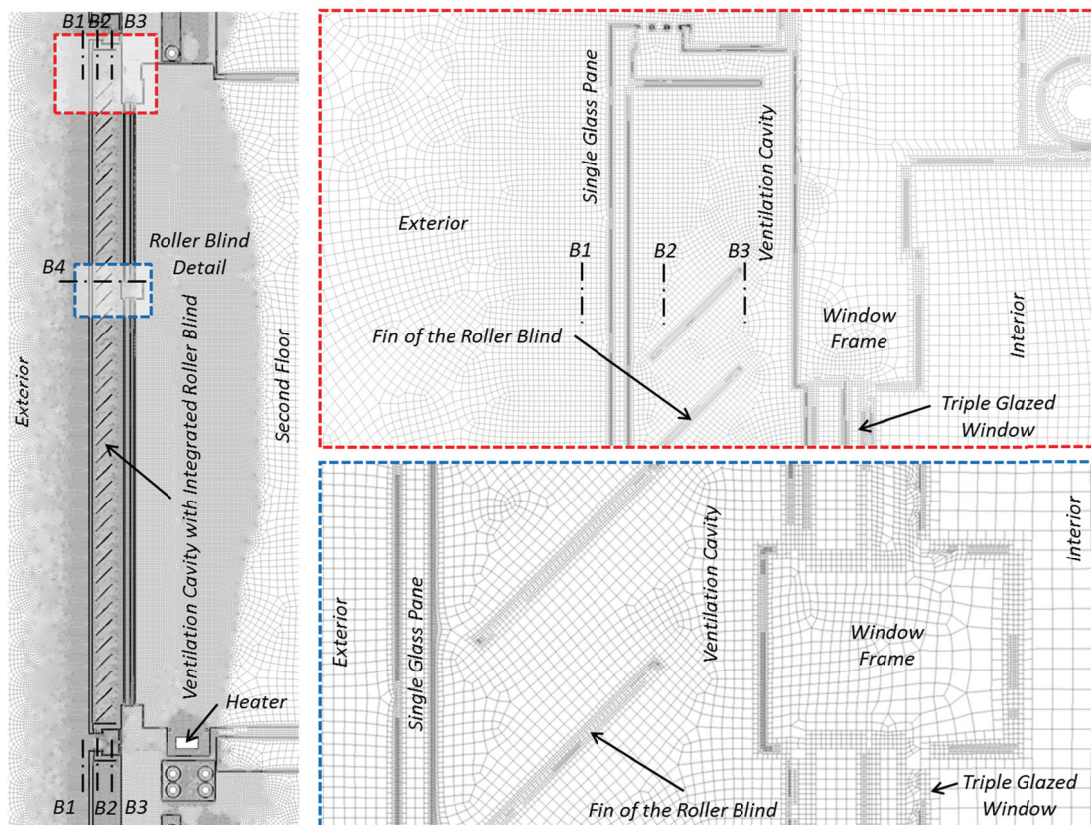
Figure 3-34: CFD Mesh from Simulation Model of the Section B-B (Figure 3-32).

The cell area of the meshes used varies between 0.01 and 10,000 mm², where the largest cells are 100 x 100 mm and the smallest cell size is 0.1 x 0.1 mm. The orthogonal quality of the cells varies between the values of 0.1 and 1.0, with an average value of 0.98. The skewness of the cells varies between 0 and 0.94, with an average value of 0.035. From the average values of the orthogonal quality and the skewness it is possible to conclude that only very few cells are of low quality in the CFD simulation using these meshes. Again, the cells of low CFD quality only occur in the simulations in the solid domains. The meshes are therefore well suited for the following CFD analysis of the MPPF façade.

Two extreme climatic situations were selected for the investigations: in the first case, a cold winter day without solar irradiation (night situation, see Chapter 3.3.6), and in the second, a hot summer day with high solar irradiation (presented in Chapter 3.3.9).

Simulations were again carried out with the help of the ANSYS Fluent software [6]. In these simulations, airflows were determined with the RNG turbulence model. The extensions, "Enhanced Wall Treatments" and "Full Buoyancy Effects," made it possible to determine the natural convection currents both inside and outside the façade, under the influence of gravity. In the simulations, air was always regarded as an incompressible ideal gas, since no serious differences of pressure were expected. The conservation of energy equation was necessary in order to determine the heat transfer, and to illustrate the natural convection currents. While the thermal impact of solar irradiation (wave length between 0.38 and 2.5 μm) was considered in the form of local surface heat sources in the simulation model (see Chapter 3.3.5), the influence of the thermal radiation (wave length > 2.5 μm) was determined with the help of the DO radiation model. This was very important in order to be able to take the exchange of radiation between the individual (opposite) surfaces into account.

The solution methods, discretization, and solution controls - similar the simulation models of the BTW (Chapter 3.2.4) - are summarized in Table 3-5 below:

Table 3-5: Numerical Solution Methods, Discretization Parameter and Under-Relaxation Factors.

Solution Methods	Pressure-velocity coupling	Gradients	Pressure	Momentum	Turbulent Kinetic Energy	Turbulent Dissipation Rate	Energy	Discrete Ordinates
	SIMPLE-scheme	Least Squares Cell Based	Body Force Weighted	Second Order Upwind	Second Order Upwind	Second Order Upwind	Second Order Upwind	Second Order Upwind
Solution Controls (URF)	Pressure	Density/Turbulent Viscosity	Body Forces	Momentum	Turbulent Kinetic Energy	Turbulent Dissipation Rate	Energy	Discrete Ordinates
	0.75	1	1	0.25	0.8	0.8	1	1

3.3.5 Pre-calculated Surface Heat Sources for the Summer Conditions

For the calculations, the radiation was split into two wavebands. The first waveband represents the visible fraction ("shortwave fraction") of the solar irradiation between a wavelength of 0.38 to 0.78 μm. A second waveband ("longwave fraction") was specified for the calculation of the surface heat sources, with a wavelength range between 0.78 and 2.5 μm. Both fractions of the solar irradiation were added from the values extracted from Duffie and Beckman´s study [66]. The fraction of radiation with a wavelength below 0.38 μm (ultraviolet) was negligible, and was therefore excluded from the simulation. The pre-calculated surfaces heat sources used for the simulations of a hot summer day are summarized in the following table, Table 3-6. The solar irradiation I_{Sol} was 1000 W/m² at a solar angle α_{Sol} of 45° in the simulations of hot summer climate conditions, which resulted in a shortwave fraction $I_{Sol,short}$ of approximately 490 W/m² and a longwave fraction $I_{Sol,long}$ of approximately 440 W/m², perpendicular to the façade (fraction of the ultraviolet radiation was approximately 60 W/m²). Considering the different solar transmission and absorption characteristics of the materials involved (shown in Table 3-7), the total surface heat sources were calculated according to the following Equation 3-10.

Equation 3-10

$$q_S = q_{S,short} + q_{S,long} = \left(I_{Sol,short} \cdot \alpha_{short} + I_{Sol,long} \cdot \alpha_{long} \right) \cdot \cos(\alpha_{Sol})$$

Because of the solar angle of 45°, the heat sources at the vertical and horizontal surfaces have the same values in the two-dimensional simulations under summer conditions.

Table 3-6: Table 3-6: Pre-calculated Surface Heat Sources for a Hot Summer Day with 1000 W/m² at a Solar Angle of 45°

Surface Heat Source in W/m^2	Short Wave Fraction $(q_{S,short})$	Long Wave Fraction $(q_{S,long})$	Total Surface Heat Source (q_S)
Exterior Glass Pane	28	292	320
Exterior Sun Glass	194	292	486
ST Absorber Behind Glass Pane	290	-	290
Exterior PV Cell/Module	308	289	598
PV Cell/Module Behind Glass Pane	271	-	271
Polished Aluminium Behind Glass Pane	76	-	76
LED Displays	87	280	367
Exterior Steel/Aluminium Plates, Black	312	286	598
Exterior Steel/Aluminium Plates, Grey	208	286	494
Steel/Aluminium Behind Glass Pane, Black	275	-	275
Steel/Aluminium Behind Glass Pane, Grey	214	-	214
Asphalt Ground	312	280	592
Semi-Transparent PV	177	292	469
Exterior Pane of Triple Glazing	24	-	24
Middle Pane of Triple Glazing	21	-	21
Interior Pane of Triple Glazing	19	-	19
Floor of the First and Second Floor	104	-	104
Floor of the Ground Floor	153	-	153
Roof of the Office Building	208	286	494

The materials used in the two-dimensional CFD simulations of the MPPF are listed in Table 3-7:

Table 3-7: Material properties for CFD Simulations of the Two-dimensional MPPF.

	Density ρ	Specific Heat Capacity c_p	Thermal Conductivity λ	Short Wave Absorptivity α_{short}	Long Wave Absorptivity α_{long}	Short Wave Transmissivity τ_{short}
	kg/m^3	$J/(kg \cdot K)$	$W/(m \cdot K)$	—	—	—
Glass	2500	720	1.0	0.08	0.94	0.88
Sunglass	2500	720	1.0	0.56	0.94	0.40
ST Absorber (Copper)	8978	381	387.6	0.95	0.95	-
PV Cell/Module	2500	720	1.0	0.89	0.93	-
Polished Aluminium	2800	896	160	0.25	0.1	-
Aluminium (Black)	2800	896	160	0.9	0.92	-
Aluminium (Grey)	2800	896	160	0.7	0.92	-
Steel (Black)	8030	502	16.3	0.9	0.92	
Steel (Grey)	8030	502	16.3	0.7	0.92	
Asphalt (Ground)	2300	2000	0.9	0.9	0.9	-
Timber	700	2310	0.17	0.5	0.9	-
Masonry (Concrete)	2200	1000	1.6	-	-	-
Masonry (Concrete-Steel)	2500	880	2.3	-	-	-
Seal (Rubber)	1100	1600	0.5	-	-	-
Mineral Wool	130	920	0.042	-	-	-
Window Profile (Aluminium-Air)	450	1310	1.0	0.25	0.1	-
Semi-Transparent PV	2500	720	1.0	0.51	0.94	0.45

3.3.6   CFD Mesh Assessment

Again, the results of different CFD meshes were compared in order to ensure the independence of the mesh structure from the simulation results. Therefore, both a coarse and a fine mesh were prepared for this assessment. Furthermore, the results before and after the y^+ adaptation of these two meshes were

considered in order to assess the impact of a finer mesh structure in the near-wall regions on the thermal and fluidal behaviour inside the ventilation cavities and their close environment. In the mesh assessment, the same boundary conditions for a hot summer day as described in Chapters 3.3.5 and 3.3.9. For the coarse mesh, the whole domain was divided into 0.35 million cells for section C-C and 0.39 million cells for section B-B. After the y^+ adaptation, the mesh of section C-C consisted of 0.82 million cells, and the mesh of section B-B was made up of 0.85 million cells. The fine meshes contained 1.18 million (C-C) and 1.45 million (B-B) cells before and 1.67 million (C-C) and 1.89 million (B-B) cells after the y^+ adaptation. Figure 3-35 presents a comparison of the temperature contours for one of the most significant regions inside the CFD model of the sections B-B (Figure 3-33) and C-C (Figure 3-34) of the MPPF façade. Generally, there are no significant differences between the results; one can only observe that the impact of the infiltrating air from the exterior on the temperature inside the ventilation cavity is stronger for the simulation results with the meshes after the y^+ adaptation. Using different meshes results in negligibly small deviations in the contours at regions close to the defined heat sources.
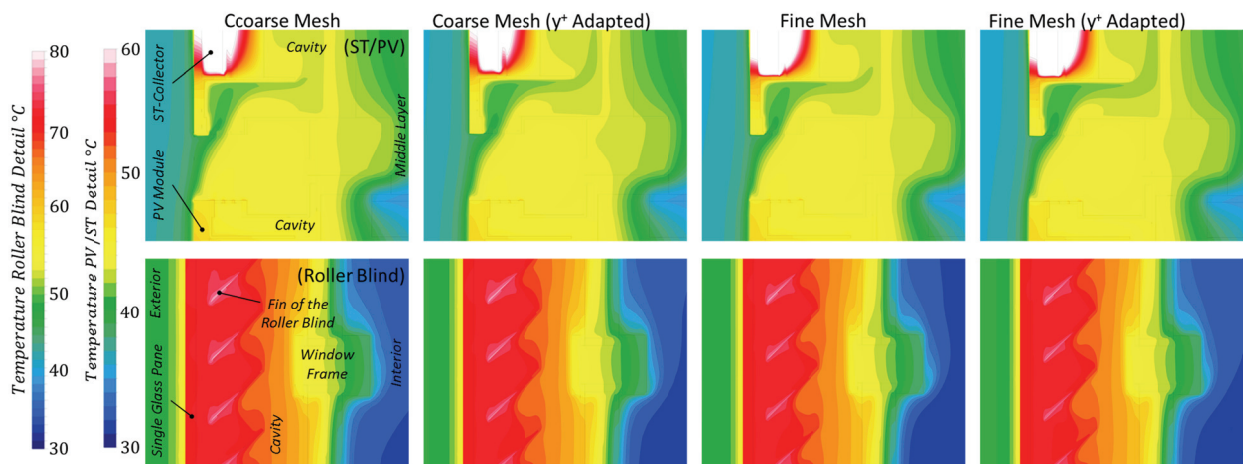
Figure 3-35: Top: Comparison of the Temperature Contours at the Transition between the PV- and the ST Façade Elements; Bottom: Comparison of the Region of the Ventilation Cavity with the Installed Roller Blind Close to the Middle Window Frame

In a further comparison of the different meshes, temperature and velocity profiles along the ventilation cavity width and the building height were compared. The profiles in the diagrams in Figure 3-36 present the temperature and buoyancy velocity characteristics for a section through the ventilation cavity width of the PV- and the ST-façade elements, and for a section through the façade element with the installed roller blind. The position of these sections (B4, C4 and C5) is indicated in Figure 3-33 and Figure 3-34.
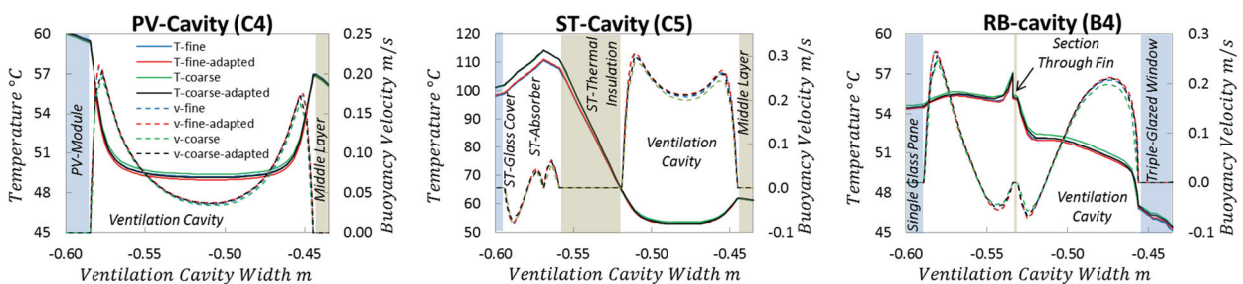
Figure 3-36: Comparison of the Temperature and Air Velocity Profiles for Well-defined Sections through the Ventilation Cavities of the MPPF Façade Elements.

The profiles through the ventilation cavity of the PV façade element are very similar; for the coarse mesh, the temperature is slightly higher inside the cavity and at the exterior. In the regions near the absorber plate, the collector´s cavity, and the glass cover, the results show higher temperatures for the coarse meshes, but their impact on the air temperature and velocity inside the ventilation cavity and the exterior is marginal.

The simulation results of the temperature and air velocity profiles for sections B2 and C2 along the building´s height, using different mesh sizes, are illustrated in Figure 3-37. The sections´ positions are indicated in Figure 3-33 and Figure 3-34.
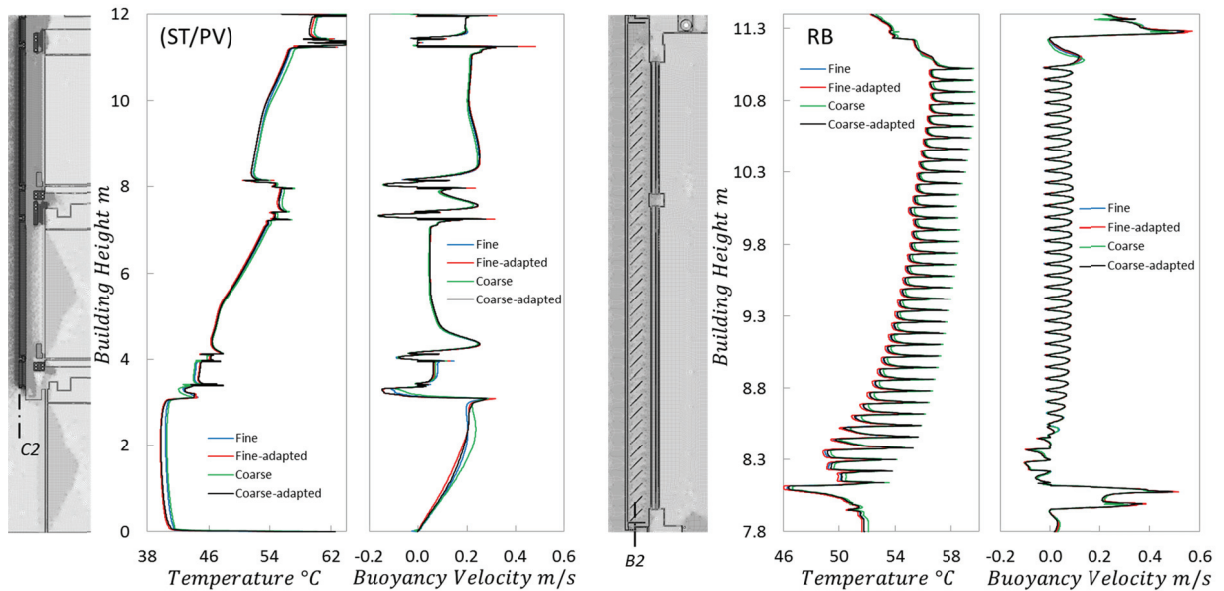
Figure 3-37: Comparison of the Temperature and Air Velocity Profiles for Sections along the Building´s Height of the MPPF Façade

Again, the resulting profiles look similar. The profiles of the façade element with the integrated roller blind match particularly well. The resulting profiles of the meshes before the y^+ adaptation deviate slightly from the profiles after adaptation. Because the results of the coarse and the fine y^+ adapted mesh did indeed match very well and also provided plausible results, the coarse meshes were chosen for further CFD simulations.

3.3.7   Comparison with Monitored Data

Before a more detailed look at the thermal behaviour inside the different functional façade elements under cold and hot climate conditions, a comparison was made between the simulation results and the hottest day of the year. In 2013, the highest exterior temperatures were detected on July 29th at 13:54 with 38.9 °C, while the solar radiation amounted to 751 W/m² at a solar angle of 58°. Because a comparison with the monitored data was not possible before determining the thermal behaviour in summer and winter (Chapters 3.3.8 and 3.3.9), the boundary conditions were deviated slightly. Therefore, the surface heat sources presented in Table 3-8 had to be pre-calculated again. The solar gains were generally lower, and, due to the solar angle of 58°, were not the same for horizontal and vertical surfaces.

Table 3-8: Pre-calculated Surface Heat Sources for the Comparison of CFD Simulation Results and the Monitored Data from 13:54 on July 29th, 2013

Surface Heat Source in W/m^2	Short Wave Fraction ($q_{S,short}$)	Long Wave Fraction ($q_{S,long}$)	Total Surface Heat Source (q_S)
Exterior Glass Pane (Vertical Surface)	16	165	180
Exterior Sun Glass (Vertical Surface)	109	165	274
ST Absorber Behind Glass Pane (Vertical Surface)	163	-	163
Exterior PV Cell/Module (Vertical Surface)	174	163	336
PV Cell/Module Behind Glass Pane (Vertical Surface)	153	-	153
Polished Aluminium Behind Glass Pane (Vertical Surface)	43	-	43
LED Displays (Vertical Surface)	49	158	206
Exterior Steel/Aluminium Plates, Black (Vertical Surface)	176	161	337
Exterior Steel/Aluminium Plates, Black (Horizontal Surface)	281	258	539
Exterior Steel/Aluminium Plates, Grey (Vertical Surface)	117	161	278
Exterior Steel/Aluminium Plates, Grey (Horizontal Surface)	187	258	445
Steel/Aluminium Behind Glass Pane, Black (Vertical Surface)	155	-	155

Steel/Aluminium Behind Glass Pane, Black (Horizontal Surface)	247	-	247
Steel/Aluminium Behind Glass Pane, Grey (Vertical Surface)	120	-	120
Steel/Aluminium Behind Glass Pane, Grey (Horizontal Surface)	192	-	192
Asphalt Ground (Horizontal Surface)	281	252	533
Semi-Transparent PV (Vertical Surface)	99	165	264
Exterior Pane of Triple Glazing (Vertical Surface)	14	-	14
Middle Pane of Triple Glazing (Vertical Surface)	12	-	12
Interior Pane of Triple Glazing (Vertical Surface)	11	-	11
Floor of the First and Second Floor (Horizontal Surface)	58	-	58
Floor of the Ground Floor (Horizontal Surface)	86	-	86
Roof of the Office Building (Horizontal Surface)	187	258	445

The computed and measured temperatures and air velocities at the measurement position (according to Figure 3-28) along with the differences are summarized in Table 3-9.

Table 3-9: Comparison of the Simulated and Monitored Temperatures and Air Velocities from 13:54 on July 29th, 2013

Measurement Position	PV-0.81	PV-0.91	PV-1.60	PV-1.61	PV-1.62	PV1.64	PV-1.65
	°C	m/s	°C	°C	°C	°C	°C
Monitored Data	49.1	0.22	52.0	59.6	46.9	53.2	44.3
Simulated Data	48.2	0.04	49.1	52.2	40.1	51.1	44.5
ΔT	0.9	0.18	2.9	7.4	6.8	2.1	-0.2
Measurement Position	PV-1.66	PV-1.67	PV-1.69	PV-3.06	PV-3.16	ST-0.88	ST-1.70
	°C	°C	°C	°C	m/s	°C	°C
Monitored Data	51.8	47.0	58.8	55.8	0.21	72.0	52.6
Simulated Data	48.9	40.1	51.4	44.5	0.11	84.8	52.5
ΔT	2.9	6.9	7.4	11.3	0.10	-12.8	0.1
Measurement Position	ST-1.71	ST-1.72	ST-1.73	ST-1.74	ST-1.75	ST-1.78	ST-1.79
	°C	°C	°C	°C	°C	°C	°C
Monitored Data	58.6	44.9	46.9	47.8	52.1	50.4	54.5
Simulated Data	53.8	40.5	54.5	47.9	54.1	52.5	56.2
ΔT	4.8	4.4	-7.6	-0.1	-2.0	-2.1	-1.7

The measured interior and exterior surface temperatures of the PV module were lower compared to the simulation results (PV-1.67, PV-1.69). The measured exterior air temperature close to the PV module was also a bit higher (PV-1.62). Both the measured and simulated air temperatures at the top inside the ventilation cavity (PV-0.81), and that above the outlet (PV-1.60) showed good agreement, while the air temperature was significantly lower at the bottom inside the ventilation cavity (PV-3.06). Furthermore, the measured surface temperature almost matched the simulation results inside the cavity (PV-1.64), below the ventilation inlet (PV-1.65), and above the ventilation outlet (PV-1.66).

The measured ST-absorber temperature inside the ST-façade element (ST-0.88) was significantly lower than the temperature resulting from the CFD simulation. The measured and simulated rear ST-collector surface temperatures (ST-1.79) did match very well, while the measured surface temperature at the middle layer (ST-1.73) was lower than that of the simulation result. Similar to the PV-façade element, the measured and computed surface temperatures also matched very well below the inlet (ST-1.74) and above the outlet (ST-1.75) for the ST-façade. Very good correlation was achieved between the measured and simulated air temperatures just above the ventilation outlet (ST-1.70) of the ST-façade element.

While the simulated and monitored temperatures matched well for the most part, larger deviations were detected between the measured and simulated air velocities inside the ventilation cavity for the PV façade element. The simulated air velocities at the corresponding monitoring positions (PV-0.91, PV-3.16) were much lower than the measured values at this moment. This is probably because the periphery opening is not taken into account in the two-dimensional simulation models. The air velocities that occur are close to the lower measurement limit of the sensors used, which could lead to measurement errors. It is generally very difficult to measure buoyancy driven air flows with good accuracy under laboratory conditions. In order to determine the influence of additional side openings,

further simulations using a three-dimensional CFD model are required. However, it is possible to assume that a two-dimensional CFD model is adequate for first estimations of the thermal behaviour in extremely hot and cold climates.

3.3.8 Thermal Behaviour and Air Flow in Winter

In a first step, the façade was simulated under the conditions of a cold winter night. A temperature of -20 °C was specified for the right external border, and, in this case, no solar irradiation impinged on the façade. An interior temperature of 20 °C was set as a boundary condition at the left border of the computational domain.

The simulation results showed an average ambient air temperature of 16.1 °C for the ground floor. The temperature on the first floor, at 18.9 °C, was the highest room air temperature averaged over the individual volumes of the three simulated floors. At 17.2 °C, the mean value of the temperature in the second floor was somewhat under that of the first floor. This was due to higher heat losses via the ceiling structure.

In order to be able to quantitatively represent the temperatures and flow rates in and around the façade construction, three vertical (C1, C2, C3) and two horizontal (C4, C5) sections were imposed on the temperature and flow fields. Figure 3-38 shows the positions of these sections.
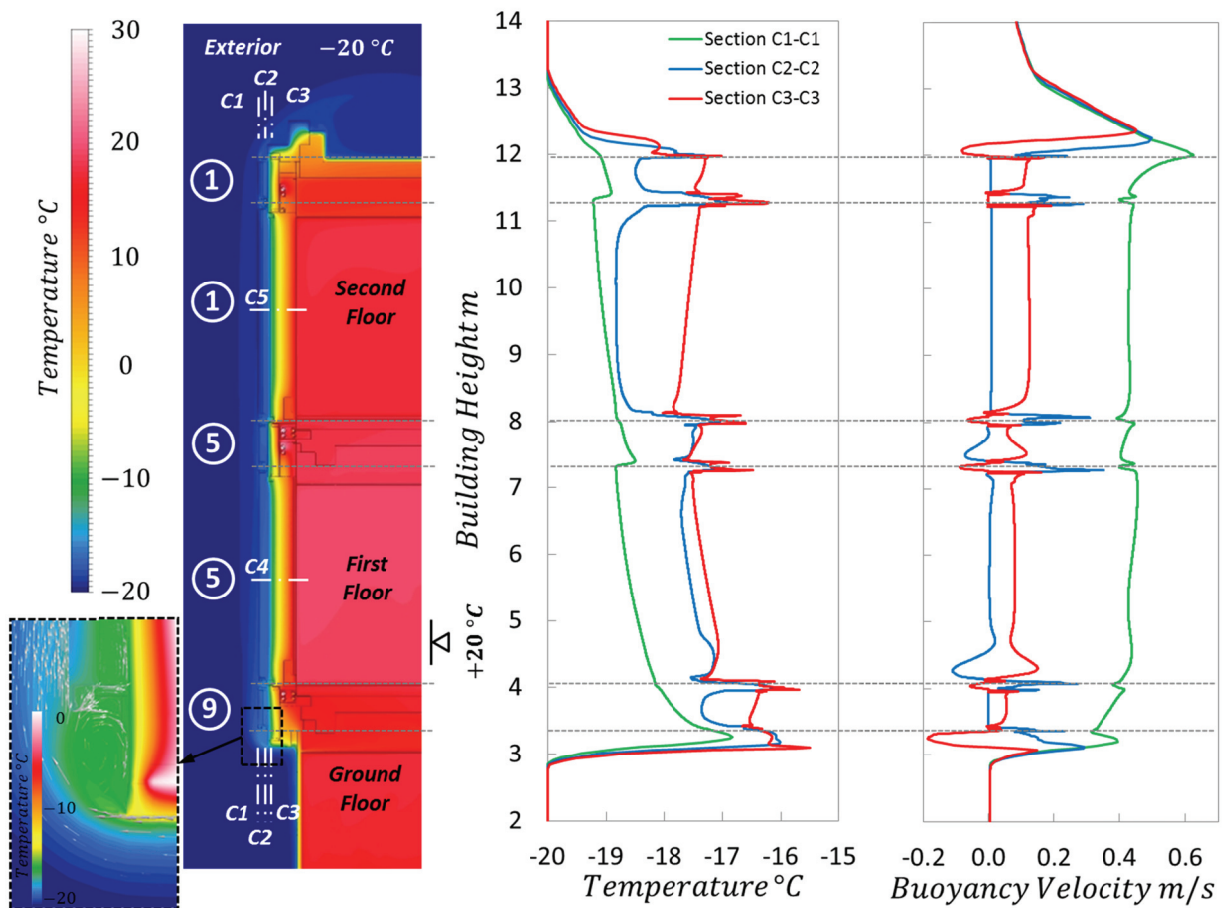
Figure 3-38: Temperature Contours in the Façade Section C-C under Winter Conditions and the Corresponding Vertical Temperature and Buoyancy Velocity Profiles in Sections C1-C1 to C3-C3

An analysis of the temperature gradient of cross-section C3 in Figure 3-38 (3 to 4 m height) shows that the highest temperatures occurred at the transition in the façade from ground floor to first floor. The air in front of the façade became constantly cooler with increasing height. The same applied for the air inside the ventilation cavities, with the exception of façade components with integrated solar thermal collectors. Due to the insulation behind the absorber, the cavity was better protected from the cold at this position. In these areas, a rise in temperature was even measured. The temperature peaks in the diagram represent areas influenced by the ventilation outlets. In the area around the parapet carrier,

thermal bridges of the integrated steel sheets were detected. With an ambient air temperature of -20 °C and a room air temperature of approximately 18 °C, the average temperature in the area of the ventilation cavity was in the range of -17 to -18 °C, as a result of heat losses in the test area.

Figure 3-38 shows the temperatures and flow rates for the three vertical sections in winter, each over the entire façade height. Section C1-C1, shows the temperature and speed of air 20 mm in front of the exterior façade surface. Section C2-C2 runs through the middle of the inlet and outlet of the ventilation cavity; its distance to the façade's outside edge amounts to approximately 40 mm. The third section, C3-C3, shows the behaviour of the air in the ventilation cavities at a distance of approximately 40 mm from the inner wall.

The buoyancy velocity diagram in Figure 3-38 shows the inlet and outlet areas with the highest flow rates in the façade. The air in the ventilation cavity generally flowed more slowly upward than the air in front of the façade. An analysis of each section shows that buoyancy over the building height was approximately constant.

Figure 3-39 (detail A, right) shows the flow and temperature behaviour in the façade, in the region of the middle parapet carrier, under winter conditions. An upwards flow occurred in the ventilation cavities due to heat from the interior, which is illustrated by the upwards-pointing white arrows (a).
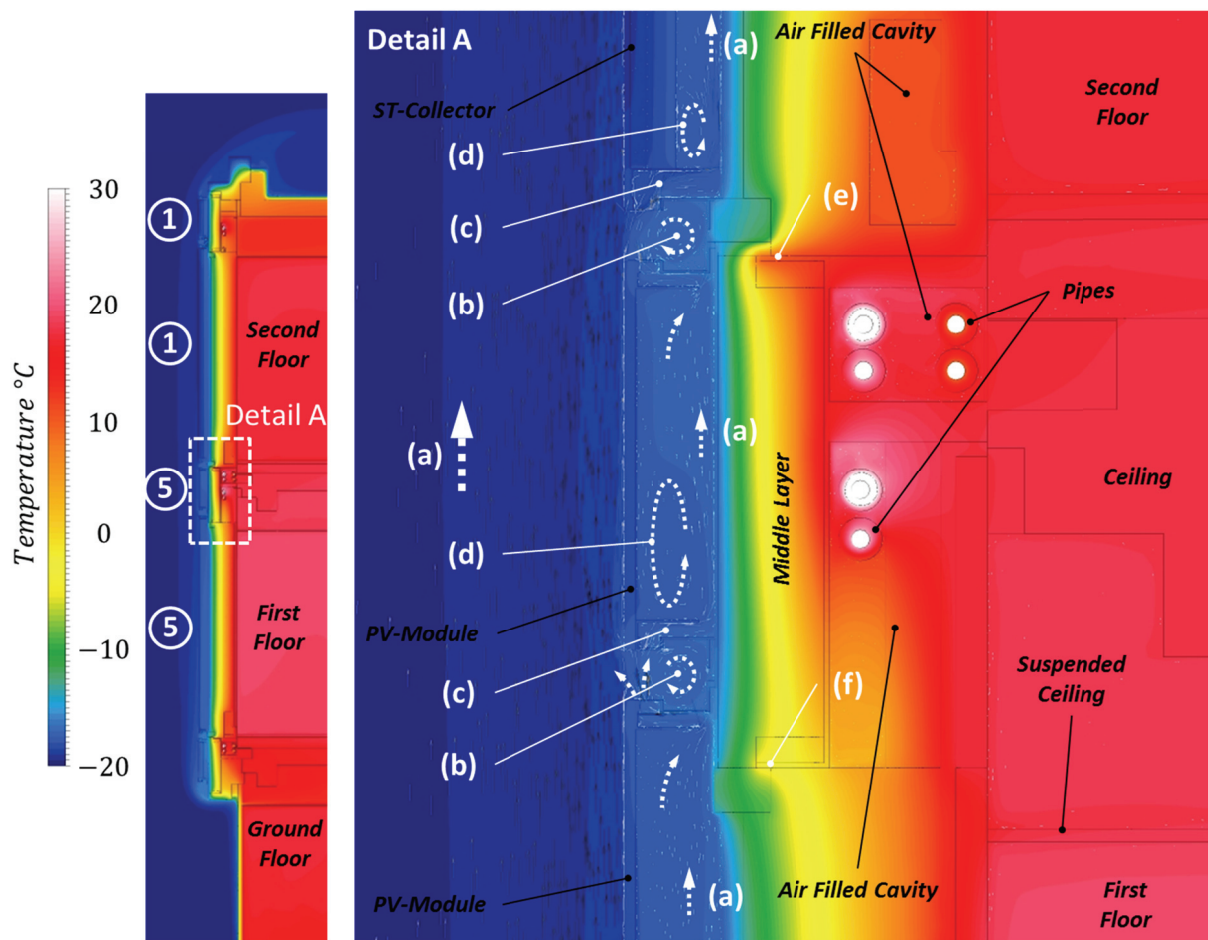
Figure 3-39: Temperature Contours and Air Flow vectors in Detail A under Winter Conditions

The construction channel elements in the sub-structure of the multifunctional façade were outwardly open, causing internal air vortices (b). At the inlets (c), air coming from the open channels was accelerated in the ventilation cavities and then slowed down by the channel extension. After the air left the narrowing inlets, turbulences (d) formed because of the edges of the ventilation inlet and/or outlet geometry. The broader the ventilation cavity became, the larger the diameter of the turbulence. This explains the different diameters of the turbulences in the ventilation cavities behind the solar thermal collector and the photovoltaic module. A thermal bridge caused by a steel sheet of the girder construction was distinctly recognizable based on the temperature profile in the upper (e) and lower (f) areas of the parapet carrier.

Figure 3-40 shows a comparison of the temperature and air velocity of section C4-C4 (photovoltaic module) and section C5-C5 (solar thermal collector) under winter conditions. The positions of the sections are represented in Figure 3-40. The main difference between the integration of the photovoltaic module (upper diagram) and the integration of the solar thermal collectors (lower diagram) is the remaining width of the air cavity. The much broader solar thermal collector considerably narrows the air cavity in comparison to the photovoltaic module, whereby the temperature and current profiles were also clearly different from each other.

The temperature in the ventilation cavity of the solar thermal collector was higher than in the ventilation cavity of the photovoltaic module. This was for two reasons: on the one hand, some of the air that was preheated in the ventilation cavity of the parapet carrier flows directly into the ventilation cavity of the solar thermal collector, whereby the inlet temperature in the ventilation cavity of the photovoltaic modules corresponded to the colder outside air; on the other hand, the solar thermal collector contained a collector insulation, which, in the current installation, acted as insulation against the cold outside air.

There was no air flow within the solids (middle layer). This is represented in the two diagrams by the horizontal sections of the flow rate. The surface roughness of the laterally-limited solids resulted in a loss of kinetic energy for air flowing upwards along the surfaces of the solids, and, as a consequence, a reduction in the flow rate caused by friction. Due to the heat passing from the interior through the middle layer, the maximum flow rate was not in the centre of the ventilation cavity, but rather shifted towards the middle layer in both cases. This shift for photovoltaic modules was approximately 0.08 m/s, and for solar thermal collectors was 0.15 m/s.
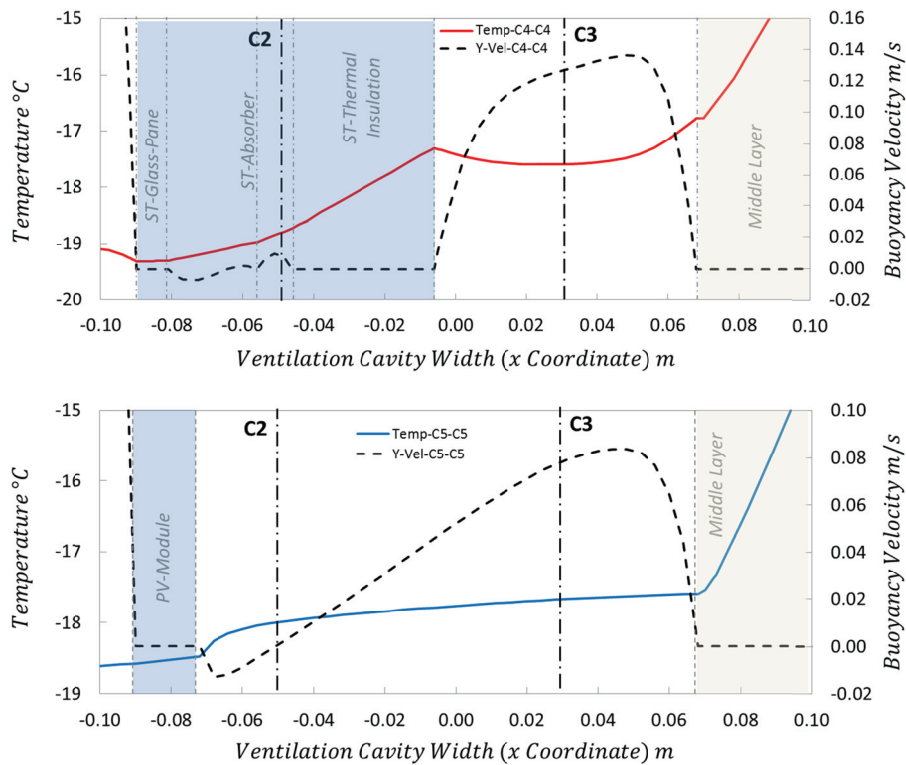
Figure 3-40: Temperature and Buoyancy Velocity Profiles in the Ventilation Cavity under Winter Conditions for the Solar Thermal Collector (Top) and the Photovoltaic Module (Bottom)

3.3.9   Thermal Behaviour and Air Flow in Summer

The second climate case in this study was a hot summer day with an ambient air temperature of 40 °C, which was set at the external border right in the simulation domain. Additionally, a solar irradiation of 1000 W/m² (at an inclination angle of 45°) heated the façade. In the simulation model, a temperature of 25 °C was set as the boundary condition at the left domain border. This is equivalent to an air-conditioned office space. The effect of solar heating was imposed on the simulation as a boundary

condition, in the form of heat sources at the respective surfaces, whereby the degree of heat was computationally pre-determined [66], [67].

Figure 3-41 shows a section of the simulation domain with the correlated temperature fields for the selected summer conditions. The simulation domain was identical to that employed for winter conditions, but with boundary conditions that corresponded to a hot summer day.

Based on the boundary conditions set for the right border of the simulation domain with an ambient air temperature of 40 °C and those for the left border of the simulation domain with a room air temperature of 25 °C, a temperature gradient resulted between the two boundary conditions. Similar to the case under winter conditions, this gradient resulted in different temperatures in the interior areas of the building. The lowest average room air temperature of 25.9 °C occurred on the first floor, followed by the second floor, with an average room temperature of 26.5 °C. For the sake of simplification, only one window pane without shading elements as separation between the interior and external environment was modelled in the ground floor simulation. The solar irradiation in this area resulted in a maximum air temperature inside the room of 31.9 °C.

The three sections through the simulation model, C1-C1, C2-C2 and C3-C3, shown in Figure 3-41, were used to present temperature and air velocity profiles under summer conditions in the diagrams. These were located in the same positions as for the evaluation of the winter scenario.
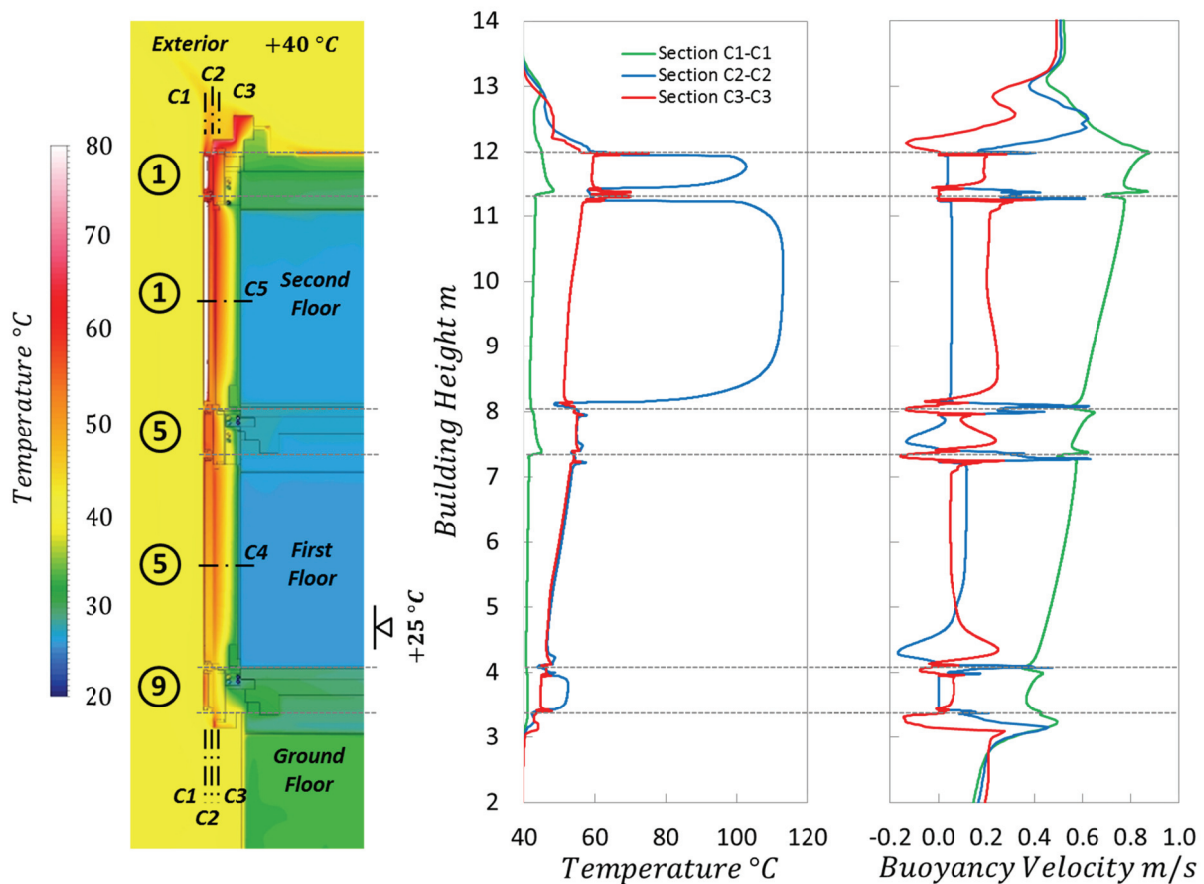
Figure 3-41: Temperature Contours in the Façade Section C-C under Summer Conditions and Corresponding Vertical Temperature and Buoyancy Velocity Profiles in Sections C1-C1 to C3-C3

Due to solar irradiation and the associated buoyancy, the temperature was constantly higher over the building height, both within and in front of the façade. Particularly high temperatures were detected in the area around the solar thermal collectors. In the ventilation cavity, the effect of these high temperatures was hardly noticeable, due to the integrated insulation directly behind the collectors. In the areas around the outlets of the individual ventilation cavities, it was possible to see that air warmed up within the façade was partially aspirated into the corresponding overlying ventilation cavities and partially flowed outwards, thereby delivering a part of the heat to the exterior environment. Figure 3-42

shows the flow and temperature behaviour in the façade in the region of the middle parapet carrier under summer conditions, analogous to the previous approach for winter conditions (Figure 3-39).

The general tendency for there to be an upwards draught (a) in the ventilation cavities and in the immediate vicinity of the façade was significantly more intense in summer than in winter, due to the higher temperatures. Air vortices also emerged under summer conditions in the open structural channel elements between the façade elements (b). The velocity of the air entering via the inlets (c) hardly slowed down in the ventilation cavity, since the external heat ingression provided a clear increase in buoyancy. The turbulence in the ventilation cavity (d) was similar in form to the winter scenario. In the area around the middle layer, two thermal bridges (e and f) were also discernible, which were brought about by a steel sheet integrated into the façade.

Figure 3-43 shows the characteristics of temperature and current of air in the ventilation cavity. Sections C4 and C5 (Figure 3-41) in the façade are located in the same positions as in the case of winter; however, the flow behaved differently for summer than it did for the winter scenario. The maximum flow rates (up to 0.3 m/s) were no longer offset from the centre of the ventilation cavity, but were rather in proximity to the two walls of the ventilation cavity on both sides.
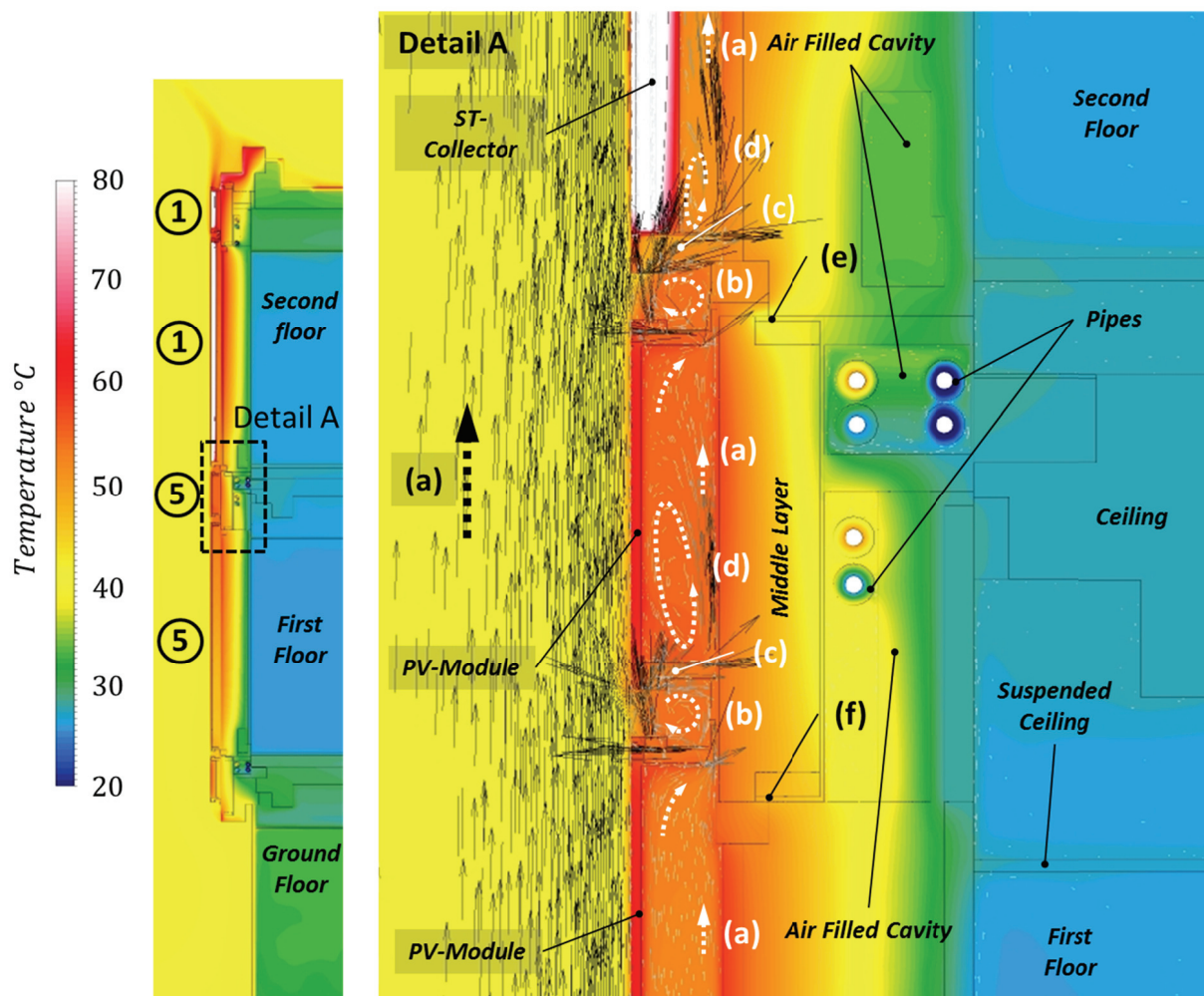
Figure 3-42: Temperature Contours and Air Flow Vectors in Detail A under Summer Conditions

The buoyancy in the ventilation cavity of the solar thermal collector resulted from the heat emission of the solar thermal collector to the ventilation cavity lying behind it. The heat of the absorber was transferred by convective heat transfer, and the exchange of longwave radiation to the thermal insulation and further to the ventilation cavity. The rear wall of the solar thermal collector thus transferred heat via longwave radiation to the upward airflow in close proximity to the wall. The maximum air velocity occurred at small distance from the wall, due to the influence of friction.

In the photovoltaic module area, buoyancy in the ventilation cavity likewise resulted from the transfer of longwave radiation to the internal surfaces of the air duct. The maximum flow rate range amounted to approximately 0.19 m/s.
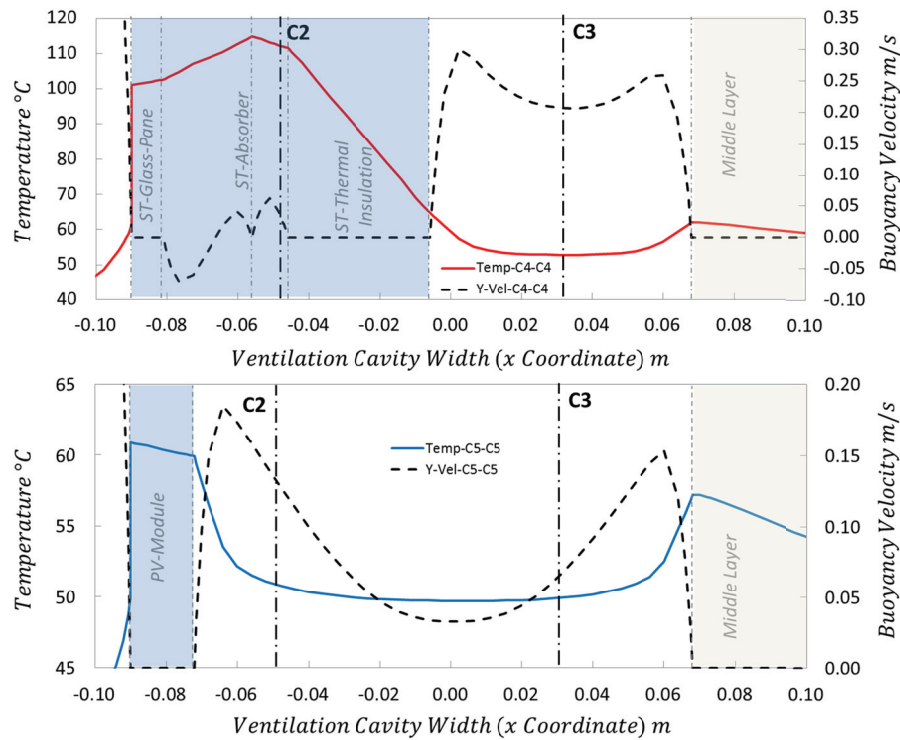
Figure 3-43: Temperature and Buoyancy Velocity Profiles in the Ventilation Cavity under Summer Conditions for the Solar Thermal Collector (top) and the Photovoltaic Module (bottom)

The highest temperatures occurred on the walls of the ventilation cavity. Due to the integrated thermal insulation behind the solar thermal collector and ventilation, the surface of the back plate of the solar thermal collector heated up to a maximum of 66.6 °C, the temperature at the rear of the photovoltaic modules reached a maximum of 62.9 °C and 60.4 °C for the PV module in section C-C.

3.3.10 Thermal Behaviour and Air Flow Characteristic of a Window with Roller Blind

This chapter presents the simulation results of the window element with roller blinds (position 3 in Figure 3-27), which is located on the second floor in façade section B-B. Again, summer and winter scenarios were considered, and the resulting temperature contours are illustrated in Figure 3-44. The window element with roller blinds consists of a triple-glazed window on the inside and a single glass pane on the outside. There is a ventilation cavity behind where the roller blind was installed in order to protect the interior room from solar irradiation.

In the winter scenario, no solar heating occurred; however, the second-floor interior was heated by a floor convector. More heat was lost via the triple glazing than via the opaque façade in section C-C (indicated in Figure 3-32), and an average room air temperature of 17.5 °C was reached on the second floor. The room air temperature was cooled at the internal window surface and coursed downwards (a). Air, heated by the floor convector, rose, and was diverted by air flowing down from the window (b). Air coming through the lower opening of the window below was able to infiltrate the ventilation cavity of the window in addition to some air from the outside (c). The air inside the cavity was slightly heated from the interior through the triple-glazed window and rose between the pane and the roller blinds (d). Air was cooled in the air cavity adjacent to the external single glass pane, and streamed downwards (e). At the upper outlet, some of the air entered the façade component above, while the rest was lost to the exterior (f).

In the summer scenario, solar heating was observed at the fins of the roller blinds (g). Thus, the air inside the ventilation cavity was also heated. Through the triple-glazed window, heat was partially transferred to the interior. The interior air close to the window was heated and flowed upward towards

the ceiling (h). On the interior side, the air temperature was between 30 and 35.5 °C, resulting in an average room temperature of 31.4 °C. Compared to the results from the simulation of section C-C (Figure 3-27), the average air temperature on the second floor was 4.6 K higher. Inside the ventilation cavity, the buoyancy of the air resulted from the solar heating at the fins and/or from the exchange of longwave radiation between the fins on both sides of the window panes (i). The maximum temperature was obtained at the highest of the five fins, with a value of 59.4 °C. Air from the exterior entered the ventilation cavity through the bottom inlet of the window element (j). Again, the air stream leaving the ventilation cavities was split and partly entered the window element above it (k).
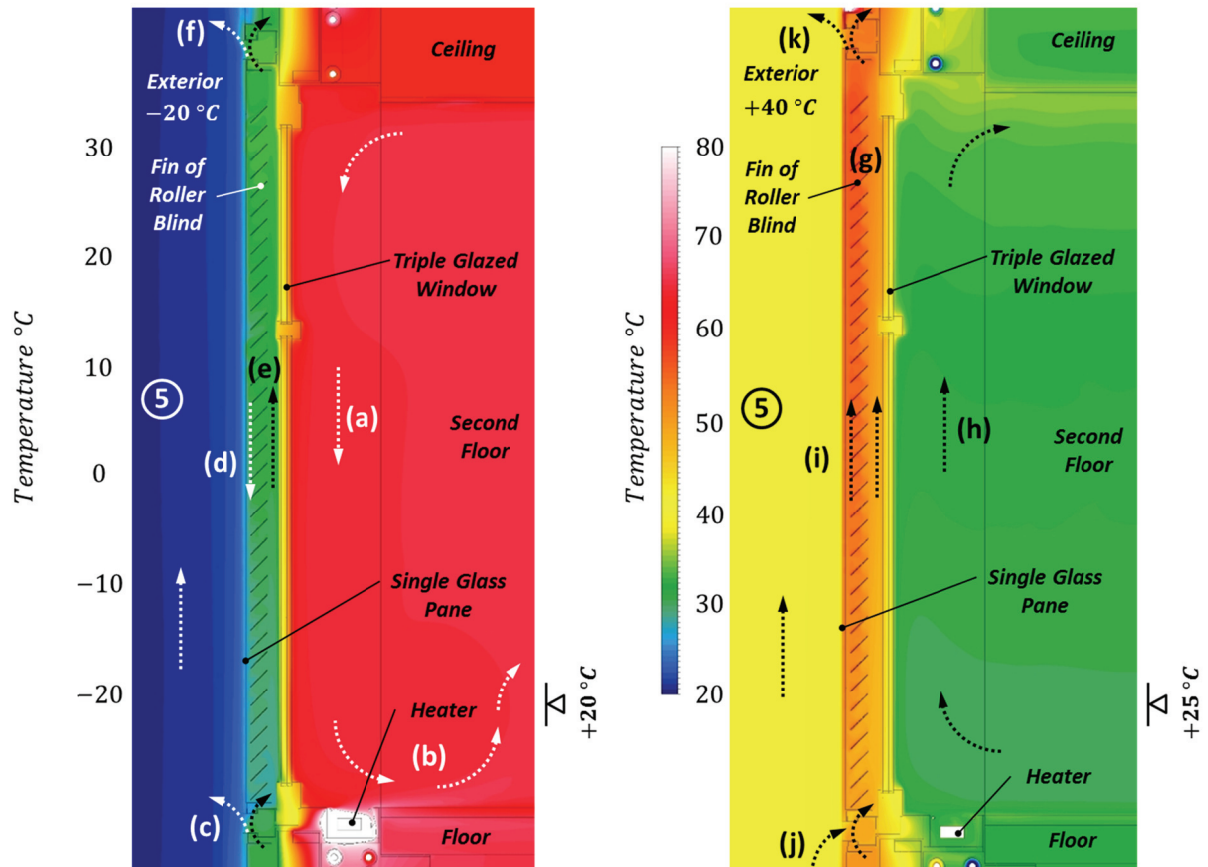
Figure 3-44: Temperature Contours for the Window Element with Roller Blind (Position 3 in Figure 3-27) under Winter Conditions (left) and Summer Conditions (right)

Inside the window's air cavity, the highest flow rates occurred toward the bottom ventilation opening. In the winter scenario, the maximum flow rate was 0.95 m/s, whereas in summer it was slightly lower with 0.91 m/s. Due to the flow resistance of the fins, the maximum flow rate oscillated with increasing altitude, between approximately 0.35 m/s in winter and 0.24 m/s in summer.

Figure 3-45 shows the temperature contours and air flow vectors for the top of the ventilation cavity, and provides deeper insight into the flow behaviour between the fins of the roller blind. Air flow vectors and temperature contours are illustrated for both summer and winter conditions as well. In the winter scenario, one vortex (a) developed between the fins, whereas in summer, two vortexes were observed (b) in the same positon. A further vortex (c) occurred in the winter scenario, just before the ventilation outlet. Because the air streamed upwards on both sides of the fins, this vortex decreased in summer (d). Figure 3-46 and Figure 3-47 show the temperature and buoyancy velocity profiles at three sections through the window with the integrated roller blind for cold winter conditions and without inclining solar radiation. The green line (section B1-B1) shows the temperature and buoyancy velocity on the exterior, 20 mm away from the exterior glass; the blue profile (B2-B2) shows the behaviour inside the ventilation cavity, 40 mm away from the outer edge of the façade element, while the red line shows the characteristic of buoyancy and temperature inside the cavity, 40 mm away from the interior wall.
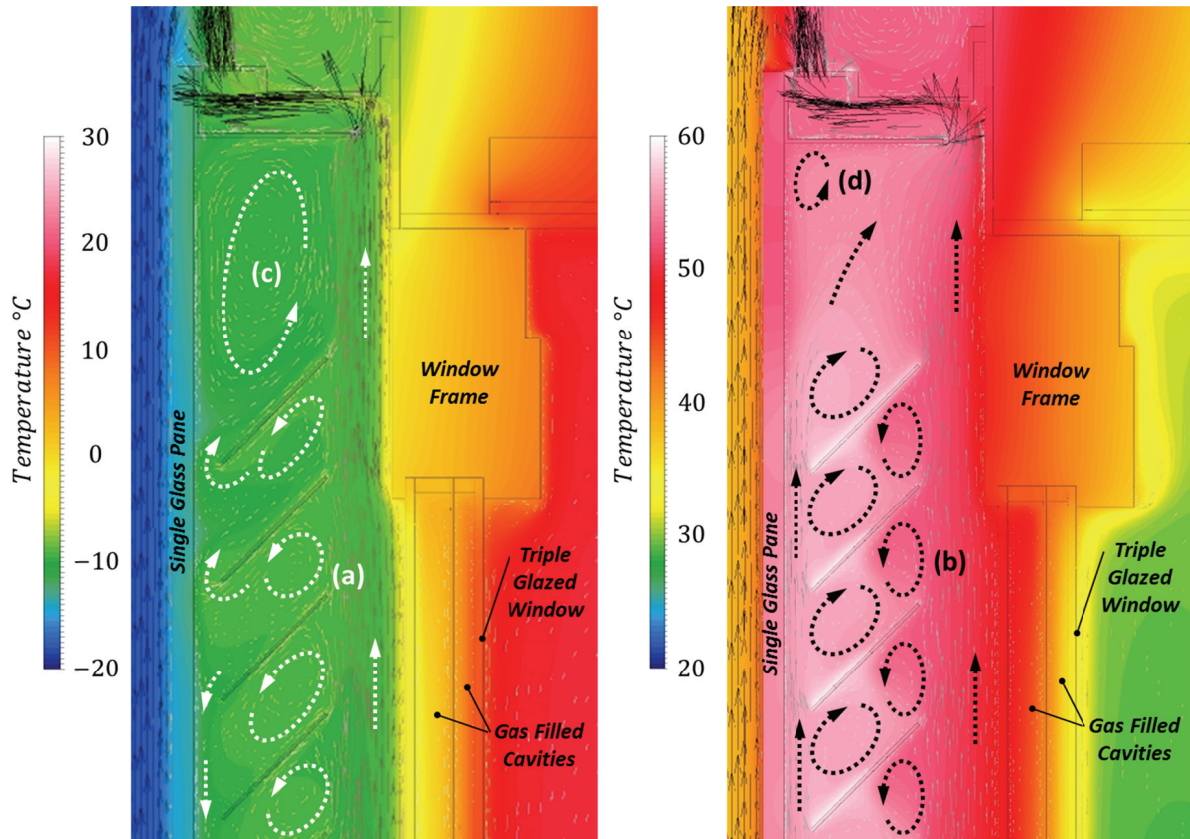
Figure 3-45: Temperature Contours and Air Flow Vector Patterns at the Top of the Ventilation Cavity with Installed Roller Blind under Winter (left) and Summer Conditions (right)
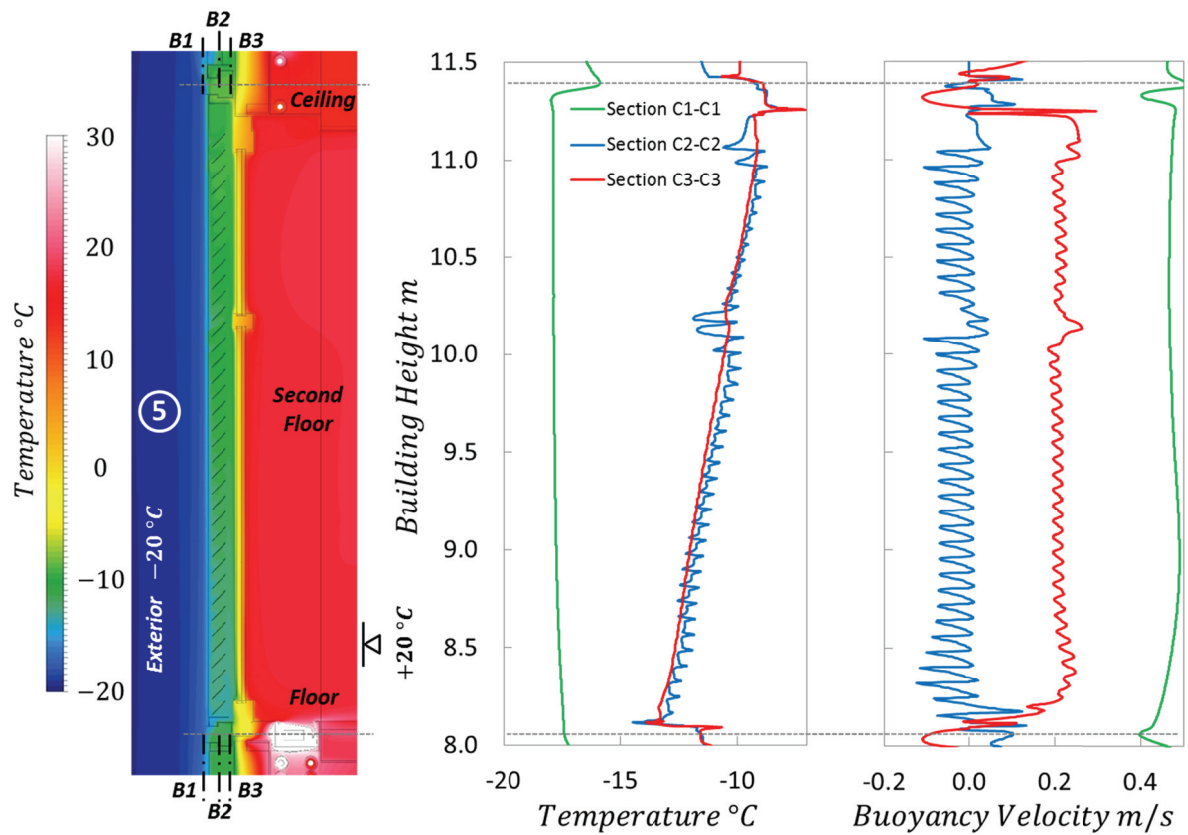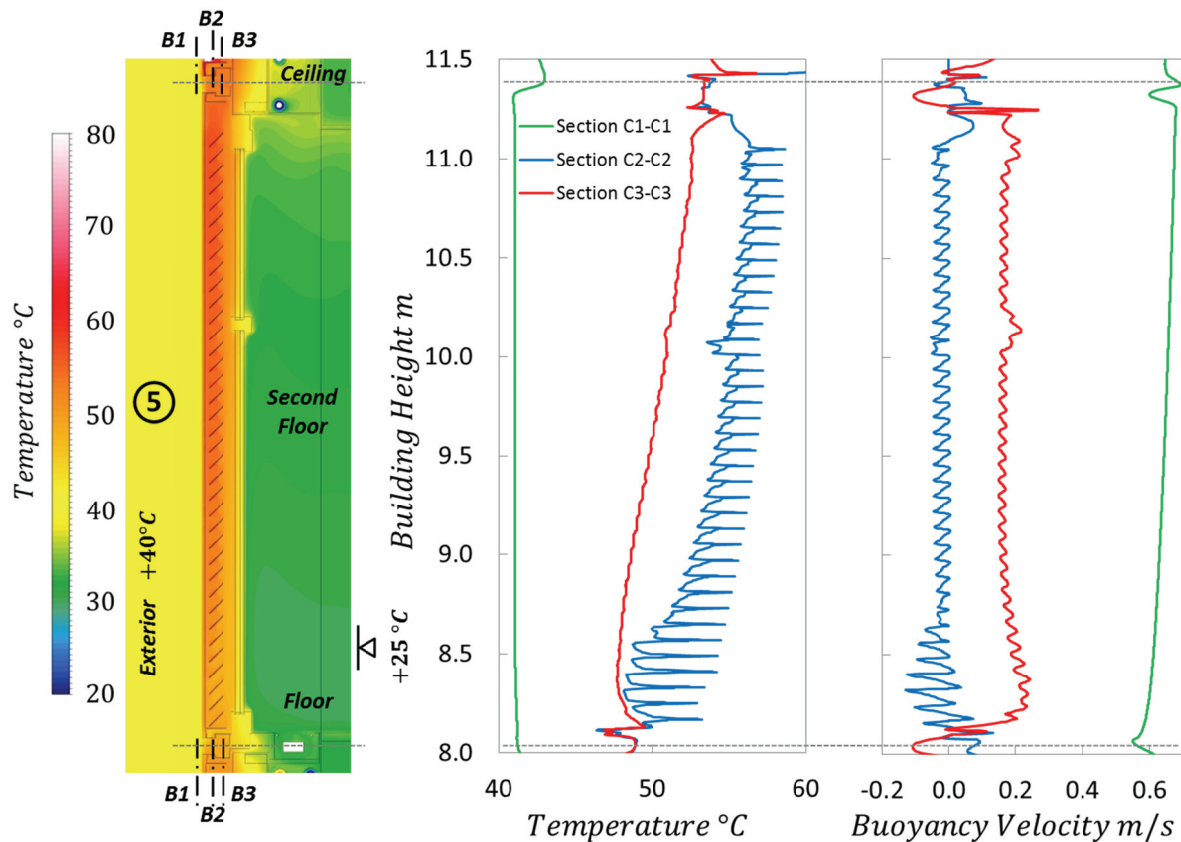

Figure 3-46: Illustration of the Temperature and Buoyancy Velocity Profiles for Three Sections through the MPPF Window with Integrated Roller Blind along the Building's Height for Cold Winter Conditions

For cold winter conditions (Figure 3-46) and without the influence of solar irradiation, the temperature decreases from -17.4 to -17.9 °C 20 mm away from (B1-B1) the exterior glass. As a result of air escaping from the window's ventilation cavity, the air temperature increases to -15.9 °C in the region around the ventilation outlet. Inside the cavity, the temperature increases from -14.5 to -8.8 °C for the profile B2-B2 and from -13.9 to -8.9 °C for profile B3-B3. The profile B2-B2 intersects the lamellas of the roller blind. In this profile, temperature fluctuations can be observed in the corresponding diagram of Figure 3-46. These fluctuations are a result of the section through the vortices caused by the fins of the roller blind. The maximum fluctuation - of approximately 1.8 K - occurs in the region around the window frame, located at the building´s height of 10.1 m. Generally, the temperature fluctuations are higher in regions of cavity cross-section restrictions. In contrast to the temperature, the buoyancy velocity remains almost constant after entering the window's cavity. Fluctuations in buoyancy velocity occur in the profiles of the sections B2-B2 and B3-B3. Only very low fluctuations are obtained for section B3-B3, with a maximum range of 0.05 m/s. In section B2-B2, the fluctuations have maximum range of approximately 0.2 m/s, which occur at the bottom of the ventilation cavity immediately after the inlet. 20 mm away from the exterior glass (B1-B1), the buoyancy velocity is approximately 0.48 m/s on average. Section B2-B2 is located between the lamellas of the roller blind and the interior wall, and the average buoyancy velocity inside the ventilation cavity is approximately 0.2 m/s in this profile. The peaks of negative buoyancy velocity in the profile B2-B2 indicate the recirculation of air.

For hot summer conditions (Figure 3-47) and the influence of heated surfaces, there was a constant temperature from the simulation 20 mm away from the window's exterior glass. Inside the ventilation cavity and 40 mm away from the outer edge of the window (B2-B2), the air temperature increases from 46.4 °C (immediately after inlet) to a maximum of 58.6 °C, at the highest lamella of the roller blind. Furthermore, there were high temperature fluctuations due to the lamellas being heated by solar irradiation. The deviations have a maximum of 6.5 K in the bottom region of the ventilation cavity. In the temperature profile of section B3-B3, the air temperature increases from 46.9 to 54.7 °C.

Figure 3-47: Illustration of the Temperature and Buoyancy Velocity Profiles for Three Sections through the MPPF Window with Integrated Roller Blind along the Building's Height for Hot Summer Conditions

For the profile of section B1-B1, the buoyancy velocity increases from 0.55 to 0.68 m/s. In the remaining two profiles, B2-B2 and B3-B3, the buoyancy velocity is nearly constant along the window´s cavity

height, with fluctuations similar to those of cold climate conditions. The profile of section B2-B2 shows the maximum fluctuations immediately after the ventilation inlet, with an amount of 0.2 m/s. The maximum fluctuations of approximately 0.06 m/s occurred in the velocity profile B3-B3, with 0.17 m/s on average. The peaks of negative buoyancy velocity in the profile B2-B2 again indicate the recirculation of air.

3.3.11 Ventilation Performance Calculation

The measured mass flows are listed in Table 3-10, along with the ventilation performance of the individual façade components. While the mass flows were simply taken from the simulation results, the ventilation performance was calculated knowing the difference in the average air temperature between the upper and lower ventilation outlets, the computed mass flow in the ventilation cavity, and the specific heat capacity of the fluid (Equation 3-11). This equation describes how much heat was absorbed (positive values) or delivered (negative values) from the air inside the ventilation cavity per second.

$$\dot{Q}_{Vent} = \dot{m} \cdot cp \cdot \Delta T$$

Equation 3-11

A few phenomena were obtained in the course of the evaluation of the air mass flow and ventilation performance. The air mass flow of the ventilation cavities of the opaque solar thermal collectors and photovoltaic modules were lower in the winter scenario than in the summer scenario. In contrast, the air mass flow in the façade components with integrated windows (sections B-B and D-D) was higher in the winter scenario than in the summer scenario. In the ventilation cavities of the two photovoltaic modules, the air hardly absorbed heat in winter, meaning that there was very little ventilation performance. In summer, the heated air coming from the bottom façade´s ventilation cavity (D/1) partly entered the air cavity of the façade element above (D/2) and led to an additional – though small – increase in the interior room temperature.

Table 3-10: Mass Flow and Ventilation Performance of the Ventilation Cavity of the Façade Components under Winter and Summer Conditions

Section/Floor	Façade Element	Massflow Rate g/s		Ventilation-Efficiency J/s	
		Summer	Winter	Summer	Winter
A/1	Polycrystalline Glass-Glass Module 01	12.8	7.9	165.2	0.9
A/2	Opaque Element with Fan Coil Unit	30.8	32.7	93.5	831.0
B/1	Photovoltaic Daylight Module	12.1	13.1	75.5	91.4
B/2	Roller Blind	9.6	15.5	91.4	76.2
C/1	Polycrystalline Glass-Glass Module 02	12.2	8.5	126.3	1.1
C/2	Solar Thermal Collector	17.6	10.5	160.3	7.9
D/1	Semi-Transparent Thin-Film Modules	12.3	12.9	111.2	88.8
D/2	Photovoltaic Daylight Module	11.1	15.0	-11.1	56.6

4 Stationary, Three-dimensional Numerical Models[5]

4.1 Applications and CFD Approaches

This chapter on three-dimensional steady state CFD simulations of façade elements consists of two recently published studies. The first of these studies, published in the well-known Journal *Energy and Buildings* [62], deals with the prototype of the multifunctional façade [2] from Chapter 3.3. In contrast to the previous chapter, which investigated a larger section of the whole building in the CFD model, only single façade elements and their integrated functional components were observed with the help of the three-dimensional CFD models (in Chapter 4.2). This was due to the increasing number of cells of the CFD mesh and the limitations of computing power. The influence of the periphery openings of each single façade element on the thermal behaviour and the flow characteristic inside the ventilation cavities can only be considered using three-dimensionally resolved simulation geometries, and thus justifies the efforts put into the creation of these complex three-dimensional simulation models. In the CFD simulations described in Chapter 4.2, the influence of the solar irradiation was considered in the form of pre-calculated heat sources according to the surfaces' absorption, reflection, and transmission ability. A large number of measurement sensors, installed in a test façade, monitored temperatures and were further used to optimize the three-dimensional CFD models. By making a comprehensive comparison of the monitored data and the simulation results, it was possible to determine the thermal behaviour of hot climate conditions.

The second study (presented in Chapter 4.3), published in *Solar Energy* [68], contains a different numerical radiation model approach, where the DO model was used for both shortwave (solar) radiation and long wave (thermal) radiation. From the existing literature, it was evident that such a model had not yet been used in a simulation of the thermal behaviour of a façade element. Generally, the DO radiation model makes it possible to define a variety of wavebands with different absorption behaviour. Increasing the number of wavebands involved dramatically increases the CPU power and computing period necessary to complete the simulation. Furthermore, an appropriate method was found for the creation of a simple model of a special passive solar segment inside a ventilated façade to consider the absorption of solar radiation within this segment. Further models, such as a model for the perforated plate at the façade´s in- and outlets, or the thermal influence of attached PV cells were also developed. The development of all models was supported by results from a sophisticated laboratory experiment with a solar simulator. In Chapter 4.3, the main objective was the assessment of an existing SHC façade element [69]. This research was made possible by the research project alpS-project "B02 eNVELOP Teil C" which was supported within the framework of COMET (Competence Centers for Excellent Technologies) [3].

---

5. Segments of this section have already been published in [19] and [20].

4.2 Analysis of the Ventilation Effects and the Thermal Behaviour of Multifunctional Façade Elements using Three-dimensional Numerical CFD Models[6]

4.2.1 Objectives and Contents

The study presented in Chapter 4.2 provides a comprehensive analysis and comparison of the thermal behaviour inside a multifunctional façade element, as well as a detailed analysis of the airflow characteristics inside the cavity and in its immediate surroundings. For this analysis, three-dimensional CFD simulation models were used to compare a transparent single layer glass panel with peripheral ventilation used as an impact pane (TR), a double façade element with peripheral ventilation and an integrated PV module (PV), and, for the first time in recent literature, a double façade with peripheral ventilation and an integrated solar thermal collector (ST). This study also presents a novel design that allows the natural ventilation of each single façade element separately. Therefore, this chapter also provides a comparison of naturally ventilated and closed-cavity facades. With the help of data collected from in-situ measurements on an existing test façade, it was possible to set the boundaries of temperature and heat sources in the three-dimensional CFD simulations for a detailed determination of airflow characteristics and temperature profile, and to provide a comprehensive comparison of the thermal effects of the functional components to be analysed.

The structure of MPPF has already been described in Chapter 3.3.1 for the investigation of the two-dimensional thermal behaviour of the façade. See Figure 3-27 and Figure 3-32 for a picture and a schematic of the multifunctional façade in Stallhofen, Austria. The façade element (TR), on the right side of the second floor (position 4 in Figure 3-27), bears a conventional Raffstore shading device which was considered to be "not activated" (pulled upwards) in the CFD analysis. Two façade elements on the first floor contain different types of polycrystalline photovoltaic modules for the production of electrical power (position 5 in Figure 3-27), one of which was observed in the CFD analysis (PV). One façade element on the second floor (ST) was equipped with a solar thermal collector (position 1 in Figure 3-27).

4.2.2 CFD Model Design

For a more detailed view of the flow characteristics and thermal behaviour of the façade elements, three-dimensional CFD simulation models were created, which allowed the physical behaviour of the façade elements, the inner cavity and the close external environment to be reproduced. A three-dimensional simulation was required for the determination of the ventilation effects of the MPPF-prototype in particular. It was only possible to consider thermal influence of the ventilation openings on the side of the façade element using a three-dimensional geometry. The simulation domain's dimensions (Figure 4-1) were 1.13/4.40/1.25 m ($x/y/z$). The zones and boundaries of the domain are described below.

In the CFD model for the TR and PV façade element, an interior fluid zone and three solid zones formed the façade element, i.e. the interior and exterior aluminium panel and the exterior glass or PV-module, the ventilation cavity, and the periphery openings. Further fluid zones situated in front, next to, above and below the façade element represented exterior air. A pressure inlet was defined at the bottom boundary, and a pressure outlet at the top of the domain in order to enable the ventilation of the façade element. Geometrical symmetries were set at the model's left and right boundaries, 40 mm away from the façade element's side edges, as a consideration of the façade elements' neighbours, which implied the thermal influence of neighbouring façade elements with peripheral openings. The interior boundary of the CFD model was the exterior plate of the middle layer adjacent to the ventilation cavity. Among other components and materials, the middle layer contained the thermal insulation. This thermal insulation package was defined as a virtual layer between the ventilation cavity and the interior room in order to take the thermal resistance into account.

In the CFD model of the ST façade element, the PV module was replaced by a solar thermal collector. The solar thermal collector model is divided into four different zones, as seen in the schematic in Figure 3-28. The first zone is the ST-absorber plate, made of copper. The next two zones are the glass cover and the thermal insulation at the rear of the ST-collector. The fourth is an additional fluid zone: the air-filled cavity inside the collector.

---

6. Segments of Chapter 4.2 have already been published in [19].
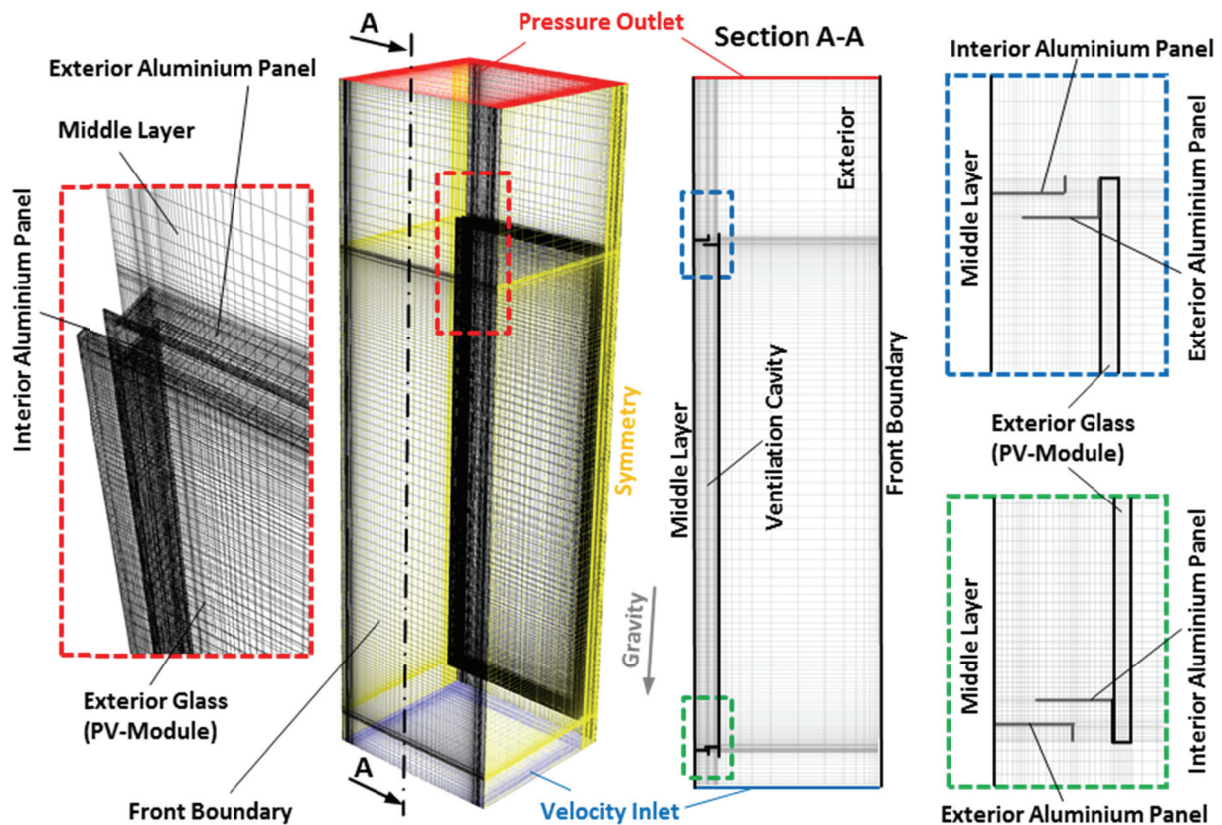
Figure 4-1: CFD Model and Corresponding Boundaries

The three-dimensional CFD simulation models were built with the design modeller and meshing tool of the ANSYS Workbench [6]. The meshing strategy was to create meshes that consisted of only hexahedral cells. Creating these meshes required a great deal of effort, but the advantage was that the mesh size was dramatically reduced. Another advantage of using a pure hexahedral mesh was that the simulation´s iterations ran more smoothly, and convergence was reached much more quickly. Furthermore, in the meshes, the cell size was reduced towards the edges and walls of the façade element. At the periphery openings in particular, a finer mesh structure was created in order to capture the air flow characteristic in more detail in these regions.

The meshes used for the CFD simulation of the TR, PV, ST façade elements (shown in Figure 4-1) were of a very good quality. Figure 4-2 shows the distribution of the mesh's cells aspect ratio. The meshes mainly consist of cells with an aspect ratio smaller than 4. In the meshes for the TR and the PV façade element, only 12% of the cells have an aspect ratio greater than 20. In the mesh of the ST façade element, only 6% of the cells exceed an aspect ratio of 20. On average, the aspect ratio is 10.8 for the TR/PV façade element and 8.1 for the ST façade element. The cells with a higher aspect ratio are only found in regions of the CFD mesh where very low gradients of temperature and air velocity were expected. Due to the conformal hexahedral mesh structure, skewness does not exceed a value of 0.17 for the TR/PV façade element or 0.32 for the ST façade element. On the whole, the skewness values are all far from critical, which makes it possible to obtain rapid convergence and good quality simulation results.

To take the thermal effect of the incoming solar radiation into account in the simulations, heat sources were attached to the corresponding surfaces of the façade. The heat sources were derived from the measured solar radiation, and considered the characteristics of the reflexion, transmission, and absorption of the materials (Table 4-1). These pre-calculated heat sources, which were calculated according to the method described in Chapter 3.3.5, are summarized in Table 4-2. The boundary conditions for the three-dimensional simulations were extracted from the data collected on August 21st, 2013 at 13:15. The external temperature was approximately 25 °C and the (vertically measured) global radiation amounted to 501 W/m².
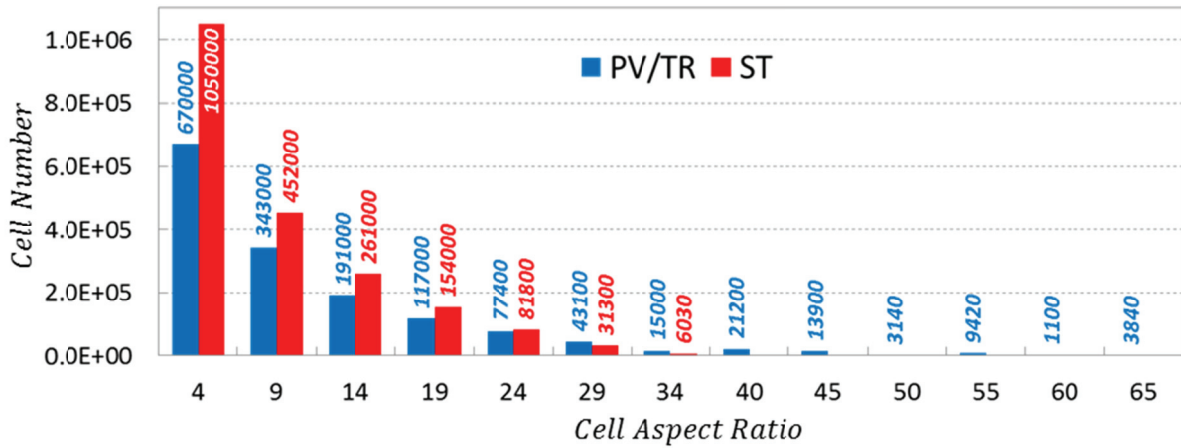
Figure 4-2: Comparison of the Cell Number with the Corresponding Aspect Ratio between the Meshes of the PV/TR and ST Façade Element

Table 4-1: Material Properties

	Density	Specific Heat Capacity	Thermal Conductivity	Short Wave Absorptivity	Short Wave Transmissivity
	kg/m^3	$J/(kg \cdot K)$	$W/(m \cdot K)$	—	—
Aluminium (Plates)	2800	896	160	0.9	-
Thermal Insulation (EPS)	100	1400	0.03	-	-
Glass (Exterior, Interior Pane)	2500	720	1.0	0.08	0.88
Copper (ST Absorber Plate)	8978	381	388	0.95	-
PV Module	2500	720	1.0	0.89	-
Mineral Wool	130	920	0.045		

Table 4-2: Pre-calculated Heat Sources of the Significant Surfaces exposed to Solar Irradiation

Surface Heat Source	W/m^2
Exterior Glass Pane (Vertical Surface)	226
Glass Pane Behind Glass Pane (Vertical Surface)	151
PV Cell/Module (Vertical Surface)	423
ST Absorber behind Glass Pane (Vertical Surface)	205

In the simulations of this study, the "RNG" turbulence model with "Standard Wall Functions" was used. In the CFD simulations, the y^+ value was between 25 and 30 in the fluid cells adjacent to the walls. There are a number of recent papers using this turbulence model for the CFD simulations of ventilated facades and double pane windows. The study of Coussirat et al. [70], for example, contains an evaluation of the most common turbulence models used for numerical simulations in the field of natural convective air flow. In this evaluation, simulations using the "RNG" turbulence model and the "SKE" model showed the best results.

The influence of the external wind was negligible between 13:00 and 13:30 August 21st, 2013 (see Figure 3-31). Data monitored on August 21st at 13:15 was used for the comparison between measurements and steady state CFD simulations, and therefore, the influence of wind was excluded from the external boundary conditions. This means that the air flow was only influenced by the effects of heating due to solar radiation where only natural convective flows occurred. To verify the assumption that the air flow in the façade's cavity is turbulent, the Rayleigh number (Ra) was determined. The calculated Ra numbers of the interior as well as of the exterior convective layers of the ventilation cavity are shown in Table 4-3.

The transition from laminar to turbulent flow is within the range of a Rayleigh number of 10E+8 to 10E+9; a higher Ra number indicates a turbulent flow characteristic. All of the calculated Ra numbers from the table indicate a turbulent air flow characteristic, and it can therefore be concluded that the "RNG" turbulence model is suitable for the CFD simulations of this study.

Table 4-3: Calculated Rayleigh Numbers using the Results of the CFD Simulations of the Comparison between the Three Façade Elements (Chapter 4.2.5)

		$Ra_{TR\text{-}int}$	$Ra_{PV\text{-}int}$	$Ra_{ST\text{-}int}$	$Ra_{TR\text{-}ext}$	$Ra_{PV\text{-}ext}$	$Ra_{ST\text{-}ext}$
l	m	3.1	3.1	3.1	3.1	3.1	3.1
ϑ_W	K	311.1	314.6	309.4	314.9	323.2	310.9
ϑ_0	K	304.2	306.3	302.9	304.2	306.3	302.9
ν	m^2/s	1.64E-05	1.66E-05	1.62E-05	1.66E-05	1.71E-05	1.63E-05
$\beta = 1/\vartheta_0$	$1/K$	3.29E-03	3.27E-03	3.30E-03	3.29E-03	3.27E-03	3.30E-03
Gr	$-$	2.49E+10	2.92E+10	2.43E+10	3.77E+10	5.58E+10	2.94E+10
Pr	$-$	0.72	0.72	0.72	0.72	0.72	0.72
Ra	$-$	1.79E+10	2.10E+10	1.75E+10	2.71E+10	4.02E+10	2.12E+10

The influence of longwave radiation between surfaces was also implemented by means of the DO radiation model. The DO radiation was solved every 25th iteration step in order to reduce simulation time. Further specifications of this DO model were the number 5 for the "Theta" and "Phi Division" as well as for the "Theta" and "Phi Pixel", in order to provide an adequate radiation distribution through the simulation models' cells.

All simulations were performed at "Steady State" conditions by using a "Pressure-Based" solver. The solution methods, discretization, and solution controls are summarized in Table 4-4. The "SIMPLE" formulation was used for the pressure-velocity coupling. Further discretisation in the solution methods included the "Least Squares Cell-based" formulation for the gradient, the "Body Force-weighted" formulation for the pressure, and the "Second Order Upwind" scheme for the momentum, as well as the turbulent kinetic energy and dissipation rate, for the energy and DO-radiation, respectively.

Table 4-4: Numerical Solution Methods, Discretization Parameter and Under-Relaxation Factors

Solution Methods	Pressure-velocity coupling	Gradients	Pressure	Momentum	Turbulent Kinetic Energy	Turbulent Dissipation Rate	Energy	Discrete Ordinates
	SIMPLE-scheme	Least Squares Cell Based	Body Force Weighted	Second Order Upwind	Second Order Upwind	Second Order Upwind	Second Order Upwind	Second Order Upwind
Solution Controls (URF)	Pressure	Density/Turbulent Viscosity	Body Forces	Momentum	Turbulent Kinetic Energy	Turbulent Dissipation Rate	Energy	Discrete Ordinates
	0.5	1	1	0.5	0.8	0.8	1	1

The Under-Relaxation Factors (URF) in the solution controls were set to 0.5 for the pressure and momentum, while the density, body forces, turbulent viscosity, energy and discrete ordinates were set to a value of 1.0. The URF was 0.8 for the turbulent kinetic energy and the turbulent dissipation rate in all simulations. Compared to the two-dimensional simulations, a lower URF for pressure and a higher URF for momentum are feasible in the solution controls, and reduced the calculation time by about half.

4.2.3 CFD Mesh Assessment

For the CFD model with the PV/TR façade element and the model with the ST façade element, two different mesh sizes were used in the simulations. The coarse PV/TR façade model consists of 1.16 million cells, while the fine mesh contains 9.27 million hexahedral cells. The mesh of the coarse three-dimensional ST façade model has 2.03 million cells, whereas the fine mesh has 16.28 million cells. The fine mesh of the ST façade model was very close to the upper limit of the available computing power: no further refinement of the mesh was possible. Well selected profiles of sections through the three-dimensional models were prepared in order to determine the quality of the meshes. The resulting temperature and air velocity profiles are illustrated for comparison in the next figures.

Figure 4-3 presents the comparison of the temperature (solid lines) and air velocity (dashed lines) profiles along the ventilation cavity´s width (x-length) between the fine and the coarse mesh of the PV/TR façade model for a section through the centre of the façade element. The temperature profiles of the coarse and the fine meshes showed very good agreement; only the temperature of the PV module was slightly higher for the coarse CFD mesh. The velocity profiles also matched very well; the velocity

peak close to the PV module inside the ventilation cavity was marginally higher for the fine mesh. Furthermore, the air velocity was a little bit higher at the exterior environment for the fine mesh.
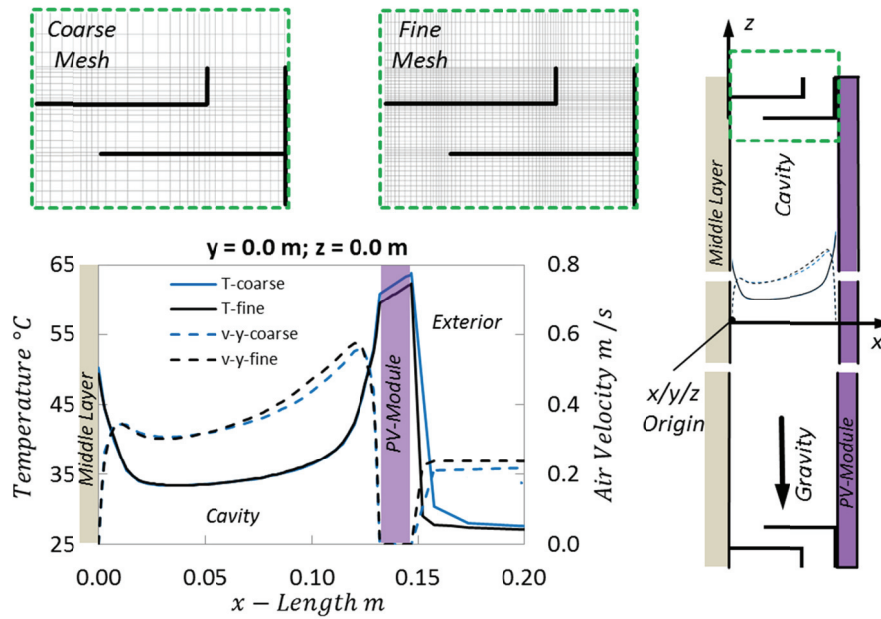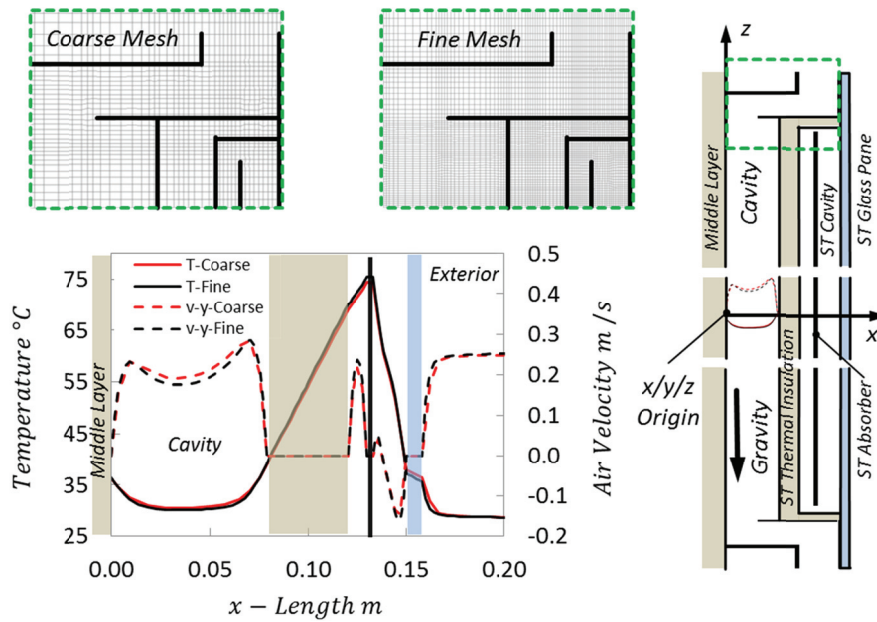

Figure 4-3: Comparison of Temperature and Air Velocity Profiles for a Section along Centre the Ventilation Cavity PV/TR Façade using a Fine and a Coarse Mesh

Figure 4-4 shows a comparison of different temperature profiles (left) and air velocity profiles (right) along the façade´s height (y-length), to compare the simulation results using a fine and the coarse mesh of the PV/TR façade model. The solid lines represent the profiles in the middle of the ventilation cavity, 0.02 m away from the middle layer, while the dashed lines illustrate the profiles in the middle of the ventilation cavity, 0.02 m from the PV module, and the dotted lines show the profiles along the left opening of the façade element.
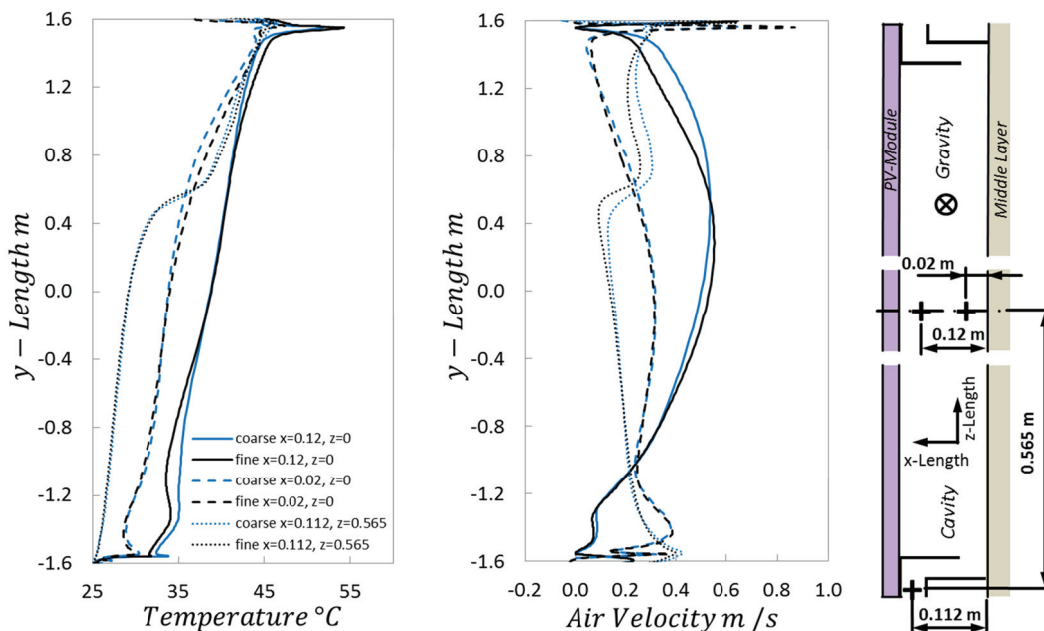
Figure 4-4: Comparison of Temperature and Air Velocity Profiles at Three Different Positions along the Height of the PV/TR Façade using a Fine and a Coarse Mesh

Generally, the air temperature and velocity profiles of the fine and the coarse meshes were similar. The temperature profile of the coarse mesh showed a marginally lower temperature from the middle of the façade's height to the upper ventilation outlet, 0.02 m from the middle layer. Close to the PV module,

the air temperature of the coarse mesh was a little higher at the bottom and slightly lower at the top of the façade´s cavity. Furthermore, near the side openings and close to the PV module, there were minor deviations between the air velocity profiles resulting from the coarse and fine meshes.

The same method of analysis was used for the comparison between the two meshes of the ST façade model. Figure 4-5 shows the comparison of the profiles for a section through the centre of the façade element in x-length. Again, the solid lines represent the temperature, and the dashed lines, the air velocity profiles. The temperature resulting from the coarse mesh did correlate with the temperature of the fine mesh; only in the region of the ST absorber plate was the temperature slightly higher using the fine mesh in the numerical simulation. In the middle of the ventilation cavity, the air velocity resulting from the fine mesh was slightly lower than that from the coarse mesh.

Figure 4-5: Comparison of Temperature and Air Velocity Profiles for a Section along the Centre of the Ventilation Cavity ST Façade using a Fine and a Coarse Mesh

Figure 4-6 illustrates the temperature (left) and air velocity profiles (right) resulting from the fine and coarse meshes of the ST façade model.
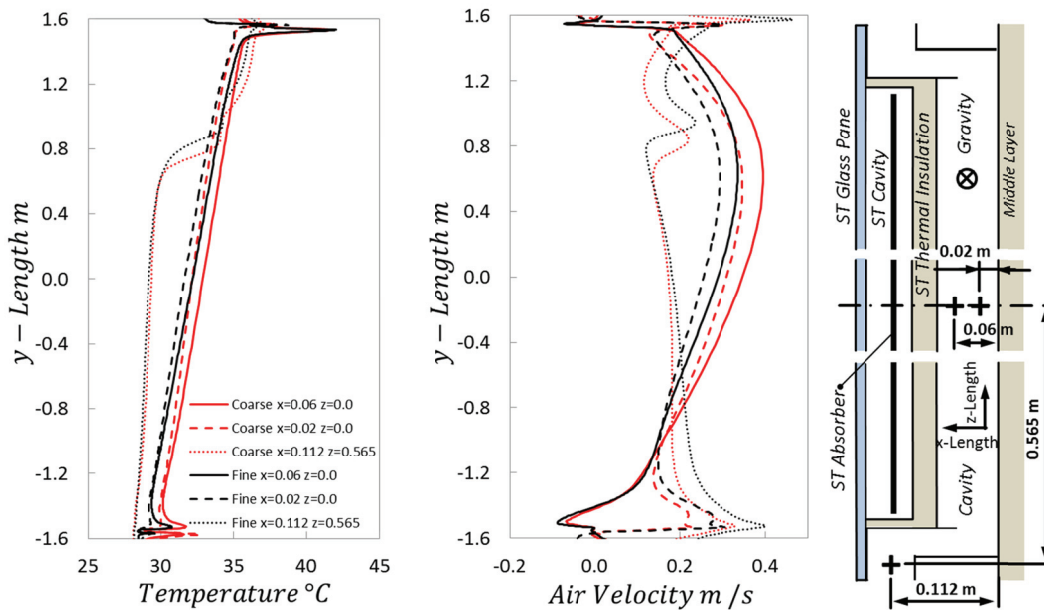
Figure 4-6: Comparison of Temperature and Air Velocity Profiles at Three Different Positions along the Height of the ST Façade using a Fine and a Coarse Mesh

The solid lines represent the profiles in the middle of the ventilation cavity, 0.02 m from the middle layer. The dashed lines illustrate the profiles in the middle of the ventilation cavity, 0.02 m from the thermal insulation at the rear of the solar thermal collector, while the dotted lines show the profiles along the left opening of the façade element.

Generally, the temperature and air velocity profiles look similar; small temperature differences occurred between the profiles of the fine and the coarse meshes in the upper region of the ventilation cavity and immediately after the ventilation inlet. Some differences were also detected in the air velocity profiles in comparison to the mesh assessment of the PV façade model: this deviation was slightly larger than that for the ST façade model. Nevertheless, the mesh assessment only resulted in deviations in the profiles that were within an acceptable limit, thus implying that both meshes qualified for use in further CFD investigations.

4.2.4   Validation of the CFD Model

Before the comparison of the thermal behaviour and the flow characteristics, the simulation models were compared with data from the measurements. This comparison used data collected from the façade elements on August 21st, 2013 at 13:15 (Figure 3-29). Between 13:00 and 14:00, the external conditions varied within a range for which a steady state CFD simulation is still plausible. Furthermore, the façade elements consist almost exclusively of very thin plates and panels, meaning that the thermal mass is very small, and both the heating and ventilation effects do come about very rapidly. One advantage of steady state CFD simulations is that they require much less time than transient calculations. The temperatures of the interior wall, at the bottom and top of the façade elements, in addition to the exterior temperature, were used as boundary conditions in the simulation cases. These boundary temperatures were indicated with BC in the following diagrams, which show a comparison between the measurements and simulations (Figure 4-7, Figure 4-8 and Figure 4-9). In these figures, the simulated temperature/velocity profiles along the width (x-length) of the air cavity are shown. Additionally, the value measured at the sensor's corresponding position was inserted for comparison (sensor positions are shown in Figure 3-28).

Figure 4-7 shows the results of the validation of the TR façade element. The temperature of the interior wall inside the air cavity (TR-1.43) and the air temperature in front of the façade element (TR-1.40) from the simulation correlated very well with the measured values.
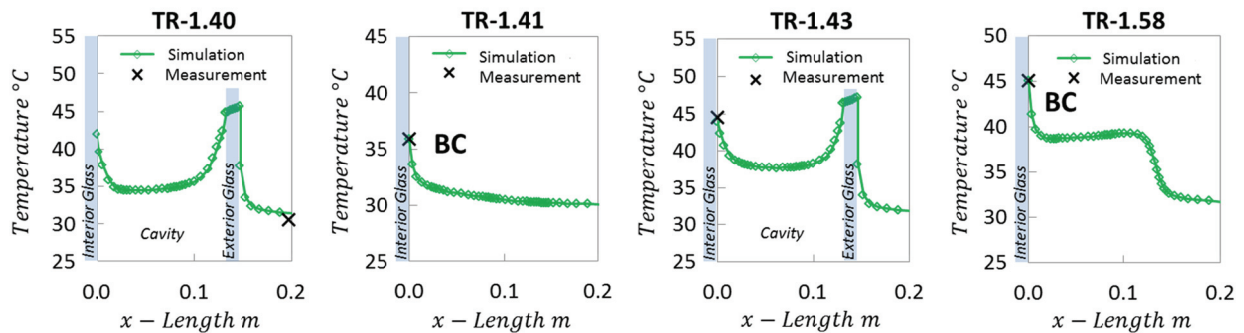
Figure 4-7: Diagrams show the Actual Temperatures (from August 21st, 2013, 13:15) compared with the Results of the CFD Model from the TR Façade Element. The Values indicated with BC were used as Boundary Conditions in the CFD Simulation

The validation of the PV façade element is shown in Figure 4-8. This figure also contains a comparison of the air velocity inside the cavity (PV-0.81 and PV-3.16). The surface temperatures from the simulation did match the measured values for most of the comparison. The simulation slightly overestimated the interior wall´s temperature (PV-1.64), while the computed surface temperature at the PV module (PV-1.69) was slightly lower than the monitored value. The monitored air velocity from the hot wire anemometer (PV-0.81) did accord very well with the result of the simulation. The computed air velocity at the position of the hot wire anemometer (PV-3.16) was lower than the monitored value.

The last figure in this Chapter (Figure 4-9) shows a comparison between the simulation and measurement results of the ST façade element. Again, most of the simulated values correlated with the measurements. The computed surface temperature at the interior wall (ST-1.73) was slightly higher than

the measured one. The air temperature measured above the ventilation opening was higher than the simulation result.
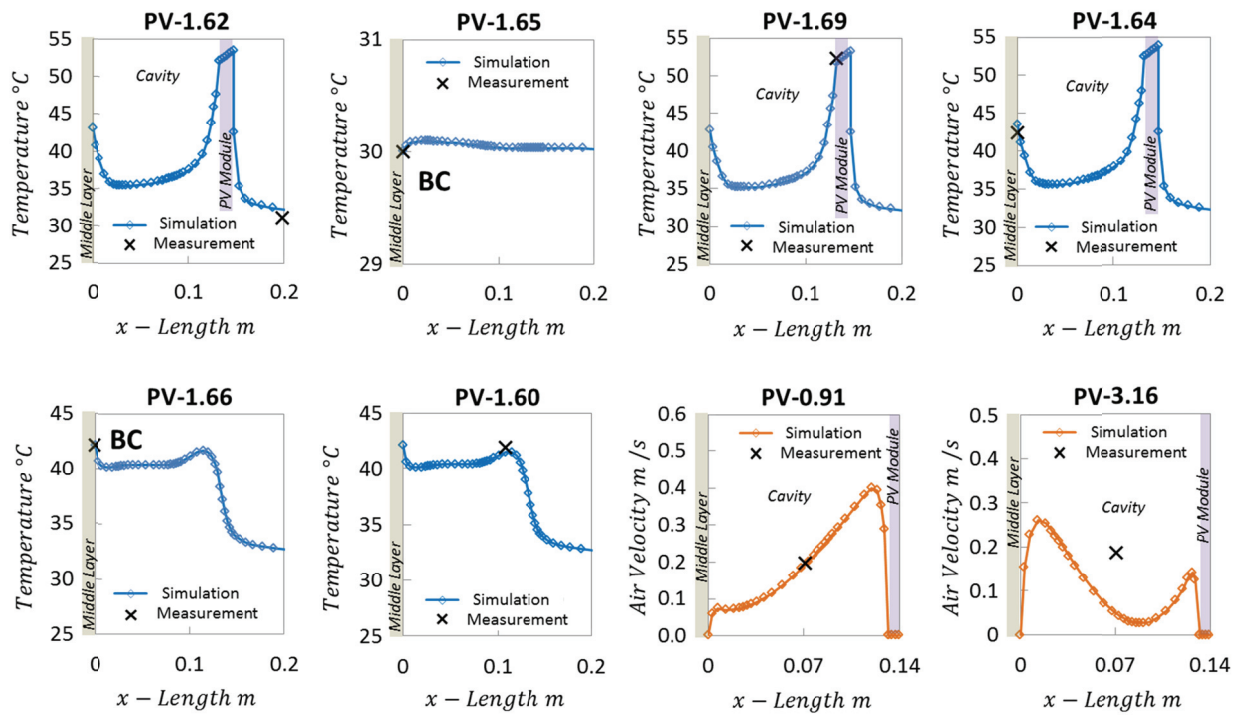
Figure 4-8: Measured Temperatures and Air Velocities (from August 21st, 2013 at 13:15) for the Validation of the Results of the CFD Model of the PV Façade Element. The values indicated with BC were used as Boundary Conditions in the CFD Simulation

The results of the simulation were in good accordance with the measurement data. Uncertainties in the monitored data could be caused by the influences of the test façade's neighbouring façade elements. Furthermore uncertainties could also be caused by the influence of the transient behaviour of the external environment such as a short gust of wind which not captured by the monitoring, for example.
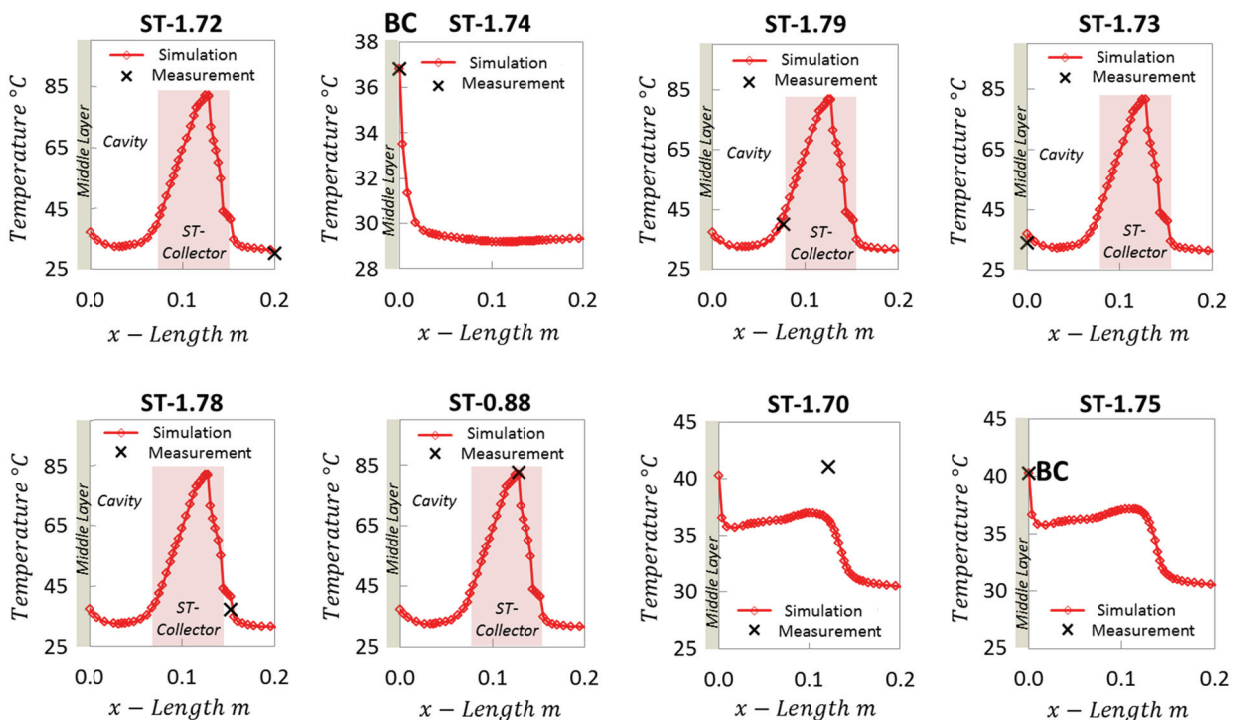
Figure 4-9: Diagrams of Measured Temperatures (from August 21st, 2013, 13:15) compared to the Results of the CFD Model of the ST Façade Element. The values indicated with BC were used as Boundary Conditions in the CFD Simulation

4.2.5 Flow and Temperature Characteristics of the TR, PV and ST Facades

While the position of each façade element in the MPPF-façade was considered in the validation process in the form of data collected on August 21st, 2013, and implemented as boundary conditions (different bottom-infiltrating air temperatures were input for the PV and ST façade elements, for example), uniform boundary conditions were set for each façade element for all simulations in order to compare the thermal behaviour and convective airflow of the three different façade elements. For these comparisons of convective airflow inside the façade elements, the external temperature was set to 25 °C, and the incoming solar radiation was set to 1000 W/m² for the simulation. At a solar angle of 60°, the resulting vertical radiation on the façade was 500 W/m². The room temperature was set to 25 °C in all simulation cases, while in the model, a virtual wall layer was used between the interior wall/glass and the room, and a convective temperature layer with a value of 5 W/m² was chosen.
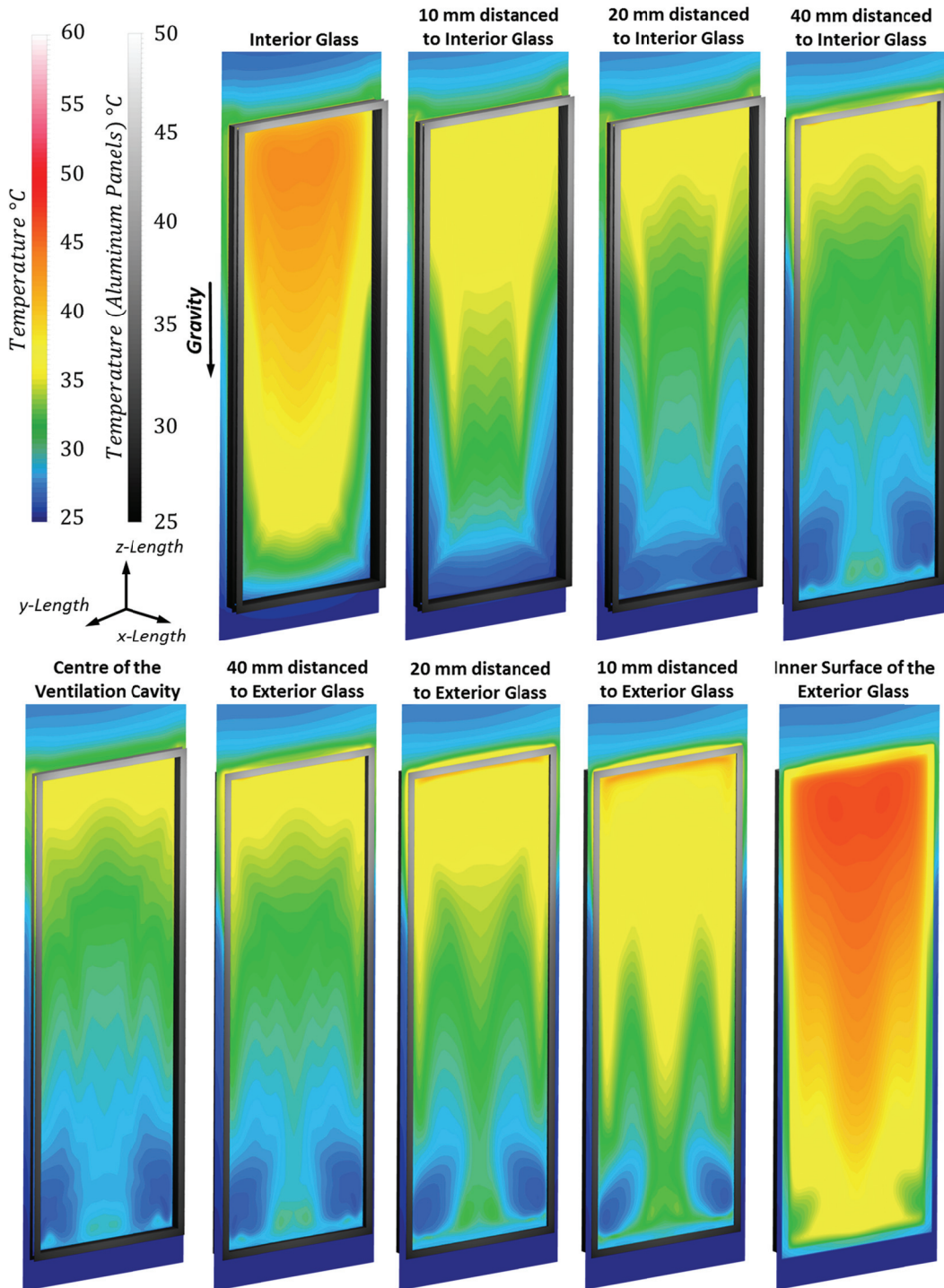
Figure 4-10: Illustration of the Temperature Contours for the TR-Façade Element at Different Sections Parallel to the yz-Plane between the Interior Glass and the Inner Surface of the Exterior Glass

Before comparing the thermal behaviour of the three façade types, this chapter presents each individual temperature and airflow characteristic, beginning with the TR façade. Figure 4-10 shows the temperature contours of the interior and exterior glass surfaces and a few sections between and parallel to these surfaces (yz-plane). Furthermore, in Figure 4-11, both the temperature contours and the airflow vectors for several sections through the TR façade element are illustrated parallel to the xy-plane in the CFD domain.
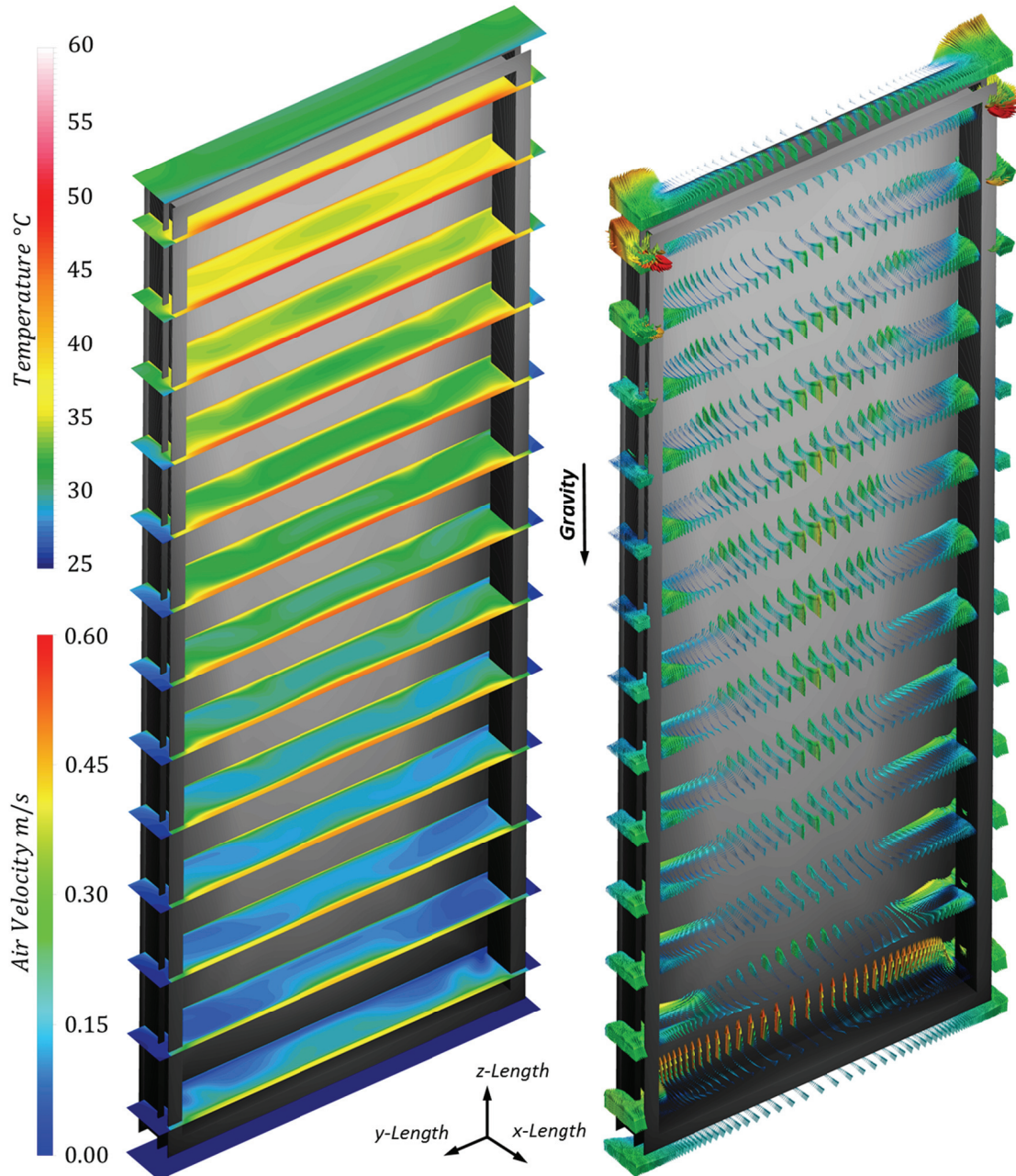
Figure 4-11: Temperature Contours and Air Flow Vectors of the TR-Façade Element at Different Sections Parallel to the xy-Plane from Shortly Before the Bottom to Immediately after the Top of the Ventilation Cavities´ Openings

Generally, air flows upwards along the whole façade element. At the bottom of the ventilation opening, the air infiltrates the façade element, passes the aluminium panels, and enters the cavity. These aluminium panels cause turbulence at all corners, as well as inside the cavity. The maximum air velocity in the bottom region of the façade occurs at the entrance to the cavity, with about 0.5 m/s at the bottom of the façade element. The influence of the infiltrating air is identified by the blue temperature contour at the bottom of the sections parallel to the yz-plane presented in Figure 4-10. The infiltrating air does not fully arrive at the middle bottom region of the TR façade element before it drifts upwards. The airflow expands upwards after the façade element's entrance. For the most part, inside the façade´s cavity the lowest temperatures occur between the yz-sections in the centre of the cavity and 40 mm

away from the interior glass. The radiative heat transfer has a significant impact on the thermal behaviour inside such narrow ventilation cavities, thus, the surface temperature of the middle layer is only a little bit lower than the temperature at the exterior surfaces.

Both the temperature contours and the air flow characteristic for the PV façade element (presented in Figure 4-12 and Figure 4-13) are similar to the results of the TR façade element. Generally, higher temperatures occur inside the façade´s cavity compared to the TR façade. The highest air velocity inside the cavity occurs near the top ventilation opening, with a value of 0.88 m/s, and the bottom region of the cavity, immediately after the ventilation inlet, with a value of 0.53 m/s.
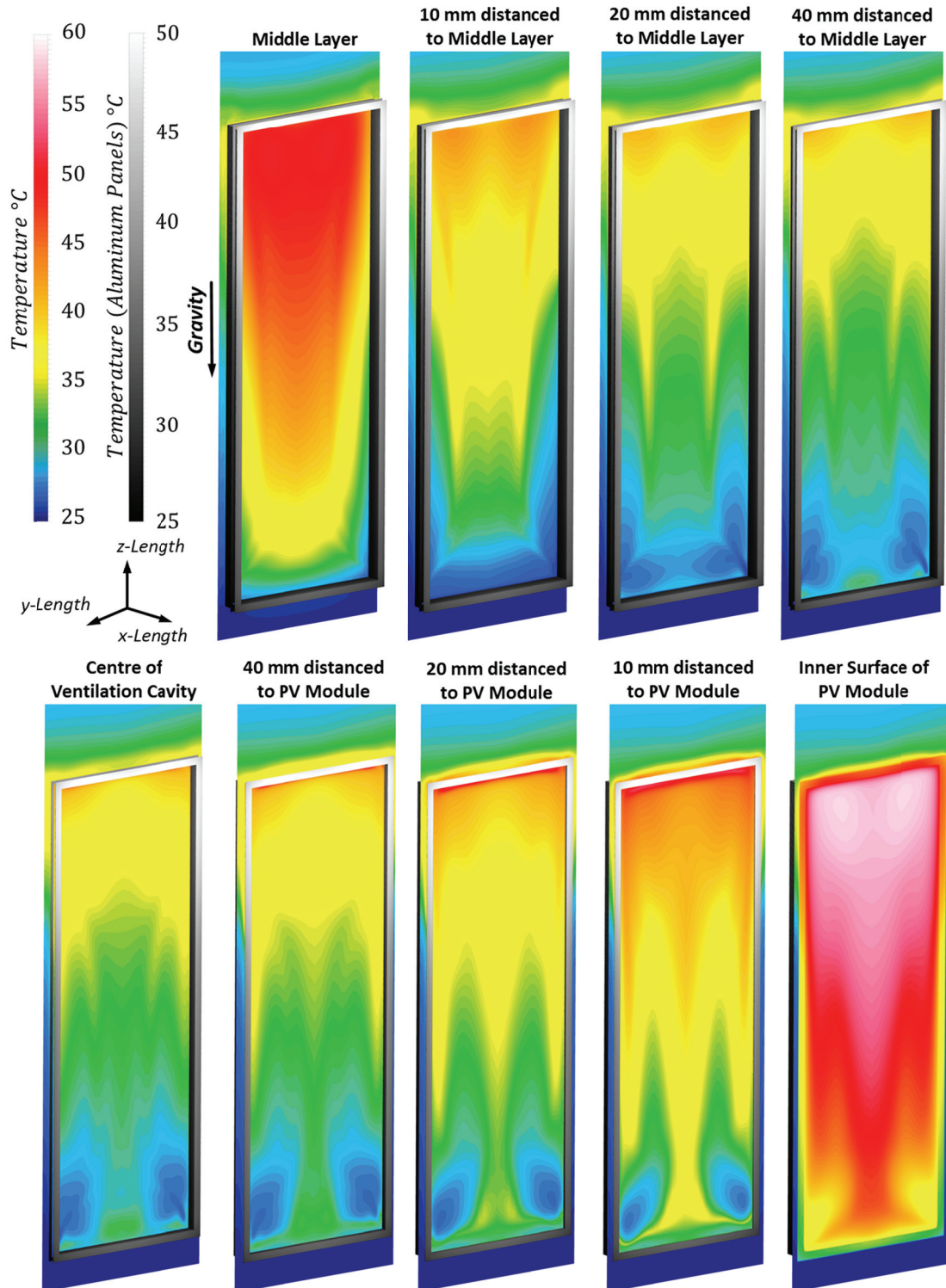
Figure 4-12: Temperature Contours for the PV-Façade Element at Different Sections Parallel to the yz-Plane between the Middle Layer and the Inner Surface of the PV Module
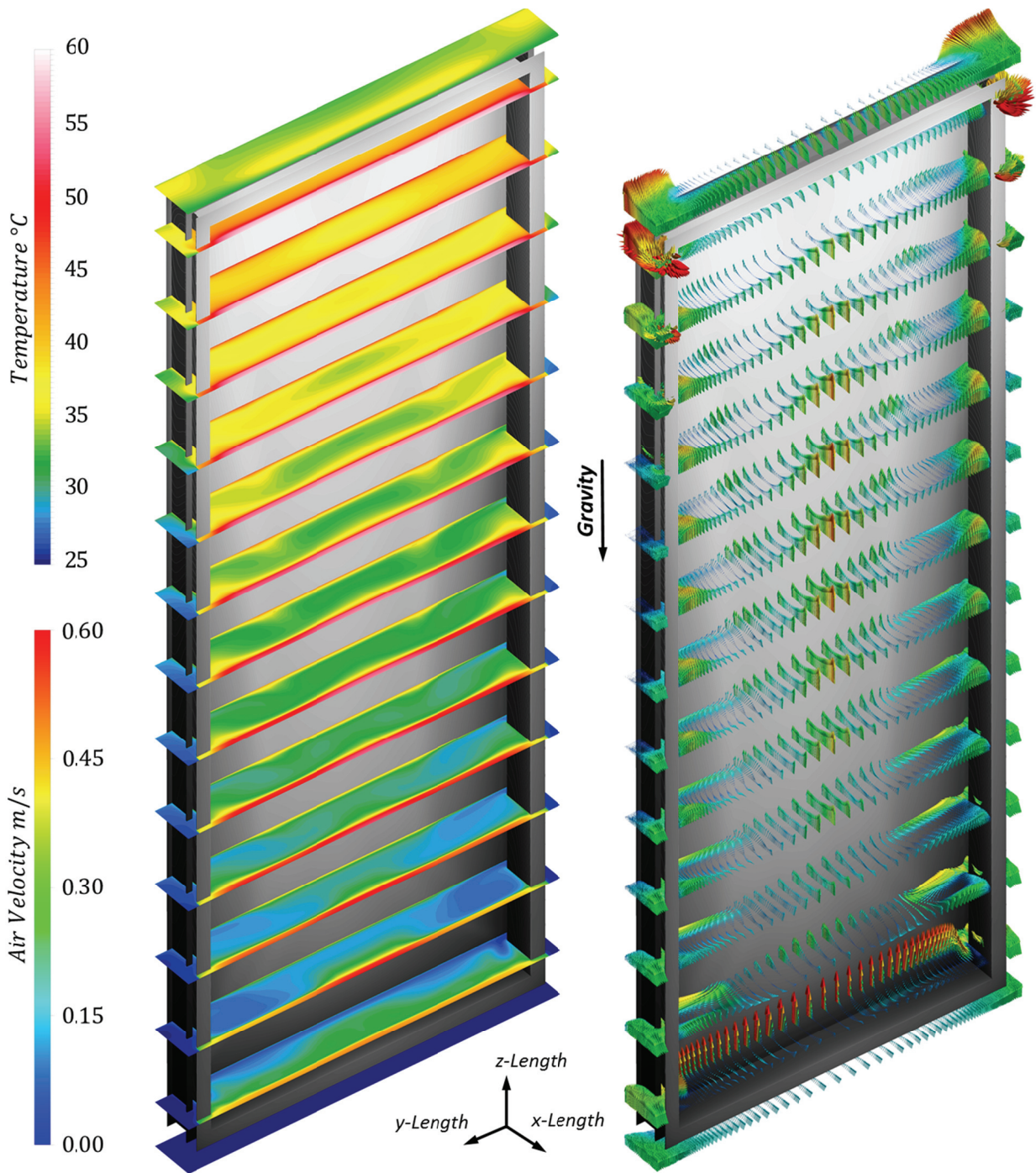
Figure 4-13: Temperature Contours and Airflow Vectors of the PV-Façade Element at Different Sections Parallel to the xy-Plane from Shortly before the Bottom to Immediately after the Top of the Ventilation Cavities' Openings

For the façade element with the integrated solar thermal collector, both the thermal behaviour and the airflow characteristic deviated from the results of the TR and PV façade element. The temperature contours between the middle layer and the exterior glass of the solar thermal collector for several sections parallel to the yz-plane are presented in Figure 4-14, while the temperature contours and flow vectors for sections parallel to the xy-plane are illustrated in Figure 4-15.

As in the TR and PV façade´s cavity, the infiltration of air at the bottom corners can also be observed for the ST façade element. The gap between the two infiltrating air streams is larger compared to the TR and PV façade element. The lowest temperatures can clearly be identified in the yz-section through the centre of the ST façade´s cavity. While the flow characteristic results in the formation of two peaks close to the interior and the exterior surfaces of the ventilation cavity, an almost uniform vector flow profile occurs in the cavity (along the x-length) of the ST façade. Only very small peaks with a slightly higher velocity are obtained in the flow vector profiles in Figure 4-15. The highest air velocity, of 0.71 m/s, is

obtained at the top corner of the façade element with integrated solar thermal collector. The highest air velocity occurs immediately after the bottom ventilation inlet, at 0.34 m/s.
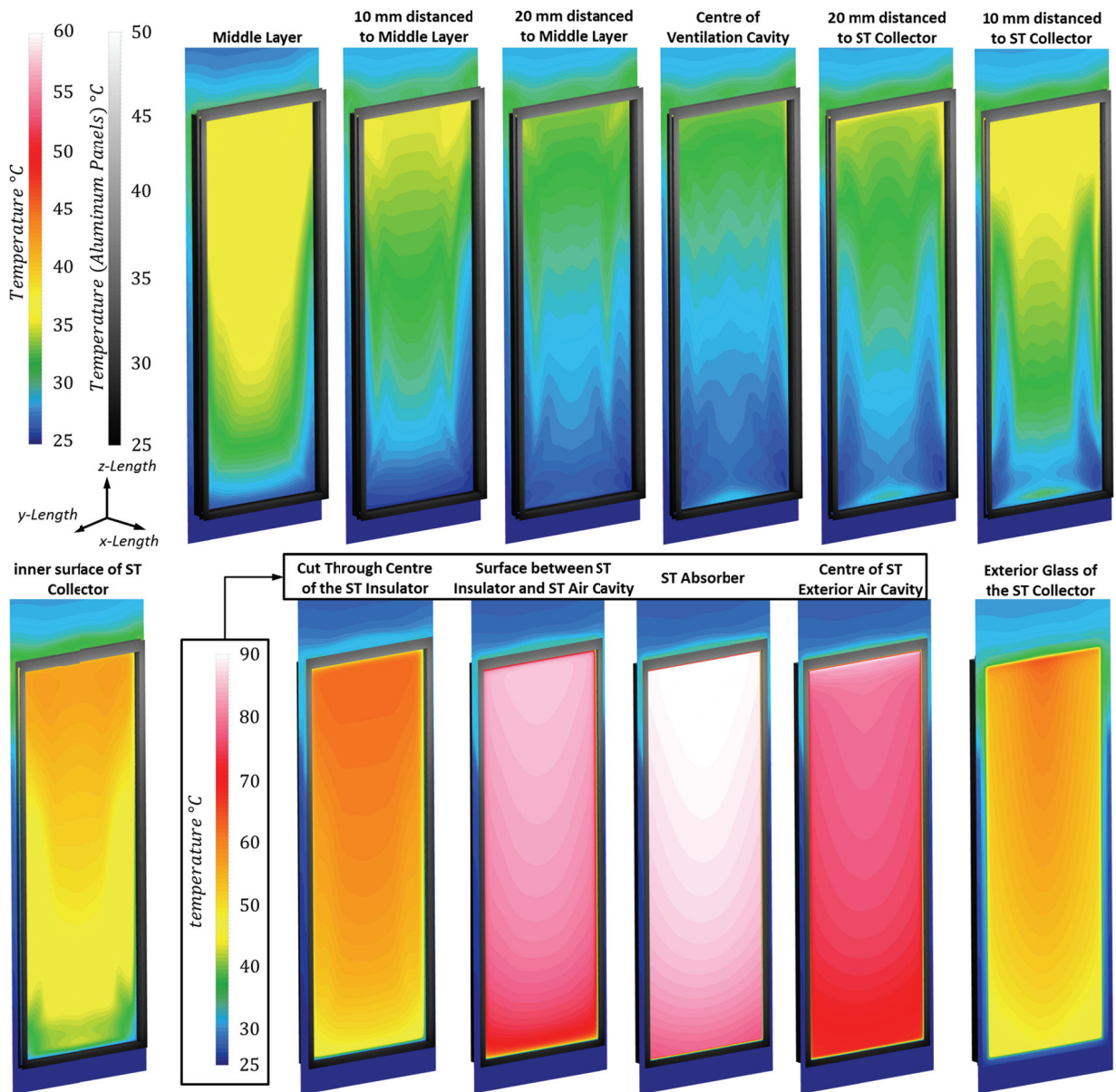
Figure 4-14: Temperature Contours for the ST-Façade Element at Different Sections Parallel to the yz-Plane between the Middle Layer and the Exterior Glass of the ST Collector

In the CFD simulation of the ST façade element, the airspace around the absorber plate is assumed to be an (airproof) closed cavity. The magnitude of the circulating air in the collector cavity is significantly lower compared to the air velocities inside the ventilation cavity. Inside the solar thermal collector there is a maximum air velocity of 0.17 m/s. As expected, the temperature contours show their maximums in the centre and at the top of the solar thermal collector. The temperature decreases towards the side of the collector pan as a result of the air infiltrating the façade´s ventilation cavity. Furthermore, the heat transfer rate from the ST collector to the ventilation cavity is reduced by the installation of thermal insulation.
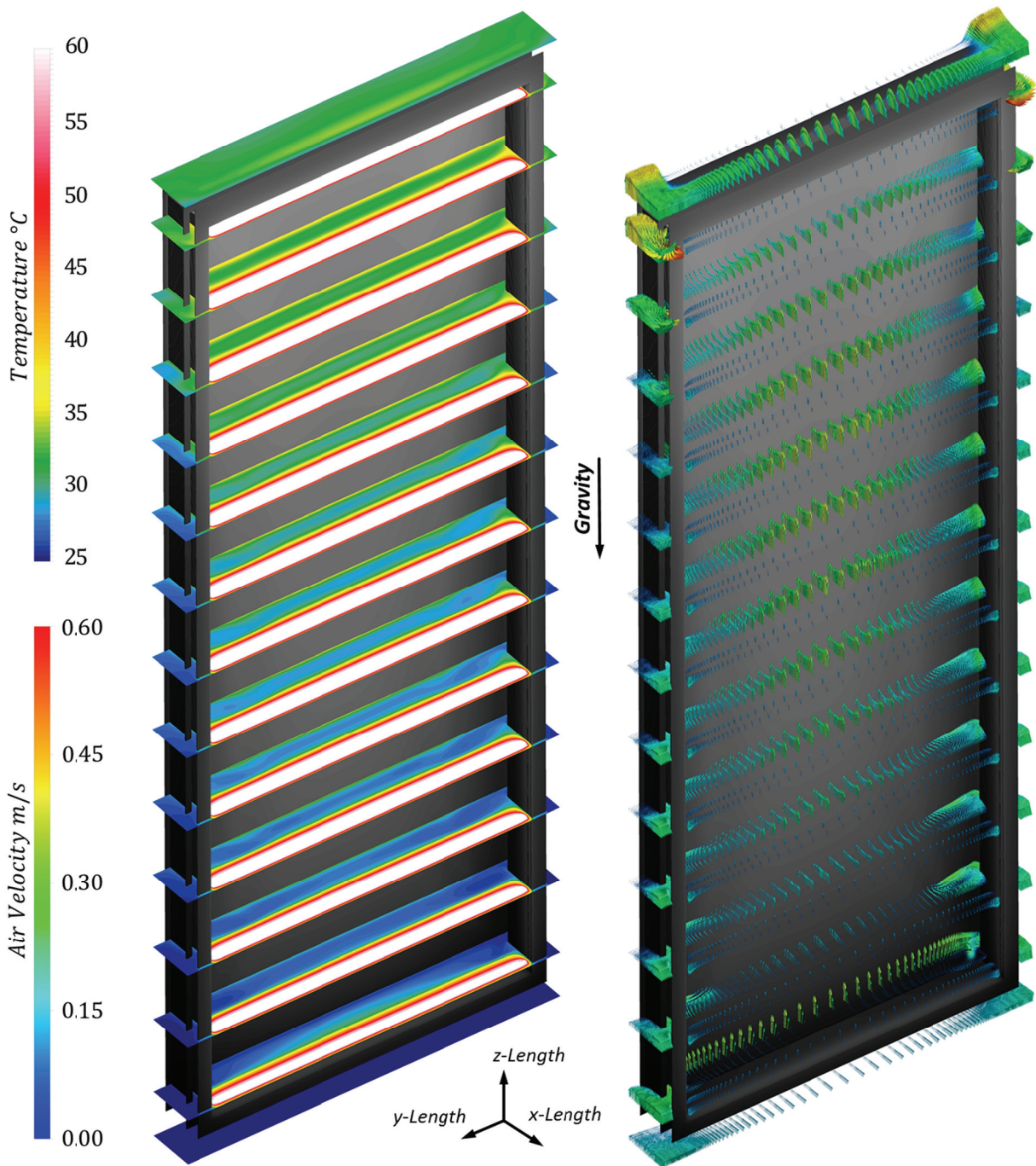
Figure 4-15: Temperature Contours and Air Flow Vectors of the ST-Façade Element at Different Sections Parallel to the xy-Plane from Shortly before the Bottom to Immediately after the Top of the Ventilation Cavities' Openings

4.2.6   Comparison of the TR, PV and ST Facades' Thermal Behaviour

Figure 4-16 displays the surface temperature contour plots for TR, PV and ST façade elements at the same boundary conditions, in order to compare the thermal behaviour of these three different façade applications. The highest surface temperatures in the ventilation cavity occurred for the PV façade element. The surface temperatures of the TR façade element were lower compared to the PV façade, although the temperature contour shapes developed similarly. The surface temperature contours of the ST façade differed slightly from the PV and TR facades' behaviour. This difference was obviously caused by the absorber of the solar thermal collector. The maximum absorber surface temperature was about 88.4 °C. Nevertheless, the temperature of the ST façade's exterior glass surface and its exterior wall surfaces were lower than the surface temperatures of the PV and TR façade elements.

Stationary, Three-dimensional CFD Models
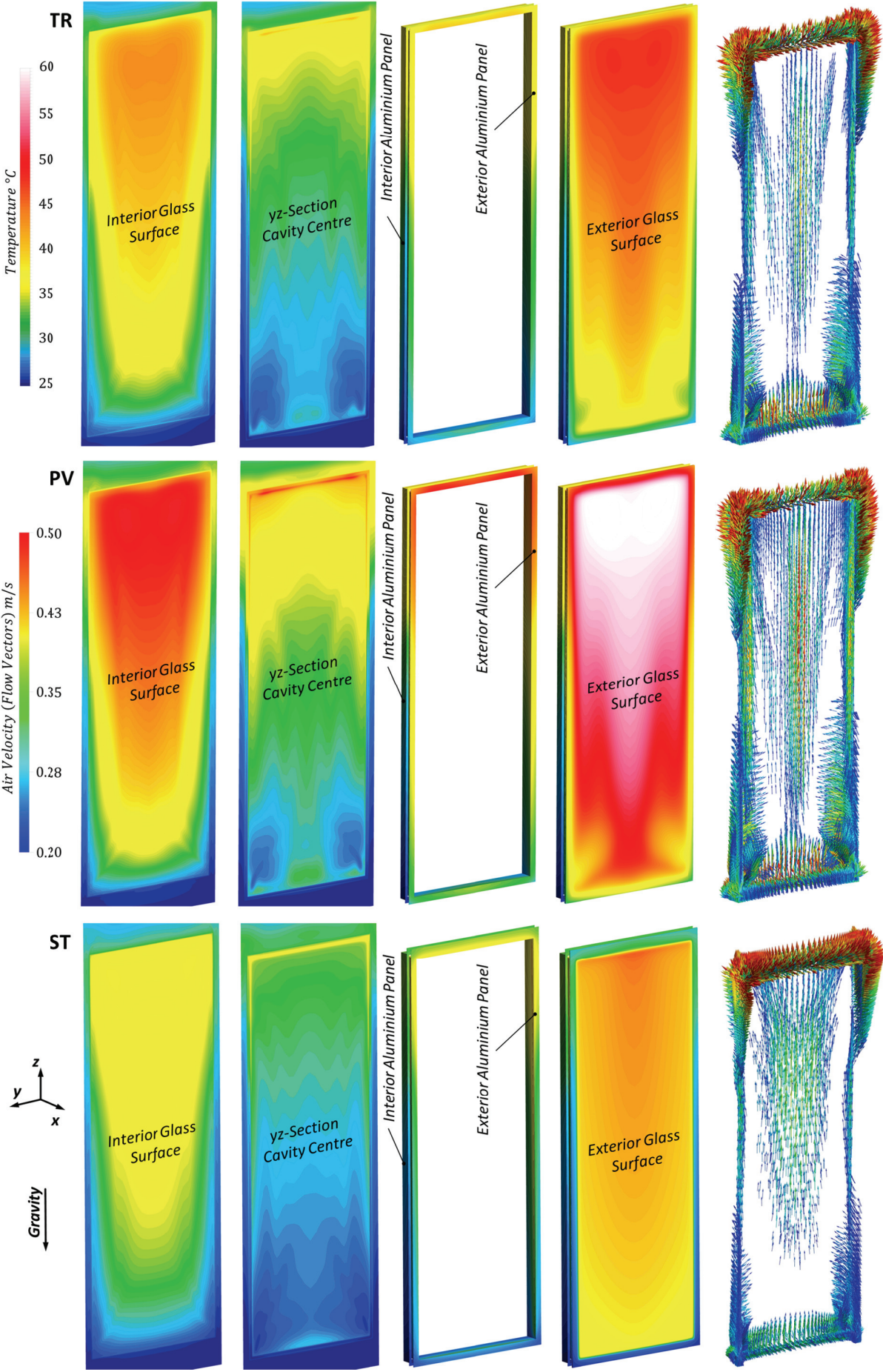
Figure 4-16: Comparison of Temperature Contours and Air Flow Vectors between the TR, PV and ST Façade Elements at the same Boundary Conditions

Figure 4-17 shows a comparison of air vector details in combination with the determined temperature contours of the TR, PV and ST façade elements on the bottom-, middle- and the top-left sides of the façade elements. The contours and air vectors of the TR and the PV facades are similar. The air flow characteristic inside the ventilation cavity of the ST façade deviates from the results of the TR and PV façade elements. The air flow inside the cavity shows a more uniform tendency to stream upwards. In the regions close to the left and the right periphery openings in particular, the air stagnates inside the PV and TR facades, but not in the ST façade's cavity.
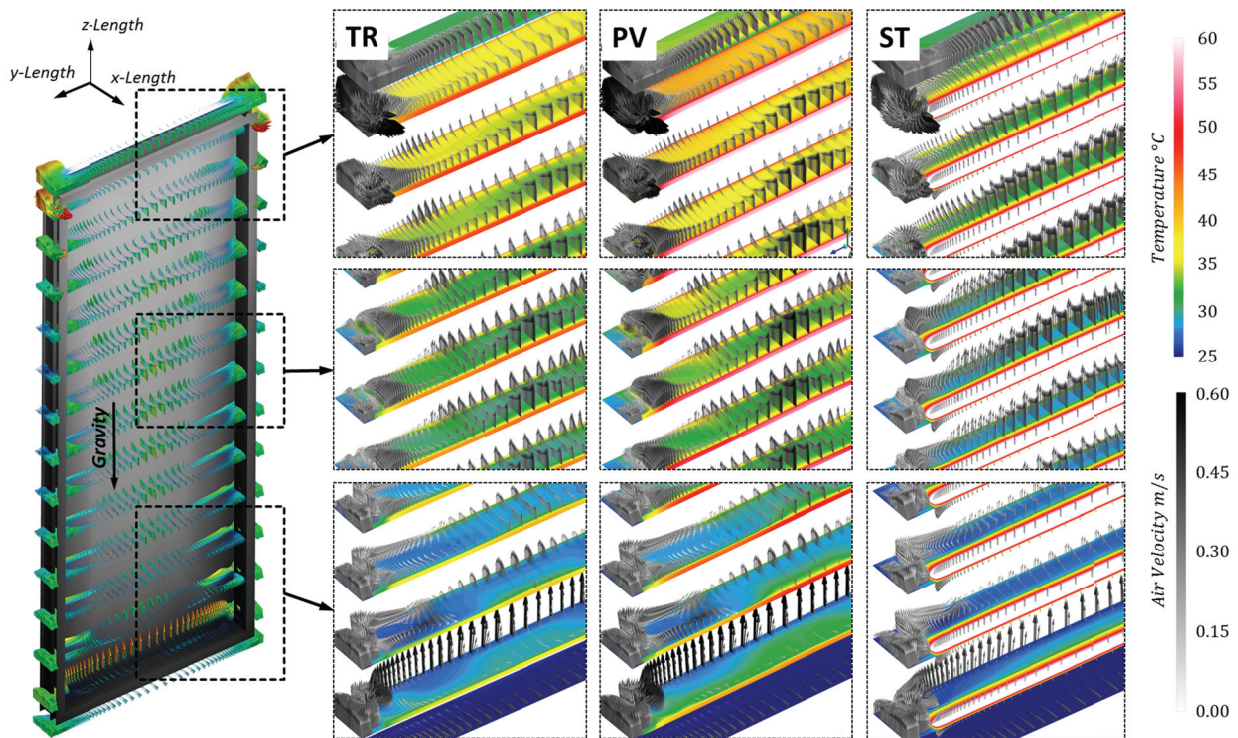
Figure 4-17: Comparison of the Combined Temperature Contours and Air Vectors at Different Sections Parallel to the xy-Plane of the TR, PV and ST Façade Elements

Table 4-5 shows a summary of the maximum and averaged values of velocities and temperatures for the main surfaces, solid components, and cavity air volume of the three CFD façade models considered in this study. The difference between the surface-averaged temperatures of the interior glass (middle layer) and the exterior glass (PV exterior glass surface, ST exterior glass cover) is 4.0 K for the TR-, 9.6 K for the PV- and 6.0 K for the ST façade element. The average surface temperature of the interior glass of the TR façade is 3.4 K lower than that of the middle layer surface of the PV façade element, and 4.1 K higher than the middle layer surface of the ST façade element. The volume-averaged temperature of the interior aluminium panel of the TR façade element is 0.7 K lower than the temperature of the interior aluminium panel of the PV façade, and 1.7 K higher compared to the interior aluminium panel of the ST façade element. The volume-averaged temperature of the exterior aluminium panel of the TR façade element is 3.8 K lower than the temperature of the exterior aluminium panel of the PV façade, and 1.3 K higher compared to the exterior aluminium panel of the ST façade element. The volume-averaged temperature of the air cavity for the TR façade is 2.3 K lower than for the PV façade and 1.6 K higher than for the ST façade.

Figure 4-18 shows the comparison of the temperature and velocity profiles of the three façade elements (TR, PV and ST) along the cavity width (x-length) at three different heights (y-lengths) in the centre of the façade (z = 0.0 m). The profile positions are in the middle of the cavity height (y = 0.0 m), close to the façade's top (y = +1.5 m) and bottom (y = -1.5 m) ventilation openings. The profiles for the TR façade are green dotted lines; the profiles for the PV façade are blue solid lines, and the profiles for the ST façade are red dashed lines. Furthermore, the ventilation cavity lengths of the three façade elements are also indicated in the diagrams.

Table 4-5: Maximum and Average Values of Temperature and Velocities of the Main Volumes and Surfaces used in the CFD Models

Surfaces TR Façade Element				Surfaces PV Façade Element			
TR Interior Glass Surface	T_{max}	$°C$	44.4	PV Middle Layer Surface	T_{max}	$°C$	50.3
	$T_{average}$	$°C$	38.0		$T_{average}$	$°C$	41.4
TR Exterior Glass Surface	T_{max}	$°C$	48.1	PV Exterior Glass Surface	T_{max}	$°C$	59.0
	$T_{average}$	$°C$	42.0		$T_{average}$	$°C$	51.0
Volumes TR Façade Element				Volumes PV Façade Element			
TR Exterior Glass Volume	T_{max}	$°C$	48.0	PV Exterior Glass Volume	T_{max}	$°C$	59.3
	$T_{average}$	$°C$	41.5		$T_{average}$	$°C$	49.9
TR Interior Aluminium Panel	T_{max}	$°C$	37.0	PV Interior Aluminium Panel	T_{max}	$°C$	39.2
	$T_{average}$	$°C$	31.1		$T_{average}$	$°C$	31.8
TR External Aluminium Panel	T_{max}	$°C$	40.8	PV Exterior Aluminium Panel	T_{max}	$°C$	48.6
	$T_{average}$	$°C$	33.5		$T_{average}$	$°C$	37.3
TR Cavity Air Volume	T_{max}	$°C$	44.8	PV Cavity Air Volume	T_{max}	$°C$	54.5
	$T_{average}$	$°C$	31.9		$T_{average}$	$°C$	34.2
TR Cavity Air Volume	$v_{abs,max}$	m/s	0.95	PV Cavity Air Volume	$v_{abs,max}$	m/s	1.10
	$v_{abs,average}$	m/s	0.15		$v_{abs,average}$	m/s	0.17
TR Cavity Air Volume	$v_{buoy,max}$	m/s	0.65	PV Cavity Air Volume	$v_{buoy,max}$	m/s	0.72
	$v_{buoy,average}$	m/s	0.13		$v_{buoy,average}$	m/s	0.14
Surfaces ST Façade Element				Surfaces ST Collector			
ST Middle Layer Surface	T_{max}	$°C$	39.3	ST Thermal Insulation Surface	T_{max}	$°C$	46.6
	$T_{average}$	$°C$	33.9		$T_{average}$	$°C$	39.9
ST Exterior Glass Surface	T_{max}	$°C$	46.6	ST Absorber Surface	T_{max}	$°C$	88.4
	$T_{average}$	$°C$	39.9				
Volumes ST Façade Element				Volumes ST Collector			
ST Exterior Glass Volume	T_{max}	$°C$	62.1	ST Absorber Volume	T_{max}	$°C$	88.4
	$T_{average}$	$°C$	47.1		$T_{average}$	$°C$	84.7
ST Interior Aluminium Panel	T_{max}	$°C$	33.6	ST Collector Air Volume	$v_{buoy,max}$	m/s	0.20
	$T_{average}$	$°C$	29.4		$v_{buoy,average}$	m/s	0.00
ST Exterior Aluminium Panel	T_{max}	$°C$	37.8	ST Collector Air Volume	$v_{buoy,max}$	m/s	0.15
	$T_{average}$	$°C$	32.2		$v_{buoy,average}$	m/s	0.00
ST Cavity Air Volume	T_{max}	$°C$	40.9	ST Thermal Insulation Volume	T_{max}	$°C$	82.4
	$T_{average}$	$°C$	30.3		$T_{average}$	$°C$	57.8
ST Cavity Air Volume	$v_{abs,max}$	m/s	0.77				
	$v_{abs,average}$	m/s	0.19				
ST Cavity Air Volume	$v_{buoy,max}$	m/s	0.57				
	$v_{buoy,average}$	m/s	0.17				

In all three façade elements, at the cavity´s bottom (y = -1.5 m; z = 0.0 m), a region of low air temperature can be observed close to the interior surface. This low temperature region indicates the influence of inflowing air from the external environment. In the velocity profile diagram, a peak of high velocity is displayed in this region. At this position, the air temperatures inside the cavity of the TR and the PV façade elements are close together. Looking into x-length direction towards the exterior glass/PV module, the temperature stays constant after the peak of lower air velocity. The air temperature inside the ST façade element's cavity increases slightly towards the solar thermal collector´s rear surface. While the air flows upwards in the TR and PV façade´s cavities, a small region with downwards streaming air occurs in the cavity of the ST façade, close to the solar thermal collector´s rear surface. The buoyancy velocity diagrams also show the air velocity profiles inside the solar thermal collector. The

air flows upwards behind the copper absorber, and streams downwards between absorber and the exterior glass of the collector.
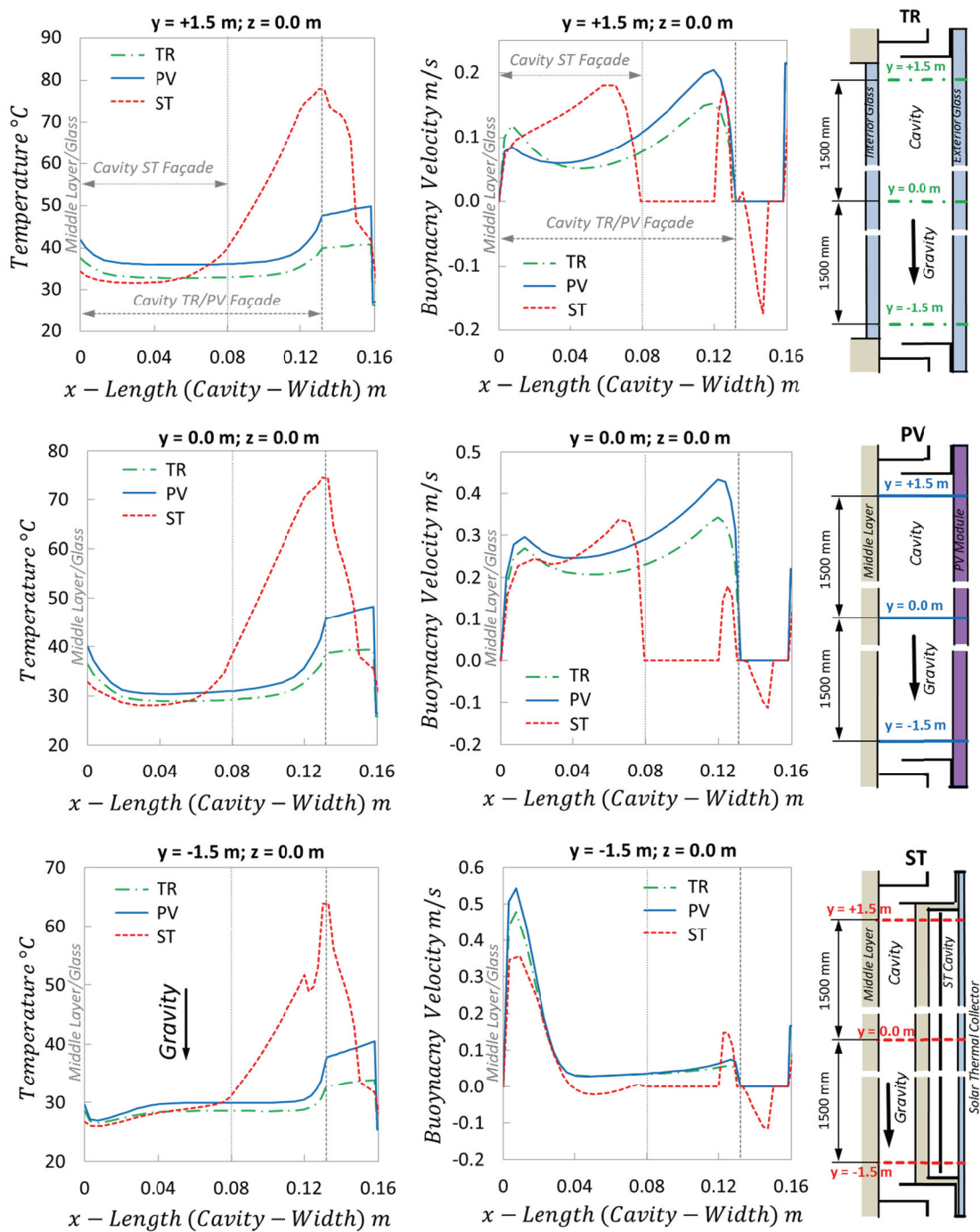
Figure 4-18: Temperature and Velocity Profiles across the Cavity Width (x-Length) at Different Heights (y-Lengths) of the Façade Element, for the TR Façade Element (Green Dotted Line), PV Façade Element (Blue Solid Line) and the ST Façade Element (Red Dashed Line)

In the middle of the cavity's height (y = 0.0 m; z = 0.0 m) the air temperature has increased in all three façade elements' cavities. The air temperature inside the PV façade is slightly higher than in the TR façade, and their profiles look similar. Due to the transparent exterior glass of the TR façade, the solar radiation that infiltrates the façade heats the interior glass surface. At this cavity height, two peaks of velocity can be seen: both a lower peak close to the interior surface and a higher peak close to the façade's exterior layer (glass, PV module and ST collector) are displayed where the heated air streams upwards. Again, the highest velocities occur in the cavity of the PV façade. While the velocity in the TR façade's cavity is still higher close to the interior surface, it is almost the same value close to the rear surface of the exterior layer.
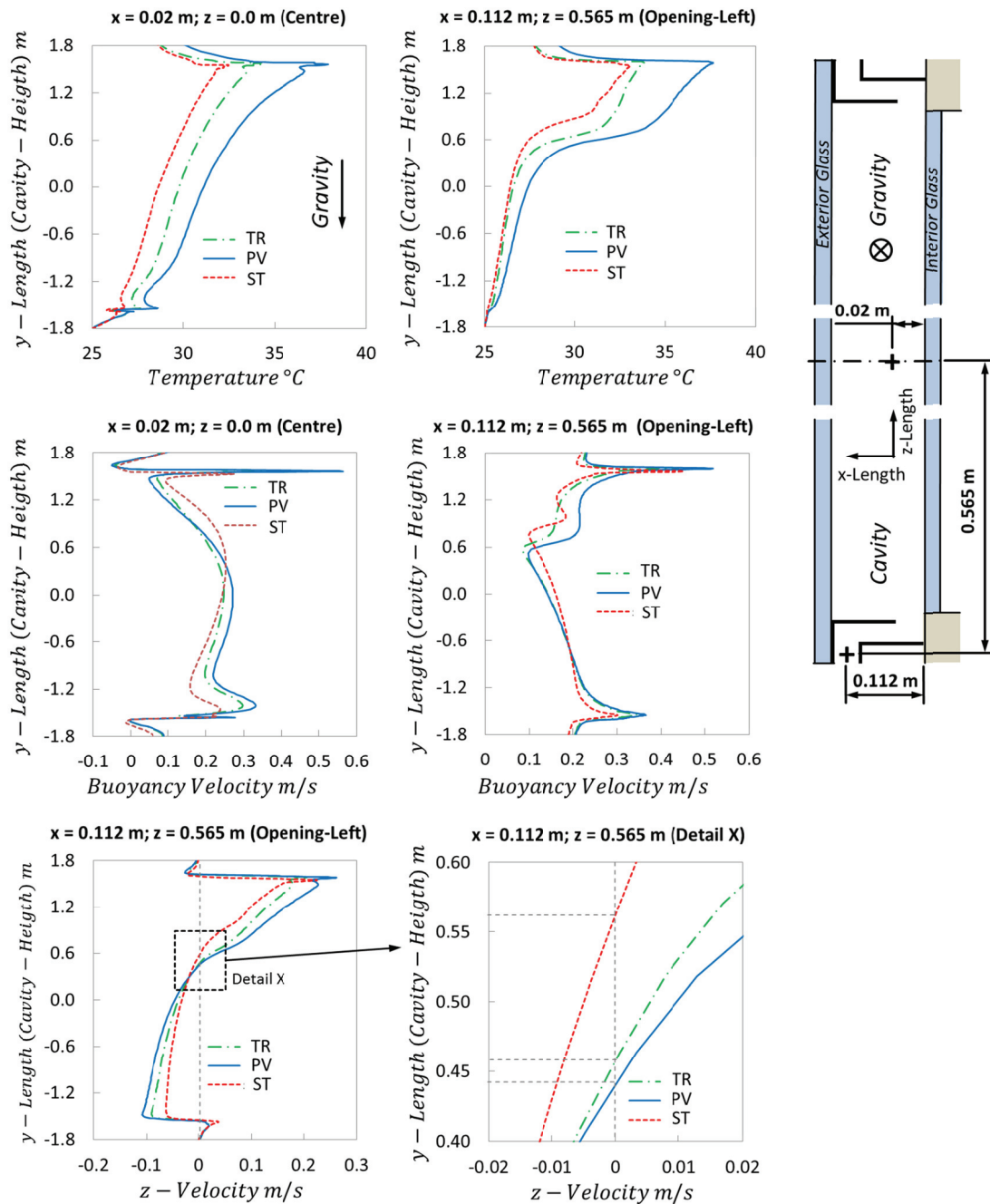
Figure 4-19: Temperature and Velocity Profiles along the Façade Element's Height (y-Length) at Two Different Positions inside the Cavity, for the TR Façade Element (Green Dotted Line), the PV Façade Element (Blue Solid Line) and the ST Façade Element (Red Dashed Line)

The air temperature inside the PV façade´s cavity is again highest at the top region (y = +1.5 m; z = 0.0 m). The air temperature profiles look similar to the profiles at the middle of the cavity´s height, although they are generally higher at the top region. At this cavity height, the exterior glass surface temperature is just a bit higher than the interior glass surface. The air velocity close to the interior glass is now higher in the TR façade´s cavity compared to the PV façade, due to the influence of solar radiation. In the ST façade´s cavity, the two velocity peaks are merged. At this cavity height, the air velocity inside the ST façade is higher than that inside the TR façade, and slightly lower than the air velocity inside the PV façade.

Figure 4-19 shows the temperature and buoyancy velocity profiles along the cavity´s height (y-length) at the middle of the cavity (z = 0.0 m), 20 mm away from the interior wall (glass) and close to the left ventilation opening. The first two diagrams in this figure show how the cavity air temperature deviates between the three façade elements along the cavities' heights. In the next two diagrams, the buoyancy velocities are compared; the last diagram displays the air entering and leaving the left ventilation

openings (z-velocity component). The flow direction at the side openings is reversed in the region 0.4 to 0.6 m above the middle of the cavities' heights. Generally, it seems that the higher the temperature inside the cavity is, the earlier the direction is reversed.

4.2.7 Comparison of Closed and Ventilated Facades

Additionally, a comparison of the three façade elements with open and closed ventilation openings was performed. The result of this comparison is shown for the temperature profiles along the cavity's height (y-length) in the diagrams in Figure 4-20. These diagrams show that the air temperature was clearly higher inside all three types of facades when ventilation was prevented. Furthermore, at the centre of the cavity, the air temperature was indeed higher than at the façade's side walls. The maximum temperature for the ventilated TR façade was 32.5 °C, while without ventilation, it was about 53 °C. The maximum air temperature was about 94.7 °C for the PV façade with closed ventilation openings, while it was 38.6 °C when ventilation was enabled. For the ventilated ST façade, the maximum air temperature was 34.2 °C, and 62.5 °C when the ventilation openings were closed.
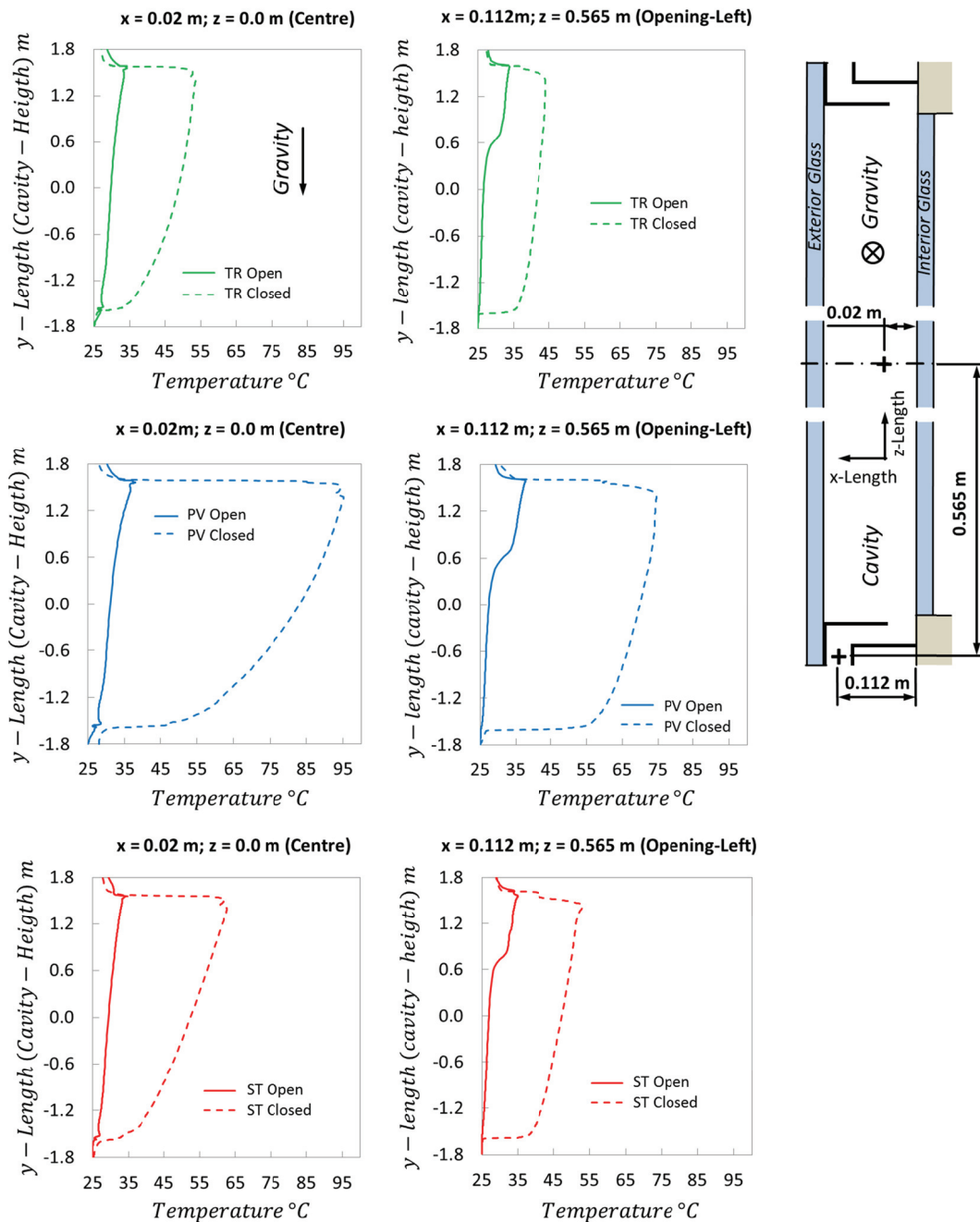
Figure 4-20: Temperature Profiles along the Façade Element's Height (y-Length) at Two Different Positions inside the Cavity to compare Closed and Ventilated Façade Elements (TR, PV and ST)

4.3 Numerical Model Development of a Solar Honeycomb (SHC) Façade Element with Integrated PV Cells[7]

4.3.1 The Ventilated SHC Façade

The thermal protection of buildings is an issue of increasing interest due to the need to improve buildings' efficiency and reduce their overall energy demand. Correspondingly, many research studies have been carried out in the field of thermal insulation for facades, and this abundance has resulted in the development of a great variety of insulation materials and applications [71]. In many of these applications, air is used as an insulation material because stagnant air has very good thermal resistance. In their paper, Kessentini et al. [72] show a detailed analysis of the three-dimensional total heat transfer effects through a transparent honeycomb.

A special, ventilated SHC façade, using an opaque honeycomb as an additional layer of thermal insulation (Figure 4-21, image 1) and referred to as "GAP-skin', was designed in order to improve the thermal resistance of the building's facades. This façade element was developed shortly before the end of the 20th century, by the company Gap[3] solutions GmbH [73], and was successfully introduced to the market in 2004. All reference projects can be found on the associated homepage of the GAP[3] solution company [69]. The building component layers of this façade element are shown in Figure 4-21, Image 2. The main part of this façade element is a SHC made of cellulose. An exterior glass panel was installed to protect the honeycomb from weathering. Between the exterior glass panel and the honeycomb, a ventilation channel prevents condensation as well as excessive air temperatures. The timbered wall and thermal insulation behind the SHC improve the thermal protection and make it easy to attach to the masonry wall.
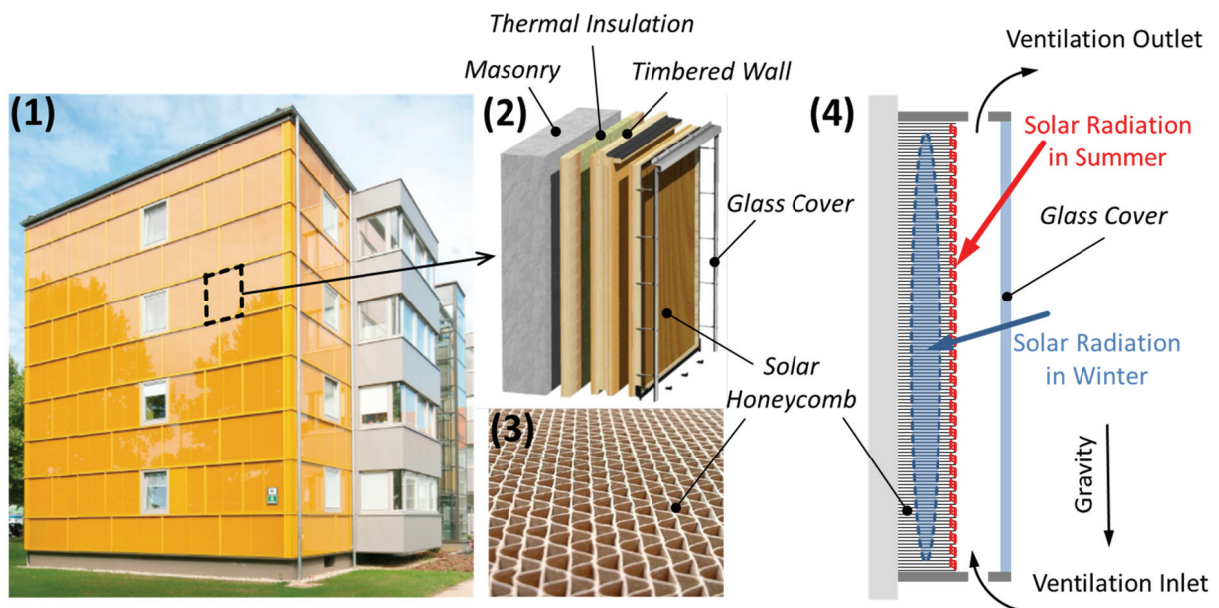
Figure 4-21: (1) Building with a Solar Honeycomb Façade, situated in Dieselweg in Graz, Austria; (2) Structure of a Solar Honeycomb Façade; (3) Detail of the Cellulose Honeycomb Structure; and (4) Schematic of a Solar Honeycomb Façade Showing its Working Principles

The special structure of the SHC (Figure 4-21, image 3) makes it possible to vary the thermal behaviour according to the inclination angle of the incoming solar radiation. The schematic (Image 4) in Figure 4-21 shows the heating characteristics of the honeycomb for different solar radiation inclination angles. Due to the small inclination angles in winter, solar radiation is able to penetrate the honeycomb and forms a heated zone that reduces the interior room's heat loss through the façade. In summer, the steeper angle of the sun's rays prevents the radiation from penetrating the honeycomb. The sun is therefore only able to heat the honeycomb's surface.

---

7. Parts of this section have already been published in [20].

4.3.2 Integration of PV Cells

Additional energy can be provided for the building via the integration of PV cells on the exterior glass of the façade element. However, every PV cell attached casts a shadow on the SHC and leads to a reduction in the solar heating effects. This study was conducted to determine the thermal behaviour and flow characteristics of the SHC with and without integrated PV cells. Another objective of the current investigation was to find the ideal number and configuration of PV cells for such a façade element, where the solar passive functionality of the SHC is still given.

Figure 4-22 shows some of the PV configurations that were chosen for a comprehensive investigation of the thermal behaviour and flow characteristics, carried out by means of numerical simulations and laboratory experiments.
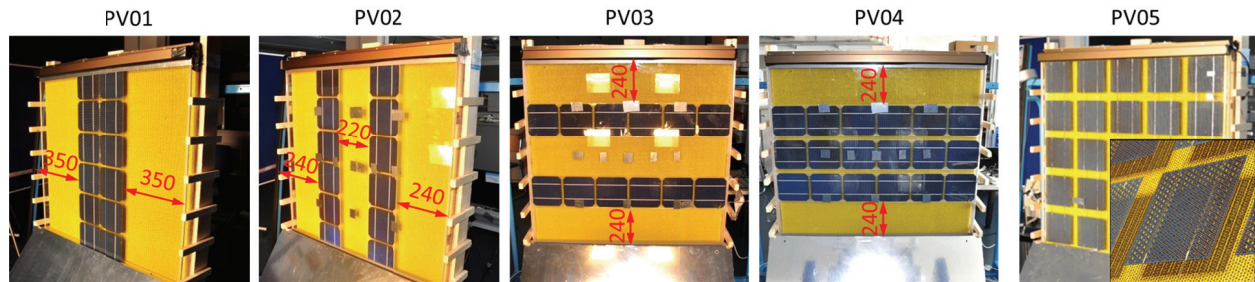
Figure 4-22: Images of the Solar Honeycomb Façade Experimental Build-Up with the Four PV Cell Configurations Tested

In the first PV configuration (PV01), two adjacent vertical rows of monocrystalline PV cells of 150 x 150 mm were installed, with six cells per row. One PV cell had an electrical power of approximately 4.08 W. The second configuration (PV02) was similar to PV01, but with a gap (of 220 mm) between the two vertical rows of PV cells. For the third configuration (PV03), there were two horizontal rows with six PV cells in each row. The upper row was placed 240 mm below the top edge of the ESG glass, while the lower row was placed 240 mm above the bottom edge of the ESG glass. In configuration PV04, one PV cell row was added between the upper and the lower rows of configuration PV03. Configuration PV05 saw the ESG glass replaced by a double layer glass module with 25 semi-transparent PV cells (ERTEX Solar type 1). The module had a transparency of 44.3% and one cell with an electrical power of approximately 2.0 W. The PV cell size was 156 x 156 mm. The sixth configuration (PV06) had the same configuration of PV cells as configuration PV05, but the semi-transparent PV cells were replaced by monocrystalline PV cells of 156 x 156 mm and an electrical power of approximately 4.0 W. In the last configuration (PV07), an opaque PV module covered the SHC façade element. The PV module contained 36 PV cells of the same size and electrical power as configuration PV06.

4.3.3 Laboratory Measurements

In order to verify the CFD simulations, this study also used data from a laboratory set-up with a solar simulator to collect the measured temperatures and air velocities at constant incident radiation.

The experimental set-up for the CFD validation is described in this chapter. Figure 4-23 shows a photo of this set-up, which consists of a base with the SHC façade element and a solar simulator placed in front of the façade. The solar simulator lamp array emits radiation in the spectrum of solar radiation (0.3 to 2.5 μm), as well as in the spectrum of thermal radiation (> 2.5 μm). A cross flow fan, positioned next to the façade element, reduces the effect of the lamp arrays thermal radiation to a minimum, and, as a result, can simulate the incoming radiation from the sun. This made it possible to reduce the average surface temperature from approximately 57 to 35 °C.

The test façade element measures 1 x 1 m and is composed of a timber wall, a cellulose honeycomb, and an ESG glass pane (Figure 4-23, Figure 4-24). A ventilation cavity with a width (x-length) of 29 mm is placed between the honeycomb and the ESG glass. The ventilation cavity is covered with ESG glass at the sides. The ventilation inlet and outlet consists of timber components with a perforated steel plate. The configurations PV01 - PV05 were performed in the laboratory experiments. In configuration PV05, the semi-transparent PV module was connected to an electrical load, where the electrical power was measured.
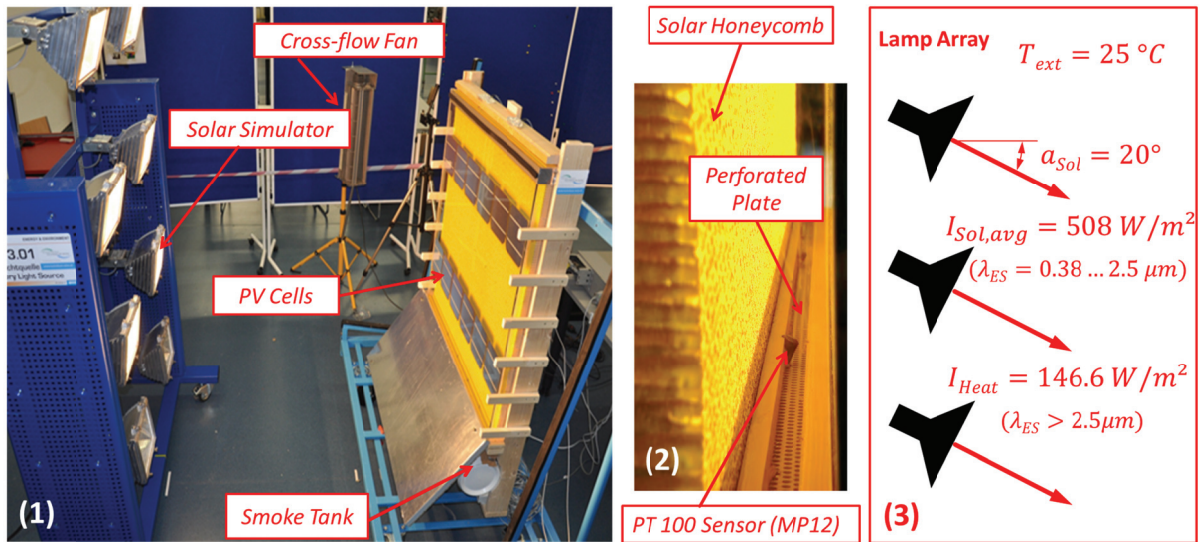
Figure 4-23: (1) Photo of the Experimental Set Up of the Solar Honeycomb Façade; (2) Detail of the Bottom of the Façade Element, showing the Inlet and the Honeycomb Structure; (3) Solar Radiation Angle and Intensity of the Lamp Array

Figure 4-24 shows the position of each sensor installed in the experimental set-up. These sensors were used to measure air temperatures and velocities. The four sensors at the inlet and outlet of the ventilation cavity (MP12-15) are Pt 100 elements, which were calibrated according to DIN EN 60751. The data from the remaining measurement positions (MP1-11) was captured by a hot sphere anemometer (TESTO 480). This sensor monitored the air temperature and velocity at the corresponding measurement positions, all while maintaining steady state conditions in the experiments. During the measurements, the hot sphere anemometer´s centre was situated 10 mm from the honeycomb. The hot sphere anemometer has a measurement accuracy of 8% of the reference value. The sensor sphere has a diameter of 3 mm and was brought into the ventilation cavity with the help of a telescopic arm through the sidewalls of the façade element (Figure 4-25).

Furthermore, the exterior glass surface temperature was measured at the measurement positions MP1-11. A contact sensor was used in combination with a portable measuring instrument (TESTO 435).
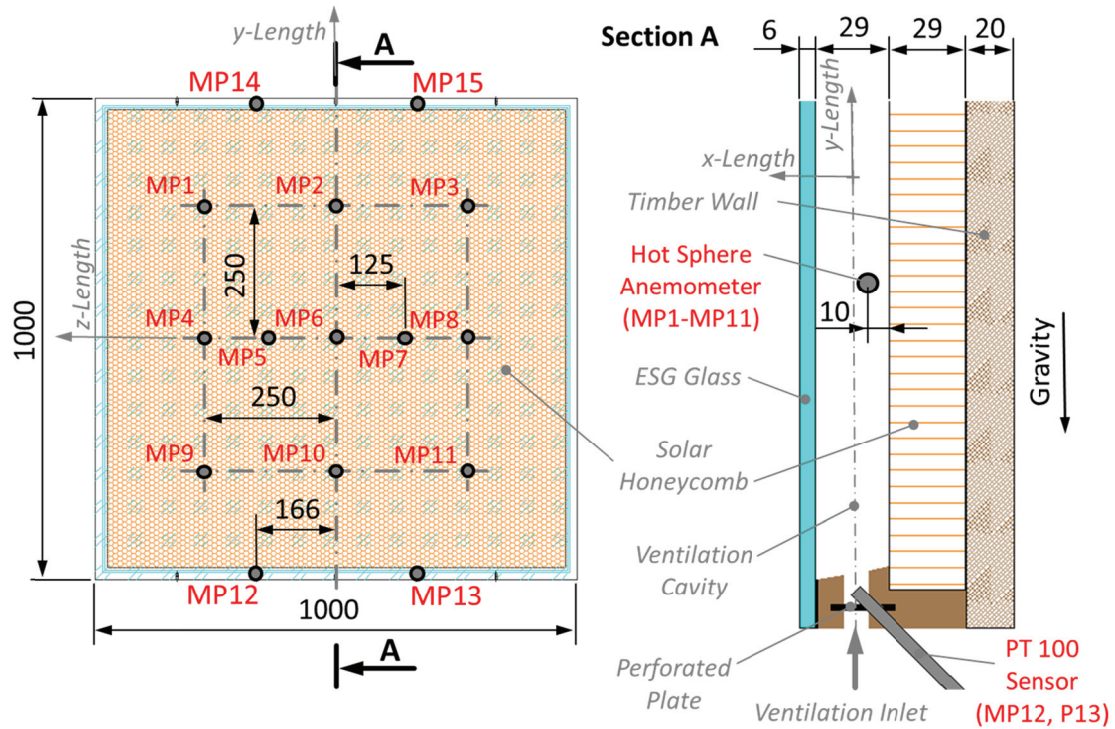
Figure 4-24: Schematic of the Solar Honeycomb Façade Element, including the Measurement Positions
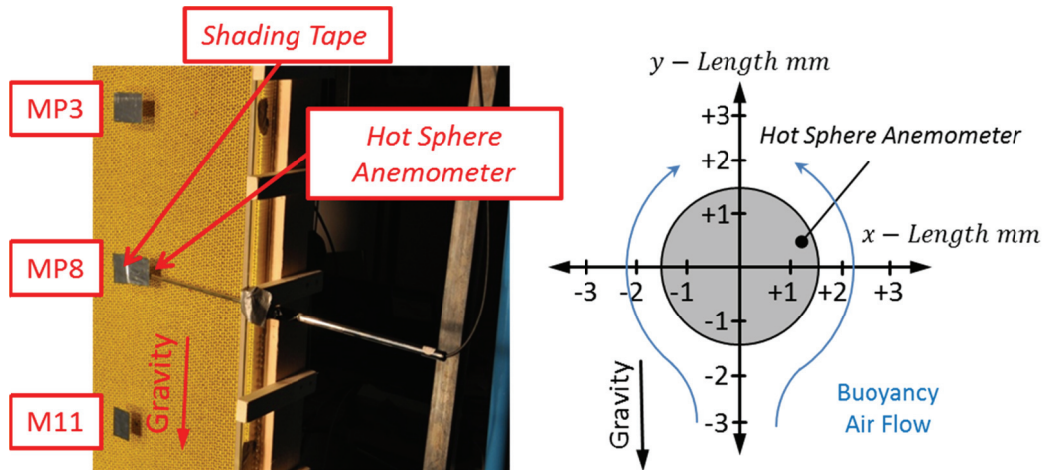
Figure 4-25: Measurement Principle of the Air Temperature and Velocity Inside the Ventilation Cavity (Left); Schematic of the Hot Sphere Anemometer (Right)

4.3.4 CFD Model Design

The numerical models and simulations were once again created using a software package from ANSYS [7]. The two- and three-dimensional geometries and meshes, which contain only hexahedral cells, were built with the ANSYS DesignModeler and ANSYS ICEM CFD. The simulations were performed with ANSYS Fluent.

For the two-dimensional simulation, a quad dominating mesh was created using the paving method. The mesh contains approximately 0.2 million cells, wherein the skewness did not exceed a value of 0.38. The average skewness of 0.012 indicates that the mesh consists mainly of less skewed quad cells (shown in Figure 4-26).
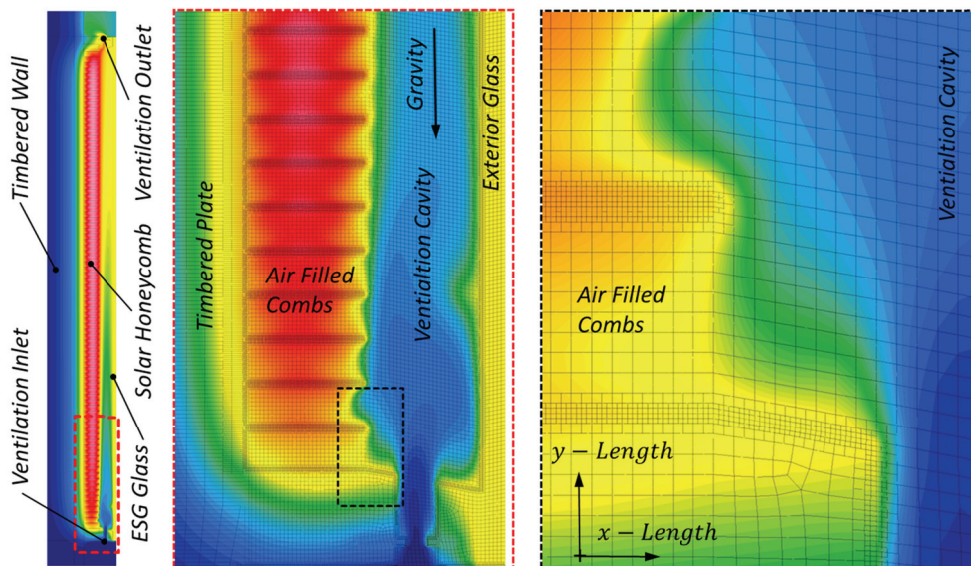
Figure 4-26: Temperature Contour and CFD Mesh for the Bottom Region of the SHC Façade from the Two-dimensional CFD Simulation

The three-dimensional CFD models varied between 0.6 and 1.1 million hexahedral cells and were created using the sweeping meshing method. The base model contained a timber wall, the SHC, the timbered solid zones with the inlet and the outlets of the ventilation cavity, the ESG glass, and the fluid ventilation cavity zone (as visible in the schematic in Figure 4-24). As an example, Figure 4-27 shows the meshes for the simulation of the SHC façade scenario without PV cells as well as with PV cell configuration PV03. Using the sweeping meshing method, a minimum orthogonal quality of 0.94 was achieved, and the maximum skewness amounted to 0.22. These values indicate a very good mesh quality, and therefore, fast convergence and very low residuals (below 10E-5 for velocities and radiation and below 10E-8 for energy) were achieved in the CFD simulation.
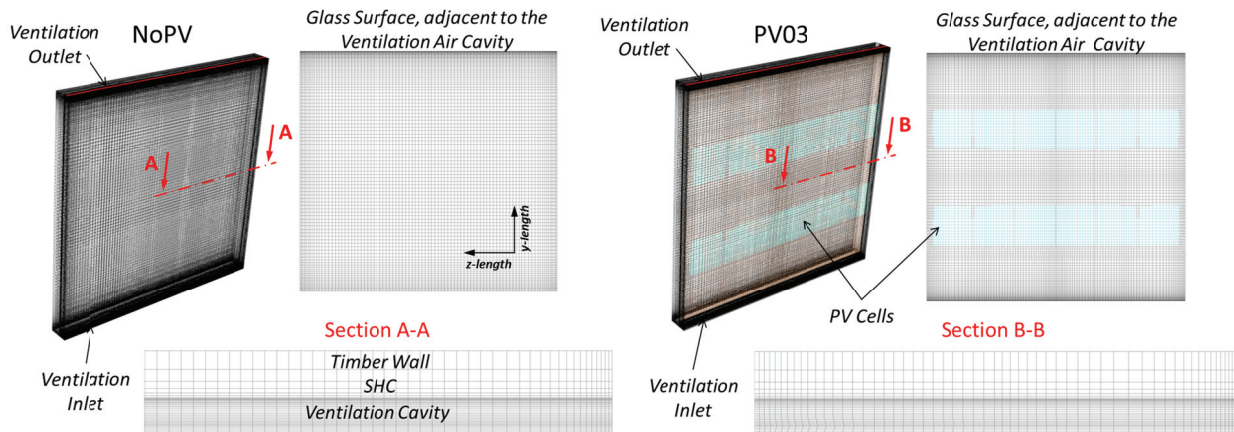
Figure 4-27: CFD Mesh for SHC Façade with PV Configurations NoPV and PV03.

While the mesh used for the calculations without attached PV cells contains approximately 0.6 million cells, the mesh for the calculation of the PV cell configuration PV03 has slightly more than 0.8 million cells. The higher number of cells in the mesh of PV03 was mainly caused by the refinement around the PV cells. The timbered parts of the CFD model are specified with a density of 1000 kg/m³, a specific heat of 2000 J/kgK, and a thermal conductivity of 0.15 W/mK, while the ESG glass has a density of 2500 kg/m³, a specific heat of 720 J/kgK, and a thermal conductivity of 1.0 W/mK. The glass has a transmissivity of approximately 0.9. The material properties are summarized in Table 4-7.

For the CFD models with integrated PV cells, the surface between the ESG glass and the ventilation cavity was split into sections of glass and sections that were defined as thin film PV cells made of silicon. This section's fractions of glass and silicon in the CFD model depended on the PV cell configurations.

The silicon used had a density of 2328 kg/m³, a specific heat of 741 J/kgK, a thermal conductivity of 150 W/mK, and a solar radiation absorption rate of approximately 0.9. In some of the following simulations, the temperature reduction of the cell due to the conversion of electrical energy was also considered with this PV-cell model. Chapter 4.3.12 describes how the simulation considers this temperature reduction effect.

Perforated steel plates were installed at the inlet and outlet of the facades air cavity. To consider the flow resistance of these plates, a porous zone (with an assumed porosity of 0.5) was created at the corresponding positions in (only the three-dimensional) CFD models. The steel used had a density of 8030 kg/m³, a specific heat of 502 J/kgK as well as a thermal conductivity of 16.3 W/mK.

All simulations (two- and three-dimensional) were performed under "Steady State" conditions, according to the laboratory boundary conditions. Solution methods, discretization, and solution controls are summarized in Table 4-6. The "Pressure-Based" solver and the "Absolute" velocity formulation were used. To reproduce the physics of the natural convective flows inside the ventilation cavity, the energy balance, the "RKE" turbulence model with "Enhanced Wall Treatment" and "Full Buoyancy Effects", and the gravitational acceleration were activated for the simulations. To consider the effect of the thermal radiation exchange between the surfaces, the DO radiation model was activated in all simulations. For angular discretization, the "Theta Divisions", the "Phi Divisions", the "Theta Pixels" and the "Phi Pixels" were set to a value of 6. The DO radiation model was solved every 10th iteration in the simulation procedure.

Additionally, the simulation results from the selected RKE model were compared to other available turbulence models. Because the "Enhanced Wall Treatment" was used for the heat transfer and the airflow close to the walls, a very low y^+ value was required. The y^+ value did not exceed a value of 1.5 in simulations with the meshes used. Furthermore, this turbulence model comparison contained a laminar flow model and a measurement point which was set as reference for the comparison in Figure 4-28.

The results of the SKE, RKE, and RNG turbulence models showed similar temperature and velocity profiles, and matched very well with the measured values. The KLW turbulence model overestimated both the temperature and velocities for this solar honeycomb façade application. For SKW turbulence, the temperature profile did match, whereas the velocities were higher than the RNG turbulence model.

The results of the SST turbulence model contained lower temperatures, but higher buoyancy velocities in this comparison. The lowest temperatures were observed in the laminar flow model. In the buoyancy velocity profile comparison in Figure 4-28, it was possible to see an oscillation of the computed air velocity for the laminar flow model. From this comparison, it was possible to conclude that the RNG turbulence approach is suitable for the evaluation of PV cell configurations.
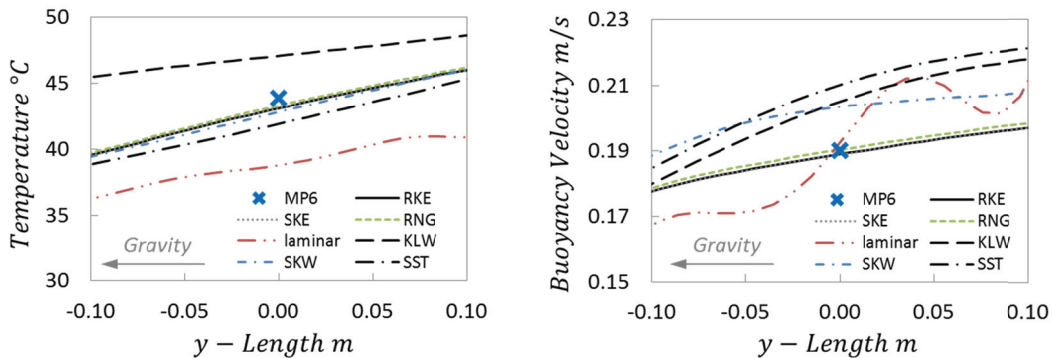
Figure 4-28: Comparison of Temperature and Buoyancy Velocity Profiles of Different Turbulence Models in Reference to the Measured Data of the Experiment

In the solution methods, the "SIMPLE" scheme was used for the pressure-velocity coupling. The spatial discretizations used were the "Least Square Cell Based" method for the gradient, and the "Body Forced Weighted" method for pressure. Further discretizations were the "Second Order Upwind" scheme for the momentum, the turbulent kinetic energy and dissipation, the energy and the discrete ordinates. In the Solution Controls, the Under-Relaxation Factors (URF) were set to 0.7 for pressure, 0.3 for momentum, and 0.8 for the turbulent kinetic energy and dissipation rate. The other URF were set to 1.

Table 4-6: Numerical Solution Methods, Discretization Parameter and Under-Relaxation Factors.

Solution Methods	Pressure-velocity coupling	Gradients	Pressure	Momentum	Turbulent Kinetic Energy	Turbulent Dissipation Rate	Energy	Discrete Ordinates
	SIMPLE-scheme	Least Squares Cell Based	Body Force Weighted	Second Order Upwind	Second Order Upwind	Second Order Upwind	Second Order Upwind	Second Order Upwind
Solution Controls (URF)	Pressure	Density/Turbulent Viscosity	Body Forces	Momentum	Turbulent Kinetic Energy	Turbulent Dissipation Rate	Energy	Discrete Ordinates
	0.7	1	1	0.3	0.8	0.8	1	1

Table 4-7: Material Properties.

	Density	Specific Heat Capacity	Thermal Conductivity	Solar Radiation Absorptivity	Solar Radiation Transmissivity
	kg/m^3	$J/(kg \cdot K)$	$W/(m \cdot K)$	–	–
Timbered Parts	1000	2000	0.15	-	-
ESG-Glass	2500	720	1.0	0.05	0.9
Steel	8030	502	16.3	-	-
Silicon	2328	741	150	0.9	-
SHC	204	2495	0.05	-	-

4.3.5 CFD Mesh Assessment

Before a comprehensive analysis of the thermal behaviour of the SHC façade element, the temperatures and air velocities resulting from the use of the three different meshes were compared. Basically, both a coarse and a fine mesh were prepared for this assessment. In both meshes, the y^+ value was below 1.0 without any further mesh refinements inside the ventilation cavity. In the coarse mesh, the fluid cells adjacent to the walls of the solid zones were further refined. Finally, there were three meshes involved in the mesh assessment: a coarse mesh, with 0.66 million cells, an adapted coarse mesh, which contains 1.63 million cells, and a fine mesh, with 5.28 million cells. In the mesh assessment, the same boundary conditions were used as in the laboratory experiments (Chapter 4.3.3). Figure 4-29 presents the

comparison of the temperature contours of the SHC surface while using the three above mentioned meshes. The simulated temperature contours of all three meshes look very similar.
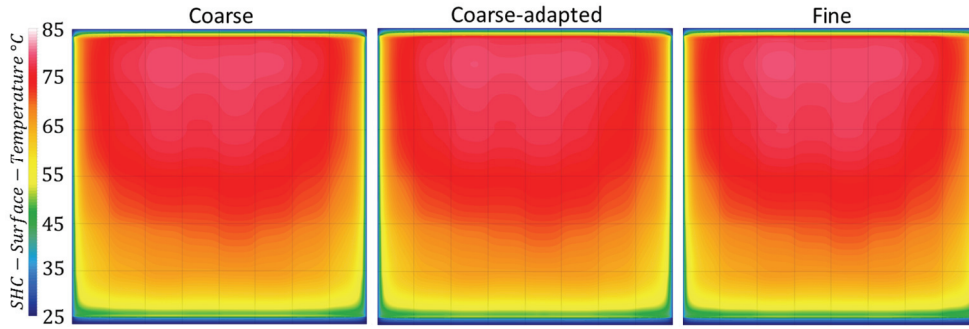
Figure 4-29: Comparison of the Temperature Contours at the SHC Surface using the Coarse (Left), Adapted Coarse (Middle), and Fine (Right) CFD Meshes

In the next two figures (Figure 4-30 and Figure 4-31), the temperature and air velocity profiles for the three sections through the SHC façade´s cavity width (x-length) and two sections along the façade element´s height (y-length) are presented. The positions of the x-length profiles (MP2, MP6 and MP10) are indicated in the schematic of the SHC façade element presented in Figure 4-24. The profiles along the y-length were positioned directly at the SHC surface, adjacent to the ventilation cavity, as well as 10 mm from the SHC in the ventilation cavity, where the hot sphere anemometer was also positioned during the measurements.
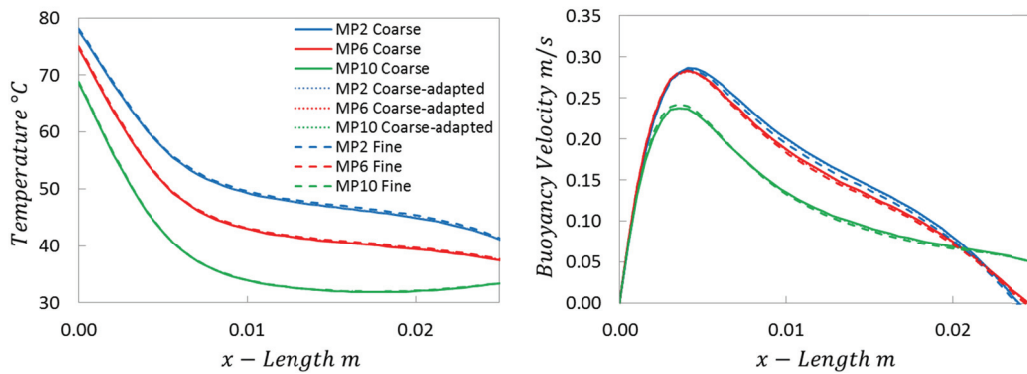
Figure 4-30: Comparison of the x-Length Temperature and Air Velocity Profiles of the Different Meshes

The profiles from the simulation results did not show any noticeable deviations, and it is possible to conclude that all three meshes are perfectly qualified for further analysis. Only in the air velocity profile along the façade´s height were very small deviations between the fine and coarse meshes identified.
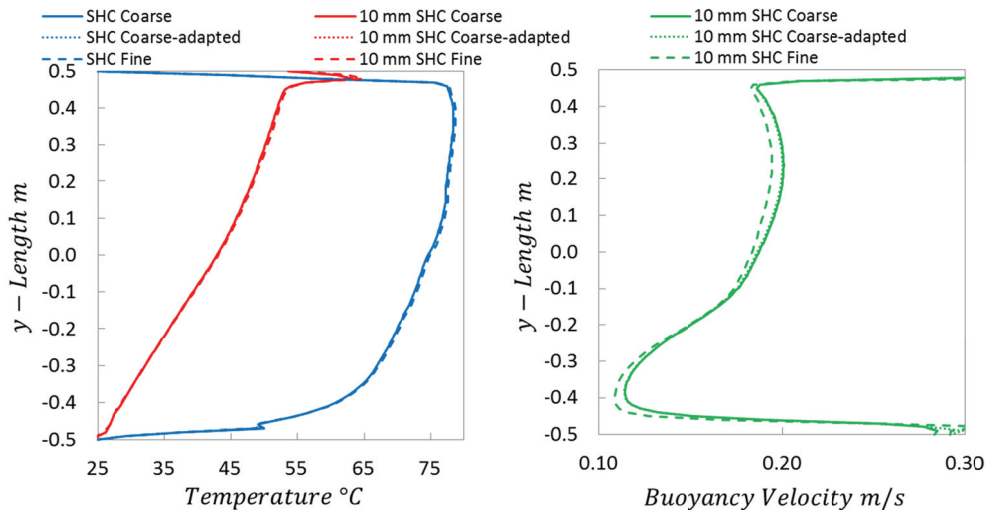
Figure 4-31: Comparison of the y-Length Temperature and Air Velocity Profiles with Different Meshes

4.3.6   Preliminary Two-dimensional Simulations

The integration of different PV cell configurations in the SHC façade element models is only possible with a three-dimensional CFD model, with the exception of the case without integrated PV cells. For this reason, a preliminary two-dimensional CFD model was developed to obtain an initial overview of the thermal effects and flow behaviour. Figure 4-32 shows the temperature contours and the air flow vectors at the inlet, the cavity centre, and the outlet region of the ventilation cavity from the preliminary two-dimensional CFD model. In the two-dimensional simulation, the SHC façade element was attached to a masonry brick wall. The exterior temperature of 20 °C, solar irradiation of 500 W/m² at an inclination angle of 20°, and a solar absorption rate (abs_{Sol}) of 0.7 of the SHC were assumed for simulation.

Due to the heated SHC, there was natural convective flow inside the ventilation cavity. The calculated Rayleigh number (Ra) was at a value of 1.38E+09. This indicates that the assumption of a turbulent flow model for the ventilation cavity was appropriate. It was observed that the air flow velocities in the chambers of the SHC were very low compared to the buoyancy-driven flows in front of the honeycomb (highlighted in details A, B, and C in Figure 4-32).

Furthermore, air circulation was observed at the entrance to the façade´s cavity. At the top of the façade, a distinct circulation was observed. This circulation occurred in the form of a thin layer, close to the ESG glass, from the centre to the top of the façade´s height (y-length).
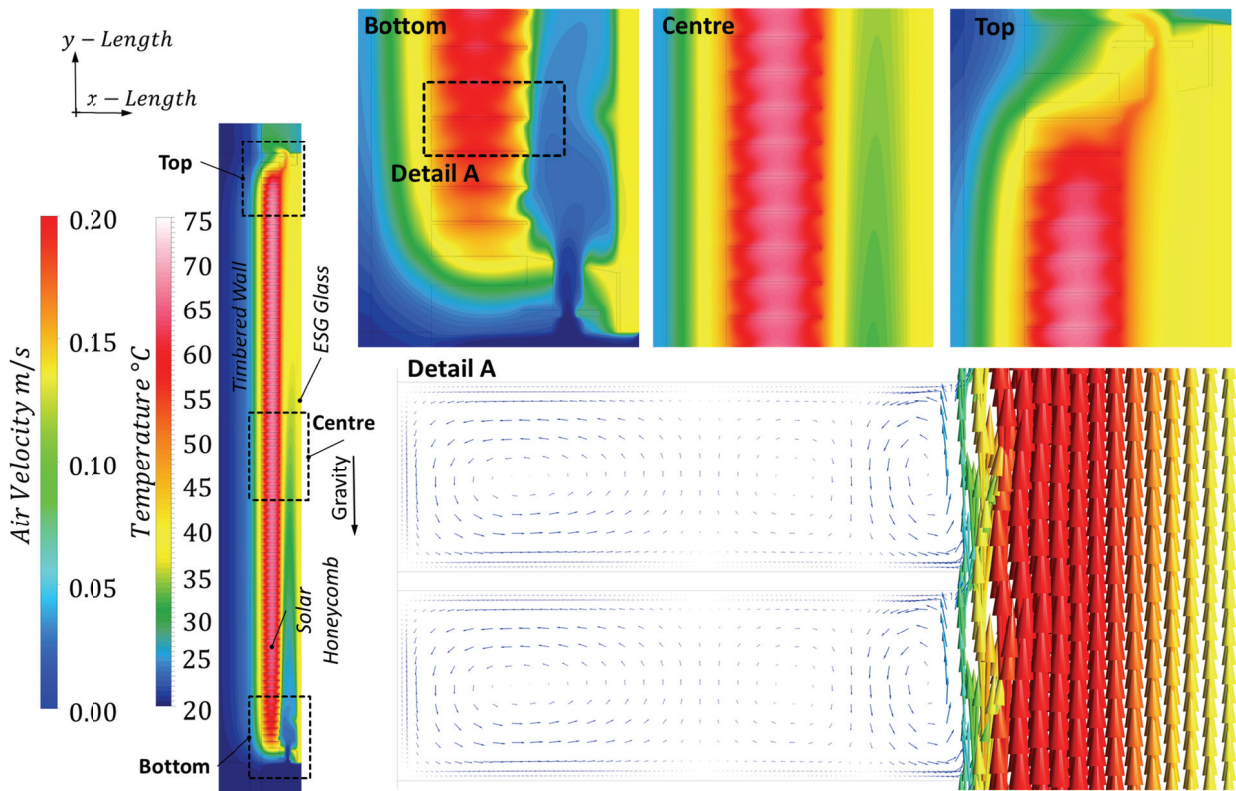
Figure 4-32: Temperature Contours and Air Flow Vectors from Two-dimensional CFD Simulations Illustrated for the Bottom, Centre, and Top Regions of the SHC Façade Element

In a further preliminary analysis using the two-dimensional CFD model, the influence of different solar angles on the thermal behaviour was observed, in addition to the impact of different values for the solar radiation absorptivity (abs_{Sol}), and the distribution of the radiation ($diff_{Sol}$) reflected from the SHC surface was observed. It is only possible to consider the radiation for each cell in the CFD model using the DO radiation model. The resulting solar irradiation distributions and heating characteristics are shown in the temperature contours in Figure 4-33. The figure shows the results for a zoomed-in region in the centre of the SHC façade's height. In the first scenario (1), a solar angle α_{Sol} of 0°, an absorptivity ab Sol of 0.7, and a radiative reflection distribution $diff_{Sol}$ of 0.0 were assumed. The $diff_{Sol}$ rate ranges from 0 to 1. For a value of 0, the whole radiation is reflected to only one direction. For a value of 1, the reflected radiation is uniformly distributed in all directions (isotopic). In the second scenario (2), the

solar angle was changed to 20°, relative to scenario (1). This scenario served as the basis scenario of this analysis. In scenario (3), the solar angle was increased to 45° and 65° in scenario (4). While the solar radiation fully penetrates the rear wall of the SHC in scenario (1), only a small fraction of the solar radiation arrives there in scenario (2). In scenario (3), the incoming solar radiation was reflected three times inside the comb, and hardly affected the rear wall. In scenario (4), the solar radiation was used up after four reflections inside the combs and did not even arrive at the rear wall.
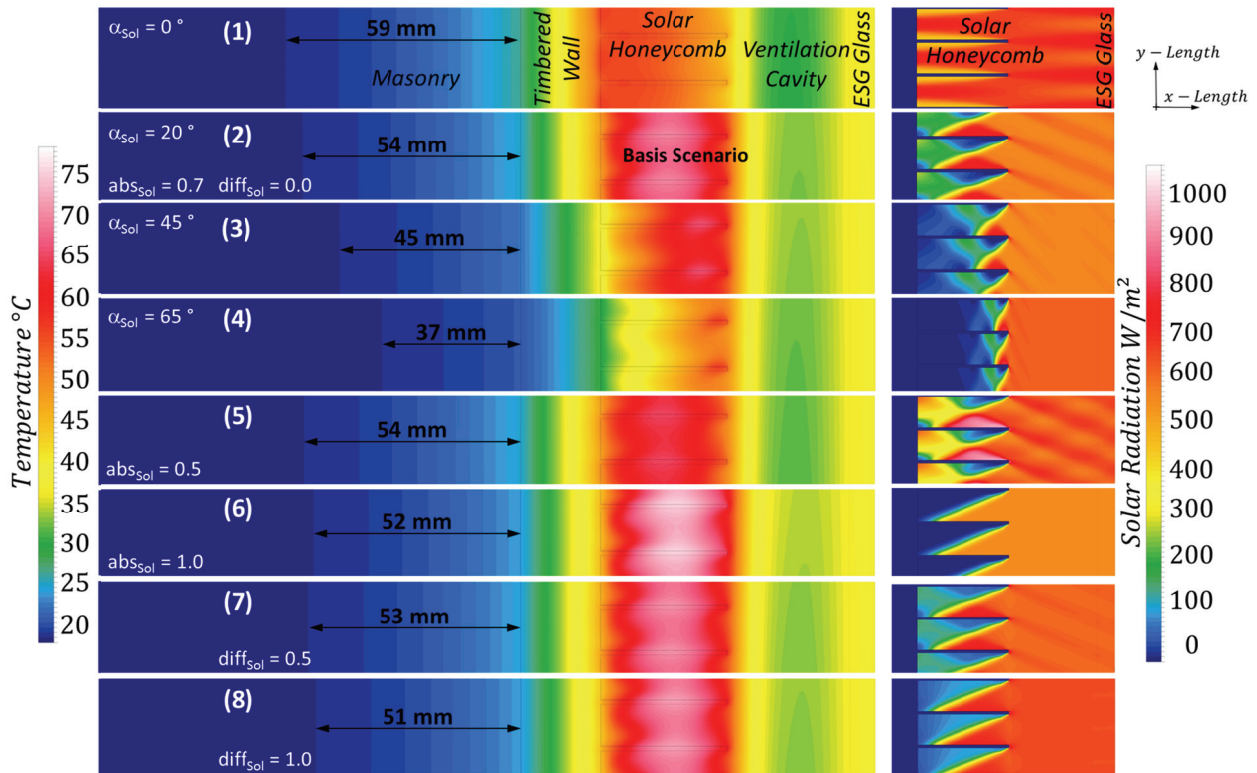
Figure 4-33: Comparison of the Temperature and Solar Irradiation Contours at the Centre of the SHC Façade Element between the Different Scenarios with Varying Absorptivity, Reflective Radiation Distribution, and Solar Angles

In the next four scenarios, the solar angle remained at 20°, but either the abs_{Sol} or the $diff_{Sol}$ were changed. Relative to the basis scenario, the solar absorptivity (abs_{Sol}) was reduced to 0.5 in scenario (5), while it was increased to 1.0 in scenario (6). In scenario (5), more radiation reached the rear wall in comparison to the basis scenario. In scenario (6), all of the incoming radiation was absorbed after the first impingement on the comb surface. In scenarios (7) and (8), the $diff_{Sol}$ values were increased from 0 to 0.5 and 1.0, respectively. In scenario (7), the fraction in direct reflection direction was reduced, and less radiation impinged on the rear wall. In scenario (6), the reflective fraction of solar radiation observed in other scenarios completely disappeared.

In basis scenario (2), the highest temperatures occurred in the middle, inside the SHC´s combs. This higher temperature also had an influence on the timbered wall and the masonry wall. The contours of temperatures higher than 20 °C (heating influence) disappeared approximately 54 mm from the rear of the timbered wall. When the solar radiation did fully arrive at the SHC´s rear wall (1), the highest temperatures also occurred in this region. The heating influence disappeared 59 mm from the timbered wall. At a solar angle of 45° (3), the region of higher temperature moved to the exterior side of the SHC´s combs and lost some intensity compared to the basis scenario. The heating influence reaches 45 mm into the wall. With a further increase of the solar angle to 65° (4), the highest temperatures occurred directly at the transition from the SHC to the ventilation cavity.

Compared to the basis scenario, the temperatures had significantly decreased, and the range of heating influence inside the masonry wall was dramatically reduced to only 37 mm from the timbered wall. Reducing the solar absorptivity from 0.7 to 0.5 (5) led to slightly lower temperatures in the middle inside the SHC combs, whereas the same heating influence was observed to the masonry wall. The maximization of the absorptivity (6) led to higher temperatures inside the combs, and slightly lowered

the heating influence on the masonry. Similar temperatures were observed inside the combs for scenarios (7) and (8) with different $diff_{Sol}$ values. Compared to the basis scenario, the difference in the heating influence on the masonry was marginal.

4.3.7   Enhancement of the Radiation Model

One major challenge of the modelling process was to find a proper method to reproduce the radiative behaviour in the simulations. Ultimately, the DO radiation model was used for this purpose, as mentioned in chapter 4.3.4. The preliminary modelling approach was enhanced by expanding from one to into two radiation wavebands. With this enhancement, the DO model vas able to switch between solar radiation (λ_{ES} = 0.38 - 2.5 μm) and thermal radiation (λ_{ES} > 2.5 mm). Using this approach, it was possible to set the solar radiation in the experiments as a boundary condition in the simulations. In the laboratory experiments, the radiation from the solar simulator was measured with a pyranometer (KIPP & ZONEN CMP 3), which was able to capture radiation within a wavelength of 0.3 and 2.8 μm with deviations of maximal 5% of the measured value. The incident radiation in front of the solar honeycomb façade element was measured at several positions and combined into a radiation matrix that can be seen in Figure 4-34. The values of this radiation matrix were used as radiative boundary in the CFD simulations.
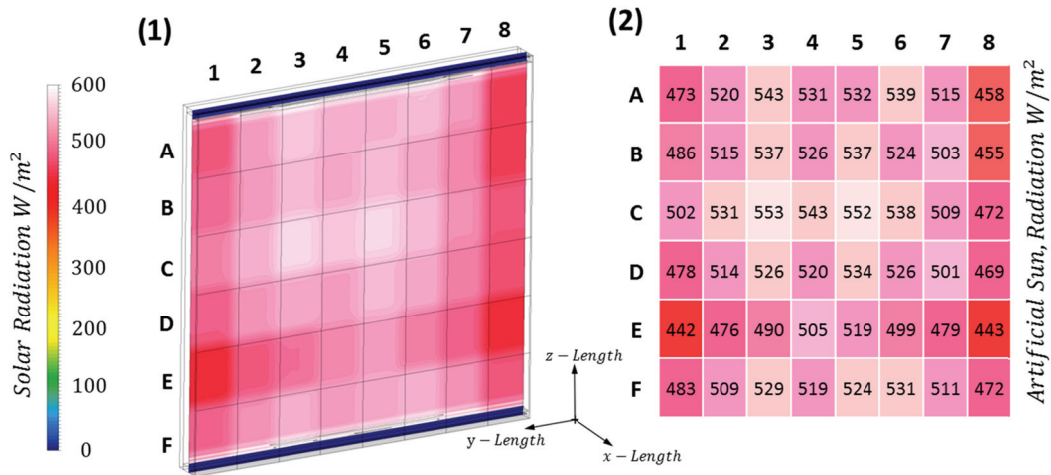
Figure 4-34: (1) Contours of Solar Radiation on the Exterior ESG Glass Surface from the CFD Simulation Case of the Solar Honeycomb Façade without Integrated PV Cells; (2) Measured Radiation Distribution from the Laboratory Experiment

4.3.8   SHC Model

Since the structure of the SHC was too complex to process in detail in the CFD simulations, a simplified model approach was needed. Because the two-dimensional simulation in Chapter 4.3.6 produced SHC combs within which the air velocity was extremely low, the composition of the honeycomb and the air inside the chambers was assumed to be one solid zone. On the one hand, the fully detailed SHC geometry containing all the air chambers could not be designed with the available computing power, and, on the other, this assumption made it possible to dramatically reduce the computation time. The solid composite zone was exposed to the solar radiation and was treated as a transparent material with the ability to absorb solar radiation according to the principle of the SHC presented in Chapter 4.3.1 and shown in Figure 4-21. This was done by means of Equation 4-1 and an absorption coefficient α for the SHC composite. The coefficient has the unit 1/length.

$$I = I_0 \cdot e^{-\alpha \cdot x}$$

Equation 4-1

Because the absorption coefficient α was an unknown parameter, several tests were performed to find a proper value for this parameter. The significant results of these tests are shown as contours of solar radiation in Figure 4-35, and in the form of the resulting temperature contours in Figure 4-36. Because these tests with different absorption coefficients were performed at the same boundary conditions as in

the laboratory experiments, the results of the measurements and the simulations were compared, and therefore, a proper value for the absorption coefficient was assumed.

The first case (2D) shows the results of the previously developed two-dimensional CFD model, calculated at the same boundary conditions as the three-dimensional simulations. The exterior temperature around the whole SHC façade was assumed to be 25 °C in the SHC model tests. While the previously determined radiation matrix (shown in Figure 4-34) was used as solar radiation boundary, the matrix's average value of 508 W/m² was used as boundary condition in the two-dimensional CFD simulation. Because the temperatures simulated inside the ventilation cavity were lower than the measured values, it was concluded that there is a heating characteristic that was not possible to capture using the two-dimensional CFD models.
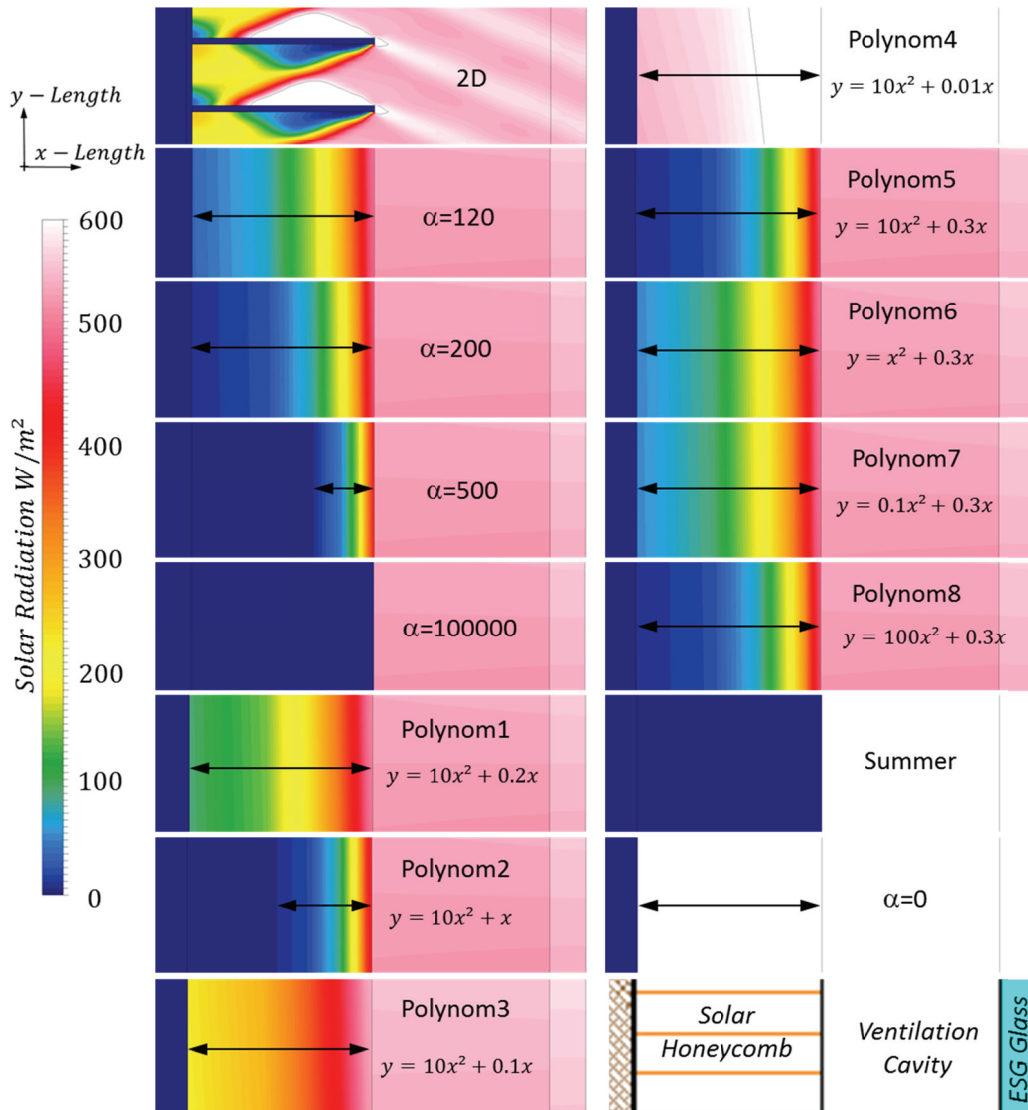
Figure 4-35: Comparison of the Solar Radiation Contours inside the Solar Honeycomb Façade Element at Different Tested Solar Absorption Characteristics

In the next four cases, the absorption coefficient α was increased from 120 to 100,000. While a part of the radiation arrived at the timber wall of the SHC façade element for an absorption coefficient of 120, almost all of the solar radiation introduced was absorbed for a α-value of 200. At an absorption coefficient of 500, the radiation was absorbed approximately 8 mm from the surface between the SHC and the ventilation cavity. For an a-value of 100,000 all of the incoming solar radiation was immediately absorbed by the SHC. In another test case (α = 0), the absorption coefficient was set to 0, and the incident solar radiation was completely let through. At the adjacent timber wall, the radiation was partly absorbed. The lowest temperatures were obtained for this case.
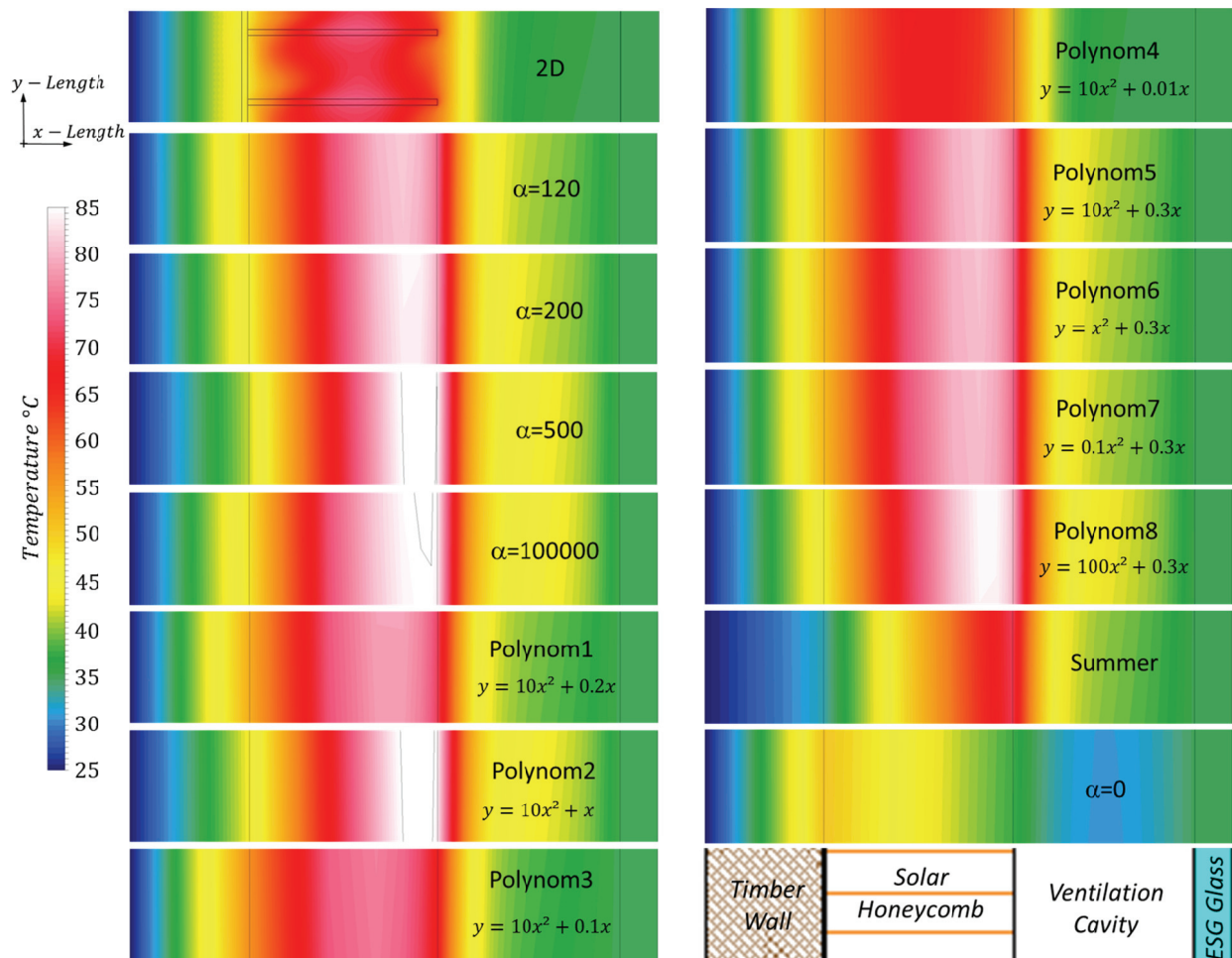
Figure 4-36: Comparison of the Temperature Contours inside the Solar Honeycomb Façade Element at Different Tested Solar Absorption Characteristics

From a comparison with the measurement results, the best agreement was achieved using an absorption coefficient of 120, where the maximum temperature occurred inside the SHC 6 mm away from the surface between the SHC and the ventilation cavity. A comparison of the measured and computed temperatures and air velocities can be found in Chapter 4.3.9.

In the CFD tool Fluent ANSYS, it was possible to replace the absorption coefficient with a Polynomial function of the temperature [7]. In order to test this option, several Polynomial functions of the second order with varying coefficients were used in order to analyse their impact on the solar absorption characteristic inside the SHC. With a square coefficient of 10 and a linear coefficient of 0.2, less radiation was absorbed by the SHC.

In the cases with Polynom2, Polynom3 and Polynom4, the linear coefficient was reduced from 1.0 to 0.1 and 0.01, while the square had a value of 10 in all three cases. For a linear coefficient of 1.0, the solar radiation was completely absorbed after 19 mm in the SHC. The resulting temperature was higher compared to the case where $\alpha = 120$. When this coefficient was reduced to 0.1, a high amount of radiation remained at the rear side of the SHC, and the resulting SHC temperature was a little bit lower compared to the case where $\alpha = 120$. Solar radiation was barely absorbed by the SHC for a linear coefficient of 0.01, and the resulting SHC temperature was significantly lower. From Polynom5 - Polynom8, the square coefficient was varied at a constant linear coefficient of 0.3 in the Polynomial consideration. For the coefficients of 10 (Polynom5) and 100 (Polynom8), similar behaviour of radiation absorption was obtained as in the case where $\alpha = 500$. While the temperature contours almost correlated with the case where $\alpha = 120$ for Polynom5, the temperature inside the SHC was higher in case Polynom8. Compared to case $\alpha = 120$, only slightly less radiation was absorbed by the SHC before reaching the rear wall for the cases Polynom6 and Polynom7, where the coefficients were 1.0 and 0.1. Again, the temperature characteristic in these cases was very similar. Figure 4-35 and Figure 4-36 contain the results of the two-dimensional simulations using the same boundary conditions as the

three-dimensional simulations. The resulting temperatures are too low compared to the measured values, and it can therefore be concluded for this two-dimensional numerical approach.

The best agreement was achieved using an absorption coefficient of 120, and is proposed for the following CFD analysis. Using the Polynomial function does not further improve the CFD model and therefore does not need to be further considered for the CFD model.

Finally, another important case was tested – the summer climate conditions – for which the SHC was excluded from radiation. Due to the high inclination angle (which can occur in summer), the radiation was only absorbed or reflected by the ventilation cavity´s adjacent surface, and did not infiltrate the SHC anymore.

4.3.9   *Numerical Results vs Experimental Data*

A comprehensive comparison of the numerical results and the experimental determined data was carried out the thermal behaviour of the different PV cell configurations was evaluated. All scenarios with different PV cell configurations, in addition to the case without integrated PV cells (NoPV) were performed with the same simulation model configurations. Figure 4-37 shows the temperature and buoyancy profiles along the x-length at the three measurement positions, MP2, MP6, and MP10, as well as along the y-length, 10 mm away from the solar honeycomb for the scenario without PV cells (Figure 4-24 and Figure 4-27). The positions of the profiles and measurement points are indicated in Figure 4-24.
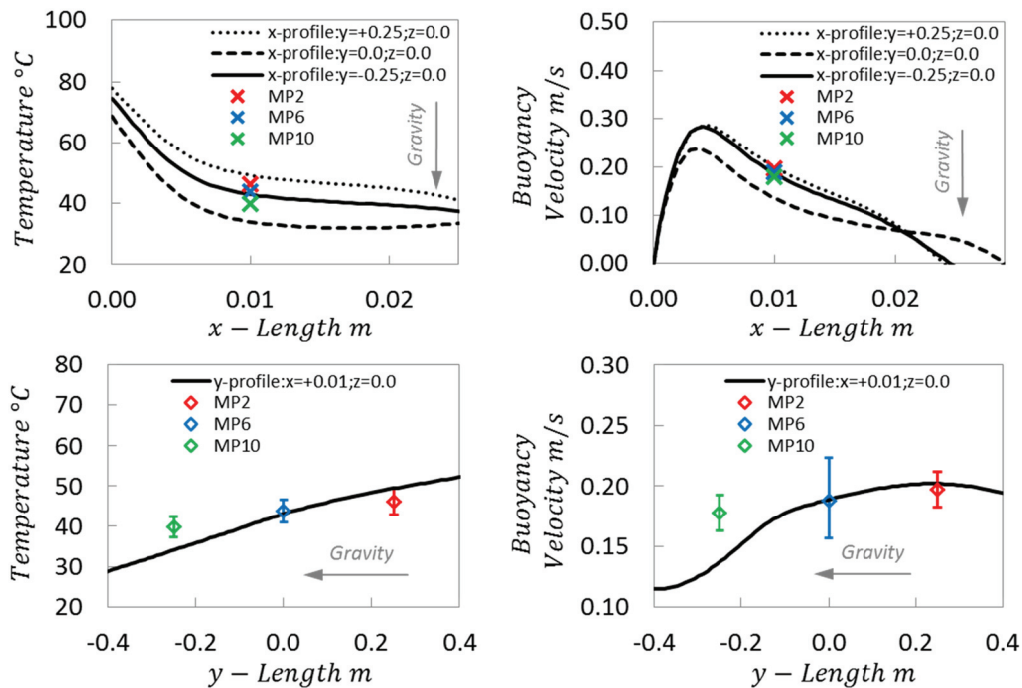
Figure 4-37: Temperature and Buoyancy Velocity Profiles along the Cavity's x-Length and x-Length compared to the Measured Values from Experiments Without Integrated PV Cells (NoPV)

The measured values are the averaged values of three measurements at same external boundary conditions. For the measured air temperatures and velocities the accuracy of the measurement and the deviation of the three measured values were considered, as illustrated in the form of error indicators in the comparison of the y-length profiles.

In the experiments as well as in the simulations, an increase of temperature was observed from the bottom to the top of the SHC façade. In all PV configurations, the simulation slightly overestimated the temperature at measurement point MP2 at the top of the façade element, whereas the computed temperature was lower than the temperature measured at the position MP10 at the bottom of the façade element.
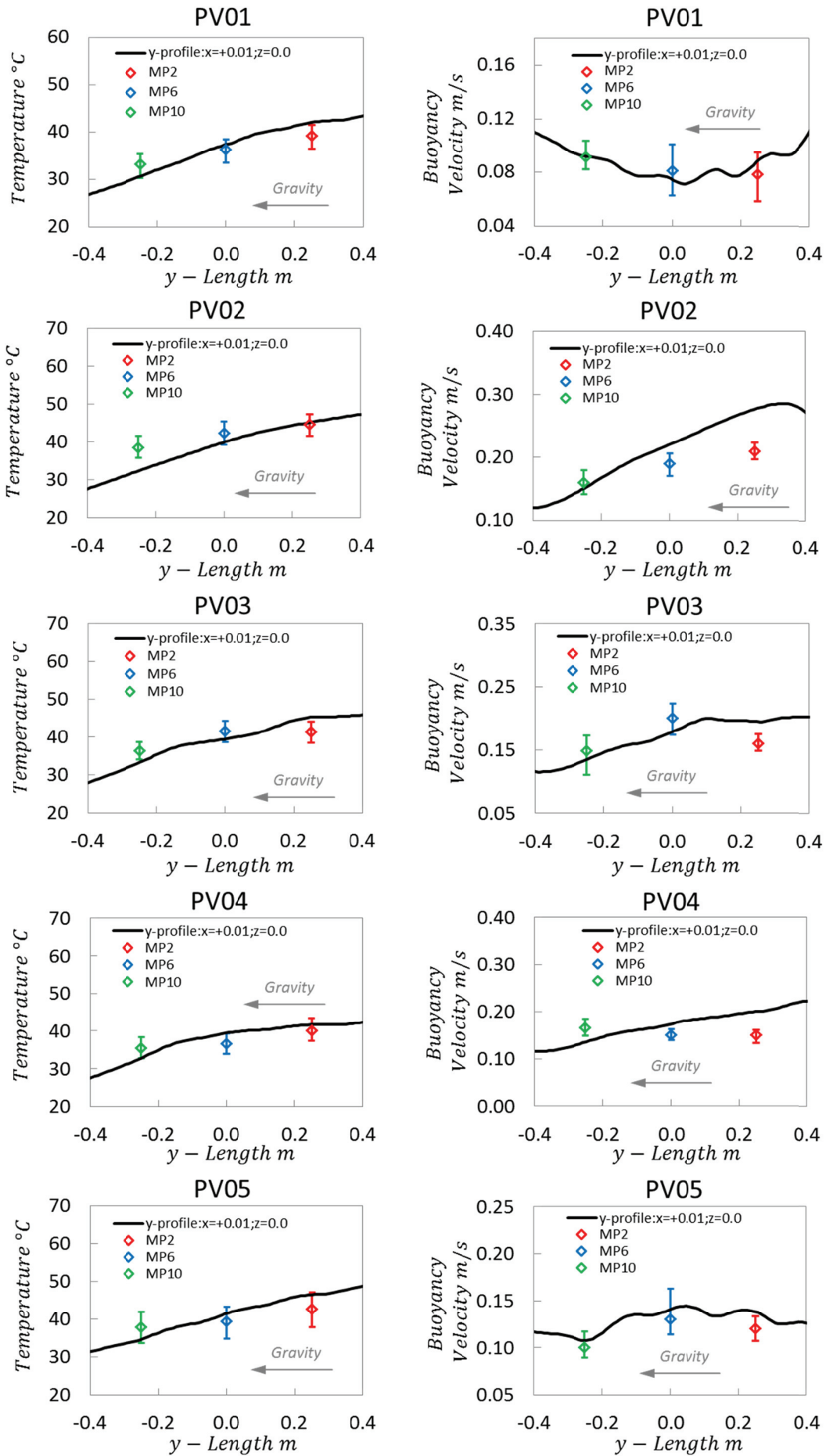
Figure 4-38: Temperature and Buoyancy Velocity Profiles Along the z-length Compared to Measured Values from Experiments for Scenarios PV01-PV05

The comparison of the buoyancy velocities showed good agreement between the measured and computed values for the PV configurations NoPV, PV01, PV02 and PV05. Figure 4-38 illustrates the temperature and air velocity profiles along the y-length (see Figure 4-24 for scenarios PV01 - PV05). In configuration nap at the bottom position, the measured air velocity was higher than the outcome of the CFD simulation. In configurations PV02 and PV04, at the top position, the simulation overestimated the measured air velocities.

In summary, the computed and measured data from the other measurement positions showed similar behaviour. The temperature and velocity profiles looked similar to those resulting from the two-dimensional CFD simulations. Again, air circulations were observed at the inlet and close to the ESG glass from the centre to the ventilation outlet, as described in Chapter 4.3.6.

Almost all of the measured data showed good agreement with the CFD simulation's results. The RMSE (root mean square error of the measured data, Equation 4-2) is illustrated in Table 4-8.

$$RMSE = \sqrt{\frac{1}{n}\sum_{i=1}^{n}(\hat{y}_i - y_i)^2}$$

Equation 4-2

Although the three-dimensional CFD model of the SHC façade was very complex, and contains many simplifications, the deviations between the simulation results and the measured values from the laboratory experiments were within an acceptable range.

Table 4-8: RMSE of the Measurements

$\Delta v\ m/s$	NoPV	PV01	PV02	PV03	PV04	PV05
MP2	0.003	0.014	0.001	0.004	0.006	0.006
MP6	0.022	0.014	0.007	0.013	0.003	0.019
MP10	0.002	0.005	0.010	0.024	0.008	0.009
$\Delta T\ K$	NoPV	PV01	PV02	PV03	PV04	PV05
MP2	0.51	0.25	0.21	0.32	0.65	2.06
MP6	0.20	0.68	0.50	0.28	0.56	1.93
MP10	0.15	0.62	0.57	0.18	0.70	1.80

In the experiment with the semi-transparent PV cells (PV05), an electrical load was connected. Therefore, the electric power of the PV array was measured and the resulting heat reduction on the PV-cells was considered in the CFD simulations. The calculated electrical power (22.7 W, determined according to Equation 4-3) was slightly higher than the measured value of 20.43 W. The measured average electrical current was 1.77 A, while the average voltage was 11.54 V. The averaged heat reduction of the PV cells was approximately 35 W/m².

4.3.10 Assessment of the PV Cell Configuration

For an evaluation of the thermal as well as the electrical output of the PV cells, see the CFD simulation results from the scenarios mentioned in Chapter 4.3.2. All simulations were performed with an external temperature of 25 °C and the radiation matrix from the experiments as boundary conditions. This chapter discusses the contour plots of radiation, temperature and air velocities at the most significant positions inside the SHC façade element. An assessment of the PV configurations was carried out with the help of these contour plots and the flow characteristic plots, as well as some temperature and velocity profiles. The electrical power and the resulting heat reduction of the PV-array were also considered.

4.3.11 Comparison of Temperatures and Natural Convective Airflow

Figure 4-39 shows the contours of solar radiation on the SHC exterior surface. As a result of the measured radiation values from the laboratory experiments, the radiation was distributed as shown in the contour plots. The regions where the PV cells cast a shadow were clearly identified. The very small

transition from the shadow zone to the irradiated surface occurred thanks to the DO radiation model's effective solutions ("Theta Divisions", "Phi Divisions", "Theta Pixels" and the "Phi Pixels" at a value of 6). Figure 4-40 shows the heating effects on the SHC in the temperature plots for the honeycomb's exterior surface. The impact of the different heating effects on the air temperature inside the ventilation cavity is also illustrated in Figure 4-40 in the form of temperature contour plots 10 and 20 mm from and parallel to the SHC surface. In configuration PV01, the middle zone of the SHC's surface was hardly influenced by radiation from the bottom up to the top, whereas in configuration PV04, a small zone with full irradiation was observed. Zones with higher radiation at the top and bottom of the honeycomb were caused by the reflection of the incident solar radiation inside the ventilation cavity, although there was no observable impact on the SHCs' surface temperatures as a result of this effect. The regions of the SHCs' surfaces without solar loads had an appreciable impact on the airflow and the air temperature inside the ventilation cavities, which is illustrated in Figure 4-40 and Figure 4-41. Figure 4-40 shows the temperature contours at the SHC surface adjacent to the ventilation cavity, as well as a section through the SHC façade 10 and 20 mm from and parallel to the SHC. Figure 4-41 shows the air vectors inside the ventilation cavity for five horizontal sections through the SHC façade element. Additionally, the figure show the temperature contours at the SHC surface (but only coloured with grey scales).
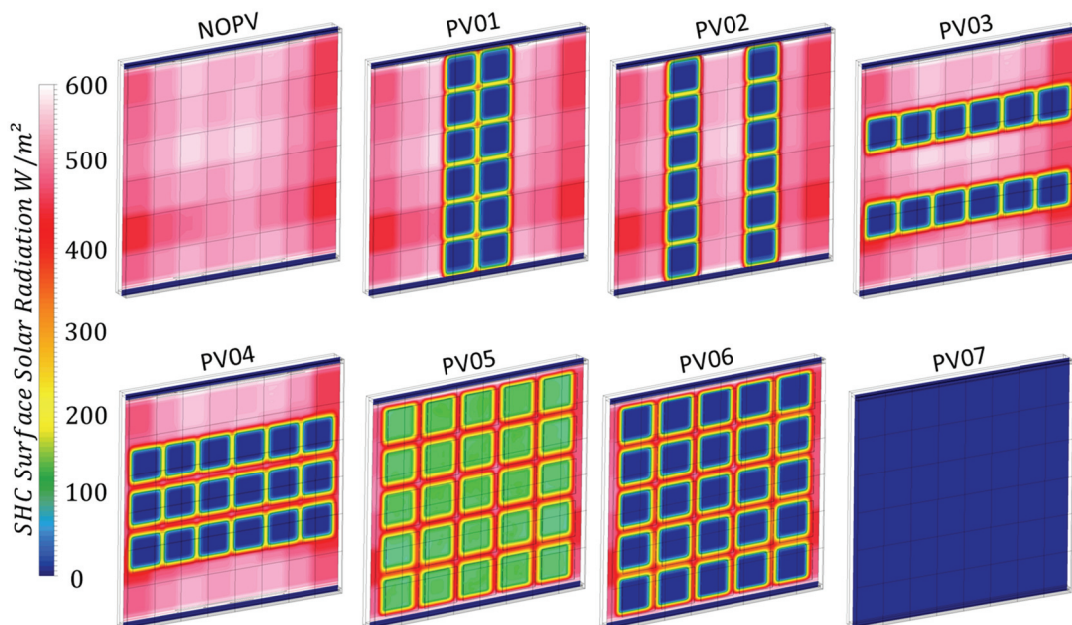
Figure 4-39: Comparison of the Solar Radiation at the SHC Surface between PV Cell Configurations.

An almost uniform enhancement of air temperature and uniform upwards-flowing air was observed inside the ventilation cavity for the case without integrated PV cells. Since the honeycomb surface was not heated behind the PV cells in PV configuration PV01, there was a wide zone with lower air temperatures. Hence, the buoyancy effect was marginal, and the uniform flow characteristic of the case without PV cells (NoPV) disappeared. In the transition from shadowed to solar influenced zones, the different buoyancy effects caused the airflow to be diverted, especially in the top region of the façade element's ventilation cavity. This diversion effect was also observed for the PV cell configuration PV02, for each PV cell row, but the impact was not as high as for configuration PV01. Due to the vertical arrangement of the PV cells, the flow and temperature contours showed a more uniform behaviour in the comparisons. Only very small differences were observed in the contours of case with no PV cells (NoPV) and PV03, although the number of PV cells in these cases was the same as in PV01 and PV02.

Due to the additional PV cell row in PV04, very thin streaks with higher temperature and airflow velocity occurred between the PV cells in the temperature contour plots. In case PV05, the radiation was not completely absorbed because of semi-transparent PV cells. In the contour plots, very thin streaks of higher temperature were observed, in addition to slightly higher air velocities. The behaviour was not as uniform as in the case of PV03 and PV04. The replacement of the semi-transparent PV cells with opaque monocrystalline cells (PV06) led to a significant reduction in air temperatures and air velocities in the CFD simulations, whereas the characteristic of the contours was similar.

Stationary, Three-dimensional CFD Models
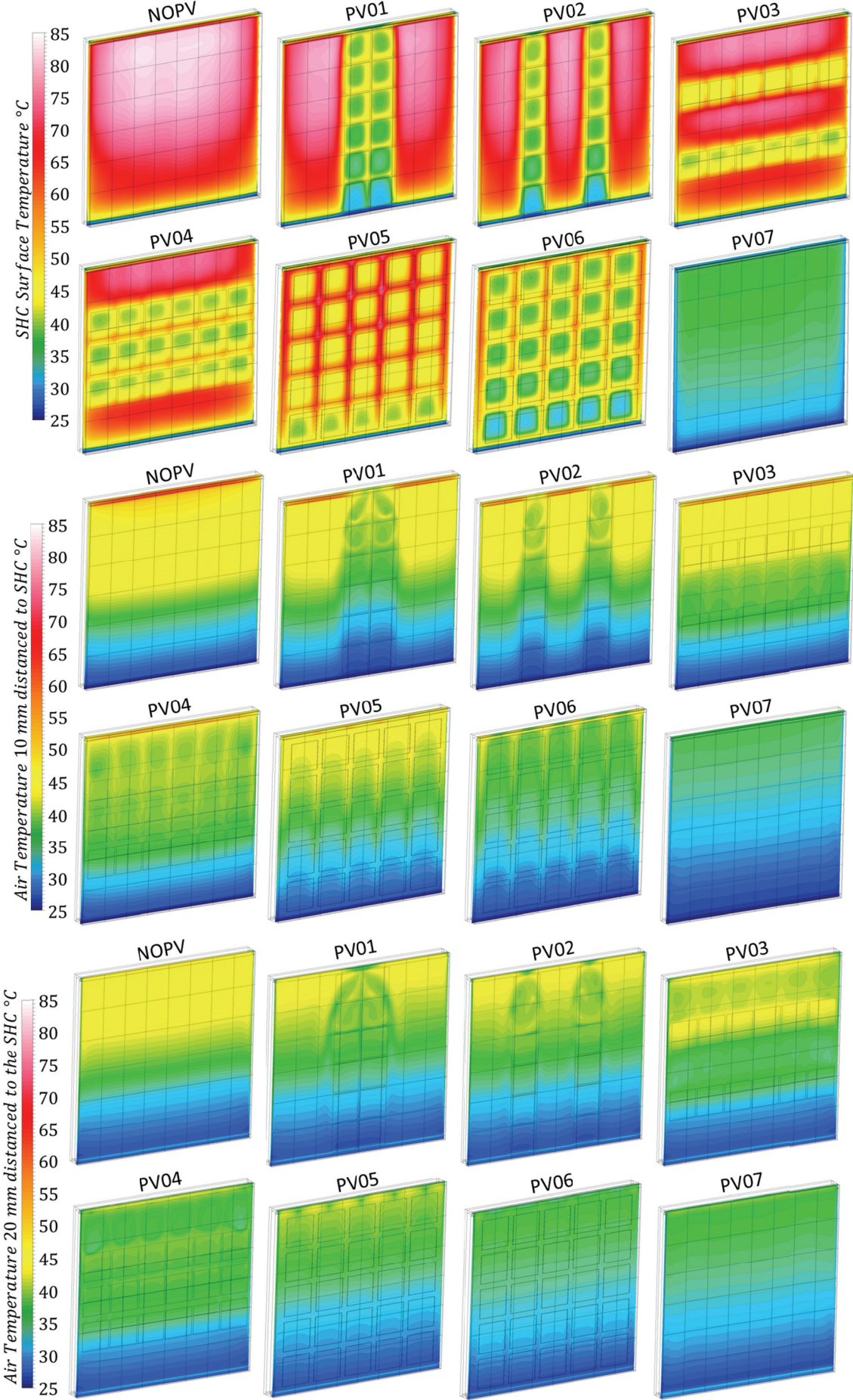
Figure 4-40: Comparison of SHC Surface Temperature, Air Temperature 10 mm and 20 mm Parallel to the SHC, Between PV Cell Configurations
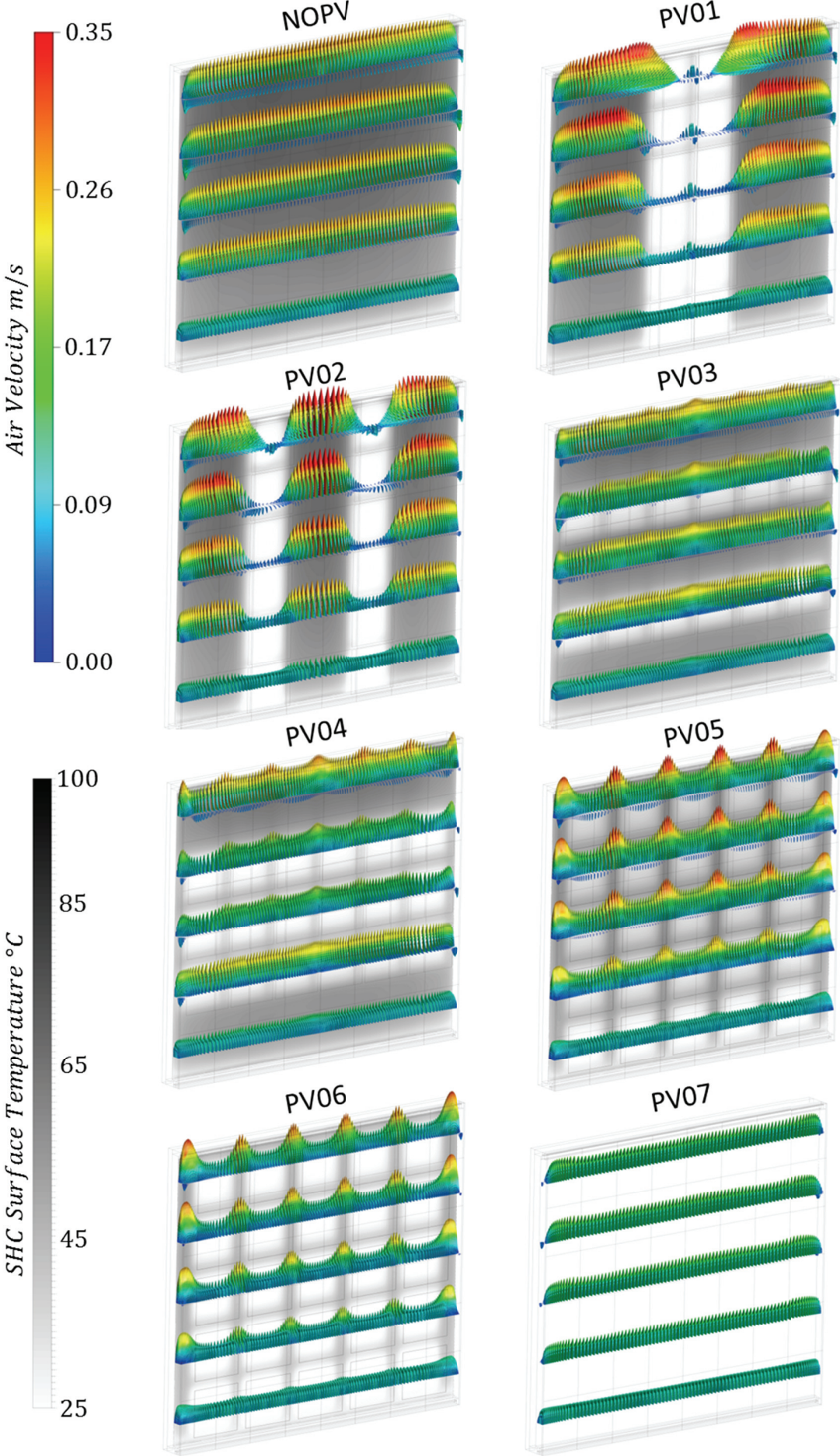
Figure 4-41: Comparison of the Air Vector Profiles, between PV Cell Configurations

In Figure 4-42, which presents a comparison of temperature contours and air vectors, the impact of a closed ventilation cavity for the basis SHC scenario without attached PV is presented. Temperature stratification was observed and presented the highest values at the top of the façade element's cavity. The maximum temperature was approximately 5.4 K higher for the closed cavity than for the ventilated SCH façade, while the volume-averaged air temperature was 12 K higher. The airflow characteristic changed to circulation inside the closed cavity, with downwards streaming airflow at the ESG glass, and an upwards streaming airflow at the SHC element, due to the heated air.
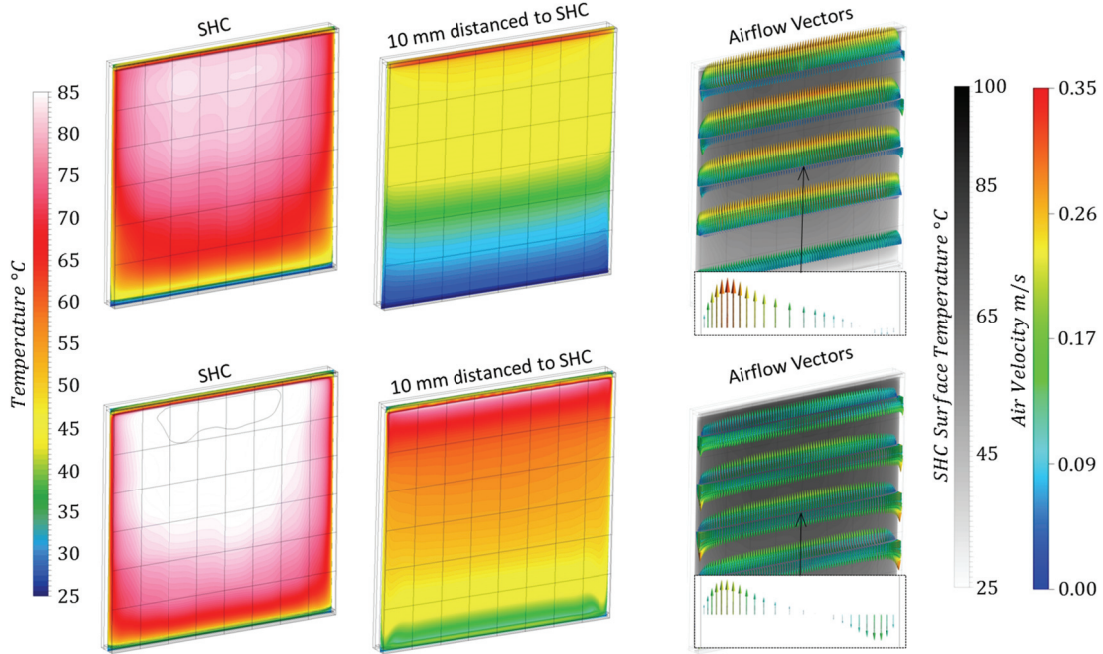
Figure 4-42: Comparison of Temperature Contours and Air Flow Characteristic of the Scenario NoPV with the Ventilation Cavity Open and Closed

Figure 4-43 provides a comparison of temperature and buoyancy velocity profiles through the SHC façade´s ventilation cavity for the different PV cell configurations. In this figure, the profiles along the x-length in the middle of the façade element are shown. Furthermore, the profiles along the y-length at the centre of the z-length 10 mm in front of the SHC are illustrated. Last but not least, the profiles along the z-length at the centre of y-length, again 10 mm in front of the honeycomb, are presented.
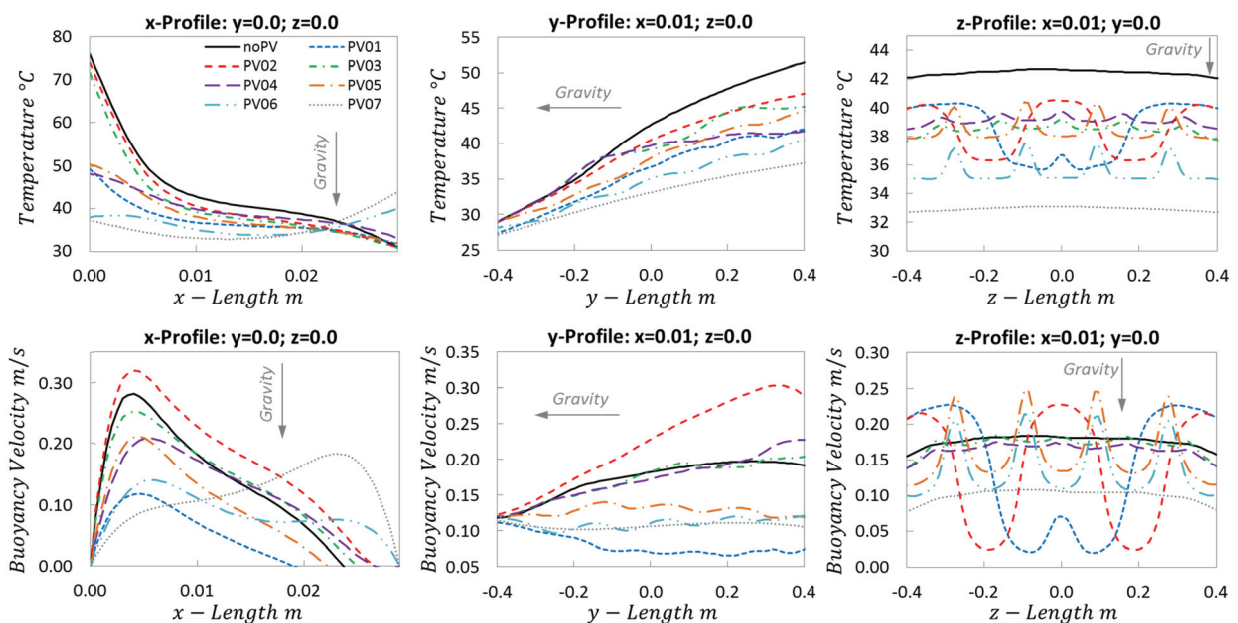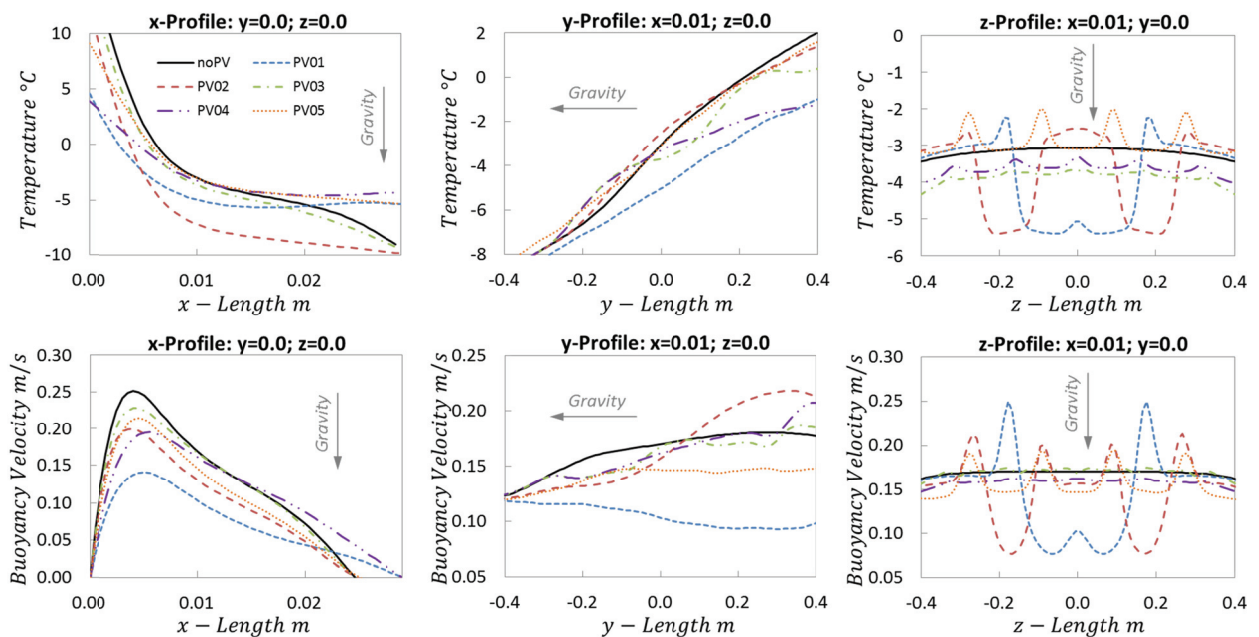

Figure 4-43: Comparison of Temperature and Velocity Profiles between the Different PV Cell Configurations along the x-, y- and z-lengths inside the Façade´s Ventilation Cavity

Concerning the temperature profiles along the x-coordinate, the highest temperature was observed for the façade element without integrated PV cells. The temperature profiles with configuration PV02 and PV03 were slightly lower at this position. For configurations PV01, PV04, and PV05, lower temperatures were detected at this position inside the ventilation cavity. The lowest temperatures were detected for the configurations PV06 and PV07 close to the honeycomb, whereas the highest temperatures were observed in the region of the front glass. Because of the configuration of the PV cells in PV02, the highest local buoyancy velocity occurred in this case, followed by the case with no PV cells. Slightly lower velocities were detected for configuration PV03, in comparison with the other vertically-arranged PV cell configuration (PV04) and configuration PV05. The lowest buoyancy velocity at this position occurred for configuration PV01. In the velocity profile of configuration PV07, higher buoyancy velocity occurred close to the ESG glass due to the heated PV cells.

Concerning the temperature along the y-coordinate in Figure 4-43, the highest temperature was observed for the case with no PV cells. The profiles of configurations PV03 and PV04 were higher than the profiles of the configurations PV01 and PV02 until the middle of the façade element´s height. In the upper region, the PV03 profile almost converged with the profile of PV02, whereas profile PV04 almost converged with the profile of PV01. Case PV07 showed the lowest temperature profile in the y-temperature plots. The temperature profiles of configurations PV05 and PV06 were located above and below the profile of PV01, respectively, and exhibited slightly oscillating behaviour which was caused by the PV cell configuration. This oscillating behaviour was also observed in the velocity profiles of these two cases. The highest local velocities along this coordinate inside the ventilation cavity were detected for configuration PV02. The profiles of PV03 and PV04 were slightly higher than the profile NoPV, while the lowest velocities were indicated for the configuration PV01.

In the z-temperature profiles, the temperature was much higher for the configuration with no PV cells compared to the other profiles. The impact of the PV cells on the temperature and the air velocity inside the cavity was clearly identified in the z-profiles of configurations PV01 and PV02. At this position, the temperature and velocity profiles of PV03 were slightly higher compared to the profiles of PV04. Furthermore, the profiles for configurations PV05 and PV06 were not as uniform as those of configurations PV03 and PV04.

4.3.12 Comparison of the Thermal Behaviour and the Electrical Performance

Before a final assessment, the thermal and electrical performance of the different cases of the SHC façade element will be presented. For this purpose, the averaged surface heat fluxes of the rear wall as well as between the SHC and the ventilation cavity are illustrated in Table 4-9. This comparison also addresses the influence of a connected electrical load (P_{PV}) on the thermal behaviour of each PV configuration. The electrical power of the PV array ($P_{PV-array}$, Equation 4-3) as well as the resulting heat (q_{PV-red}, Equation 4-4) and temperature (T_{PV-red}) reduction at the PV array´s surface are also illustrated in Table 4-9. As mentioned in Chapter 4.3.2, three different types of PV cell were involved in the comparison of the combined thermal behaviour and electrical performance analysis:

- A monocrystalline PC cell of 150 x 150 mm and a cell power of 4.08 W at reference solar radiation of 1000 W/m² (in scenarios PV01 – PV04)
- A semi-transparent PV cell with a solar transmissivity of 44.3%, a size of 156 x 156 mm, and a referenced power of 2.01 W per cell (in scenario PV05)
- Another monocrystalline PV cell of 156 x 156 mm and a cell power of 4.2 W per cell (in scenarios PV06 and PV07).

This information of the cells' power was extrapolated from the report of the laboratory experiments performed [51]. In order to determine the electrical power for the assessment, the measured solar radiation of the lamp array from the solar simulator was used (illustrated in Figure 4-34). Depending on the positions of the PV cells in the scenarios and the measured radiation intensity ($I_{Sol,i}$), the electrical power of each cell ($P_{Cell,i}$) as well as the resulting electrical power ($P_{PV-array}$) of the façade´s PV array were calculated according to Equation 4-3. Subsequently, this calculated electrical output reduced the

heating effect at the positions of the cells in the scenarios which were considered in the boundary conditions in the CFD simulations.

$$P_{Cell,i} = \frac{I_{Sol,i}}{I_{Sol,Ref}} \cdot P_{Cell,Ref} \cdot (1 - r_{glass} - \alpha_{glass}), \qquad P_{PV-array} = \sum_i P_{Cell,i} \qquad \textbf{Equation 4-3}$$

$$q_{PV-red} = \frac{1}{A_{PV-array}} \sum_i P_{Cell,i} \qquad \textbf{Equation 4-4}$$

Table 4-9 contains a comparison of the air temperature at the ventilation outlets (T_{out}), the ventilation performance (Q_{Vent}), and the volume-averaged temperature of the SHC ($T_{SHC-Vol}$).

Table 4-9: Comparison of Averaged Surface and Volume Temperatures and Heat Fluxes of the Different PV Configurations at an External Temperature of 25 °C

	T_{out}	Q_{Vent}	$q_{SHC-air}$	q_{RW}	$T_{SHC-Vol}$	$T_{air-Vol}$	A_{PV}	$P_{PV-array}$	q_{PV-red}	T_{PV-red}	$F_{PV/SHC}$
	°C	W	W/m^2	W/m^2	°C	°C	–	W	W/m^2	°C	–
NoPV	53.0	103.0	163.6	138.0	72.1	41.9	0.0	-	-	-	-
PV01	47.8	84.0	122.0	100.1	59.8	38.8	0.27	-	-	-	-
PV01-P_{PV}	47.6	83.6	121.6	99.6	59.6	38.6	0.27	21.72	80.46	1.01	0.566
PV02	47.6	83.3	121.5	99.7	59.7	38.8	0.27	-	-	-	-
PV02-P_{PV}	47.5	82.9	121.0	99.2	59.5	38.6	0.27	21.28	78.81	1.00	0.548
PV03	47.7	84.6	123.3	100.8	60.0	39.2	0.27	-	-	-	-
PV03-P_{PV}	47.5	83.9	122.9	100.3	59.9	39.1	0.27	21.35	79.06	1.01	0.566
PV04	45.3	76.2	103.4	82.5	54.0	37.8	0.41	-	-	-	-
PV04-P_{PV}	42.9	75.0	102.4	81.5	53.6	37.5	0.41	32.22	79.56	1.40	0.570
PV05	46.5	80.0	79.5	63.0	49.5	38.4	0.61	-	-	-	-
PV05-P_{PV}	45.8	77.5	76.9	60.9	48.7	38.0	0.61	22.09	36.30	1.14	0.287
PV06	41.4	61.7	54.9	32.5	41.2	36.2	0.61	-	-	-	-
PV06-P_{PV}	41.1	60.7	54.0	31.9	41.0	35.8	0.61	46.15	75.85	1.78	0.435
PV07	37.9	47.1	26.4	22.6	33.8	34.4	1.0	-	-	-	-
PV07-P_{PV}	36.0	40.5	22.7	19.3	32.6	33.1	1.0	66.19	75.55	2.36	0.558

For the comparison of the thermal performance of the SHC façade element, both the surface heat flux at the rear wall and the ventilation performance were considered. After the case NoPV, the highest surface heat fluxes were detected for the PV configurations PV01, PV02, and PV03. Moreover, these cases also showed the best ventilation performance of all PV configurations. Based on the resulting heat fluxes from the other configurations, the thermal performance was found to correlate with the ratio of the PV array (A_{PV}).

The connection of an electrical load to the PV cells resulted in a minimal reduction of the thermal performance in all simulations. Again, the reduction of the thermal performance correlated with the PV area ratio.

The electrical performance of the SHC façade element depended on the number of PV cells, the position of the cells at the ESG glass, as well as the PV cell type. The highest electrical output was obtained for PV configuration PV07, with the opaque PV panel. Although the PV area ration was higher for case PV05, with the semi-transparent PV cells, the electrical power output was only slightly higher than those of cases PV01, PV02, and PV03. Case PV06 also achieved good electrical performance, where the electrical power was almost 70% of the output from case PV07.

Taking both thermal and electrical behaviour into account, as well as the air flow characteristic, PV configurations PV03 and PV04 were found to be most suitable for the SHC façade, while configuration

PV03 is most suitable for a better thermal behaviour, and configuration PV04 is ideal for a higher electrical output.

The calculated monthly averaged electrical output (Equation 4-5) of the different PV configurations for three different façade orientations is illustrated in Figure 4-44. These calculations are valid for a façade similar to that of the demonstration building presented in Figure 4-21. The façade´s effective area was 100 m² , which was reduced to 92 m² due to three integrated windows.

$$EO_{PV,facade} = \frac{I_{Sol,avg}}{I_{Sol,Ref}} \cdot P_{Cell,Ref} \cdot \left(1 - r_{glass}\right) \cdot (A_F - A_W) \cdot t \qquad \text{Equation 4-5}$$

For this, weather data over a whole year were generated using the software program, Meteonorm [74] and subsequently used to calculate the monthly electrical output. The weather data generated were based on the last ten years of meteorological history of Graz, Austria. Additionally, the electrical output of a 100 m² photovoltaic plant was simulated with Meteonorm, also presented in Figure 4-44 in order to provide an additional point of comparison. The plant was assumed to be south-facing, with a roof inclined at a 45° angle.
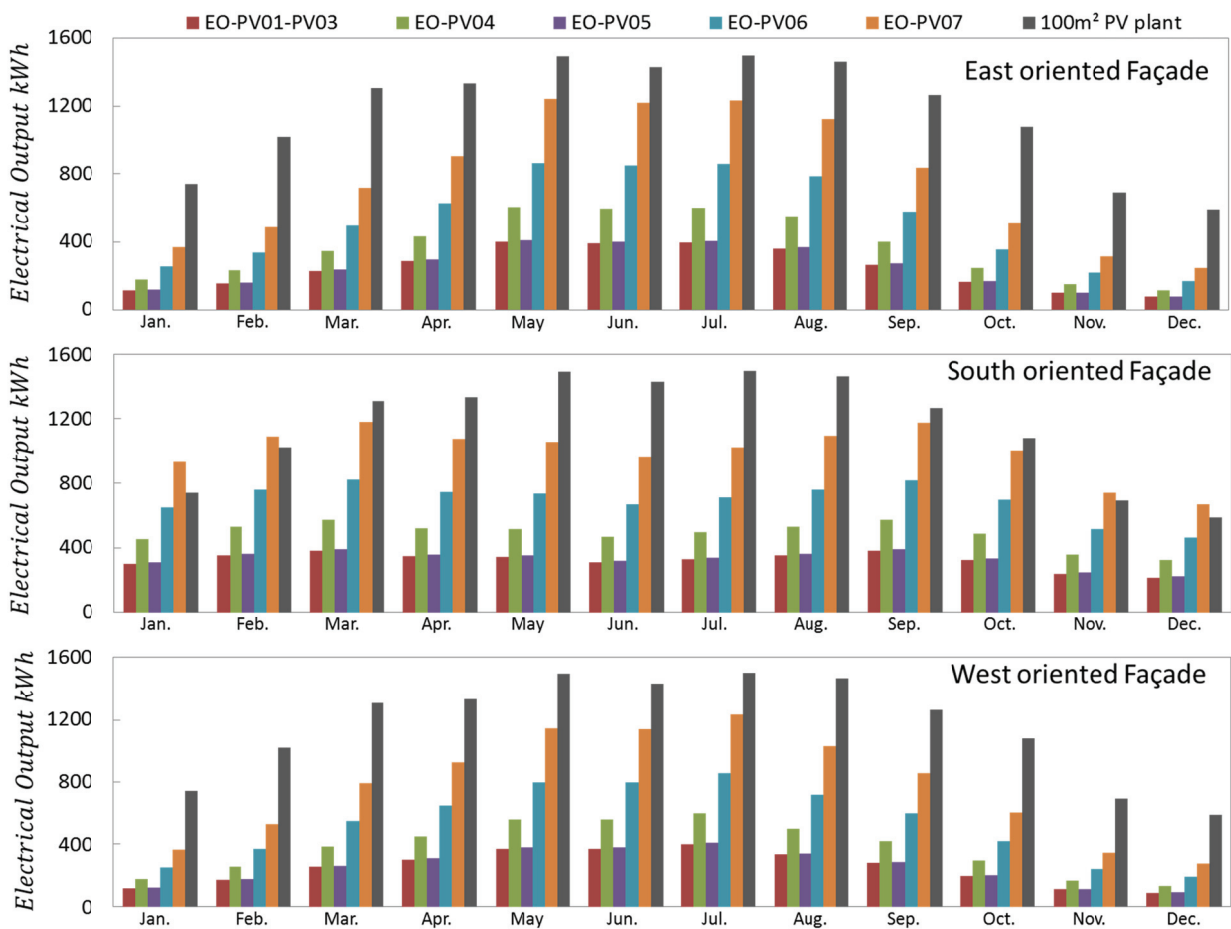
Figure 4-44: Comparison of the Monthly Electrical Output between the Different PV Configurations of a 100 m² SHC Façade at Three Different Orientations

When the SHC façade was oriented to the east or west, the highest electrical output was observed in spring and autumn, whereas for the south-oriented façade, the highest electrical output was observed in summer. The lowest yearly electrical output was received from scenarios PV01, PV02, and PV03, with an amount of 2988 kWh/a (21% compared to the electrical output of 13911 kWh/a from the 100 m² PV plant on the roof) for the east, 2995 kWh/a (22%) for the west, and 3886 kWh/a (28%) for a southern orientation. With one additional PV cell row - as was tested in scenario PV04 – an electrical output of 4482 kWh/a (32%) was assumed for east orientation, whereas this was 4521 kWh/a (32%) for west and 5829 kWh/a for south orientation (42%). The output was almost equal for scenario PV05, with the semi-

transparent PV cells, with 3067 kWh/a (22%) for east, 2995 kWh/a (22%) for west, and 3886 kWh/a (29%) for south orientation. Replacing the semi-transparent PV cells with monocrystalline cells (PV06) raised the output to 6408 kWh/a (46%) for east, 6423 kWh/a (46%) for west, and 8333 kWh/a (60%) for south orientation. The highest yearly electrical output of a façade integrated PV was achieved with scenario PV07 (PV module) with an amount of 9227 kWh/a (66%) for east, 9249 kWh/a (66%) for west and 12000 kWh/a (86%) for south orientation.

For a four-person household, electricity demand is assumed to be between 4000 and 5000 kWh/a. Therefore, it is possible to conclude that for all scenarios of a 100 m² large SHC façade gathering solar energy, the electrical demands of a four-person household could only be sufficiently met with scenarios PV04, PV06 and PV07.

4.3.13 Thermal Behaviour for Winter and Summer Climate Conditions

After the assessment of the PV cell configurations for the SHC façade element, the CFD model was used to compare the thermal behaviour for winter and summer climate conditions. The assumed climate conditions were based on data gathered over the past few years from the external environment in the region of Graz, Austria.

Data for a typical winter day in a temperate climate zone was used for the comparison of the thermal behaviour in a winter climate. The external temperature was assumed to be -10 °C, while the global radiation was 400 W/m². This global radiation was divided into a fraction of direct irradiation of 250 W/m², an inclination angle of 20°, and a fraction of diffuse radiation of 150 W/m². To implement the effect of the external wind, a virtual convective layer was created, with a heat transfer coefficient of 25 W/m²K. Furthermore, a virtual interior layer was created in the form of a masonry brick wall with a thermal conductivity of 0.43 W/mK, a density of 1100 kg/m³, and a specific heat capacity of 840 J/kgK. The thickness of the masonry wall was 0.3 m. This interior layer also had a convective layer, with a heat transfer coefficient of 5 W/m²K, while the interior room temperature was assumed to 20 °C.

Figure 4-45 shows the temperature and buoyancy velocity profiles for the façade elements with different PV configurations in comparison to the case with no PV cells for the assumed winter climate conditions. The x-length profiles show the behaviour inside the cavity between the honeycomb surface and the ESG glass in the centre of the façade element, while the y-length profiles show the behaviour along the ventilation cavity height, 10 mm from the honeycomb and the z-length profiles show the behaviour for the width of the ventilation cavity again 10 mm from the honeycomb.

Figure 4-45: Comparison of Temperature and Velocity Profiles between the Different PV Cell Configurations along the x-, y- and z-lengths inside the Façade´s Ventilation Cavity for Winter Climate Conditions

The highest temperatures occurred inside the SHC, approximately 5 mm from the ventilation cavity. The temperature and radiation distribution were similar to case α = 120 in Chapter 4.3.8 because of the flat inclination angle of the incident radiation. The profiles showed almost identical behaviour to that seen in the assessment of the PV configuration (Figure 4-43). The air temperature at the ventilation outlet (T_{out}), the ventilation performance (Q_{Vent}), the surface heat fluxes at the SHC ($q_{SHC-Air}$) and the rear wall (q_{RW}), as well as the volume-averaged temperatures of the SHC ($T_{SHC-Vol}$) and the air inside the ventilation cavity ($T_{Air-Vol}$) are illustrated in Table 4-10. The surface heat flux at the rear wall of the SHC façade element (q_{RW}) represents the heat loss (with the exception of case NoPV, where heat was introduced to the interior) from the interior room for the winter climate, which was reduced by the heated SHC.

Table 4-10: Comparison of Averaged Surface and Volume Temperatures and Heat Fluxes of the different PV Configurations for Winter Climate Conditions

	T_{out}	Q_{Vent}	$q_{SHC-Air}$	q_{RW}	$T_{SHC-Vol}$	$T_{Air-Vol}$
	$°C$	W	W/m^2	W/m^2	$°C$	$°C$
NoPV	2.8	56.4	27.8	3.3	21.6	-2.6
PV01	2.0	52.5	11.1	-18.7	17.6	-2.5
PV02	1.8	51.8	11.1	-18.7	17.6	-2.5
PV03	1.8	52.1	11.2	-18.9	17.5	-2.5
PV04	0.8	47.9	1.7	-27.7	15.2	-2.9
PV05	2.4	53.2	12.1	-31.9	14.0	-2.5

A radiation model approach was used to investigate the influence of the PV cells on the thermal behaviour of the SHC façade under summer climate conditions (case summer in Chapter 4.3.8). The incident solar radiation is no longer able to penetrate the SHC because of the steeper inclination angle. In summer, in the temperate zone, the inclination angle can be up to more than 67°. For this reason, the model approach for summer was that the incident radiation was partly absorbed at the SHC's surface. Direct solar radiation of 1000 W/m² was assumed for summer climate conditions at an inclination angle of 65°. The diffuse radiation was assumed to have a value of 250 W/m². The external temperature was assumed to be 30 °C, and the interior room temperature was set to 25 °C in the simulation of summer conditions. As in the investigations of a winter climate, the masonry wall's thickness was 0.3 m, the heat transfer coefficient was 25 W/m²K for the external and 5 W/m²K for the interior convective layer.
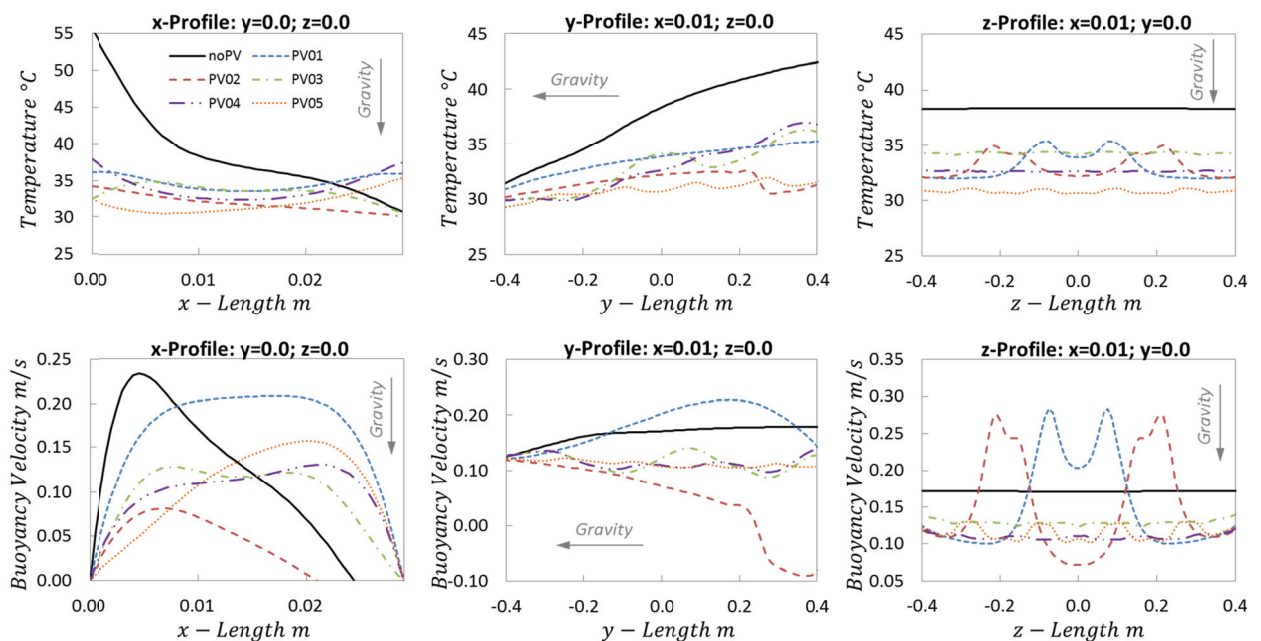
Figure 4-46: Comparison of Temperature and Velocity Profiles between the Different PV Cell Configurations along the x-, y- and z-lengths inside the Façade´s Ventilation Cavity for Summer Climate Conditions

Figure 4-46 shows the temperature and buoyancy velocity profiles for the façade elements with the different PV configurations, in comparison to the case with no PV cells for summer climate conditions. The x-length profiles show the behaviour inside the cavity, and between the honeycomb surface and the ESG glass in the centre of the façade element. The y-length profiles show the behaviour along the ventilation cavity height, 10 mm from the honeycomb, and the z-length profiles show the behaviour for the width of the ventilation cavity, again located 10 mm from the honeycomb. With this radiation model approach, the highest temperatures occurred at the surface of the SHC, adjacent to the ventilation cavity. In the x-length temperature profiles, the temperature and air flow characteristic for the case with no PV cells was similar to the winter climate and laboratory experiments. However, it is important to consider that the solar radiation was higher, meaning that the absorptivity was lower than for a winter climate.

For the façade elements with PV configurations, higher temperatures occurred in the regions where the PV cells were attached to the ESG glass. As a result, airflow inside the ventilation cavity exhibits different characteristics when compared to the simulation results from the winter climate and the laboratory experiments. The buoyancy velocity profiles in Figure 4-46, for configurations PV01 and PV04 in particular, show higher velocities close to the ESG glass than close to the surface of the SHC. The air temperature at the ventilation outlet (T_{out}), the ventilation performance (Q_{Vent}), the surface heat fluxes at the SHC ($q_{SHC-Air}$) and the rear wall (q_{RW}), as well as the volume-averaged temperatures of the SHC (TSHC-Vol) and the air inside the ventilation cavity ($T_{Air-Vol}$) for summer climate conditions are illustrated in Table 4-11. For summer climate conditions, the surface heat flux at the rear wall of the SHC façade element (q_{RW}) represented the heat introduced to the interior room.

Table 4-11: Comparison of Averaged Surface and Volume Temperatures and Heat Fluxes between the different PV Configurations for Summer Climate Conditions

	T_{out}	Q_{Vent}	$q_{SHC-Air}$	q_{RW}	$T_{SHC-Vol}$	$T_{Air-Vol}$
	°C	W	W/m^2	W/m^2	°C	°C
NoPV	38.5	40.4	39.6	37.1	40.3	36.9
PV01	39.3	40.8	34.7	32.7	38.4	37.3
PV02	39.0	39.9	34.9	32.8	38.4	37.4
PV03	38.5	40.3	34.4	32.3	38.2	37.2
PV04	37.6	37.1	30.4	28.7	36.6	36.5
PV05	31.1	10.0	9.3	10.8	28.9	31.5

5   Transient, Three-dimensional CFD Models[8]

5.1   Applications and CFD Approaches

This dissertation describes only one study that focused on transient three-dimensional CFD models. It was a further inquiry into the SHC façade element discussed in Chapter 4.3, and was published in the Journal *Solar Energy* [75]. For this purpose, the CFD model from the stationary analysis was adapted, and developed into a transient simulation. The study focused on the transient thermal behaviour, with a comparison of the monitored heating phase from the laboratory experiments and the results of an associated CFD simulation. Afterwards, both the influence of the thermal mass and the influence of the time-step on the SHC material were using three-dimensional transient CFD simulations. Finally, the SHC façade with and without attached PV cells was analysed under measured climate conditions. For these measurements, monitored weather data, under four different climate conditions in the course of a year, was used for the boundary conditions in the CFD simulations. The temperature, global radiation, and diffusive radiation used to simulate the transient behaviour over a two-day period were based on data measured hourly over a 24-hour period.

---

8. Parts of this section have been published in [21].

5.2 Analysis of the Transient Thermal Behaviour of a Solar Honeycomb (SHC) Façade Element With and Without Integrated PV Cells[9]

5.2.1 Introduction

In contrast to the majority of recent research, where only two-dimensional CFD models are used for transient analysis, this study developed and employed three-dimensional CFD-models of the SHC and the façade in order to analyse transient thermal behaviour under cold and hot climate conditions. The use of three-dimensional simulation models is especially important when there are irregularities on the façade, such as PV cells that partially shade the solar comb and therefore have an impact on the convective flow inside the ventilation cavity as well as the heating effects at the SHC.

This study presents the transient thermal behaviour of the ventilated solar honeycomb (SHC) façade element using three-dimensional CFD models that were adopted from the study presented in Chapter 4.3, and extended with the transient formulations.

For the validation of the CFD calculations, data measured from a heating phase of the SHC façade element was used in laboratory experiments with the solar simulator. Comparison of the measured and simulated temperatures showed that the recently developed CFD model was valid for further transient CFD simulations. Furthermore, a parameter analysis was performed, in which the influence of different material properties on the SHC and the influence of the size of the time-step on the thermal behaviour was observed. Finally, the thermal behaviour and its impact on the building envelope over one day were observed for hot as well as cold climate conditions in the temperate zone.

5.2.2 Measured and Simulated Transient Heating Phase of the SHC Façade

Air temperatures were monitored during the heating phase of the SHC façade. At the ventilation cavity´s inlet and outlet, fixed sensors made it possible to continuously measure the incoming and outgoing air. Because only one hot sphere anemometer was available, the air temperature was measured at only one position inside the ventilation cavity (MP3, Figure 4-24) during the entire heating phase. Additionally, the heat flux from the rear wall to the external environment was measured with a heat flux plate from Ahlborn. This 100 x 30 mm plate was attached to the rear wall, 100 mm above and 85 mm to the right of the centre of the façade element.

Since the results of the steady state calculations for the SHC façade element correlated with the measured data (see Chapter 4.3.9), this heating phase from the laboratory experiments was used to validate the transient CFD models. Figure 5-1 and Figure 5-2 show the comparison between the monitored and computed temperature and heat flux profiles during the heating phase, which lasted about 3600 seconds, and present the temperature contours from various points in the heating phase.

The simulation used the radiation matrix measured by the solar simulator. The averaged value of the field, 508 W/m², was used (Figure 4-23), the exterior temperature being approximately 20 °C. At the start of the measurement of the heating phase, an air temperature of 24.1 °C was observed at the position MP3 inside the SHC façade. Also, an air temperature of 24.4 °C at the outlet and 20 °C at the inlet of the ventilation cavity was measured at the start. In the simulation, an air temperature of 20 °C was set at the inlet as a boundary condition. The air temperatures at the outlet and the position MP3 amounted to 24 °C at the beginning of the heating phase in the CFD simulation. The time-step size in the simulation of the heating phase was 60 seconds.

The CFD models used for the stationary analysis (presented in Chapter 4.3.4) were completely adapted and extended with the required transient formulations and parameters. Again, an implicit numerical method was used in order to keep the duration of the calculations within an acceptable range, and to make it possible to simulate the thermal behaviour of a whole day. Furthermore, a fixed time stepping method was chosen, and a maximum of 20 iterations per time-step was assumed (and sufficient) in the transient simulations.

The measured and calculated temperature profiles matched very well (Figure 5-1), so that the CFD model was valid for further investigations. At the end of the heating phase, the best agreement between measurement and simulation was achieved at the inlet position, with a deviation of 0.2 K. At

---

9. Parts of this section have been published in [21].

the outlet position, the computed air temperature was 1.5 K higher than the measured value. Compared to the measurement, the air temperature at position MP3 was 1.0 K lower than in the simulation. The computed heat flux value of -55.5 W/m² was slightly higher than the measured value of -55.1 W/m² at the SHC façade´s rear wall.
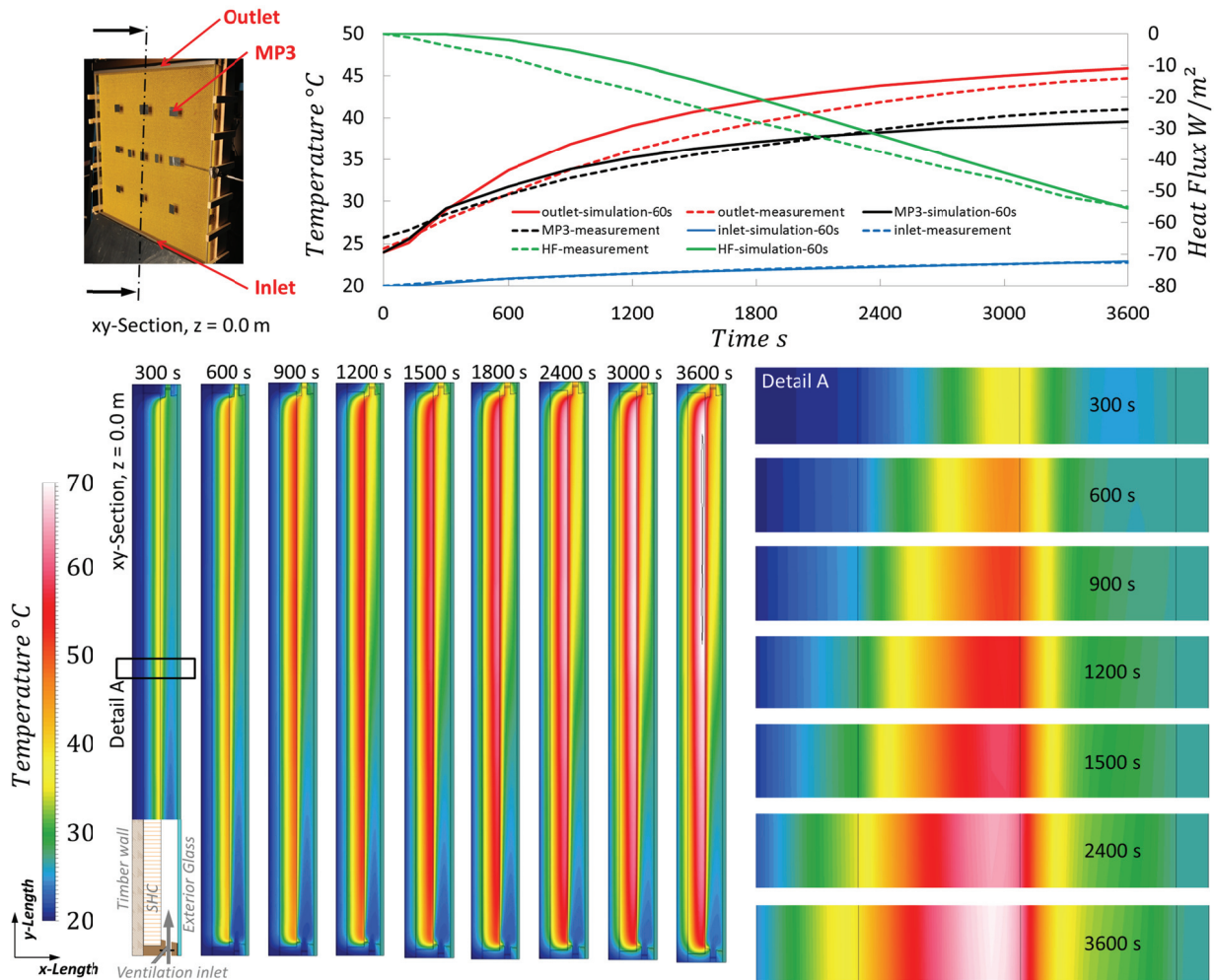
Figure 5-1: Comparison of Measured and Computed Temperature/Heat Flux Profiles and Temperature Contours during the SHC Façade's Heating Phase
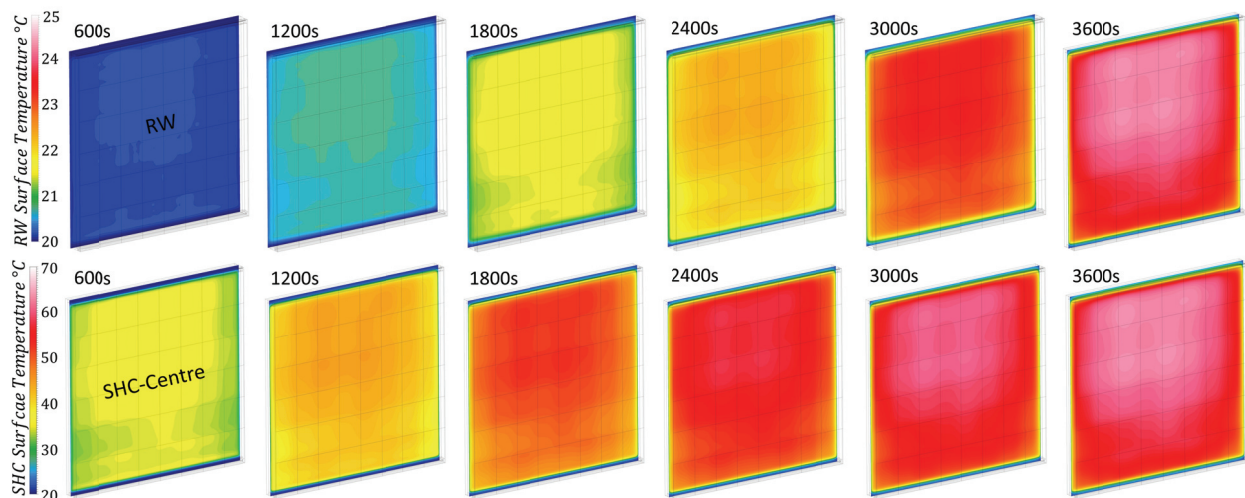
Figure 5-2: Temperature Contours during the SHC Façade's Heating Phase at the Rear Wall at the Surface between the SHC and the Ventilation Cavity

The temperature contours in Figure 5-1 and Figure 5-2 show the heating characteristic of the SHC façade element for a section along the façade's height. After 300 seconds, the SHC showed a volume-averaged temperature of 27.7 °C at a relatively uniform temperature distribution. The volume-averaged air temperature in the ventilation cavity was only slightly lower, at 27.1 °C, whereas higher temperatures occurred in the upper region of the cavity. Significant differences in temperature distribution were obtained between the top and the bottom region of the SHC after 1800 seconds of the heating phase. The highest temperatures occurred in the top region of the SHC, where the volume-averaged temperature was 47.9 °C. After 3000 seconds, the temperature contour was almost fully developed, and showed a similar characteristic as was presented in Chapters 4.3.8 and 4.3.10. After 3600 seconds, the volume-averaged SHC temperature was 55.7 °C, and the volume-averaged air temperature inside the ventilation cavity was 34.9 °C.

5.2.3 Determination of the Optimal Time-step Size

The time-step size is a very important parameter in transient CFD simulations. The larger the chosen time-step, the shorter the simulation time, or the greater the time period that can be taken into account in the CFD simulations. For this reason, the heating phase from Chapter 5.2.2 was further calculated by using time step-sizes from one second to ten minutes. The comparison of all temperature profiles using different time-step sizes is presented in Figure 5-3. This figure also contains the comparison of the heating rate that was calculated from the temperature difference after every 5 minutes. Furthermore, both the temperature and heating rate profiles from measurements are indicated in the diagrams. The diagrams in the first row of the figure (red profiles) show the comparison of temperatures and heating rate at the ventilation outlet measurement position. The diagrams in the middle row of Figure 5-3 illustrate the resulting profiles (black) from measurement position MP3 inside the ventilation cavity of the SHC façade. The diagrams in the last row of this figure show the profiles (blue) of temperature and heating rate at the ventilation inlet measurement position.
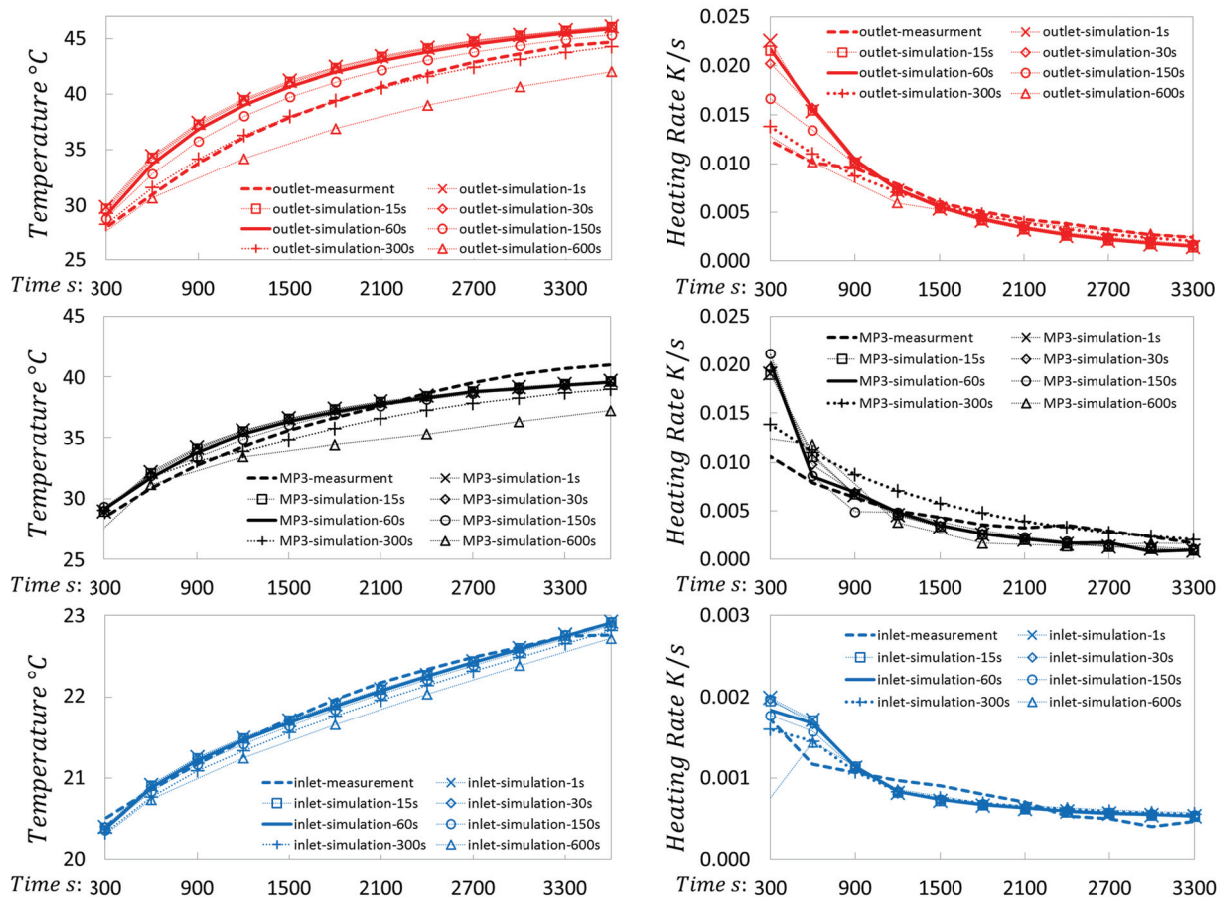
Figure 5-3: Comparison of the Temperature Profiles and Heating Rates at different Time-Step Sizes during the SHC's Heating Phase

The first transient CFD simulations were performed using a one-second time-step size. For the determination of the thermal behaviour over an hour, the entire calculation time took twelve days, using one PC with a six-core CPU. The entire calculation time was reduced to 48 hours by using a time-step size of 60 seconds. With time-step sizes over 150 seconds, it was possible to reduce the entire calculation time to less than 12 hours.

From the diagrams in Figure 5-3, it was ascertained that, with a time-step of 60 seconds, no significant deviations occurred between the temperature profiles. Compared to a time-step size of one second, the temperature was only 0.1 K lower at the position MP3 inside the SHC façade, 0.19 K lower at the ventilation outlet, and just 0.01 K lower at the ventilation inlet, after 3600 seconds of simulation. Furthermore, it was concluded from the diagrams that, up to a time-step size of 150 seconds, the deviations lie within an acceptable range. Compared to a time-step size of one second, the temperature was only 0.03 K lower at the position MP3 inside the SHC façade, 0.72 K lower at the ventilation outlet, and only 0.04 K lower at the ventilation inlet after 3600 seconds' simulation time, using a time-step size of 150 seconds.

For time-step sizes above 300 seconds, the temperature profiles at both the ventilation outlet and the measurement position MP3 deviated too much from the profiles when using smaller time-step sizes. Compared to a time-step size of one second, the temperature was 0.64 K lower at the position MP3 inside the SHC façade, 1.76 K lower at the ventilation outlet, and 0.1 K lower at the ventilation inlet after 3,600 seconds of simulation time using a time-step size of 300 seconds.

A maximum permissible time-step size of 150 seconds was determined from the simulation results, meaning that a time-step size of at least 120 seconds was proposed for the following simulations using hourly measured climate data in Chapter 5.2.5. Prior to this research project, such a CFD model did not yet exist in literature, and which suggests that this is an original contribution of this analysis of the thermal behaviour and heat transfer effects in the building and façade sector.

5.2.4 Variation of the SHC Material

After the validation of the transient CFD model, the influence of thermal mass and thermal conductivity of the SHC material on thermal behaviour was investigated. In the CFD simulation of the heating, used for the validation (Chapter 5.2.2), the cellulose honeycomb was replaced by a number of other materials with different specific masses, specific heat capacities and thermal conductivities. This is a theoretical consideration, but provides insight into the influence of material properties on heating effects. The properties of the involved materials are shown in Table 5-1.

Table 5-1: Material Properties.

Material Properties	ρ	c_p	$10^3 \cdot \rho \cdot c_p$	λ	α_{Sol}	τ_{Sol}
	kg/m^3	$J/(kg \cdot K)$	$J/(m^3 \cdot K)$	$W/(m \cdot K)$	$-$	$-$
Timbered Parts	1000	2000	2000	0.15	-	-
Glass (G)	2500	720	1800	1.00	0.05	0.9
Unalloyed Steel (St)	7800	490	3822	46.50	-	-
Aluminium (Al)	2800	896	2509	200.00	-	-
Acryl Glass (Ag)	1190	1470	1749	0.19	-	-
Silicon	2328	741	1725	150.00	0.9	-
Cellulose (C)	497	2500	1243	0.09	-	-

In the simulations, the same solar absorptivity was assumed for all materials with the same colour coating for the SHC. The whole simulation domain was initialized at 20 °C, and the air velocity started at zero value inside the cavity. An exterior temperature of 20 °C was assumed during the entire heating period, and an averaged solar radiation of 508 W/m² was used as a further boundary condition. The heating phase was stopped after 3600 seconds in the CFD simulations so as to compare the differences in thermal behaviour between the different SHC materials used.

Figure 5-4 illustrates how the temperature contours of the different SHC materials had developed after the simulated heating period of 3600 seconds. The same figure also shows the temperature contours for a xy-section through the centre of the SHC façade for each of the five SHC materials observed and

presents a comparison of the temperature contours of the SHC surface adjacent to the ventilation cavity.
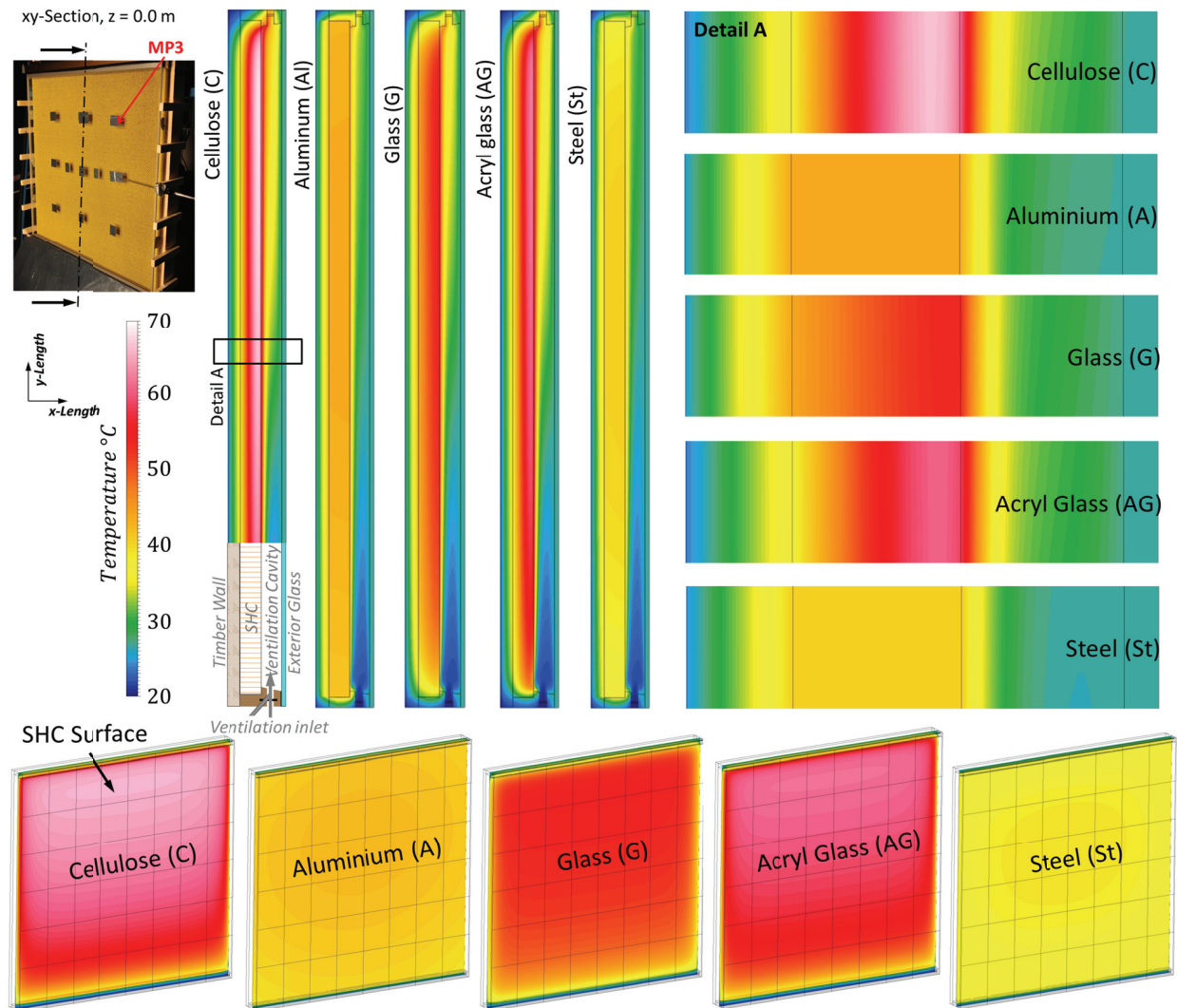
Figure 5-4: Temperature Contours for Different SHC Materials after a Heating Period of 3600 s

Figure 5-5 shows the comparison of the temperature profiles at position MP3 inside the SHC façade element (solid lines in the top diagram), the heating rate at position MP3 (in the bottom diagram) and the heat flux at the rear wall (RW) of the SHC façade element for five different SHC materials (dashed lines in the top diagram).

The results of the CFD simulations (Figure 5-4 and Figure 5-5) showed that the highest temperatures were obtained for the cellulose SHC after a heating period of 3600 seconds. Furthermore, the computed temperatures at the inlet and outlet, as well as at three points inside the SHC façade´s cavity using different SHC materials, are presented in Table 5-2. This table also presents the volume-averaged temperature of the SHC, the volume-averaged air temperature of the ventilation cavity of the SHC façade element, and the surface-averaged heat flux at the rear wall.

The highest SHC and air temperatures were achieved using cellulose as SHC material, which has the lowest density and thermal conductivity but the highest specific heat capacity of all SHC materials investigated.

With its higher density and lower specific heat capacity, but only slightly higher thermal conductivity, acryl glass exhibited similar heating characteristics and temperature contours (Figure 5-4). For acryl glass, less heat was transferred to the rear wall, although the magnitude was only marginally lower (2%) in comparison to the results from the cellulose SHC (Figure 5-5). Compared to the cellulose SHC, the air temperatures inside the ventilation cavity were slightly lower for the acryl glass SHC at the end of the heating phase, and the volume-averaged SHC temperature was approximately 4 K lower (Table 5-2).

Transient, Three-dimensional CFD Models
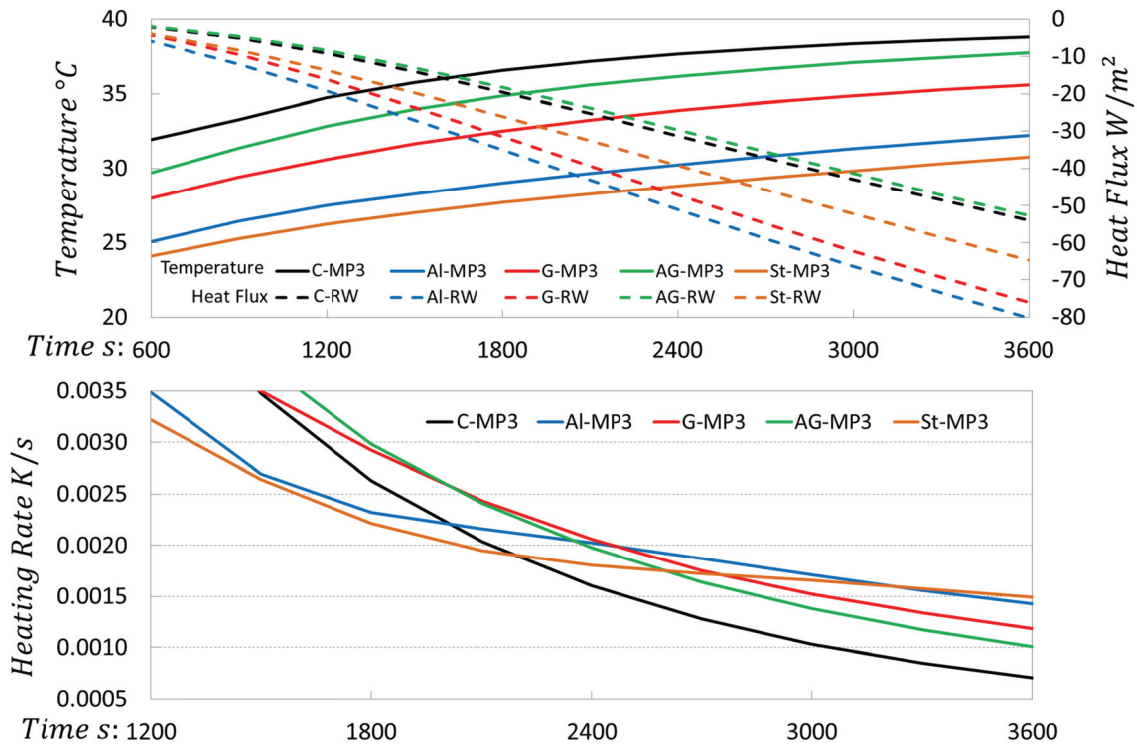
Figure 5-5: Comparison of Computed Temperature-, Heating Rate and Heat Flux Profiles during a Heating Phase of 3600 s for Different SHC Materials.

Glass has twice the density of acryl glass, only one half of the former´s large specific heat capacity, and five times higher thermal conductivity. From the heat flux profile in Figure 5-5, and from the temperature contours in Figure 5-4, it was observed that more heat was transferred to the rear wall of the façade element, although the temperature inside the glass SHC was lower than in the acryl glass SHC. Compared to the cellulose SHC, the air temperature was over 3 K lower at position MP3 and over 5 K lower at the ventilation outlet for the glass SHC (Table 5-2). The volume-averaged SHC temperature of the glass SHC was approximately 7 K lower compared to the cellulose SHC, but 41% more heat was transferred to the rear wall.

Table 5-2: Temperatures at Different Positions inside the SHC Façade Element (indicated in Figure 5-1), Volume-Averaged SHC Temperature and the Volume-Averaged Air Temperature of the Ventilation Cavity between the Five Different SHC Materials and Surface-Averaged Heat Flux at the Rear Wall of the Façade Element after 3600 Seconds of Heating

SHC-Materials	T_{outlet}	T_{inlet}	T_{MP3}	T_{MP6}	T_{MP9}	$T_{SHC-Vol}$	$T_{air-Vol}$	$q_{RW,avg}$
	$°C$	$°C$	$°C$	$°C$	$°C$	$°C$	$°C$	W/m^2
cellulose (C)	44.61	21.04	38.82	33.42	26.97	54.92	33.98	-53.97
acryl glass (Ag)	42.64	20.99	37.75	32.76	26.80	50.72	33.25	-52.77
glass (G)	39.07	21.03	35.62	31.42	26.44	47.68	31.79	-75.94
aluminium (Al)	34.75	21.36	32.23	29.51	26.15	43.10	29.74	-80.14
unalloyed steel (St)	32.66	21.13	30.76	28.40	25.36	39.52	28.59	-64.65

Due to their high thermal conductivity, the heat was rapidly transferred to the rear wall when steel or aluminium was used as SHC material. Moreover, the temperature contours in Figure 5-4 indicate almost uniform temperature distribution along the whole SHC. Compared to the cellulose SHC, the outlet temperature was approximately 10 K lower for the aluminium SHC, and almost 12 K lower using steel as the SHC material after a 3600 second heating period. Compared to the cellulose SHC, the volume-averaged SHC temperature for the aluminium SHC was approximately 12 K lower and about 49% more heat was transferred to the rear wall. The volume-averaged temperature of the steel SHC was over 15 K lower compared to the cellulose SHC and approximately 20% more heat was transferred to the rear wall. Steel, aluminium and glass are not suitable for use as SHC material because their thermal conductivity is too high, but, in the heating rate profiles in Figure 5-5, it was observed that the heating phase takes longer for SHC materials with higher thermal mass.

5.2.5 Transient Thermal Behaviour at Different Climates

Transient calculations were performed with two different SHC façade CFD models using measured climate data. The CFD model without attached PV cells (NoPV) and the model with the PV configuration PV03 were selected for this investigation [68]. For this purpose, climate data, collected hourly, in Graz during 2011 was selected in order to model the exterior temperature and solar radiation. January 1st, 2011 was chosen as representative of cold climate conditions, while August 25th, 2011 was selected to represent a day with hot climate conditions.

With this climate data, which was provided by ZAMG [76], the results of the simulation are able to provide insight into the dynamic thermal behaviour under real climate conditions. The time-step size was set to 120 seconds, as proposed in Chapter 5.2.3. To compute the thermal behaviour of one hour in the CFD model, approximately 3 hours of calculation time was needed with a six core CPU. In order to determine the thermal behaviour of one day, approximately 5 days of calculation time were necessary, when the changing of boundary conditions and the exporting of results are considered.

At first, the thermal behaviour for a cold winter's day was investigated using the climate data measured on January 1st, 2011. The first diagram in Figure 5-6 shows the measured exterior temperature, the measured global horizontal radiation, and the diffuse fraction of the measured radiation. Furthermore, this diagram also presents the actual incident radiation determined from the measured radiation value and information on the solar angle from a solar altitude diagram with the latitude of Graz. On January 1st, 2011 the exterior temperature was -5.1 °C on average, varying between -6.1 and -0.9 °C, and the daily average incident solar radiation was 73.9 W/m², with a maximum value of 627 W/m², measured at 14:00. The external boundary conditions required for the simulation were the external temperature, the actual incident radiation, the solar inclination, and azimuth angle. In the simulations, the SHC façade element was virtually attached to a façade oriented to the south. Therefore, at the rear wall of the SHC façade element, a virtual brick wall layer with a thickness (x_M) of 0.3 m was added to the CFD model, in addition to a virtual convective heat transfer layer to an interior room with an assumed average air temperature (T_{room}) of 20 °C, and a heat transfer coefficient (α_{room}) of 5 W/m². The heat transfer coefficients used were typical default values, representing the heat transfer to the interior and exterior environment. The masonry had a density of 1100 kg/m³, a thermal conductivity (λ_M) of 0.43 W/mK, and a specific heat capacity of 840 J/kgK.

The results of transient simulations of the cold winter's day, the hourly determined surface-averaged temperatures for four different xy-section planes through the SHC façade, and the surface heat flux to the interior masonry brick wall are all summarized in Figure 5-6. Plane 1 in the diagrams is the rear wall of the façade element, while plane 2 is a section through the centre of the SHC, plane 3 is the exterior surface of the SHC adjacent to the ventilation cavity, and plane 4 is a section plane through the façade element at a distance of 10 mm from the SHC. For the start of the transient simulation, the data from the steady state CFD simulation, with the boundary conditions of midnight, January 1st, 2011, was used. To determine the influence of the thermal storage ability, the data collected from the end of day 1 was used to simulate the thermal behaviour of the SHC façade for a further day, under the same external boundary conditions (day 2). For the days before day 1, no solar radiation loads on the SHC façade were assumed.

The temperatures inside the SHC and the ventilation cavity were mainly influenced by the solar radiation that occurred. The highest surface-averaged temperatures were detected inside the SHC (plane 2). While temperatures decreased rapidly beyond the influence of the solar radiation, inside the SHC and the ventilation cavity, the rear wall cooled down slowly. The difference in the average surface temperature of the rear wall of the SHC façade without PV cells (plane 1) was 5 K between the beginning and the end of day 1, and only 0.6 K between the beginning and the end of day 2. For PV configuration PV03, the difference in the average surface temperature of the rear wall was 3.7 K from the beginning to the end of day 1, and only 0.4 K between the beginning and end of day 2. It was observed that this difference decreased towards the exterior. For the SHC façade without PV cells, the difference in the average surface temperature of plane 4 was 1.0 K between the beginning and the end of day 1 and almost zero between the beginning and the end of day 2.

Due to the assumed constant interior temperature and heat transfer coefficient, the surface-averaged heat flux at the rear wall correlated with the rear wall's surface-averaged temperature, and was calculated as follows, in Equation 5-1.

$$q_{RW,avg} = \frac{1}{\frac{1}{\alpha_{room}} + \frac{x_M}{\lambda_M}} \cdot \left(T_{room} - T_{RW,avg}\right)$$

<div align="right">**Equation 5-1**</div>

In the course of day 1, an average heat flux of 15.5 W/m² was detected from the masonry brick wall towards the SHC façade without PV cells, whereas the heat loss was only 13.7 W/m² on average for day 2. This lower heat loss was explained by the stored heat after day 1. The average heat loss from the brick wall towards the façade with PV configuration PV03 was 17.6 W/m² for day 1 and 16.3 W/m² for day 2. The results show that the history of the thermal behaviour from the previous day had an impact on the thermal behaviour of the actual day.
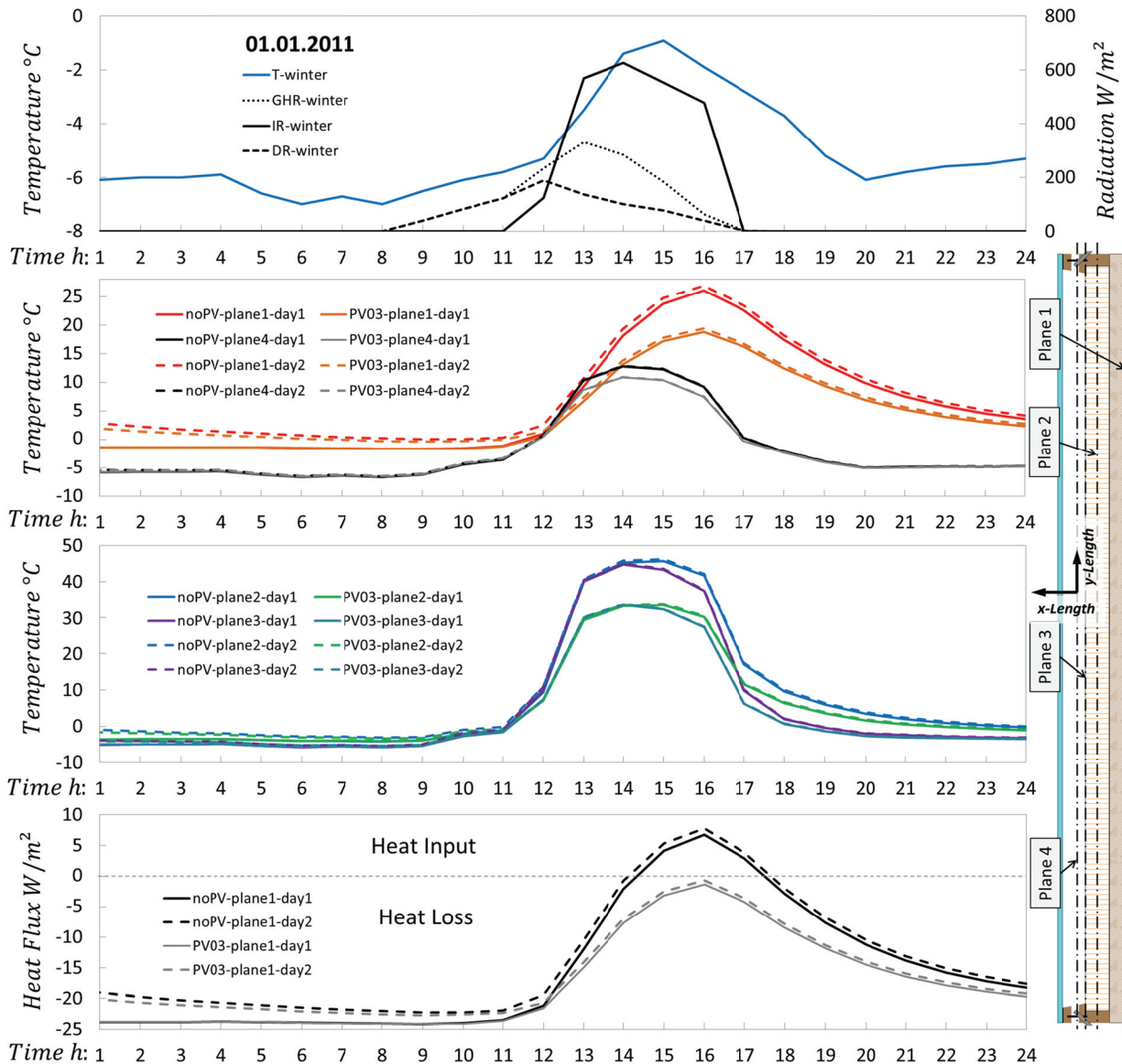
Figure 5-6: Temperature and Radiation Profiles of the SHC Façade Element Without PV Cells and PV Cell Configuration PV03 for a Cold Winter's Day (1st January 2011)

Figure 5-7 presents the temperature contours of the xy-section through the middle of the SHC façade, the rear wall (plane 1) and the honeycomb surface adjacent to the ventilation cavity (plane 3) for the SHC façade element without integrated PV cells. Figure 5-8 presents the same for PV cell configuration PV03. At 12:00 on day 2, for the SHC without PV cells and the PV cell configuration PV03, the maximum temperature was 14.9 °C on plane 4 and 7.5 °C on plane 1 at an external temperature of -5.3 °C and an incident solar radiation of 124 W/m². For PV cell configuration PV03, the maximum temperature was 12.9 °C on plane 3 and 6.5 °C on plane 1. In contrast to the symmetrical contours of temperature and air

velocity at 12:00, there were indicators of asymmetrical behaviour at other times of day due to the varying azimuth angles. For example, higher temperatures occurred on the right side of the illustrated contours at 15:00. The maximum temperature was 57.4 °C on plane 3 and 32.0 °C on plane 1 at an external temperature of -0.9 °C and with an incident solar radiation of 553 W/m² for the SHC façade without PV cells. For case PV03, the maximum temperature was 54.3 °C on plane 3 and 29.9 °C on plane P.
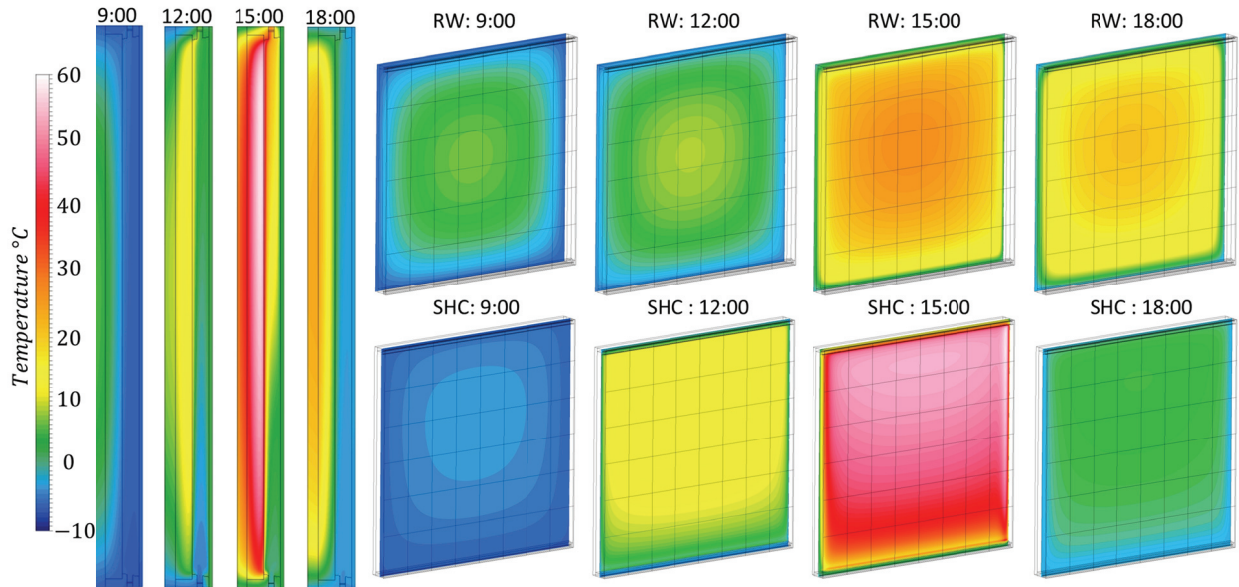
Figure 5-7: Temperature Contours for the Rear Wall and the SHC Surface Adjacent to the Ventilation Cavity for the SHC Façade without PV Cells at Four Different Times of Day Two in the Simulation for Cold Winter Climate
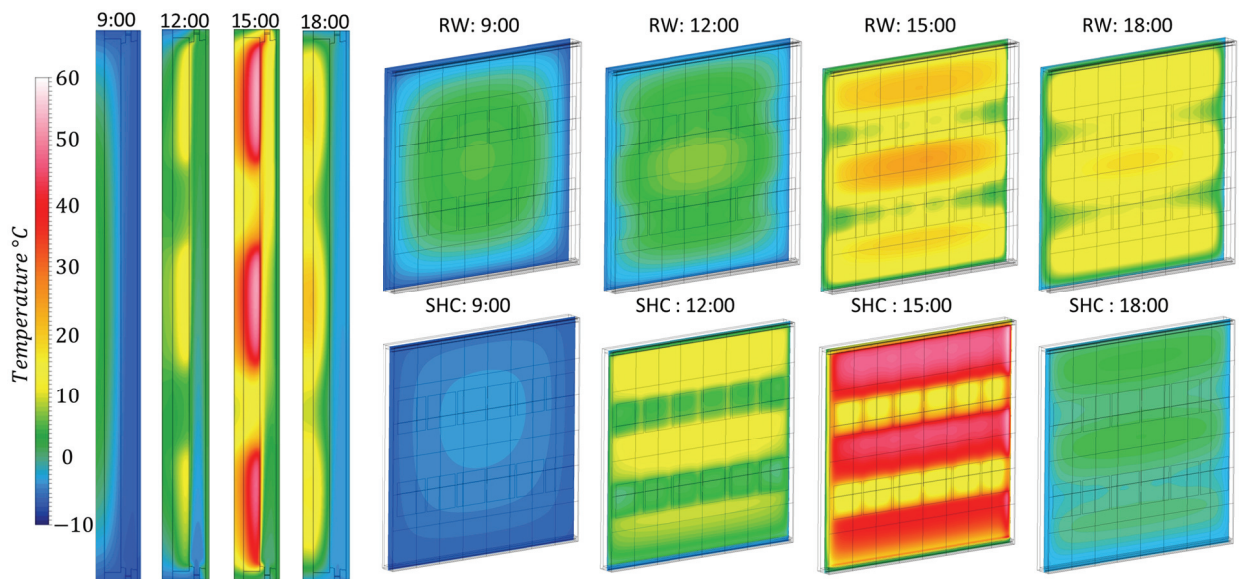
Figure 5-8: Temperature Contours for the Rear Wall and the SHC Surface adjacent to the Ventilation Cavity for the SHC Façade with PV-Cell Configuration PV03 at Four Different Times of Day Two in the Simulation for Cold Winter Climate

The thermal behaviour of the SHC façade element was also investigated under hot summer conditions in Graz. For the determination of the transient behaviour, the approach for steep solar angles from the CFD model development in Chapter 4.3.8 was used, in which the solar radiation did not penetrate the SHC, but was partly absorbed at the SHC´s surface adjacent to the ventilation cavity. Similar to Figure 5-6, the profiles of external temperature, measured global horizontal radiation, diffuse fraction, and the actual incident solar radiation are indicated in the first diagram in Figure 5-9. On the selected day (August 25th, 2011), the external temperature varied between 19.8 and 33.6 °C based on an average value of 25.8 °C. The averaged incident solar radiation was 309 W/m², while the maximum radiation of

810 W/m² occurred at 13:00. Because the same virtual room layer from investigations at cold climate conditions was used for the simulations of hot climate conditions, the same material properties of the masonry and the same heat transfer coefficient were used; only the interior room temperature were changed from 20 to 25 °C in summer.

Figure 5-9 shows the resulting surface-averaged temperature and heat flux profiles over the day at four different sections through the SHC façade, in the same way as Figure 5-6. Again, the data collected at the end of day 1 was used for the starting conditions of day 2, where the same external boundary conditions were assumed as for day 1. The resulting temperature and heat flux profiles are represented as dashed lines in the diagrams.

Similar to the results from the winter's day, the surface-averaged temperature profiles of planes 2, 3 and 4 were strongly influenced by the appearance of solar radiation in summer. The highest temperatures occurred at the SHC surface adjacent to the ventilation cavity (plane 3). Again, slower heating and cooling effects were observed at the rear wall (plane 1) of the SHC façade compared to the other surfaces.

After day 1, the surface-averaged temperature of plane 1 for the SHC façade without PV cells was 5.6 K higher, while after day 2, the temperature had increased by only 0.7 K. Between day 1 and day 2, smaller temperature differences occurred at the other investigated planes. Inside the SHC (plane 2), the temperature difference was 3 K after day 1 and 0.4 K after day 2. The SHC surface adjacent to the ventilation cavity showed a 0.9 K higher average surface temperature after day 1, whereas the difference between the end of day 1 and the end of day 2 was only 0.1 K. For the case PV03, the difference between the surface-averaged temperature at the rear wall (plane 1) between start and end of day 1 was 4.9 K and 1.6 K between start and end of day 2. The difference in temperature inside the SHC (plane 2) was 2.6 K after day 1 and 0.3 K after day 2, while at plane 3, very small temperature differences occurred, with 1.7 K after day 1 and only 0.1 K after day 2.

The daily-averaged heat emitted to the masonry for the SHC façade without PV cells was 4.7 W/m² on day 1, while for PV03, it was slightly lower, with 3.3 W/m². Due to the stored heat, after day 1, the heat input was generally higher. During day 2, the masonry was heated by 6.8 W/m² using the SHC façade without PV cells and 5.1 W/m² using PV configuration PV03. The results of the transient CFD simulations under hot summer conditions also showed significant differences in the thermal behaviour when using different start conditions. Furthermore, from the temperatures profile in Figure 5-9, it was possible to see that the temperatures at the exterior SHC surface (plane 3) inside the ventilation cavity nearly stopped increasing between 10:00 and 13:00, although the measured solar radiation was still increasing. This effect was caused by the very high solar angle at noon.

In Figure 5-10, the thermal behaviour at four different times of day is presented for the SHC façade element without attached PV cells, and in Figure 5-11, for the façade with PV cell configuration PV03. This figure illustrates the temperature contours for a section through the centre of the façade (xy-section, z=0.0 m) at the rear wall (plane 1) as well as at the exterior SHC surface (plane 3) at 09:00, 12:00, 15:00 and 18:00.

The solar radiation impinged on the façade at a solar angle of 56° and an azimuth of 0°. Due to the higher solar angle, less heat penetrated the SHC under hot summer conditions. While in summer, the highest temperature occurred at the exterior surface of the SHC, the highest temperatures were detected inside the SHC for cold winter conditions with steeper solar angles. While in winter the temperature and air velocity contours indicated symmetrical behaviour, slightly higher temperatures occurred on the left side of the contours in summer. These deviations were mainly caused by the heating effects of the sun before 12:00, at a negative azimuth angle.

At 12:00 on day 2, the maximum temperature at the rear wall (plane 1) of the SHC façade without PV cells was 36.1 °C, whereas it reached 61.2 °C at the exterior SHC surface (plane 3). For the façade with PV configuration PV03, the maximum temperature at the rear wall (plane 1) was 34.2 °C and 55.9 °C at the exterior SHC surface (plane 3).
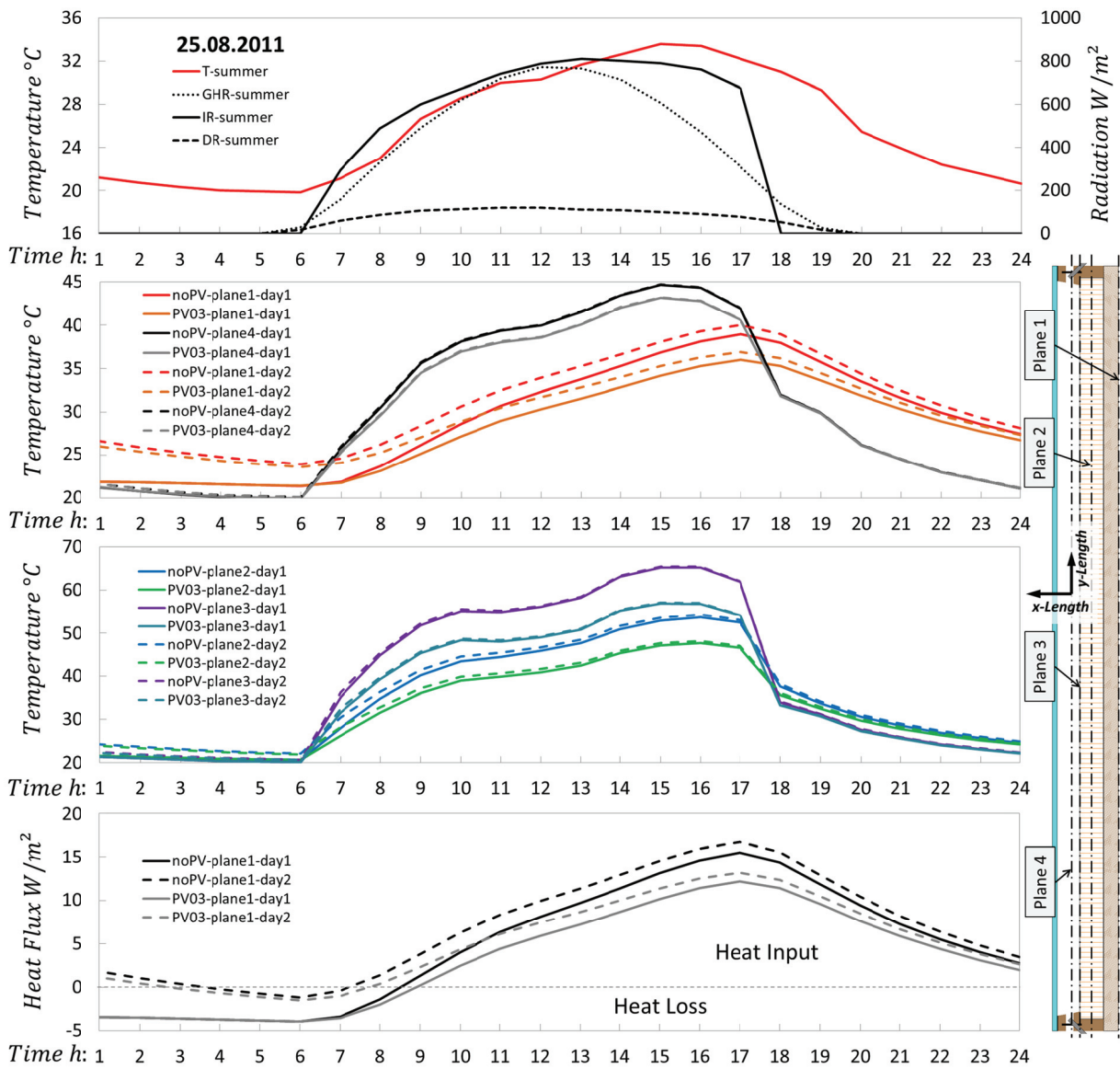
Figure 5-9: Temperature and Radiation Profiles of the SHC Façade Element Without PV Cells and PV Cell Configuration PV03 for a Hot Summer's Day (August 25th, 2011)

Maximum temperatures of 34.2 °C on plane 1 and 78.7 °C on plane 3 of the SHC façade without PV cells were detected at 15:00 on day 2 of the simulation. At this time of day, maximum temperatures of 37.9 °C on plane 1 and 75.8 °C on plane 3 were detected for PV configuration PV03. In contrast to the temperature contours at 12:00, higher temperatures occurred on the inner right side of the façade element due to the positive azimuth for the time after noon. This asymmetrical thermal behaviour was observed up to the rear wall of the SHC façade with configuration PV03 as well as without PV cells (NoPV). Compared to the thermal behaviour at 12:00, the maximum temperatures inside the façade element and the shadows of the PV cells in configuration PV03 were detected at a higher position at 15:00.

Furthermore, it was determined that the highest temperature of the exterior glass (NoPV = 40.3 °C, PV03 = 44.1 °C) was detected at 15:00, and the highest temperature of the SHC (NoPV = 78.8 °C, PV03 = 75.9 °C) occurred at 16:00, whereas the highest temperature of the timber wall (NoPV = 42.4 °C, PV03 = 40.9 °C) was observed at 17:00 on day 2. The volume-averaged air temperature inside the ventilation cavity was at its highest at 15:00 (NoPV = 45.7 °C, PV03 = 43.9 °C).
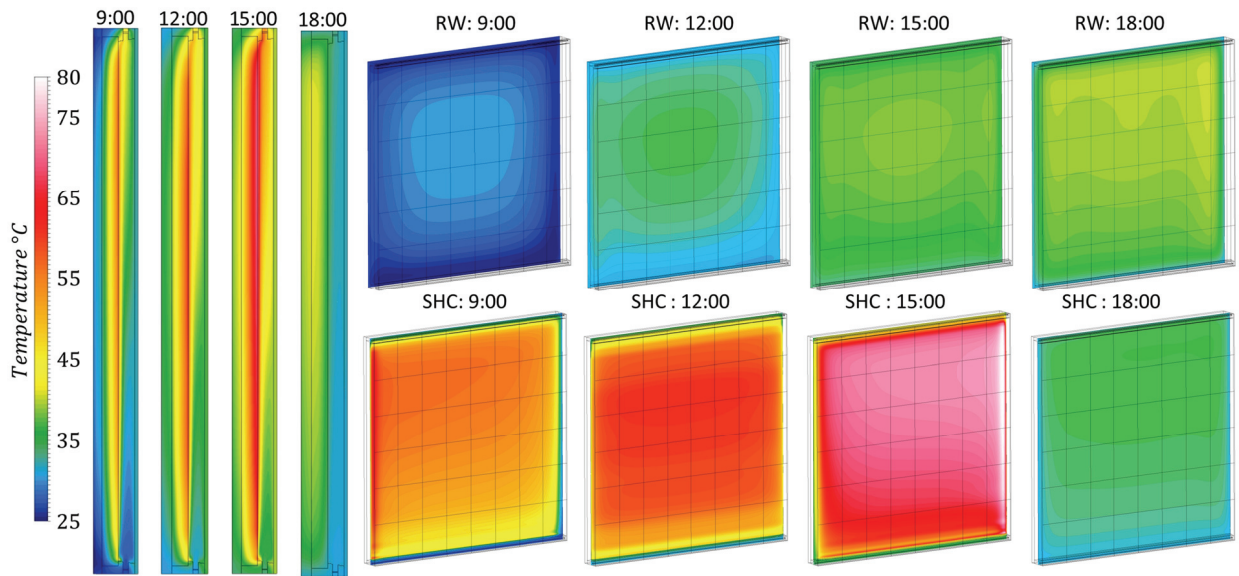
Figure 5-10: Temperature Contours for the Rear Wall and the SHC Surface Adjacent to the Ventilation Cavity for the SHC Façade Without PV Cells at Four Different Times of Day Two in the Simulation for Hot Summer Climate
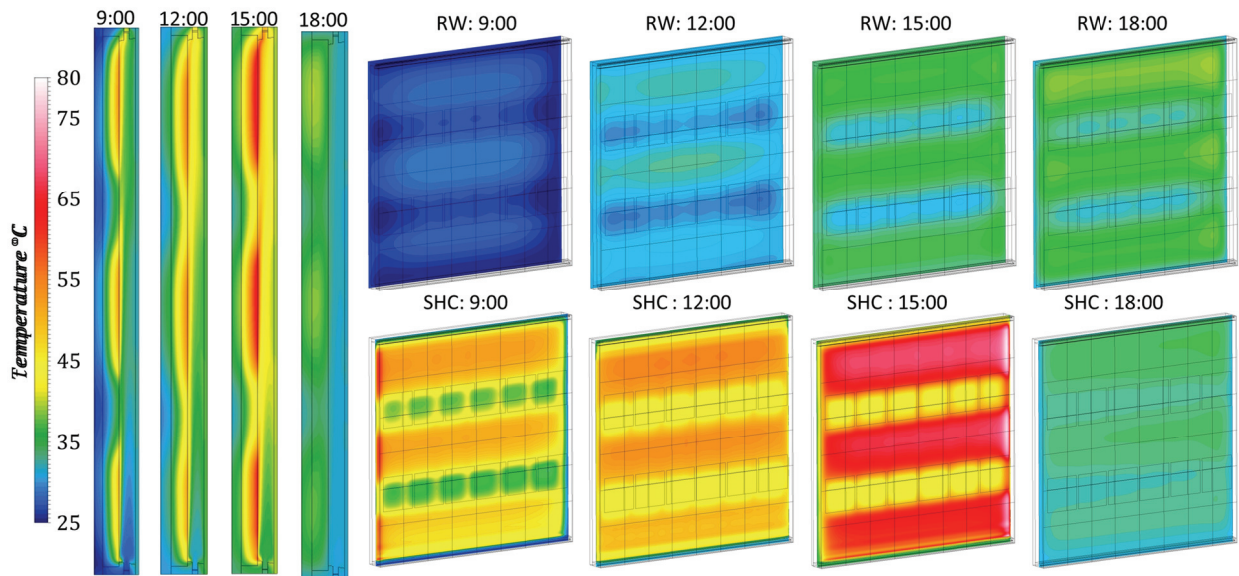
Figure 5-11: Temperature Contours for the Rear Wall and the SHC Surface Adjacent to the Ventilation Cavity for the SHC Façade with PV-Cell Configuration PV03 at Four Different Times of Day Two in the Simulation for Hot Summer Climate

6 Conclusions[10]

In this final chapter, the highlights of this dissertation are reviewed, and the knowledge gained with regard to the façade application and the numerical model approach is summarized and presented in the same order as it was introduced.

In the course of this research project, the CFD tool Fluent ANSYS, and the CFD method generally, makes it possible to create a broad range of simulation scenarios that cover the combined physical behaviour of conductive and radiative heat transfer effects as well as the natural and forced convective air flow inside and around the building's facade.

This study presents the progress from simple two-dimensional considerations up to very complex three-dimensional simulation models, as different functional components are added to the façade. The knowledge gained from this work can be used in the building sector in order to quickly obtain results for special issues relating to the thermal characteristics of facades or sections of a façade without the effort of expensive experiments. Someday it might be possible to extend the three-dimensional domain in the CFD simulation from small ventilation cavities to the whole building and a large part of its environment, or even to consider several buildings at one time.

6.1 Conclusions from the Stationary, Two-dimensional CFD Models

In the first step of the numerical modelling of façade applications within this work, two-dimensional geometries were used. Generally, two-dimensional meshing is simpler, the difference between the largest and the smallest fluid cells is larger, and they are less time-intensive to create in comparison to the creation of three-dimensional models. Moreover, it is possible to cover both very fine details, such as the air permeable joints of box type windows (BTW), and whole interior rooms or large sections of the external environment.

6.1.1 Box Type Windows (BTWs)

The study of the BTW in Chapter 3.2 covers a detailed prediction of the thermal behaviour of a traditional BTW´s inner cavity and close exterior environment via CFD Dynamics for cold winter climate conditions. Such a comprehensive analysis of the thermal behaviour and combined air flow of this special form of a partly ventilated double façade has not yet been done, according to current literature.

The simulation model domain covers the façade with the integrated BTW, the whole interior room, and a section of the exterior, in order to determine the flow characteristic of the inner cavity as well as the effects of infiltration due to natural ventilation. Sectional profiles of temperature and buoyancy velocity describe the shape, stratification, and magnitude of the convective flow along the window casements at the inner cavity. The maximum buoyancy effect occurs in the middle of the BTW´s height.

The comparison with results from in-situ measurements showed good agreement between the simulation and measurement results of the refurbished (A) and the improved BTW (G), with an inner gasket frame and low emission coating. Furthermore, it was possible to create a virtual hot box to determine U values, which can be used for a comparison with other window types.

6.1.2 Multifunctional façade Construction

Contrary to the study of old, historical facades the multifunctional façade construction is one of the very promising new concepts for the future of building facades. This type of façade has a very complex structure and integrates solar collector systems as well as ventilation channels and other components. As a consequence also the CFD model is getting very complex and consists of a large number of different fluid and solid zones. A similar meshing strategy as for the BTW is used.

In the simulations not only cold climate conditions were considered, but also a hot summer day was simulated, which requires the integration of the heating effects due to solar radiation in the CFD model. This was realized by means of pre-calculated heat sources, which were implemented in the form of surface heat sources. This enhancement of the CFD model performed very well and the simulation results show a good agreement with monitored data. Finally, the thermal behaviour and flow

---

10. Parts of this section have been published earlier in [17], [18], [58], [19], [60], [20] and [21].

characteristics of four vertical façade sections of a new prototype of a façade construction attached to a test building were determined using two-dimensional CFD simulations. The thermal impact of installed solar thermal collectors and photovoltaic panels on the ventilation performance was analysed. In the course of a literature review no previous work was found with CFD simulations using such a large and complex domain with this large number of involved zones. Also the consideration of a façade integrated (flat plate) solar thermal collector using water as heat carrier medium in a CFD simulation has not been a topic in literature before.

6.2   Conclusions from Stationary, Three-dimensional CFD Models

While two-dimensional simulations quickly provide good results for a first estimation of heat transfer effects and flow behaviour, only three-dimensional simulations can assess all of the necessary details in many ventilated façade applications. For example, the analysis of the influence of the periphery openings on the ventilation effects of the façade in Chapter 4.2 was only possible with the help of three-dimensional CFD models. Generally, for two-dimensional simulation models, the number of cells is orders of magnitude lower than in three-dimensional models. The two-dimensional meshes were constructed using the paving meshing method, where the maximum skewness slightly exceeded a value of 0.9. Meanwhile, three-dimensional meshes were developed using the sweeping meshing method, containing only hexahedral cells; therefore, skewness did not exceed a value of 0.35.

This study presents two sophisticated three-dimensional CFD simulation models, which constitute an original contribution, as these had not yet been presented in scientific literature. A crucial part of this dissertation, especially in the three-dimensional CFD simulations, is the consideration of the radiative heat transfer mechanism and heating effects due to solar radiation. The influence of the radiative heat transfer in the range of the thermal radiation (that is, radiation with a wavelength higher than 2.5 μm) could easily be implemented in the CFD simulations. Basically, two of the radiation models provided by ANSYS Fluent were perfectly suited for the consideration of thermal radiation in the simulations: the S2S and the DO radiation model. Although the S2S model required less computing performance in all simulations of this study, the DO radiation was used because this model also makes it possible to consider different wavebands. This was essential in order to consider the dependence of the absorption characteristics of the materials on the wave-length. Finally, with the help of the DO model, it was possible to sufficiently consider the transmission, absorption, and reflection of solar radiation (λ_{ES} = 0.38 - 2.5 μm) and the thermal radiation (λ_{ES} > 2.5 μm) for the simulations. If required, the accuracy of the absorption characteristic could be further improved by using more wavebands, covering the range of solar and thermal radiation.

6.2.1   Functional Façade Element Models

The thermal behaviour and the characteristics of air flow for the three most interesting façade elements of the "Multifunctional Plug & Play Façade" (MPPF) test façade were analysed, especially at the region around the air-ventilated cavity between the interior wall and the three different modules. Consequently, three-dimensional CFD models were developed for the different façade elements (PV, TR, and ST). Because of the façade elements' characteristics, the steady state CFD simulation strategy is the proper method to determine the thermal behaviour and ventilation effects. When the simulation results were compared with corresponding monitored data from a summer day, the two showed good agreement.

The influence of the side openings of the façade was clearly identifiable only by using three-dimensional CFD models. This dissertation marks the first time that such a CFD façade model with periphery openings has been presented in scientific literature. The ventilation effect is boosted by these openings, and, thus, the heat loads on the interior wall are further reduced. The air infiltrates the façade´s cavity from the side until a height (y-length) of approximately 0.5 m above the middle of the cavity´s height (y-length), where the airflow changes direction and the heated air leaves the cavity.

A comprehensive comparison of the three façade elements was performed, and led to the following conclusions: the highest air temperature inside the ventilation cavity occurs in the façade element with the integrated PV module at the exterior layer (PV façade). Due to the thermal insulation behind the solar thermal collector in the ST façade, the air temperature in the ventilation cavity is lower than in the PV façade, although the temperature for the absorber is clearly higher than for the PV module.

Additionally, the temperatures inside cavities with closed and open façade elements were compared. This comparison shows a significant difference in air temperatures inside the façade´s cavities. Therefore, it is necessary for this façade system to be ventilated, in order to reduce the high heat loads of the interior room in the summer, when a functional component such as a PV module is integrated.

6.2.2   Solar Honey Comb Façade Element Models

From the investigation of the solar honeycomb (SHC) façade element and the comparison of numerical simulations and laboratory experiments, the following conclusions can be drawn. Different approaches to the SHC were modelled and tested with the help of CFD models built specifically for this investigation. Based on the comparisons of laboratory experiments and preliminary two-dimensional CFD simulations, an adequate three-dimensional model was created, the first of its kind to be presented in literature. The results from the final model of the SHC façade without PV cells match the data from the experimental measurements very well.

The simulation results from the CFD models of the SHC façade with the integrated PV cells, where the parameters of the SHC façade model without PV cells were used, also matches very well with the data from the experimental measurements. Only the three-dimensional model made it possible to determine the influence of the varying PV cell arrangements at the exterior glass. With this approach, it is also possible to calculate the transient behaviour of an SHC façade element, where the variation of the external temperature and the solar radiation over the day can be considered. The SHC façade´s functionality with seven different PV cell configurations was confirmed with the help of CFD simulations. The evaluation of the functionality involved the thermal behaviour and the ventilation performance as well as the electrical output of the PV array.

Fewer disturbances of the flow behaviour were found through when using horizontal rows of PV cells (PV03 and PV04), as shown by the cross-comparison of the different PV cell configurations for the façade element. The overall performance of the very promising semi-transparent PV cell array (PV05) was not as good as expected. The ventilation performance was acceptable, but the thermal performance was too low in comparison to configurations PV03 and PV04. Furthermore, the electrical output was not significantly higher than that of configuration PV03, and was, in fact, considerably lower than configuration PV04.Depending on application of priority – whether that is the higher electrical power or better thermal behaviour of the SHC - configurations PV03 and PV04 are recommended, respectively.

After the evaluation of the PV cell configuration, the thermal behaviour and airflow characteristics of the SHC façade elements were analysed for summer and winter climate conditions in a moderate zone.

For winter climate conditions, the thermal behaviour and the air flow characteristics were similar to the results of the simulations under laboratory conditions because the flat inclination angle of the solar radiation, which occurs in winter, was used in the laboratory experiments. For summer climate conditions, especially around noon, the solar radiation no longer penetrates the SHC, because of the steep solar radiation angles. Therefore, there are some differences in the thermal behaviour and airflow characteristics between summer and winter climate conditions.

In summer, the PV cells exhibit higher temperatures than the SHC, but the ventilation of the cavity still works well for PV cell configurations PV03 and PV04. For the PV cell configurations PV01 and PV02, the disturbances are higher in summer as a result of the heating effects of the PV cells. Generally, more heat is transferred to the masonry wall and further to the interior room for the chosen cold climate conditions than for the hot climate conditions, even though the solar radiation is much higher in summer.

6.3   Conclusions From Transient, Three-dimensional CFD Models

6.3.1   The Transient Solar Honey Comb Façade Element Model

The complex three-dimensional CFD model created for the PV cell assessment (Chapter 6.2.2) was further developed in order to determine the transient thermal behaviour of a single SHC façade element. This research made it possible to carry out a detailed analysis of the transient thermal behaviour and the heat transfer effects of complex façade constructions within a reasonable simulation

time. The following conclusions can be drawn from the research on the transient behaviour of the SHC façade element conducted in the course of this dissertation.

Measured data from transient laboratory experiments were compared with the results CFD simulation results. The temperature and heat flux profiles resulting from the simulations match very well with the measured profiles. Furthermore, the maximum time-step size was again determined using measured data and external boundary conditions from the experimental heating phase. The time-step size was increased from the initial assumption of one second to 600 seconds. A time-step size of up to 150 seconds still resulted in good agreement between the transient CFD model and the measured temperature profiles, and the overall simulation time was reduced significantly.

In an investigation of the influence of the SHC material on thermal behaviour, the cellulose SHC was replaced by materials with different densities, specific heat capacities, and thermal conductivities. From the resulting temperature profiles, it was possible to conclude that materials with a thermal conductivity of 1.0 W/mK or higher are not suitable for use as SHC material. From the heating rate profiles, it was ascertained that the duration of the heating phase was extended using materials with higher thermal masses.

The increased time-step size makes it possible for this complex three-dimensional CFD model to simulate the dynamic thermal behaviour of a cold winter day and a hot summer day. Hourly changing external temperatures and the influence of hourly-varying intensity and direction of solar radiation were considered in the analysis. Two different initial conditions were used in the analysis of the daily dynamic thermal behaviour. The first was assumed for a day after a longer period without sunshine (day 1). For the second initial condition, one previous day with the same external conditions as the observed day itself was assumed (day 2). Using the climate data January 1st, 2011 (cold winter day) in Graz, an average heat loss of 15.5 W/m² from a masonry brick wall to the SHC façade was determined for day 1. The heat loss was approximately 12% lower for day 2. Using the climate data from August 25th, 2011 (hot summer day) a daily average heat input to the masonry of 4.7 W/m² was obtained. The heat input increased by almost 45 % in the simulation results of day 2. Additionally, the influence of PV cells on the dynamic thermal behaviour of the entire SHC façade was analysed. Generally, the simulated surface-averaged temperature profiles for the SHC façade with PV cells were lower compared to the façade element without PV attached cells, because the PV cells partly shaded the SHC surface during periods of sunshine. The gap between the temperature profiles of the two variants with (PV03) and without (NoPV) PV cells increased under higher solar radiation.

6.4   Outlook

The successful models and the results that they provided constitute a big step forward in the field of numerical simulations of thermal behaviour and fluid dynamics in the field of façade constructions and in the building sector. With the CFD method, it was possible to describe the most important physical phenomena both inside a façade and in its close environment, which have an impact on the thermal behaviour. It is possible to assume that access to computing power will continue to increase, and that simulation tools will continue to improve as well. Consequently, in the future, it could be interesting to consider the realisation of the enhanced façade models on larger domains. Even though the CFD model cannot currently match building simulation tools in terms of determining thermal behaviour over the course of a year or more, this could become possible sometime in the near future.

With regard to the facades that were investigated herein, and the numerical models used, the following should be taken into consideration for future research projects. For the historical box type window, it would be enlightening to develop a three-dimensional CFD model in order to also consider the sideward occurring permeable joints in the analysis of the thermal behaviour and fluid dynamics. The radiation model that was used in the assessment of the solar honeycomb façade element could also be used for further simulations of the BTW.

For the multifunctional façade, it would be interesting to conduct further simulations in which more than one façade element is involved in the three-dimensional simulations. Furthermore, the influence of external wind loads might have a considerable impact on the thermal behaviour and the ventilation effects inside the façade elements´ cavities.

In terms of the solar honeycomb façade, the numerical model could be enhanced by dividing the honeycomb into several solid layers with different degrees of solar absorptivity.

Conclusions and Outlook

In the building sector in general, consideration of condensation is becoming more and more important, in particular when functional components with very dynamic thermal behaviour are integrated, for example, a solar thermal collector and hydraulic installations. For this reason, it is necessary to develop a further CFD model in order to be able to model regions with high degrees of moisture or even condensation inside of facades that are becoming increasingly complex as a result of the functional components integrated.

7 Literature

[1] *"denkmalaktiv I, Sanierung alter, denkmalgeschützter Häuser (refurbishment of old, historical buildings)",* project Nr. 82120.

[2] *Multifunctional Plug & Play Façade (Project-No.: 815075), K-Project in course of Austrian COMET (Competence Centers for Excellent Technologies), (2008-2013)..*

[3] *alpS-project ''B02 eNVELOP Teil C'' (Project-No.: 826388).*

[4] *Meshing software „Gambit 2.4.6", Fluent, Incorporated, Centerra Resource Park 10 Cavendish Court Lebanon, NH 03766 (Link to User's Guide: http://aerojet.engr.ucdavis.edu/gambithelp/index.htm) Release 2.4 (2007).*

[5] *Fluid Dynamics software "ANSYS Fluent 14.0.0",ANSYS Inc., Southpointe 275 Technology Drive Canonsburg, PA 15317, http://www.ansys.com, Release 14.0 (2011).*

[6] *ANSYS Fluent 14.0. Userguide/Theoryguide.*

[7] *ANSYS Fluent 15.0. Userguide/Theoryguide.*

[8] G. Brenn und W. Meile, Strömungslehre un Wärmeübertragung I, Graz: Institut für Strömugslehre und Wärmeübertragung, Technische Universität Graz, 2015.

[9] G. Brenn, *Materialien zu den Vorlesungen und Übungen Strömungslehre und Wärmeübertragung,* Graz: Institut für Strömungslehre und Wärmeübertragung, Technische Universität Graz, 2005.

[10] A. Baïri, „Transient free convection in passive buildings using 2D air-filled parallelogram-shaped enclosures with discrete isothermal heat sources, Energy and Buildings," *Energy and Buildings,* Bd. 43, Nr. 2–3, pp. 366-373, February–March 2011.

[11] H. Manz, „Numerical simulation of heat transfer by natural convection in cavities of facade elements," *Energy and Buildings,* Bd. 35, pp. 305-311, 2003.

[12] O. Aydin, „Conjugate heat transfer analysis of double pane," *Building and Environment,* Nr. 41, pp. 109-116, 2006.

[13] J. Xamán, G. Álvarez, L. Lira und C. Estrada, „Numerical study of heat transfer by laminar and turbulent natural convection in tall cavities of façade elements, Energy and Buildings," *Energy and Buildings,* Bd. 37, Nr. 7, pp. 787-794, 2005.

[14] J. Wright, H. Jin, K. Hollands und D. Naylor, „Flow visualization of natural convection in a tall, air-filled vertical cavity," *International Journal of Heat and Mass Transfer,* Bd. 49, pp. 889-904, 2006.

[15] O. Aydin, „Determination of optimum air-layer thickness in double-pane windows," *Energy and Buildings,* Bd. 32, pp. 303-308, 2000.

[16] G.-M. Armando, B.-B. J. Armando, V.-C. Christian, V. Rangel-Hernández und J. Belman-Flores, „Analysis of the conjugate heat transfer in a multi-layer wall including an air layer," *Applied Thermal Engineering,* Bd. 30, pp. 599-604, 2010.

[17] A. Pappas und Z. Zhai, „Numerical investigation on thermal performance and correlations of double skin façade with buoyancy-driven airflow," *Energy and Buildings,* Bd. 40, pp. 466-475, 2008.

[18] H. Manz, „Total solar energy transmittance of glass double façades with free convection," *Energy and Buildings,* Bd. 36, pp. 127-136, 2004.

[19] A. Guardo, M. Coussirat, C. Valero, E. Egusquiza und P. Alavedra, „CFD assessment of the performance of lateral ventilation in Double Glazed Facades in Mediterranean climates," *Energy and Buildings,* Nr. 43, pp. 2539-2547, 2011.

[20] C. Sanjuan, M. Suarez, M. Gonzalez, J. Pistono und E. Blanco, „Energy performance of an open-joint ventilated facade compared with a conventional sealed cavity facade," *Solar Energy,* Nr. 85, pp. 1851-1863, 2011.

[21] C. Balocco, „A simple model to study ventilated facades energy performance," *Energy and Buildings,* Bd. 34, pp. 469-475, 2002.

[22] M. Ciampi, F. Leccese und G. Tuoni, „Ventilated facades energy performance in summer cooling of buildings," *Solar Energy,* Bd. 75, pp. 491-502, 2003.

[23] D. Faggembauu, M. Costa, M. Soria und A. Oliva, „Numerical analysis of the thermal behaviour of ventilated glazed facades in Mediterranean climates. Part I: development and validation of a numerical model," *Solar Energy,* Bd. 75, pp. 217-228, 2003.

[24] G. Baldinelli, „Double skin façades for warm climate regions: Analysis of a solution with an integrated movable shading system," *Building and Environment,* Bd. 44, Nr. 6, pp. 1107-1118, 2009.

[25] T.-t. Chow, Z. Lin, K.-f. Fong, L.-s. Chan und M.-m. He, „Thermal performance of natural airflow window in subtropical and temperate climate zones – A comparative study," *Energy Conversion and Management,* Bd. 50, pp. 1884-1890, 2009.

[26] A. Guardo, M. Coussirat, E. Egusquiza, P. Alavedra und R. Castilla, „A CFD approach to evaluate the influence of construction and operation parameters on the performance of Active Transparent Façades in Mediterranean climates," *Energy and Buildings,* Bd. 41, Nr. 5, pp. 534-542, 2009.

[27] G. Gan, „Impact of computational domain on the prediction of buoyancy-driven ventilation cooling," *Building and Environment,* Bd. 45, Nr. 5, pp. 1173-1183, 2010.

[28] C. Suárez, P. Joubert, J. L. Molina und F. J. Sánchez, „Heat transfer and mass flow correlations for ventilated facades," *Energy and Buildings,* Bd. 43, Nr. 12, pp. 3696-3703, 2011.

[29] F. P. López, R. Jensen, P. Heiselberg und M. R. d. A. Santiago, „Experimental analysis and model validation of an opaque ventilated facade," *Building and Environment,* Bd. 56, pp. 265-275, 2012.

[30] M. Bhamjee, A. Nurick und D. Madyira, „An experimentally validated mathematical and CFD model of a supply air window: Forced and natural flow," *Energy and Buildings,* Bd. 57, pp. 289-301, 2013.

[31] E. Sanvicente, S. Giroux-Julien, C. Ménézo und H. Bouia, „Transitional natural convection flow and heat transfer in an open channel," *International Journal of Thermal Sciences,* Bd. 63, pp. 87-104, 2013.

[32] J. S. Carlos und H. Corvacho, „Evaluation of the thermal performance indices of a ventilated double window through experimental and analytical procedures: Uw-values," *Rewnewable Energy,* Bd. 63, pp. 747-754, 2014.

[33] W. Pasut und M. De Carli, „Evaluation of various CFD modelling strategies in predicting airflow and temperature in a naturally ventilated double skin façade," *Applied Thermal Engineering,* Bd. 37, pp. 267-274, 2012.

[34] R. Safer, M. Woloszyn und J. Roux, „Three-dimensional simulation with a CFD tool of the airflow phenomena in single floor doubleskin facade equipped with a venetian blind," *Solar Energy,* Nr. 79, pp. 193-203, 2005.

[35] M. Collins, S. Tasnim und J. Wright, „Determination of convective heat transfer for fenestration with between-the-glass louvered shades," *International Journal of Heat and Mass Transfer,* Nr. 51, pp. 2742-2751, 2008.

[36] M. Collins, S. Tasnim und J. Wright, „Numerical analysis of convective heat transfer in fenestration with between-the-glass louvered shades," *Building and Environment,* Bd. 44, Nr. 10, pp. 2185-2192, 2009.

[37] R. Dalal, D. Naylor und D. Roeleveld, „A CFD study of convection in a double glazed window with an enclosed pleated blind," *Energy and Buildings,* Nr. 41, pp. 1256-1262, 2009.

[38] J. Han, L. Lu und H. Yang, „Numerical evaluation of the mixed convective heat transfer in a double-pane window integrated with see-through a-Si PV cells with low-e coatings," *Applied Energy,* Nr. 87, pp. 3421-3437, 2010.

[39] J. Han, L. Lu, J. Peng und H. Yang, „Performance of ventilated double-sided PV façade compared with conventional clear glass façade," *Energy and Buildings,* Bd. 56, pp. 204-209, 2013.

[40] O. Zogou und H. Stapountzis, „Flow and heat transfer inside a PV/T collector fo rbuilding application," *Applied Energy,* Nr. 91, pp. 103-115, 2012.

[41] B. Brinkworth, R. Marshall und Z. Ibarahim, „A validated model of naturally ventilated PV cladding,"

Solar Energy, Bd. 69, Nr. 1, pp. 67-81, 2000.

[42] R. Charron und A. K. Athienitis, „Optimization of the performance of double-façades with integrated photovoltaic panels and motorized blinds," *Solar Energy,* Bd. 80, Nr. 5, pp. 482-491, 2006.

[43] G. Y. Yun, M. McEvoy und K. Steemers, „Design and overall energy performance of a ventilated photovoltaic façade, Solar Energy," *Solar,* Bd. 81, Nr. 3, pp. 383-394, 2007.

[44] B. Jiang, J. Ji und H. Yi, „The influence of PV coverage ratio on thermal and electrical performance of photovoltaic-Trombe wall," *Renewable Energy,* Bd. 33, Nr. 11, pp. 2491-2498, 2008.

[45] G. Gan, „Numerical determination of adequate air gaps for building-integrated photovoltaics," *Solar Energy,* Bd. 83, Nr. 8, pp. 1253-1273, 2009.

[46] B. K. Koyunbaba und Z. Yilmaz, „The comparison of Trombe wall systems with single glass, double glass and PV panels," *Renewable Energy,* Bd. 45, pp. 111-118, 2012.

[47] G. Lau, E. Sanvicente, G. Yeoh, V. Timchenko, M. Fossa, C. Ménézo und S. Giroux-Julien, „Modelling of natural convection in vertical and tilted photovoltaic applications," *Energy Buildings,* Bd. 55, pp. 810-822, 2012.

[48] J. Cipriano, G. Houzeaux, D. Chemisana, C. Lodi und J. Martí-Herrero, „Numerical analysis of the most appropriate heat transfer correlations for free ventilated double skin photovoltaic façades," *Applied Thermal Engineering,* Bd. 57, Nr. 1-2, pp. 57-68, 2013.

[49] W. Sun, J. Luo und W. He, „Performance of PV-Trombe wall in winter correlated with south facade design," *Applied Energy,* Nr. 88, pp. 224-231, 2011.

[50] Y. Liu, D. Wang, C. Ma und J. Liu, „A numerical and experimental analysis of the air vent management and heat storage characteristics of a trombe wall," *Solar Energy,* Bd. 91, pp. 1-10, 2013.

[51] P. Kaltenecker und R. Sterrer, „Experimentelle Untersuchung der Funktionalität eines solaraktiven Fassadenpaneels," (in the course of the project ''B02 enVELOP Teil C"). FH Technikum ViennaWien (not published), 2013.

[52] A. Zöllner, E. Winter und R. Viskanta, „Experimental studies of combined heat transfer in turbulent mixed convection fluid flows in double-skin-façades," *International Journal of Heat and Mass Transfer,* Bd. 45, pp. 4401-4408, 2002.

[53] U. Eicker, V. Fux, U. Bauer, L. Mei und D. Infield, „Façades and summer performance of buildings," *Energy and Buildings,* Bd. 40, pp. 600-611, 2008.

[54] F. Kuznik, T. Catalina, L. Gauzere, M. Woloszyn und J.-J. Roux, „Numerical modelling of combined heat transfers in a double skin façade – Full-scale laboratory experiment validation," *Applied Thermal Engineering,* Bd. 31, Nr. 14-15, pp. 3043-3054, 2011.

[55] P. Strachan und V. Vandaele, „Case studies of outdoor testing and analysis of building components," *Building and Environment,* Nr. 43, pp. 1-10, 2008.

[56] L. H. Mortensen, C. Rode und R. Peuhkuri, „Investigation of airflow patterns in a microclimate by particle image velocimetry (PIV)," *Building and Environment,* Nr. 43, pp. 1929-1938, 2008.

[57] D. Brandl, T. Mach, M. Grobbauer, U. Ruisinger und C. Hochenauer, „Analysis of Natural Convection and Heat Transfer for Traditional Box Type Windows," *International Journal on Energy Conversion,* Bd. 1, Nr. 6, pp. 278-287, 2013.

[58] D. Brandl, T. Mach, M. Grobbauer, U. Ruisinger und C. Hochenauer, „Analysis of the thermal behaviour of historical box type windows for renovation concepts with CFD," *Sustainable Building Conference 2013,* Nr. 1, pp. 181-194, 2013.

[59] D. Brandl, T. Mach und W. Lerch, „Box Type Windows," *SHC IEA TASK 47,* pp. 86-99, 2015.

[60] T. Mach, M. Grobbauer, W. Streicher und M. Müller, mppf-The Multifunctional Plug&Play Approach in Facade Technology, Graz: Verlag der Technischen Universität Graz, 2015.

[61] D. Brandl und T. Mach, „Flow Characteristics of Multifunctional Facade Constructions," in *The Multifunctional Plug&Play Approach in Facade Technology*, Graz, Verlag der Technischen Universität Graz, 2015, pp. 115-134.

Literature

[62] D. Brandl, T. Mach, M. Grobbauer und C. Hochenauer, „Analysis of ventilation effects and the thermal behaviour of multifunctional facade elements with 3D CFD models," *Energy and Buildings,* Nr. 85, pp. 305-320, 2014.

[63] H. Gamerith, K. Höfler, G. Vabitsch, H. Ferk und E. Reiterer, „historical windows: Criteria for the determination of the conservation worthiness of historical windows," Graz, 1997.

[64] R. Müller, wooden windows: structure, damage, renovation, service, Köln: Rudolf-Müller, 2011.

[65] D. Appelfeld und S. Svendsen, „Experimental analysis of energy performance of a ventilated window for heat recovery under controlled conditions," *Energy and Buildings,* Nr. 43, pp. 3200-3207, 2011.

[66] J. Duffie und W. Beckman, Solar engineering of thermal processes, second edition, a Wiley-Interscience Publication: John Wiley & Sons, Inc., 1991.

[67] H. C., *Angewandte Wärmeübertragung und Heizflächenauslegung, Skriptum für Wärmetechnik 2, Teil 2, Technische Universität Graz.*

[68] D. Brandl, T. Mach, P. Kaltenecker, R. Sterrer, C. Neururer, M. Treberspurg und C. Hochenauer, „CFD assessment of a solar honeycomb (SHC) facade element with integrated PV cells," *Solar Energy,* Nr. 118, pp. 155-174, 2015.

[69] *gap-solution GmbH (http://www.gap-solutions.at/referenzen/referenzen/).*

[70] M. G. A. Coussirat, E. Jou, E. Egsquiza, E. Cuerva und P. Alavedra, „Performance and influence of numerical sub-models on the CFD simulation of free and forced convection in doubleglazed ventilated facades," *Energy and Buildings,* Nr. 40, pp. 1781-1789, 2008.

[71] N. Kaushika and K. Sumathy, "Solar transparent insulation materials: a review," *Renewable and Sustainable Energy Reviews,* vol. 7, pp. 317-351, 2003.

[72] H. Kessentini, R. Capdevila, J. Castro, A. Oliva und C. Bouden, „Three dimensional heat transfer analysis of combined conduction and radiation in honeycomb transparent insulation," *Solar Energy,* Bd. 105, pp. 58-70, 2014.

[73] *Gap3 solutions GmbH, Welser Str. 41, A-4060 Leonding <http://gap-solution.at>.*

[74] *meteonorm V7.1.2.15160.*

[75] D. Brandl, T. Mach und C. Hochenauer, „Analysis of the transient thermal behaviour of a solar honeycomb (SHC) facade element with and without integrated PV cells," *Solar Energy,* Nr. 123, pp. 1-16, 2016.

[76] *Zentralanstalt für Meteorologie und Geodynamik (www.zamg.ac.at).*

[77] S. Cristina, J. S. María, B. Eduardo und d. R. H. María, „Development and experimental validation of a simulation model for open joint ventilated façades," *Energy and Buildings,* Bd. 43, Nr. 12, pp. 3446-3456, 2011.

[78] H. Manz, A. Schaelin und H. Simmler, „Airflow patterns and thermal behavior of mechanically ventilated glass double facades," *Building and Environment,* Nr. 39, pp. 1023-1033, 2004.

[79] C. Sanjuan, M. Suarez, E. Blanco und M. Heras, „Experimental analysis of natural convection in open joint ventilated facades with 2D PIV," *Building and Environment,* Nr. 46, pp. 2314-2325, 2011.

[80] D. Brandl, M. Grobbauer und T. Mach, *CFD Untersuchung der Aufheizungs- und Strömungseffekte am Science Tower (not published).*

[81] A. Kay und M. Grätzel, „Low cost photovoltaic modules based on dye sensitized nanocrystalline titanium dioxide and carbon powder," *Solar Energy Materials and Solar Cells,* Bd. 44, Nr. 1, 1996.

[82] G. Quesada, D. Rousse, Y. Dutil, M. Badache und S. Hallé, „A comprehensive review of solar facades. Opaque solar facades," *Renewable and Sustainable Energy Reviews,* Nr. 16, pp. 2820-2832, 2012.

[83] G. Quesada, D. Rousse, Y. Dutil, M. Badache und S. Hallé, „A comprehensive review of solar facades. Transparent and translucent solar facades," *Renewable andSustainable Energy Reviews,* Nr. 16, pp. 2643-2651, 2012.

8 Abbreviations

AG	acryl glass
Al	aluminium
BC	boundary condition
BTW	Box Type Window
buoy	buoyancy
C	cellulose
CFD	Computational Fluid Dynamics
CPU	central processing unit
DO	Discrete Ordinate
DR	diffusive radiation
EPS	extruded polystyrene
ext	exterior (environment)
G	glass
GHR	horizontal measured global radiation
HVAC	heating, ventilation and cooling
int	interior (room)
IR	actual incident radiation
KLW	transition k-kl-ω turbulence model
LDV	Laser Doppler Velocimetry
mag	magnitude
max	maximum
MP	measurement position
MPPF	Multifunctional Plug and Play Façade
mw	mineral wool
P1	P1 radiation model
PIV	Particle Image Velocimetry
PV	photovoltaics
PPV	electrical activated photovoltaic
RKE	Realizable k-ε turbulence model
RNG	Re-Normalisation Group k-ε turbulence model
RW	rear wall
SHC	solar honey comb
SKE	Standard k-ε turbulence model
SKW	Standard k-ω turbulence model
SST	SST k-ω turbulence model
St	(unalloyed) steel
ST	solar thermal
S2S	Surface to surface radiation model
TR	transparent
URF	Under-Relaxation Factors

9 Nomenclature

abs_{Sol}	solar surface absorption coefficient $[-]$	
A_F	façade surface $[m^2]$	
A_{PV}	PV area ratio $[-]$	
AR	window/cavity aspect ratio $[-]$	
A_W	window fraction of the façade's surface $[m^2]$	
a	thermal diffusivity $[m^2/s]$	
a_R	absorption coefficient $[-]$	
a_γ	spectral absorption coefficient $[-]$	
$C_1, C_{1\varepsilon}, C_2, C_{2\varepsilon}, C_\mu$	$k - \varepsilon$ turbulence model constants $[-]$	
c	speed of sound $[m^2/s]$	
c_p	specific heat capacity $[J/(kg \cdot K)]$	
E	total energy $[J]$	
EO	electrical output $[kWh]$	
$diff_{Sol}$	solar radiation diffusivity coefficient $[-]$	
$\vec{F}$	external body force $[kg/(m^2 \cdot s^2)]$	
G_b	generation of turbulent kinetic energy due to the mean velocities gradients $[-]$	
G_k	generation of turbulent kinetic energy due to buoyancy $[-]$	
Gr	Grashof number $[-]$	
$g, \vec{g}$	gravity acceleration $[m/s^2]$	
h	enthalpy $[J/kg]$	
H_{BTW}	box type window's height $[m]$	
H_{ac}	air cavity's height $[m]$	
I	radiation intensity $[W/sr]$	
$I_{b\gamma}$	black body radiation intensity $[W/sr]$	
I_γ	spectral radiation intensity $[W/sr]$	
I_0	incident radiation intensity $[W/sr]$	
I_{Heat}	Thermal radiation $[W/m^2]$	
I_{Sol}	solar radiation $[W/m^2]$	
$I_{Sol,long}$	long wave fraction of the solar radiation $[W/m^2]$	
$I_{Sol,short}$	short wave fraction of the solar radiation $[W/m^2]$	
J	mass flux $[kg/(m^2 \cdot s)]$	
k	kinetic energy $[J/kg]$	
L, l	characteristic length $[m]$	
L_{BTW}	box type window's length $[m]$	
L_{ac}	air cavity's length $[m]$	
$\dot{m}$	mass flow $[kg/s \, ; kg/h]$	
Ma	Mach number $[-]$	
M_W	molecular weight $[mol]$	
n	refractive index $[-]$	
Nu	Nusselt number $[-]$	
P	power $[W]$	
p	static pressure $[Pa]$	
p_{op}	operating pressure $[Pa]$	
$\dot{Q}_{Vent}$	ventilation performance $[W; J/s]$	
q	surface heat flux $[W/m^2]$	
$\dot{q}_Q$	heat source $[W/m^2]$	
R	gas constant $[J/(mol \cdot K)]$	

Nomenclature

R_S	specific gas constant $[J/(kg \cdot K)]$
$\vec{r}$	radiation position vector $[-]$
r_{glass}	reflection coefficient of glass $[-]$
r	reflection coefficient $[-]$
Ra	Rayleigh number $[-]$
Re	Reynolds number $[-]$
$RMSE$	root mean square error $[-]$
s	radiation path length $[-]$
$\vec{s}$	radiation direction vector $[-]$
$\vec{s}'$	scattering direction vector $[-]$
S_k, S_ε	turbulence source terms $[-]$
S_h	energy source $[J/(m^2 \cdot s)]$
S_m	mass source $[kg/(m^2 \cdot s)]$
T	temperature $[°C \; ; \; K]$
T_{dim}	dimensionless temperture $[-]$
T_h	heater surface temperature $[°C]$
ΔT	temperature difference $[K]$
ΔT_{m-s}	difference between measured and simulated temperature $[K]$
T_s	surface temperature $[K]$
T_∞	fluid temperature outside the influence of the surface $[K]$
T_{abs}	absolute temperature $[K]$
t	time $[s]$
U, U_W	U value $[W/(m^2 \cdot K)]$
u_τ	friction velocity $[m/s]$
v	velocity $[m/s]$
$\vec{v}$	velocity vector $[m/s]$
v_0	reference velocity $[m/s]$
v_{abs}	magnitude of velocity $[m/s]$
v_{Wind}	wind speed $[m/s]$
v_y, v_{buoy}	buoyancy velocity $[m/s]$
Δv	velocity difference $[m/s]$
W_{BTW}	box type window's width $[m]$
W_{ac}	air cavity's width $[m]$
x	characteristic length $[m]$
y	predicted value (mean value) $[-]$
$\hat{y}$	measured value $[-]$
y_c	size of the cell adjacent to the wall $[m]$
Y_M	contribution of the fluctuating dilatation in compressible turbulence to the overall dissipation rate $[-]$
y^+	dimensionless wall distance $[-]$
α	absorption coefficient $[1/m]$
$\alpha_\varepsilon, \alpha_k$	inverse effective Prandtl number $[-]$
α_{glass}	absorption coefficient of glass $[-]$
α_S	characteristic swirl number $[-]$
α_{long}	long wave absorbtivity of a surface $[-]$
α_{short}	short wave absorbtivity of a surface $[-]$
α_{Sol}	Angle of incident solar radiation $[°]$
β	volumetric thermal expansion coefficient $[1/K]$
γ	wavelength $[\mu m]$
ε	turbulent dissipation rate $[m^2/s^3]$
ϑ	characteristic temperature $[K]$

Nomenclature

ϑ_W	surface temperature $[K]$	
ϑ_0	bulk temperature $[K]$	
κ	isentropic exponent $[-]$	
λ	thermal conductivity $[W/(m \cdot K)]$	
λ_{eff}	effective thermal conductivity $[W/(m \cdot K)]$	
λ_{ES}	wave length (electromagnetic spectrum) $[\mu m]$	
μ	dynamic viscosity $[Pa\ s]$	
μ_{eff}	effective turbulent viscosity $[Pa\ s]$	
μ_t	turbulent viscosity $[Pa\ s]$	
ν	kinematic viscosity $[m^2/s]$	
ρ	density $[kg/m^3]$	
σ	$Stefan-Boltzmann\ constant\ (5.669E-8\ [W/(m^2 \cdot K^4)]$	
$\sigma_k, \sigma_\varepsilon$	turbulent Prandtl numbers $[-]$	
σ_S	scattering coefficient $[-]$	
τ	stress $[Pa]$	
$\bar{\bar{\tau}}$	stress tensor $[Pa]$	
$(\tau_{ij})_{eff}$	deviatoric stress tensor $[Pa]$	
τ_{short}	short wave transmissivity of a surface $[-]$	
τ_{Sol}	solar surface transmission coefficient $[-]$	
τ_w	wall shear stress $[kg/(m \cdot s^2)]$	
Φ	phase function $[-]$	
Ω'	solid angle $[-]$	

10 List of Figures

List of Figures

List of Figures

List of Figures

11 List of Tables